

Comment Edition

N9370636

Infrared Detector Technology Workshop

Compiled by Craig R. McCreight

NASA LIBRARY
JOHN F. KENNEDY CENTER
HOUSTON FIELD, CALIF.

August 1983

| |
|-------------|
| COPY NO. |
|-------------|

(NASA-TM-108110) INFRARED DETECTOR
TECHNOLOGY WORKSHOP (NASA) 344 p

N93-70636
--THRU--
N93-70652
Unclass

Z9/74 0133804



Comment Edition

Infrared Detector Technology Workshop

Craig R. McCreight, Ames Research Center, Moffett Field, CA 94035



National Aeronautics and
Space Administration

Ames Research Center
Moffett Field, California 94035

TABLE OF CONTENTS

| | <u>Page</u> |
|---|-------------|
| FOREWORD | v |
| AGENDA | vi |
| IR DETECTOR WORKSHOP ATTENDEES | viii |
| A BRIEF REVIEW OF THE IRAS DETECTORS | 1-1 |
| <i>J. R. Houck</i> | |
| IMPROVED FABRICATION TECHNIQUES FOR INFRARED BOLOMETERS | 2-1 |
| <i>A. E. Lange, E. Kreysa, S. E. McBride, P. L. Richards,</i> <i>and E. E. Haller</i> | |
| PERFORMANCE OF Ge:Ga FAR INFRARED DETECTORS | 3-1 |
| <i>M. R. Hueschen, P. L. Richards, and E. E. Haller</i> | |
| DEVELOPMENT OF INTEGRATING JET PREAMPLIFIERS | 4-1 |
| <i>F. J. Low and E. T. Young</i> | |
| Ge:Be FAR INFRARED PHOTOCONDUCTORS | 5-1 |
| <i>N. M. Haegel, E. E. Haller, W. L. Hansen, M. R. Hueschen,</i> <i>P. N. Luke, P. L. Richards, C. H. Townes, and D. M. Watson</i> | |
| NEUTRON TRANSMUTATION DOPED Ge BOLOMETERS | 6-1 |
| <i>E. E. Haller, E. Kreysa, N. P. Palaio, P. L. Richards,</i> <i>and M. Rodder</i> | |
| 0.1K BOLOMETERS COOLED BY ADIABATIC DEMAGNETIZATION | 7-1 |
| <i>T. Roellig, L. Lesyna, P. Kittel, and M. Werner</i> | |
| DESIGN CONSIDERATIONS FOR 0.1K BOLOMETERS | 8-1 |
| <i>Harvey Moseley</i> | |
| REVIEW OF AMCID TECHNOLOGY | 9-1 |
| <i>C. M. Parry</i> | |
| CONCEPTUAL DESIGN OF A MULTIPLEXED Ge:Ga DETECTOR ARRAY | 10-1 |
| <i>C. M. Parry</i> | |
| LOW BACKGROUND IR DETECTOR AND DETECTOR ARRAY EVALUATIONS | 11-1 |
| <i>J. H. Goebel, D. A. Jared, J. H. Lee, C. R. McCreight,</i> <i>M. E. McKelvey, and P. S. Stafford</i> | |
| UCSD IR DETECTOR DEVELOPMENT PROGRAMS | 12-1 |
| <i>B. Jones, R. Puetter, R. Heir, A. Schmidt, J. Casler,</i> <i>S. Nelson, and J. Hujsak</i> | |
| SI:B1 ARRAY DETECTORS AND ASTRONOMICAL APPLICATIONS OF THE GODDARD 10 MICRON CAMERA | 13-1 |
| <i>Gerald Lamb, Daniel Gezari, Peter Shu, Richard Tresch-Fienberg,</i> <i>Giovanni Fazio, and William Hoffman</i> | |

| | |
|--|---------------------|
| A MOSAIC INFRARED SENSOR FOR SPACE ASTRONOMY | <u>Page</u> 14-1 |
| <i>Ashok K. Sood and Nancy Boggess</i> | |
| HYBRID SILICON FOCAL PLANE ARRAYS | 15-1 |
| <i>D. Pommerrenig, D. Enders, L. Trousil, R. Capps, E. Irwin,</i> | |
| <i>E. Tollestrup, and E. Dereniak</i> | |
| EVALUATION OF A 32x32 InSb CCD FOR USE IN ASTRONOMY | 16-1 |
| <i>W. J. Forrest and J. L. Pipher</i> | |
| InSb ARRAY TECHNOLOGY IN ASTRONOMY AT KITT PEAK NATIONAL OBSERVATORY | 17-1 |
| <i>A. M. Fowler and J. P. Britt</i> | |
| INTEGRATING INDIUM ANTIMONIDE LINEAR ARRAYS AT 65K AND BELOW | 18-1 |
| <i>Gary C. Bailey</i> | |

Foreword

By the fall of 1982 it was clear that a workshop on infrared detector technology was needed to help in planning NASA's future space astronomy missions. The infrared scientific community needed an opportunity to explore the status of this technology in depth, in an open forum where there could be a good exchange of information and discussion.

The workshop was organized to be a review and discussion of all the astronomical infrared detector research supported by NASA within the Office of Space Science and Applications (OSSA) and the Office of Aeronautics and Space Technology (OAST). The technologies of both discrete detectors and integrated detector arrays were included. Additional presentations describing related work and a review of the detector technology used in the highly successful Infrared Astronomical Satellite (IRAS) mission were given. The large attendance by the scientific community, industry, and government is indicative that there is a great deal of interest in this area, and that real progress has been and is being made.

The theme of the meeting was technology for low-background space infrared astronomical applications. The speakers were encouraged to comment on the extent to which the performance of devices has actually been proven, and the availability and relative maturity of detectors. In this regard, the presentation on the detectors in use on IRAS, including their successes and their limitations, served as a good starting point.

At the close of the workshop, invited summary statements were given by P. Richards, U. California, Berkeley, R. Capps, U. Hawaii, and E. Young, U. Arizona. Among the points made was the view that some very significant and encouraging progress had been presented, in terms of improved sensitivity of detector systems, and in identifying the usefulness of arrays. The summaries emphasized that a great deal remains to be done, that continued research is needed in both the new and the more established technologies if we are to capitalize fully on the capabilities of telescopes in space. The Announcement of Opportunity for the Shuttle Infrared Telescope Facility (SIRTF) has been released; advances in detector technology are needed now to greatly enhance the scientific return from this major astronomical facility of the future. SIRTF and other future space opportunities present tremendous technical challenges in advancing the capabilities of scientific instrumentation. Financial and intellectual resources, and determination, need to be applied if we are to meet these challenges.

Craig R. McCreight
Ames Research Center

Nancy W. Boggess
NASA Headquarters

AGENDA

Infrared Detector Technology Workshop
NASA Ames Research Center
Auditorium, Building 201*

Tuesday, July 12, 1983

- | | | |
|-------|---|---|
| 8:30 | Introductory Remarks | N. W. Boggess (NASA Headquarters) |
| | Opening Remarks | C. R. McCreight (Ames Research Center) |
| 9:00 | IR Detector Applications in Space Astronomy/IRAS Detector Anomalies | J. R. Houck (Cornell U.) |
| | "Performance of Gallium-Doped Germanium Far-Infrared Photoconductors" | M. R. Hueschen (Hewlett-Packard), P. L. Richards, E. E. Haller (U. California) |
| 10:15 | Break | |
| 10:40 | Extrinsic Photoconductor and Preamplifier Development | F. J. Low, E. T. Young (U. Arizona) |
| | "Progress Report on Ge:Ga and Ge:Be Extrinsic Photoconductors" | E. E. Haller, N. Haegel (UC/Lawrence Berkeley Laboratory) |
| | "Neutron Transmutation Doped Ge for Bolometers" | E. E. Haller, N. Palaio (UC/LBL) |
| 12:00 | Lunch | |
| 1:00 | "0.1 K Bolometers Cooled by Adiabatic Demagnetization" | T. Roellig, L. Lesyna, P. Kittel, M. Werner (Ames Research Center) |
| | "Design Considerations for 0.1 K Bolometers" | S. H. Moseley (Goddard Space Flight Center) |
| | "Accumulation Mode CID Technology" | C. M. Parry (Aerojet ElectroSystems Company) |
| 3:00 | Break | |
| 3:15 | "Low-Background IR Detector and Detector Array Evaluations" | J. H. Goebel, J. H. Lee, C. R. McCreight, M. E. McKelvey, P. S. Stafford (Ames Research Center) |
| | 2 x 64 Si:Bi CID Observing Experience | D. M. Rank (UC Santa Cruz) |

*Message Phone: (415) 965-5256, or FTS 448-5256

Wednesday, July 13, 1983

| | | |
|-------|---|--|
| 9:00 | Si:Bi Detectors and Arrays | B. Jones (UC San Diego) |
| | "Si:Bi AMCID Array Detectors and Astronomical Applications of the Goddard 10 Micron Camera" | G. Lamb, D. Gezari, P. Shu (Goddard Space Flight Center), G. Fazio, R. Tresch-Fellner (Center for Astrophysics), W. Hoffman (U. Arizona), C. McCreight (Ames Research Center) |
| 10:15 | Break | |
| 10:40 | "Si:x Array Experience" | J. F. Arens (U. California) |
| | 64 x 64 HgCdTe CCD Arrays | A. K. Sood (Honeywell Electro-Optics Center) |
| 12:00 | Lunch | |
| 1:00 | "Hybrid Silicon Focal Plane Arrays" | D. Pommerrenig (Rockwell International), R. Capps, E. Irwin, E. Tollestrip (U. Hawaii), E. Dereniak (U. Arizona), D. Enders, L. Trousil (Rockwell International) |
| | "Evaluation of a 32 x 32 InSb CCD for Use in Astronomy" | W. J. Forrest, J. L. Pipher (U. Rochester) |
| 2:20 | Break | |
| 2:30 | "InSb Array Technology in Astronomy at Kitt Peak National Observatory" | A. M. Fowler, P. B. Brit (KPNO) |
| | "Integrating Indium Antimonide Linear Arrays at 65 K and Below" | G. C. Bailey (Jet Propulsion Laboratory) |
| 4:00 | Summary and Conclusion | |

IR DETECTOR WORKSHOP ATTENDEES

| <u>NAME</u> | <u>ADDRESS</u> | <u>PHONE NO.</u> |
|--------------------|---|----------------------------|
| George Anderson | M.S. 245-6 NASA-Ames Research Center | 415-965-6586 |
| John F. Arens | Space Sciences Laboratory University of California Berkeley, CA 94720 | 415-642-7287 |
| Gordon W. Autio | Lockheed Palo Alto Research Labs 3251 Hanover St. Palo Alto, CA 94304 | 415-493-4411 Ext. 45227 |
| Gary Bailey | Jet Propulsion Laboratory Mail Code 11-116 4800 Oak Grove Dr. Pasadena, CA 91109 | 213-354-3462 |
| Frank Bartko | Martin-Marietta PO Box 179 Denver, CO 80201 | 303-977-4120 |
| Eric Becklin | Institute for Astronomy University of Hawaii 2680 Woodlawn Dr. Honolulu, HI 96822 | 808-926-2126 |
| Ramesh Bharat | Rockwell International 3370 Miraloma Ave. Anaheim, CA 92667 | 714-632-1428 |
| Donald E. Bode | Santa Barbara Research Center 75 Coromar Drive Goleta, CA 93110 | 805-968-3511 Ext. 2377 |
| Nancy W. Boggess | NASA Headquarters, Code EZ-7 Washington, DC 20546 | 202-755-3800 |
| Michael Blessinger | Jet Propulsion Laboratory 11-116 4800 Oak Grove Dr. Pasadena, CA 91109 | 213-354-4866 |
| Jesse Bregman | M.S. 245-6 NASA-Ames Research Center | 415-965-6136 |
| Paul Callary | Lockheed Palo Alto Research Labs Org 52-54, Bldg. 201 3251 Hanover St. Palo Alto, CA 94304 | 415-493-4411 Ext. 5513 |

| | | |
|-----------------|---|--------------------------|
| Rich Capps | Institute for Astronomy 2680 Woodlawn Dr. Honolulu, HI 96822 | 808-948-8429 |
| Jack G. Carlin | Santa Barbara Research Center 75 Coromar Drive Goleta, CA 93110 | 805-968-3511 |
| Rudy Decher | NASA Marshall Space Flight Center ES-61 Huntsville, AL 35812 | 205-453-5130 |
| P.B. Duffy | M.S. 245-6 NASA-Ames Research Center | 415-965-5511 |
| Bill Dyer | Honeywell EOD 2 Forbes Road Lexington, MA 02173 | 617-863-3274 |
| W.L. Eisenman | Naval Ocean Systems Center Code 5521 San Diego, CA 92152 | 619-225-6591 |
| Jan Emming | Ball Aerospace TT-5 PO Box 1062 Boulder, CO 80301 | 303-441-4124 |
| Don Enders | Rockwell (Seal Beach) 2546 N. Forest Ave. Santa Ana, CA 92706 | 213-594-3306 |
| Byron G. Fehler | Cincinnati Electronics Corp. 2630 Glendale-Milford Rd. Cincinnati OH 45241 | 513-563-6000 Ext. 281 |
| William Forrest | Dept. of Physics and Astronomy University of Rochester Rochester, NY 14627 | 716-275-4343 |
| Al Fowler | Kitt Peak National Observatory Box 26732 Tucson, AZ 85726 | 602-325-9339 |
| Steve Gaalema | Hughes Aircraft Company 6155 El Camino Real M.S. 102 Carlsbad, CA 92008 | 619-438-9191 |
| Bob Gehrz | Dept. of Physics and Astronomy University Station Box 3905 University of Wyoming Laramie, WY 82071 | 307-766-6176 |

| | | |
|-------------------|---|--------------|
| John Goebel | M.S. 244-7 NASA-Ames Research Center | 415-965-6525 |
| Sherm Goleb | Lockheed Palo Alto Research Lab Org. 52-54, Bldg. 202 3251 Hanover St. Palo Alto, CA 94304 | 415-493-4411 |
| Gary Grasdalen | Dept. of Physics and Astronomy University of Wyoming Laramie, WY 82071 | 307-766-4385 |
| Richard Griffiths | Space Telescope Science Institute Homewood Campus Baltimore, MD 21218 | 301-338-4824 |
| Steve Grossman | Lockheed Palo Alto Research Lab Org. 52-54, Bldg. 202 3251 Hanover St. Palo Alto, CA 94304 | 415-493-4411 |
| John Hackwell | Dept. of Physics and Astronomy University of Wyoming University Station Box 3905 Laramie, WY 82071 | 307-766-6296 |
| Victor Hadek | Jet Propulsion Laboratory 4800 Oak Grove Dr. Pasadena, CA 91109 | 213-354-7054 |
| Nancy M. Haegel | Lawrence Berkeley Lab 70A/3363 University of California Berkeley, CA 94720 | 415-486-5632 |
| Eugene E. Haller | Lawrence Berkeley Lab 70A/3307 University of California Berkeley, CA 94720 | 415-486-5294 |
| D.A. Harper | Yerkes Observatory University of Chicago Williams Bay, WI 53191 | 414-245-5555 |
| Paul Harvey | Astronomy Department University of Texas Austin, TX 78712 | 512-471-4461 |
| S.R. Hawkins | Lockheed Palo Alto Research Lab Org. 52-54, Bldg. 202 3251 Hanover St. Palo Alto, CA 94304 | 415-493-4411 |
| Mark Herring | Jet Propulsion Laboratory M.S. 11-116 4800 Oak Grove Dr. Pasadena, CA 91109 | 213-354-7222 |

| | | |
|-----------------|--|---------------------------|
| J.R. Houck | Cornell University Dept. of Astronomy 220 Space Sciences Bldg. Ithaca, NY 14853 | 607-256-4805 |
| Mark Hueschen | Department of Physics University of California Berkeley, CA 94720 | 415-857-2834 |
| David Jared | M.S. 244-7 NASA-Ames Research Center | 415-965-5525 |
| Paul E. Johnson | Dept. of Physics and Astronomy Univ. of Wyoming Laramie, WY 82071 | 307-766-6150 |
| Dick Joyce | Kitt Peak National Observatory Box 26732 Tucson, AZ 85726 | 602-325-9323 |
| Barbara Jones | CASS, C-011, UC San Diego La Jolla, CA 92093 | 619-452-4066 |
| Peter Kittel | M.S. 244-7 NASA-Ames Research Center | 415-965-6525 |
| D.E. Kleinmann | Honeywell EOD/SSC 110 Fordham Rd. Wilmington, MA 01887 | 617-657-6100 Ext. 6110 |
| L.J. Kroko | 2822D Walnut Tustin, CA 92680 | 714-832-8761 |
| Andrew Lange | Dept. of Physics University of California Berkeley, CA 94720 | 415-642-4359 |
| Harold Larson | Lunar and Planetary Laboratory University of Arizona Tucson, AZ 85721 | 602-621-6495 |
| Jeff Lee | M.S. 244-7 NASA-Ames Research Center | 415-965-6525 |
| Larry Lesyna | M.S. 245-6 NASA-Ames Research Center | 415-965-5537 |
| Frank Low | Steward Observatory Univ. of Arizona Tucson, AZ 85721 | 602-621-2779 |

| | | |
|--------------------|---|--------------|
| Paul N. Luke | Lawrence Berkeley Lab 70A/3361 University of California Berkeley, CA 94720 | 415-486-5632 |
| Craig McCreight | M.S. 244-7 NASA-Ames Research Center | 415-965-6549 |
| Mark McKelvey | M.S. 244-7 NASA-Ames Research Center | 415-965-6525 |
| Harvey Moseley | Code 693.2 Goddard Space Flight Center Greenbelt, MD 20771 | 301-344-5758 |
| Kevin O'Brien | M.S. 245-6 NASA-Ames Research Center | 415-965-6151 |
| Steve O'Dell | Physics Department Virginia Tech Blacksburg, VA 24061 | 703-961-5186 |
| Chris Parry | Aerojet ElectroSystems Company Box 296 Azusa, CA 91702 | 213-812-2816 |
| Michael Peck | Space Sciences Lab University of California Berkeley, CA 94720 | 415-642-7287 |
| J.L. Pipher | Dept. of Physics and Astronomy Univ. of Rochester Rochester, NY 14627 | 716-275-4402 |
| Dieter Pommerrenig | Rockwell International SISSD Seal Beach, CA 90740 | 213-594-3621 |
| Ron Probst | M.S. 245-6 NASA-Ames Research Center | 415-965-6136 |
| Richard Puetter | CASS, C-011 UC San Diego La Jolla, CA 92093 | 619-452-4066 |
| Ruben Ramos | M.S. 244-15 NASA-Ames Research Center | 415-965-5698 |
| D.M. Rank | Lick Observatory University of California Santa Cruz, CA 95064 | 408-429-2277 |
| Paul Richards | Dept. of Physics University of California Berkeley, CA 94720 | 415-642-3027 |

| | | |
|-------------------|--|---------------------------|
| George Rieke | Steward Observatory University of Arizona Tucson, AZ 85721 | 602-621-2832 |
| Marcia Rieke | Steward Observatory University of Arizona Tucson, AZ 85721 | 602-621-2731 |
| Tom Roellig | M.S. 245-6 NASA-Ames Research Center | 415-965-5755 |
| George S. Rossano | M.S. M2-266 Aerospace Corporation P.O. Box 92957 Los Angeles, CA 90009 | 213-648-6426 |
| Ray Russell | M.S. M2-266 Aerospace Corporation PO Box 92957 Los Angeles, CA 90009 | 213-648-5528 Ext. 6960 |
| Ryan Sanders | University of Colorado/LASP Boulder, CO 80309 | 303-492-7177 |
| K. Shivanandan | Naval Research Laboratory Washington, DC 20375 | 202-767-2749 |
| Francois Sibille | Observatoire de Lyon 69230 Saint Genis Laval France | 33-7-856 0705 |
| Peter Silverglate | Perkin Elmer Corporation Space Science Division 100 Wooster Heights Rd. Danbury, CT 06810 | 203-797-5566 |
| Howard Smith | Code 4138 SM Space Science Division Naval Research Laboratory Washington, DC 20375 | 202-767-3050 |
| Ashok Sood | Honeywell EOD 2 Forbes Road Lexington, MA 02173 | 617-863-3100 |
| Paul Stafford | M.S. 244-7 NASA-Ames Research Center | 415-965-6525 |
| Wayne Stein | CASS, C-011, UC San Diego La Jolla, CA 92093 | 619-452-4066 |

| | | |
|-------------------------|---|--------------|
| Don Strecker | Ball Aerospace Systems Division TT-5 P.O. Box 1062 Boulder, CO 80306 | 303-441-4346 |
| Charles Telesco | NASA Marshall Space Flight Center ES-63 Huntsville, AL 35812 | 205-453-5132 |
| Rodger Thompson | Steward Observatory University Of Arizona Tucson, AZ 85721 | 602-621-1531 |
| Richard Tresch-Fienberg | Center for Astrophysics 60 Garden St. Cambridge, MA 02138 | 617-495-3774 |
| Eugene Urban | NASA Marshall Space Flight Center ES-63 Huntsville, AL 35812 | 205-453-5132 |
| Russ Walker | Jamieson Science and Engineering P.O. Box 11698A Palo Alto, CA 94306 | 415-858-2310 |
| R.E. Warren | Hughes Aircraft Company M.S. C106 Bldg. E1 Box 902 El Segundo, CA 90245 | 213-616-9530 |
| Michael Werner | M.S. 245-6 NASA-Ames Research Center | 415-965-5101 |
| Jim Wimmers | Cincinnati Electronics Corp. 2630 Glendale-Milford Rd. Cincinnati, OH 45241 | 513-563-6000 |
| Fred C. Witteborn | M.S. 245-6 NASA-Ames Research Center | 415-965-5520 |
| J.P. Wright | National Science Foundation Washington, DC 20550 | 202-357-7639 |
| G.W. Van Citters | National Science Foundation Washington, DC 20550 | 202-357-7639 |
| Erick Young | Steward Observatory University of Arizona Tucson, AZ 85721 | 602-621-4119 |

OMIT

A BRIEF REVIEW OF THE IRAS DETECTORS

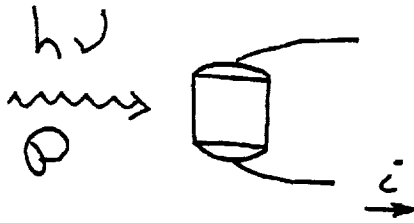
BY
J. R. HOUCK
CORNELL UNIVERSITY

SIXTY-TWO PHOTOCONDUCTIVE DETECTORS WITH ION IMPLANTED CONTACTS

| BAND | $\lambda_0[\mu\text{M}]$ | $\Delta\lambda$ | MATERIAL | SIZE (MM) ³ |
|------|--------------------------|-----------------|----------|---------------------------|
| 1 | 12 | 6.07 | SI:AS | 1 x 1.8 x .64 |
| 2 | 25 | 10.4 | SI:SB | 1 x 1.8 x .71 |
| 3 | 60 | 30.5 | GE:GA | 1.5 x 1.5 x 1 |
| 4 | 100 | 33.6 | GE:GA | 1.5 x 1.5 x 1.2 |

ALL OF THE DETECTORS OPERATE AT A COMMON FOCAL PLANE
TEMPERATURE OF 2.5 K. MORE OR LESS CONVENTIONAL TIA
AMPLIFIERS WITH COLD (~60 K) JFET STAGES IN THE FOCAL
PLANE ASSEMBLY ARE USED.

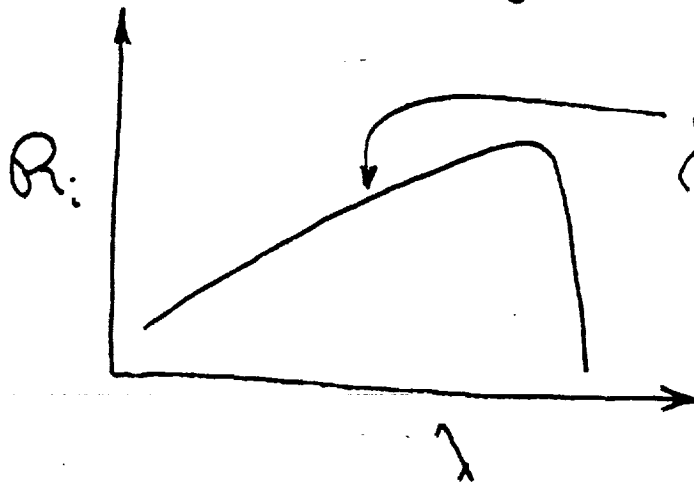
RESPONSIVITY



$$R_i = \frac{i}{P} = \frac{g e \dot{N}_e}{h\nu \dot{N}_p} = g \frac{e \epsilon}{h\nu}$$

g = photo. gain
 ϵ = quantum ef.

$$= 0.8 \epsilon g \lambda \quad [\text{Amps/watt}] \quad \lambda \text{ in } \mu\text{m}$$



OPTICAL DEPTH < 1
 (BECAUSE OF DROP
 IN PHOTOIONIZATION
 CROSS SECTION)?

ALSO

Fewer e^- 's/watt of
 photon power.

NOISE

$$NEP_{\text{BLIP}} = \left(4 h\nu P / \epsilon \right)^{1/2}$$

IRAS INFORMATION

| Band | λ | Optical Efficiency | NEP (E-17 W/Hz) | NEFD 10 per pass | RESPONSIVITY (A/W) |
|------|-----------|--------------------|-----------------|------------------|--------------------|
| 1 | 12 μ | .40 | 30 | 0.12 Jy | 0.5 |
| 2 | 25 | .31 | 6 | .10 | 2.4 |
| 3 | 60 | .33 | 10 | .13 | 1.8 |
| 4 | 100 | .13 | 6 | .42 | 2.2 |
| | | | | | <u>Added data</u> |

< 1 ARC MIN, sometimes < 0.5 arc min

- Pointing Control Error
- Reconstructed Pointing Error rms

12 arc sec cross scan
4 arc sec in scan

- % time lost in IRAS survey due to radiation hits

SAA - 10.1 %

Horns - variable

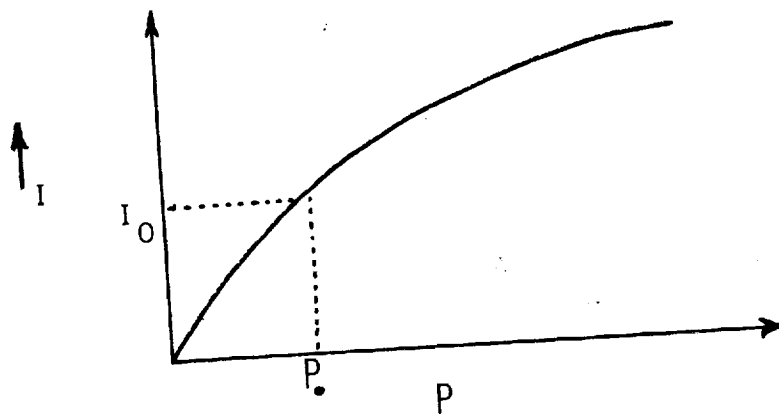
when strong 6.6 %
when weak 0.8 %

- Celestial background at 60, 100 μ m greater than previously thought

P R O B L E M S :

1. NONLINEAR - DETECTOR AND/OR R_L
2. IONIZING RADIATION SPIKES
3. SPONTANEOUS SPIKES
4. MEMORY, HOOK, TWO TIME CONSTANT EFFECTS
5. NONUNIFORM ILLUMINATION
6. ELECTRONIC PICKUP

NONLINEAR RESPONSE



NOTE:

1. R_L 'S MAY BE VOLTAGE DEPENDENT.
2. $R_I(AC) \neq R_I(DC)$
3. IN CAPACITIVE SYSTEMS THE STORAGE CAPACITOR MAY BE VOLTAGE DEPENDENT.
4. SPECIALLY SELECTED AND CALIBRATED LOAD RESISTORS ARE USED IN IRAS.

IONIZING RADIATION

1. PROTONS (≈ 40 MeV) IN SAA
2. ELECTRONS (\sim FEW MeV) IN POLAR HORNS

SPIKES

VERY FAST RISE TIME (SLEW-RATE LIMITED)

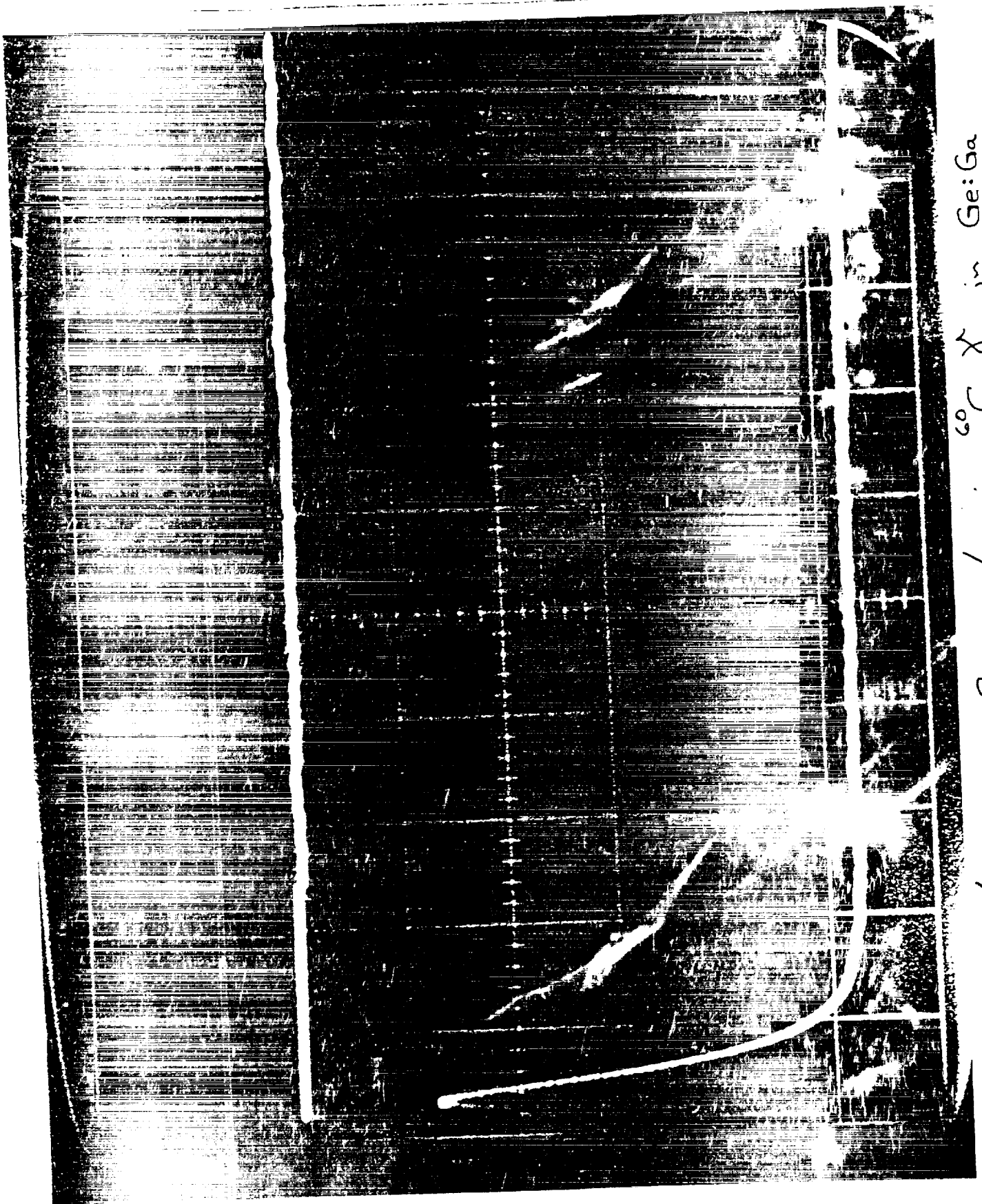
SLOW FALL TIME (RC LIMITED)

CAN BE 10'S OF MV TO VOLTS HIGH

RESPONSIVITY EFFECT

1. THE RESPONSIVITY INCREASES WITH EXPOSURE
2. THE RESPONSIVITY FALLS EXPONENTIALLY AFTER EXPOSURE
3. ANNEALED BY BIAS BOOST (OR HEATING)

ORIGINAL PAGE IS
OF POOR QUALITY



10 mv/div Φ 2 vms/div ^{60}Co γ in Ge:Ga

SAA
BAND 4
Ge: Ga

2 STIM. FLASHES

256
seconds

TIME

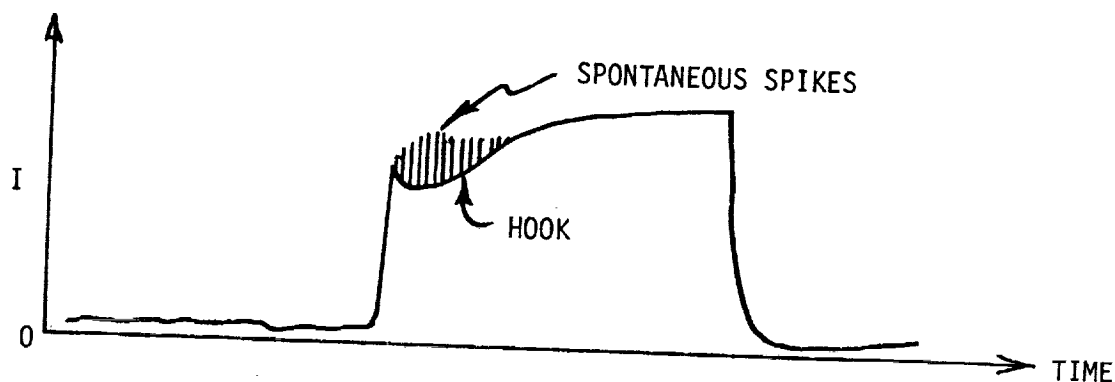
ORIGINAL PAGE IS
OF POOR QUALITY

S P O N T A N E O U S S P I K E S

FAST SPIKES ASSOCIATED WITH SOME FORM OF INTERFACIAL
BREAKDOWN (SEE LITERATURE ON UNIPOLAR SEMICONDUCT-
ING DEVICES).

USUALLY ASSOCIATED WITH CHANGING SIGNAL POWER.

MEMORY, HOOK...

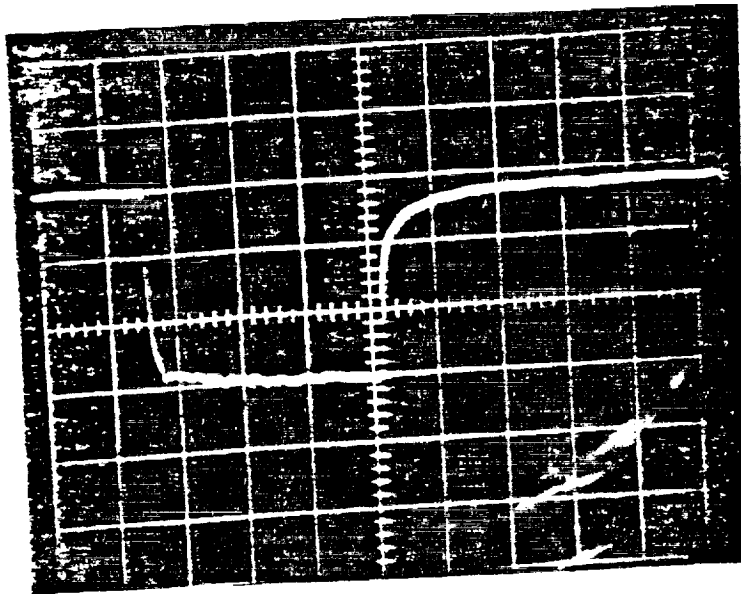


THE LEADING TIP OR HOOK MAY BE LARGER OR SMALLER THAN THE EVENTUAL HEIGHT.

MOST OFTEN SEEN WHEN SIGNAL INCREASES FROM A LOW LEVEL TO A HIGHER ONE.

NOTE: BOTH SPONTANEOUS SPIKES AND MEMORY EFFECTS ARE STRONGLY CORRELATED WITH BIAS. THESE EFFECTS CAN BE REDUCED BY LOWERING THE BIAS WITH A RESULTANT (PERHAPS LARGE) LOSS IN PHOTOCONDUCTIVE GAIN BUT NOT QUANTUM EFFICIENCY.

$$P = 3.37 \times 10^{-13} \text{ W}$$

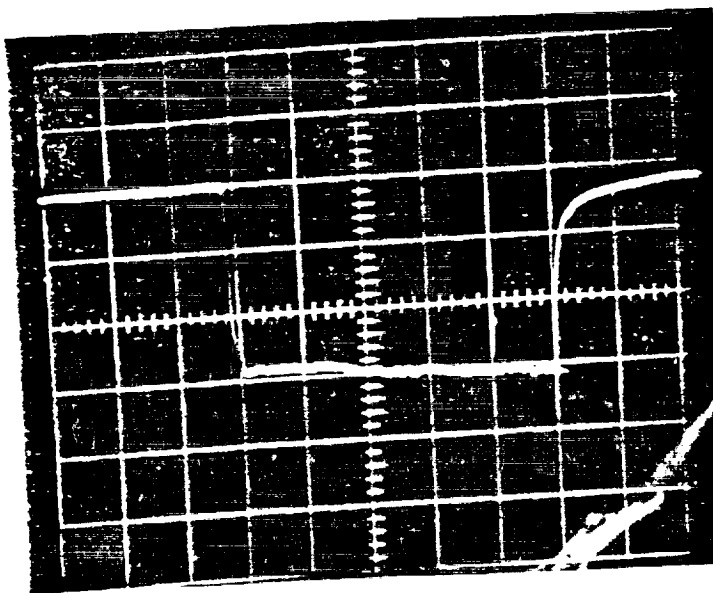


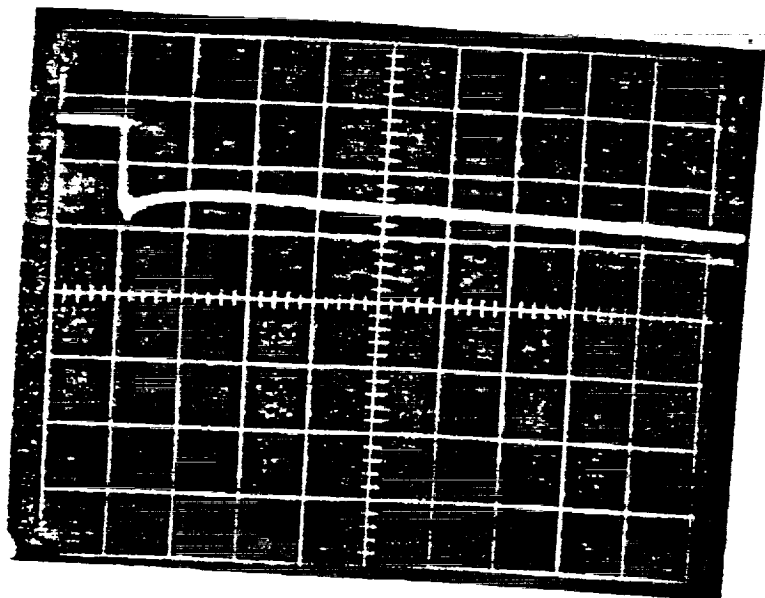
$$R_L \sim 4 \times 10^{10} \Omega$$

--Closed

--Open

50 mV x 0.5 sec





Ge:Ga

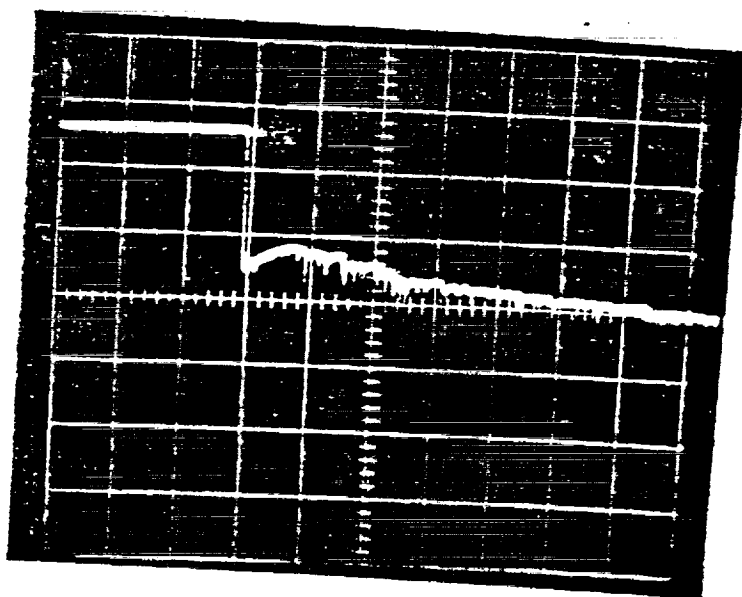
--Closed

--Open

$$V_B = 0.1$$

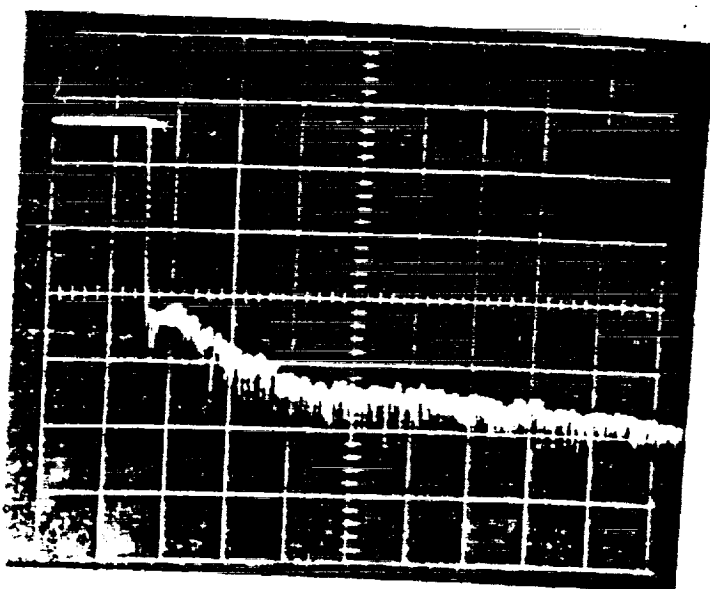
$$R_L \sim 4 \times 10^{10} \Omega$$

$$50 \text{ mV} \times 0.5 \text{ sec}$$



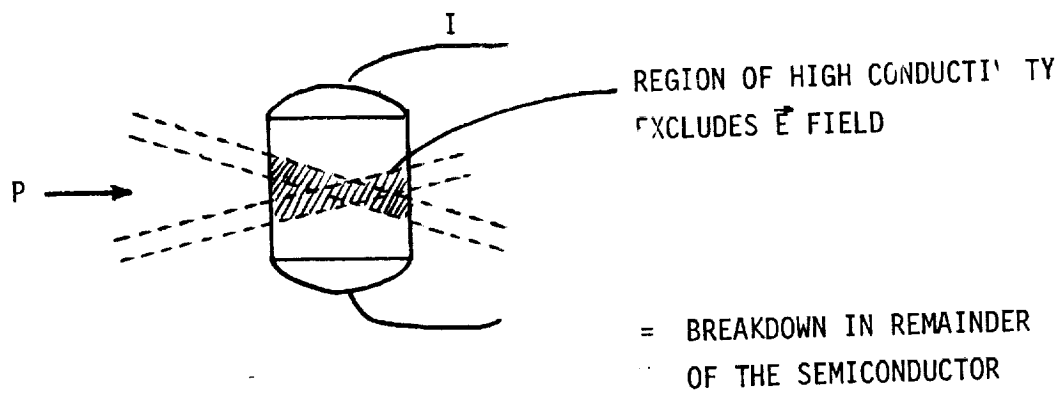
$$V_B = 0.2$$

$$P = 3.37 \times 10^{-13} \text{ W}$$



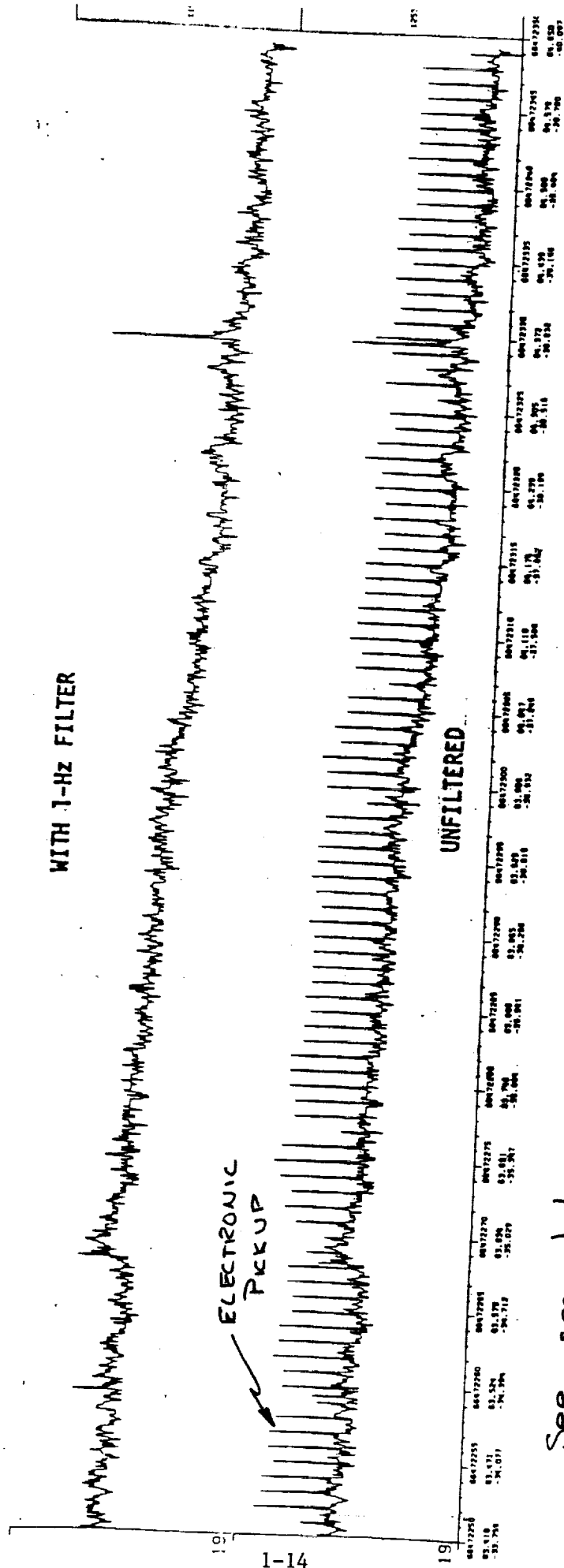
$$V_B = 0.3$$

NONUNIFORM ILLUMINATION



SCAN DIRECTION DEPENDENT RESPONSE (?)

DETECTOR 19 DATA

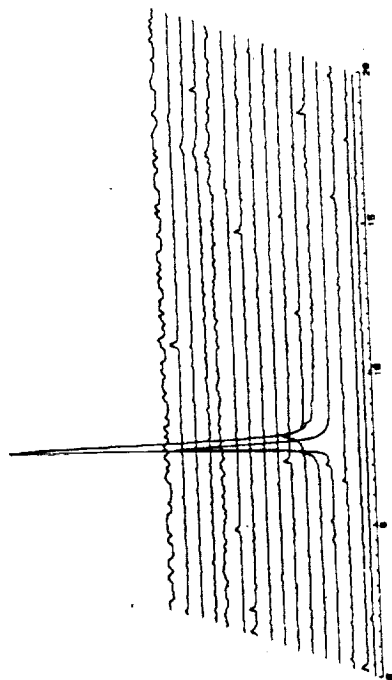


See second trace
up from time axis on the
25µm map of M82+M81!

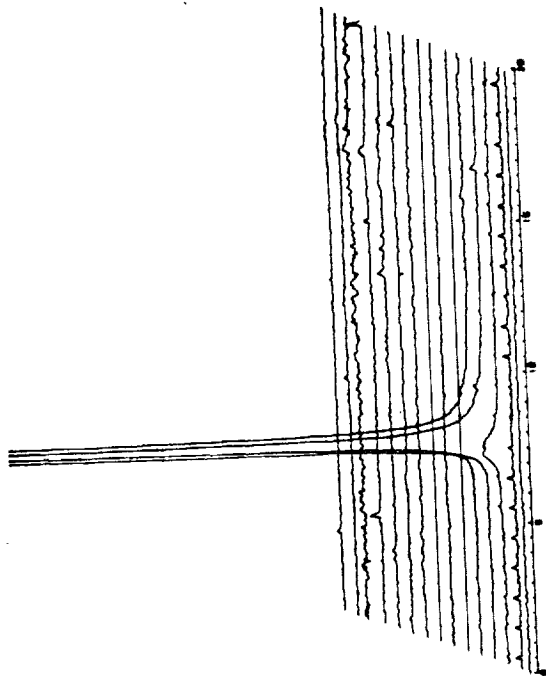
PH 3/30/83

M82 AND M81 IRAS

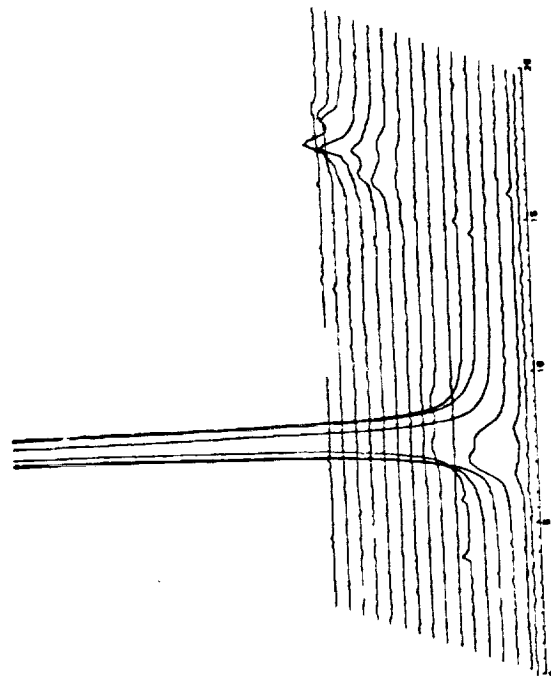
12 microns



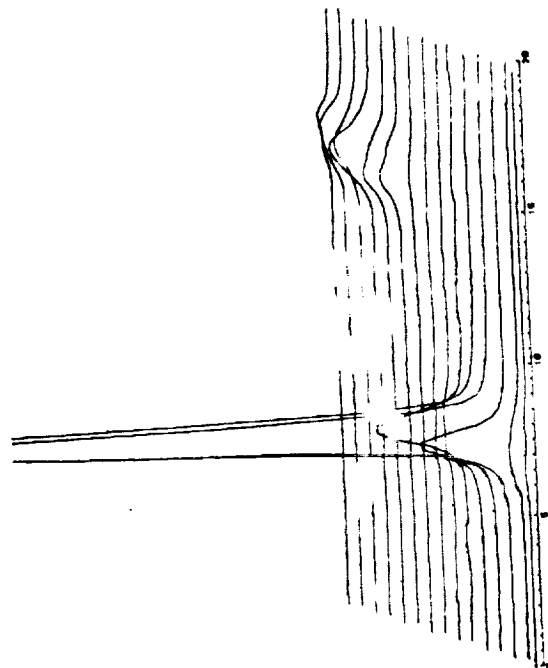
25 microns



60 microns



100 microns



19
26

(Preliminary report of work to be published more completely in the
International Journal of Infrared and Millimeter Waves, September, 1983.)

N 93-708/37

133705
p. 24

IMPROVED FABRICATION TECHNIQUES FOR
INFRARED BOLOMETERS

CC 787610

MN 738126

A. E. Lange, E. Kreysa,[†] S. E. McBride, and P. L. Richards

Department of Physics, University of California;
and Materials and Molecular Research Division,
Lawrence Berkeley Laboratory, Berkeley, CA 94720

and

E. E. Haller

Department of Materials Science, University of California;
and Materials and Molecular Research Division,
Lawrence Berkeley Laboratory, Berkeley, CA 94720

[†]Permanent address: Max-Planck-Institut für Radioastronomie,
D-5300 Bonn 1, West Germany

Abstract

Techniques are described for producing improved infrared bolometers/ from doped germanium. Ion implantation and sputter metalization have been used to make ohmic electrical contacts to Ge:Ga chips. This method results in a high yield of small monolithic bolometers with very little low-frequency noise. When one of these chips is used as the thermometric element of a composite bolometer, it must be bonded to a dielectric substrate. The thermal resistance of the conventional epoxy bond has been measured and found to be undesirably large. A procedure for soldering the chip to a metalized portion of the substrate is described which reduced this resistance. The contribution of the metal film absorber to the heat capacity of a composite bolometer has been measured. The heat capacity of a NiCr absorber at 1.3K can dominate the bolometer performance. A Bi absorber has significantly lower heat capacity. A low-temperature blackbody calibrator has been built to measure the optical responsivity of bolometers. A composite bolometer system with a throughput of $\sim 0.1 \text{ sr cm}^2$ has been constructed using our new techniques. In negligible background it has an optical NEP of $3.6 \cdot 10^{-15} \text{ W}/\sqrt{\text{Hz}}$ at 1.0K with a time constant of 20 ms. The noise in this bolometer is white above 2.5 Hz and is somewhat below the value predicted by thermodynamic equilibrium theory. It is in agreement with calculations based on a recent nonequilibrium theory.

Introduction

Low-temperature semiconductor bolometers are commonly used as detectors of mid- and far-infrared radiation. They have high sensitivity, are easy to use, and are adaptable to a wide variety of experimental conditions. The bolometers constructed at Berkeley use germanium doped with gallium (Ge:Ga) and compensated with unknown shallow donors as the thermometric element. In applications where a large throughput is desired a composite structure is used.

The thermometric element is glued to a sapphire substrate with an absorbing metal film on one side [1]. This provides a large increase in absorbing area with only a modest increase in heat capacity. The surface resistance of the metal film is chosen to be $\sim 190 \Omega/\square$. Theory predicts that radiation incident from the sapphire side of the sapphire-metal interface should be absorbed with 50% efficiency, independent of frequency. This behavior has been verified experimentally [2].

Electrical NEPs as low as $3 \cdot 10^{-15} \text{ W}/\sqrt{\text{Hz}}$ have been reported for ⁴He temperature bolometers constructed in this manner [1]. However, there have been circumstances under which the performance of these bolometers has fallen far short of expectations. Excess, current dependent noise, thought to be associated with the contacts to the Ge thermometer, often dominates fundamental noise sources, especially at low frequencies. In addition, the optical efficiency of the composite bolometers occasionally appeared to be much less than the predicted 50%. The absorptivity of the metal film itself has been questioned, as well as the thermal conductivity of the epoxy bond between the sapphire substrate and the Ge thermometer. Although little has been published, these concerns about composite bolometers have been widely circulated and believed in the infrared community.

We have investigated and resolved each of these issues. In this paper, we describe new techniques for constructing composite bolometers that greatly reduce the excess noise and improve the thermal link between the thermometer and the substrate. The optical efficiency of the bolometer system has been measured directly using a low temperature blackbody source, and agrees with predicted values. The presence of small amounts of helium exchange gas has been identified as a likely cause of poor performance of some bolometer systems. Bolometers produced using our new techniques consistently approach the ideal limits of performance.

Bolometer Noise

Doped semiconductor bolometers have long been observed to exhibit an excess current-dependent noise voltage which often seriously degrades their performance. Although not fully understood, the excess noise often appears to be associated with the electrical contacts to the semiconductor material. In the Ge:Ga composite bolometers developed at Berkeley [1], the contacts were formed by soldering leads to the etched germanium chip using pure indium and a flux containing zinc-chloride. Similar techniques have been traditionally used by others to produce both monolithic and composite bolometers [3]. Our bolometers produced by this method exhibit a contact noise of the form $V_n^2 = NI^2R^2/\omega$ where N is a dimensionless number $\lesssim 10^{-11}$; I is the bolometer current, and R its resistance.

In order to appreciate the effect of this noise source on the bolometer's performance, we examine the expression for the electrical noise equivalent power (NEP_E). The NEP_E is the product of the optical NEP and the optical absorptivity ϵ . It is the amount of power which must be absorbed in the bolometer to yield a signal to noise ratio of unity, and thus provides a measure of the bolometer's performance which is independent of the optical coupling to the bolometer. The NEP_E for a bolometer operating at temperature T with voltage responsivity S can be written [4] in the form:

$$(NEP_E)^2 = 2kT_B \epsilon P_B + 4kT^2 G + \frac{4kTR}{S^2} + \frac{4kT_L R_L}{S^2} \left(\frac{R}{R_L + R} \right)^2 + \frac{NI^2 R^2}{\omega S^2} + (\text{amplifier noise terms}) \quad (1)$$

These contributions to the NEP_E are, respectively, the fluctuations in the background power P_B from a Rayleigh-Jeans source at temperature $T_B \gg T$,

phonon noise arising from fluctuations in the transport of energy through the thermal conductance G , Johnson noise in the thermometer resistance R , and load resistance R_L , and the excess noise term. A bolometer for which the first term in (1) dominates the NEP_E can be referred to as ideal, because further improvements in the bolometer's performance would not yield a higher signal to noise ratio.

Figure 1 shows the contribution to the NEP_E due to background fluctuations, and also the contribution due to all other terms in Eq. (1) as a function of background loading in the limit of wave statistics. The curves were calculated [1] using parameters typical of a composite bolometer operated at 1.2K. The solid curves include the excess noise term with $N \approx 10^{-11}$, while the dashed curves are plotted for $N = 0$. As the curves show, the excess noise dominates the NEP_E for all values of P_B , its relative contribution becoming larger as P_B increases. This is because the optimized values of G and I_{bias} scale as P_B and $P_B^{1/2}$ respectively, while the responsivity scales as $S \propto I/G \propto P_B^{-1/2}$. Thus, the phonon and Johnson noise scale as $P_B^{1/2}$ while the excess noise scales as P_B .

Ion-Implanted Contacts

In an effort to increase the yield of bolometers that will perform well, particularly at high backgrounds, we have investigated the use of ion-implanted electrical contacts to the germanium chips. A process involving the implantation of boron ions has been shown to produce low noise contacts on Ge:Ga photoconductors [5]. Related techniques have been used to implant low noise thermometers in silicon bolometers [6]. We have applied the boron implantation techniques to the production of Ge:Ga thermometers and have obtained a high yield of thermometers which have very little current noise, even at high bias currents and low frequencies.

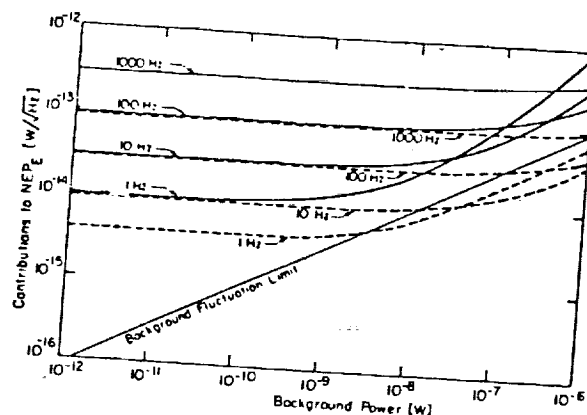


Fig. 1. Calculated contributions to the electrical NEP_E of a composite bolometer which has been optimized for varying amounts of absorbed Rayleigh-Jeans background power. The straight line is the background fluctuation contribution, and the curved lines are the contributions from all other terms in Eq. (1) at four different modulation frequencies. The solid lines include the excess noise term with $N = 8.8 \times 10^{-12}$. The dashed lines show the performance that could be achieved with $N = 0$.

A typical contact fabrication procedure begins with a 330 μm thick slice from a boule of Ge:Ga which has long been used at Berkeley for He^4 temperature bolometers. Boron ion implantation is used to produce a thin, degenerately doped p^+ -layer on both sides of the Ge:Ga slice. Both faces of the slice are lapped with 1900 mesh aluminum slurry, and then etched in a 4:1 HNO_3 :HF mixture for one minute. The etching process is rapidly stopped by quenching with a large quantity of electronic grade methanol. Rinsing with methanol, soaking in 1% HF in H_2O for five minutes to remove oxides, and blowing dry with a nitrogen jet completes the pre-implantation steps. The two surfaces to be implanted are now shiny and free of damage. The implantation schedule consisted of two implants for each surface. Singly ionized boron ions with energies of 25 keV and 50 keV are implanted in random orientation with doses of 10^{14} cm^{-2} and $2 \times 10^{14} \text{ cm}^{-2}$ respectively. A simple annealing cycle in a nitrogen atmosphere (heating from room temperature to 250°C in a few minutes, holding at this temperature for 30 to 60 min. and cooling to room temperature slowly over more than 30 min.) activates more than 90 percent of the boron atoms. Etching of the two implanted surfaces with 5% NaOCl in H_2O for five seconds is followed by sputtering of a 400Å thick Ti and then an 8000Å Au layer on each contact face. The metal layers are annealed at 200°C for one-half hour in a nitrogen atmosphere to reduce the built-in stress.

The implanted and metalized slice of germanium is cut into cubic chips using a wire saw. The chips are etched in 5:1 (HNO_3 :HF). The progress of the etching can be observed by watching the metalized side of the chip through a low power microscope. As germanium is removed, the free-standing gold-titanium film bends toward the gold side to relieve ^{residual} internal stress. Thus, the point of attack of the etch at the germanium-titanium interface

is clearly defined. No significant undercutting of the metal film has been observed. Even starting with a roughly cut chip, a polished germanium surface is produced very quickly. Etching is terminated by quenching with electronic grade methanol. After rinsing several times with methanol, the chip is left to dry on a filter paper. In the next step the free-standing Au-Ti film is removed by pressing gently with a wooden stick along the sharp edges of the Ge chip. A neat and easy separation of the metal film from the edge of the chip is achieved this way. Finally, bolometer wires are soldered to the gold surfaces with indium, using a resin flux obtained from the core of commercial solder.

Composite bolometers with contacts made in this way were tested in a dark cavity, at a bath temperature of 1.0K. The noise was measured by a digital computer which sampled the voltage across the bolometer at discrete intervals and computed the spectral amplitude of the noise voltage.

Fig. 2 shows noise spectra of a high background ($P_B = 100 \text{ nW}$) composite bolometer for a variety of bias currents. The sharp features are due to mechanical resonances that are sometimes present in our high background bolometers. The contributions to the noise due to phonon and Johnson noise (the second and third terms in Eq. 1) have been calculated at each of the bias currents and are indicated by dashed lines. With the exception of the mechanical resonances, there is little or no excess noise above 3 Hz. Below 3 Hz, the excess noise rises steeply, no longer obeying the simple form $V_n^2 \propto I^2 R^2 / \omega$. At 2 Hz it is still an order of magnitude less than that reported by Nishioka et al. Similar results for a low background bolometer with essentially no microphonic noise are shown in Fig. 7.

In conjunction with the development of low noise contacts, we have developed a new method of bolometer construction which yields a stronger thermal link between the germanium thermometer and the sapphire substrate.

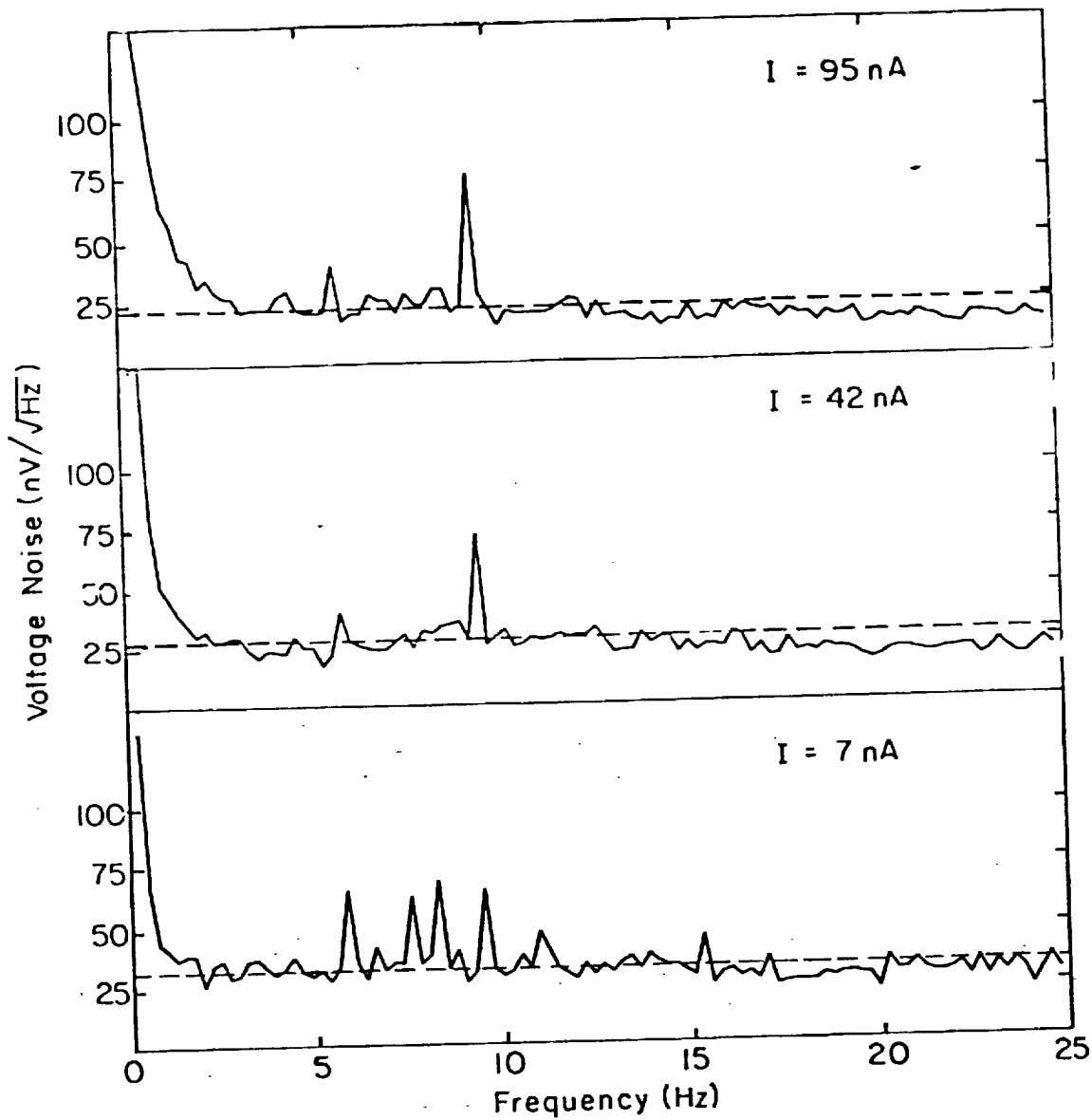


Fig. 2. Noise spectra of a high background composite bolometer with ion-implanted contacts. The sharp spikes are due to mechanical resonances in the bolometer and its leads. The dashed lines indicate the estimated fundamental noise $V_n^2 = 4kT^2G|S|^2 + 4kTR$. This white noise level decreases with increasing bias current in the way expected from the decreasing bolometer impedance. Current-dependent excess noise is apparent, rising steeply below 3 Hz.

Previous methods of bolometer construction employed an epoxy bond. The relatively high heat capacity of epoxy limits the amount that can be used in making such bonds to $\sim 10^{-7} \text{ cm}^3$. Occasional discrepancies between calculated electrical responsivities and measured optical responsivities suggested that the thermal link provided by the epoxy was not always adequate and could be effectively shorted by the presence of very small amounts of exchange gas in the bolometer cavity.

In order to measure the thermal conductivity between the germanium thermometer and the sapphire substrate, we constructed a composite bolometer with two germanium thermometers attached with epoxy in the usual way [7] as is shown in Fig. 3(a). Each thermometer had one 50 μm copper lead with high thermal conductivity and one 25 μm manganin lead with low thermal conductivity. Attached to one of the high conductivity leads was a heater through which we could introduce a known amount of power. By measuring the temperature difference between the two thermometers as power flowed from one, through the sapphire, and into the other, we found the thermal conductance of the two Ge-epoxy-sapphire interfaces. For a typical bond made with $\sim 3 \cdot 10^{-7} \text{ cc}$ of Stycast epoxy [7], with a heat capacity of $2 \cdot 10^{-10} \text{ T}^3 \text{ J/K}$, we measured a thermal conductance of $G \approx 1 \cdot 10^{-6} \text{ T}^3 \text{ W/K}$. This is considerably smaller than one would expect from the bulk properties of the material, but is consistent with measurements of the thermal boundary resistance across metal-dielectric interfaces [8]. For high background bolometers, where the conductance between the thermometer and the heat sink is typically $G \sim 10^{-5} \text{ W/K}$, the low conductance of the epoxy bond leads to increased time constants or, if small quantities of exchange gas are present, discrepancies between calculated electrical and measured optical responsivities, as is illustrated in Fig. 4.

The new method of construction, shown in Fig. 5, eliminates the use of epoxy altogether. A small area of the substrate is first coated with

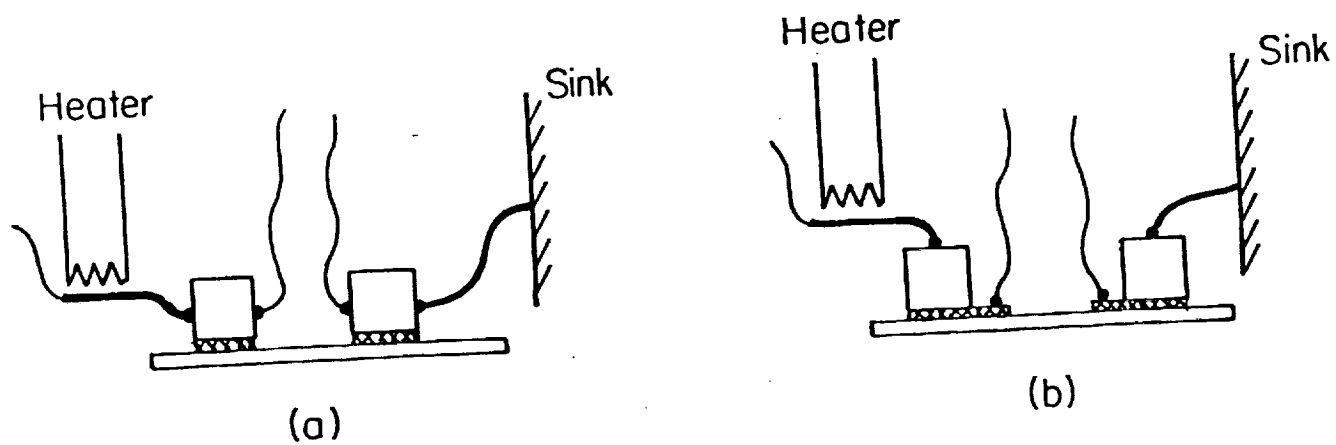


Fig. 3. Configurations used to measure the thermal conductance G_B of the bond between the thermometer and the substrate of a composite bolometer, (a) with epoxy bond, and (b) with solder bond. Low thermal conductance manganin leads are shown as thin lines, high conductance copper leads as thick lines.

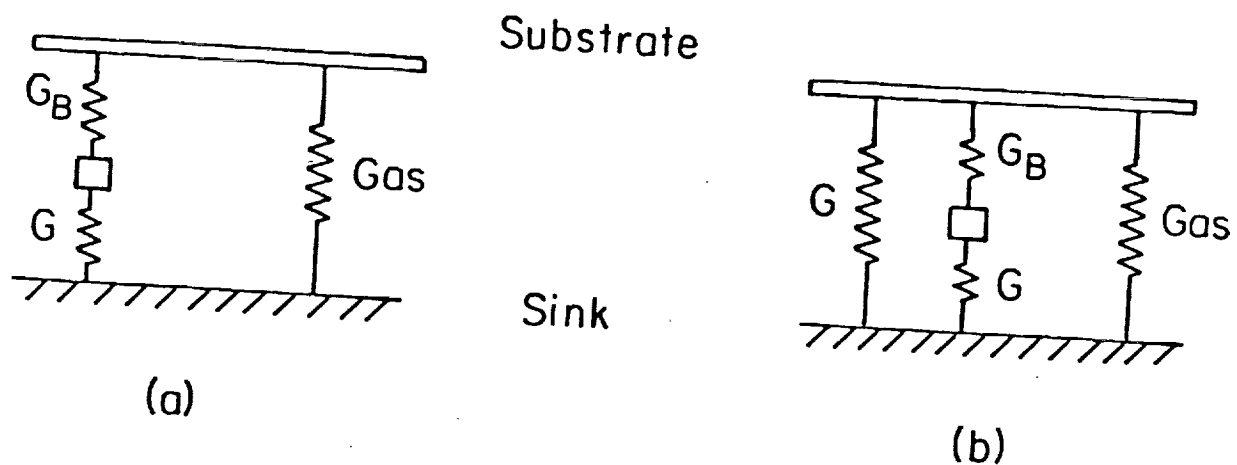


Fig. 4. The thermal circuits for composite bolometers with the conventional epoxy bond (a) and with the solder bond (b). If the thermal conductance G_B of the bond is too small, then the presence of a thermal shunt due to unwanted He exchange gas can seriously degrade the optical sensitivity of a bolometer whose electrical properties appear quite satisfactory.

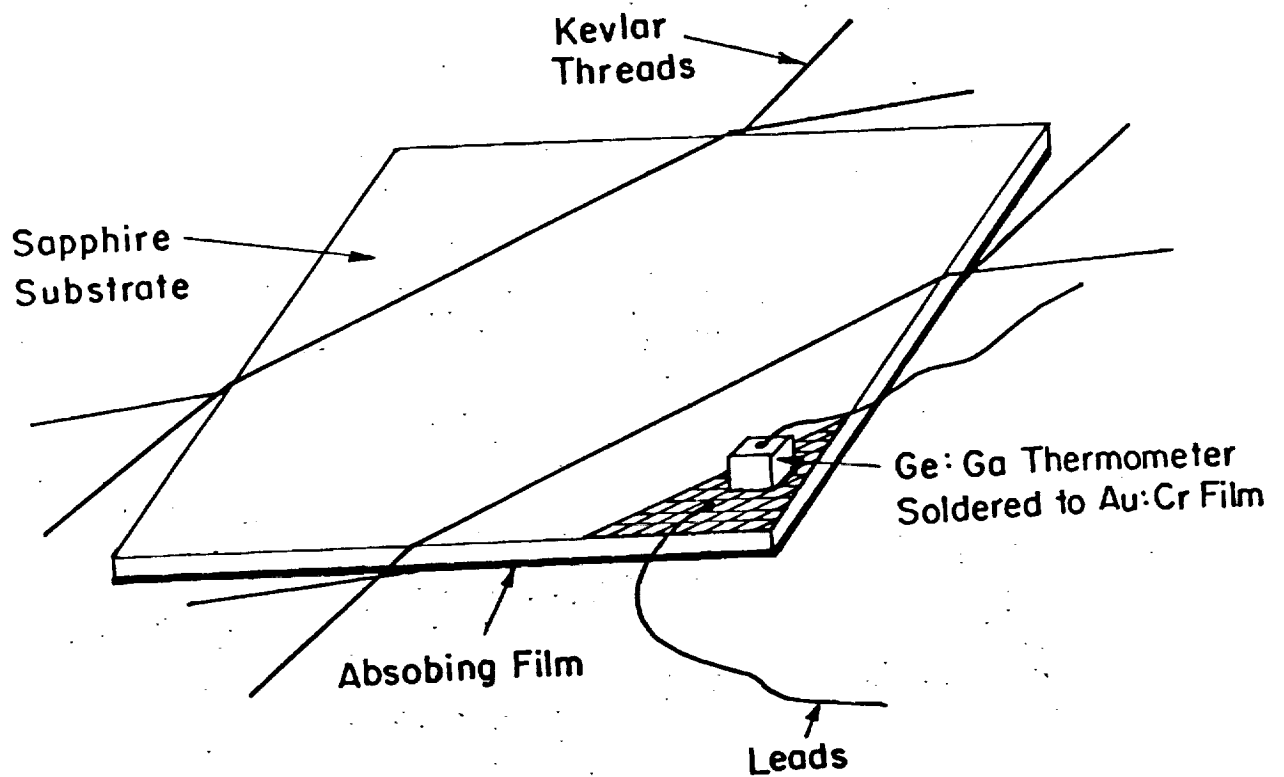


Fig. 5. Schematic diagram of a composite bolometer. The doped Ge thermometer is soldered to a metalized portion of the sapphire substrate.

$\sim 100\text{\AA}$ of chromium followed by 1000\AA of gold. The germanium chip is indium soldered directly to the gold film. A small flake of indium is pressed onto the gold film and the Ge chip is placed on top. The entire substrate is then heated briefly by an electrical strip heater with a short (~ 0.5 s) time constant. A small amount of pressure applied to the Ge chip during heating results in a thin, uniform contact between the chip and substrate. Leads are then indium soldered using resin flux to the exposed contact on the Ge chip and to the gold film to complete the electrical circuit. The controlled temperatures and the short duration of heating used result in contacts which are mechanically sturdy and consistently low in noise.

The thermal conductance of the indium bond between thermometer and sapphire was measured using the same technique described above. For a bond made with $\sim 3 \cdot 10^{-7} \text{ cm}^3$ of indium, with a heat capacity of $4 \cdot 10^{-11} T^3 \text{ J/K}$, the thermal resistance was measured to be $G = 2 \cdot 10^{-5} T^2 \text{ W/K}$. The solder bond both reduces heat capacity and increases the thermal conductance by one order of magnitude.

Absorbing Element

Composite bolometers produced previously in Berkeley used a bismuth film of about $200\Omega/\square$ as an absorbing layer on the sapphire substrates. While this technique was generally satisfactory, reports of problems with bismuth led us to look for better alternative materials for the absorbing film. The evaporated bismuth film is rather fragile. It was necessary to do the evaporation as the last step in the bolometer fabrication in order to avoid damage to the film. Also, some workers have reported that bismuth undergoes slow chemical changes on exposure to the atmosphere.

Because of these disadvantages, we have investigated the use of nichrome as the material for the absorbing film. An extensive literature exists which

describes the use of this material for thin film resistors [9]. We adopted a deposition technique which involves the sublimation of the alloy from the solid state [10]. A 1.3 mm diameter nichrome wire (80:20 Ni:Cr) was bent into a circle and was suspended in a horizontal plane. The distance from the circle to the base plate was equal to its radius. This ring source geometry, which is described by Holland [11], produces a uniform deposition on substrates placed on the base plate within the nichrome ring. The nichrome ring was heated by current to just below the temperature at which it began to sag. Due to the higher evaporation rate of chromium, it is necessary to age the source for a few hours until equilibrium is reached between the preferential evaporation of chromium from the surface and the diffusion of chromium from deeper layers [12]. After aging the nichrome wire once, it can be used for many depositions. Once equilibrium is reached, the alloy should be deposited with the original composition which was 80:20 Ni:Cr. Sublimation downward from the ring-source has the advantages of coating many substrates in one operation and avoiding the problem of supporting the very thin substrates in a downward-looking configuration. The substrates were placed on a glass cloth to thermally insulate them from the base-plate so that their temperature rose during coating, as is recommended for nichrome [12]. Finally, the films were heated in air at 300 C for 3 hours to improve adhesion [13]. Resistances values around $200\Omega/\square$ were obtained without difficulty in about five minutes of evaporation. The resistance decreased by ~4 percent when the film was cooled to 1.2K. Changes of this magnitude are not important for the optical properties of the film [2].

The nichrome films are mechanically very tough and may, therefore, be preferable to bismuth films in many applications. The films that we have prepared, however, show an undesirably large heat capacity. A nichrome film with an area of 4 mm^2 and a surface resistance of $200\Omega/\square$ was measured to have

a heat capacity of $3 \cdot 10^{-9}$ J/K at 1.3K. This is twice that of the rest of the bolometer, and thus seriously compromises the bolometers performance in the low-background limit. A bismuth film of the same area and surface resistance has a heat capacity of $3 \cdot 10^{-10}$ J/K, an order of magnitude less than the nichrome film.

Because of its low heat capacity, we continue to use bismuth films in our low-background ($P \lesssim 3 \cdot 10^{-8}$ W) bolometers. Resistance measurements on bismuth films stored in air for several years have not revealed any sign of deterioration. We have found, however, that composite bolometers which undergo a bismuth evaporation as the last step in the construction process consistently show a marked increase in low-frequency noise. Although the thermometric element is in the shadow of the sapphire substrate during the evaporation, we speculate that a very thin layer of bismuth forms an alternate conduction path on the surface of the Ga:Ge chip. Because of the increase in noise associated with the bismuth evaporation, we now attach the Ga:Ge thermometer to the sapphire substrate after the absorbing film has been deposited.

Optical Efficiency

A blackbody calibrator was constructed to directly measure the optical responsivity of our bolometers and thus to determine their optical efficiency. This calibrator, shown in Fig. 6, uses a blackbody cavity formed by casting an infrared absorbing epoxy [7] in a copper form. A heater and a calibrated thermometer are mounted on the copper form with the same epoxy. In order to minimize the size of the blackbody required to fill the aperture of the detector optics, the exit to the blackbody is a Winston light concentrator [14] with an aperture of $f/1.5$. This whole structure is separated from the bolometer vacuum by a 50 μ m thick Mylar window. The bolometer itself is fed

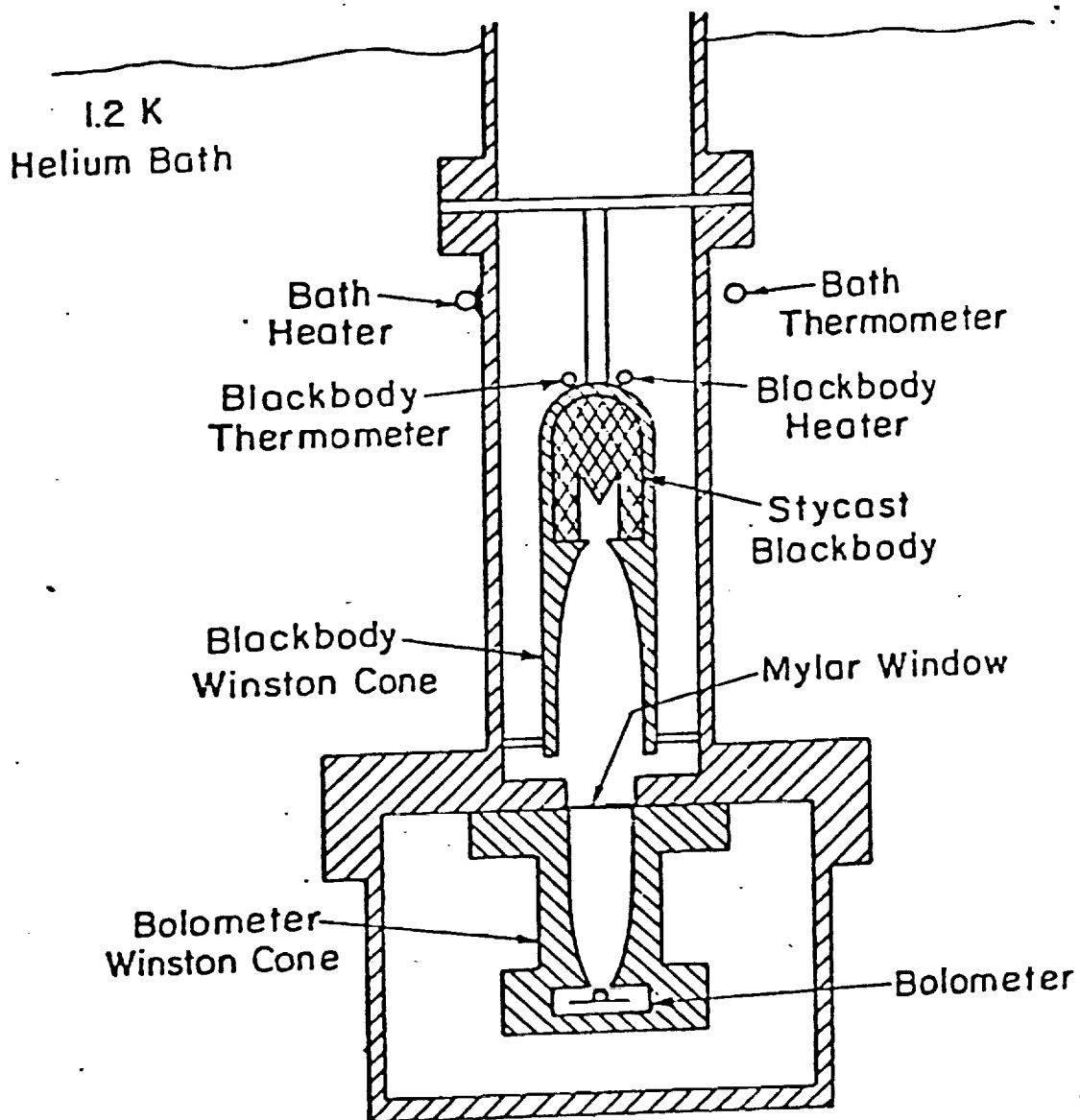


Fig. 6. Low temperature blackbody calibrator used to measure the optical responsivity of detector systems. A detailed description is given in the text.

by a Winston light cone with an aperture of $f/2$. All rays entering the acceptance angle of the lower Winston cone come from inside the acceptance angle of the upper cone, and thus from the blackbody. The Winston concentrator closest to the bolometer determines the throughput of the system. The calibrator thus measures the total efficiency of the bolometer system, including the transmission of the window, the lower Winston concentrator, the absorbing film on the bolometer, and the cavity surrounding the bolometer.

In order to compare the optical power absorbed by the bolometer with the power expected from the blackbody, we must measure the bolometer's electrical responsivity. The conventional procedure is to compute this quantity from the measured I-V curve. This procedure is not reliable if the I-V curve contains significant nonlinearity at fixed temperature due to non-ohmic contacts. To avoid this problem, we attached low thermal conductance leads to the metal absorbing film of a composite bolometer so that a known quantity of power could be dissipated in a way that closely mimics the absorption of optical power. With our bolometers, the two methods agree within 20 percent. This effect of non-ohmic contacts has been important in the past, but it does not appear to be important with our new ion-implanted contacts.

The measurement procedure involved choosing a bias current for the bolometer and measuring the DC responsivity using the metal absorbing film to heat the substrate. The blackbody heater was then turned on and the system was allowed to come to equilibrium. The blackbody temperature, the bolometer voltage, and the bath temperature were recorded when equilibrium was reached. A rise in the bath temperature of order 0.1K typically occurred due to power dissipation in the blackbody heater. Power to the blackbody was removed and a heater in the bath was then adjusted until the bath was at the temperature previously measured with the blackbody hot. The

power absorbed by the bolometer was computed from the difference in bolometer voltage divided by the responsivity measured with the metal film heater.

The total optical power expected to reach the bolometer was calculated by multiplying the spectral intensity of the blackbody radiation by the previously measured transmission of the cold Mylar window, and integrating to find the total flux. The bolometer system efficiency is then just the ratio of the power absorbed to this expected power.

A bolometer on which the metal film was painted with Nextel Velvet Black paint [15] was mounted with the painted surface facing the Winston concentrator and tested as described above. The optical efficiency of the bolometer system measured with a variety of blackbody temperatures between 25K and 45K was found to be 70 ± 5 percent. The paint was then removed and the bolometer was remounted with the metal film facing away from the entering radiation. The optical efficiency of this system was measured to be 44 ± 4 percent.

The integrating cavity around the bolometer had larger than normal openings to accommodate the extra leads attached to the absorbing film. Because of this, the efficiency of the cavity used in these experiments was less than could normally be achieved. The measured efficiencies are thus somewhat less than the best that can be expected from an optimized cavity.

These measurements also point out the efficacy of black paint as an absorber in the 50 cm^{-1} to 100 cm^{-1} frequency range. Unfortunately, its heat capacity slows the response time of the bolometer to the extent that it cannot be used to obtain high sensitivity, low background bolometers.

Summary

The dominant source of excess noise in our germanium bolometers is connected with the contacts to the Ge and can be greatly reduced by the use of ion-implanted contacts.

The large absorbing area of composite bolometers makes them exceptionally vulnerable to He exchange gas. Pressures as low as 10^{-5} Torr measured at 295K begin to degrade the performance of our low-background bolometers. For this reason, the use of a charcoal pump in the bolometer vacuum space is highly recommended. If the thermal link between the substrate and the thermometer is not good, the presence of exchange gas will not affect the electrical responsivity, but will degrade the optical efficiency. Our new method of construction improves the thermal link between substrate and thermometer by over an order of magnitude, while contributing one order of magnitude less heat capacity than on the epoxy bond previously used.

Using these new techniques, we have been able to significantly improve the performance of low-background bolometers. Table I lists the design and performance parameters for a well characterized low-background bolometer. The noise spectrum for this bolometer at its optimum bias point is shown in Fig. 7. The electrical NEP is $1.6 \pm 0.3 \times 10^{-15} \text{ W}/\sqrt{\text{Hz}}$, for modulation frequencies as low as 2 Hz. The calculated value for the electrical NEP given by the Johnson and phonon terms in Eq. (1) is $2.1 \times 10^{-15} \text{ W}/\sqrt{\text{Hz}}$. A more detailed analysis of bolometer noise has been given by Mather [16] which takes into account the electrothermal feedback in the bolometer and the distributed nature of the thermal link to the heat sink. These effects lead to reductions in the Johnson and phonon noise,

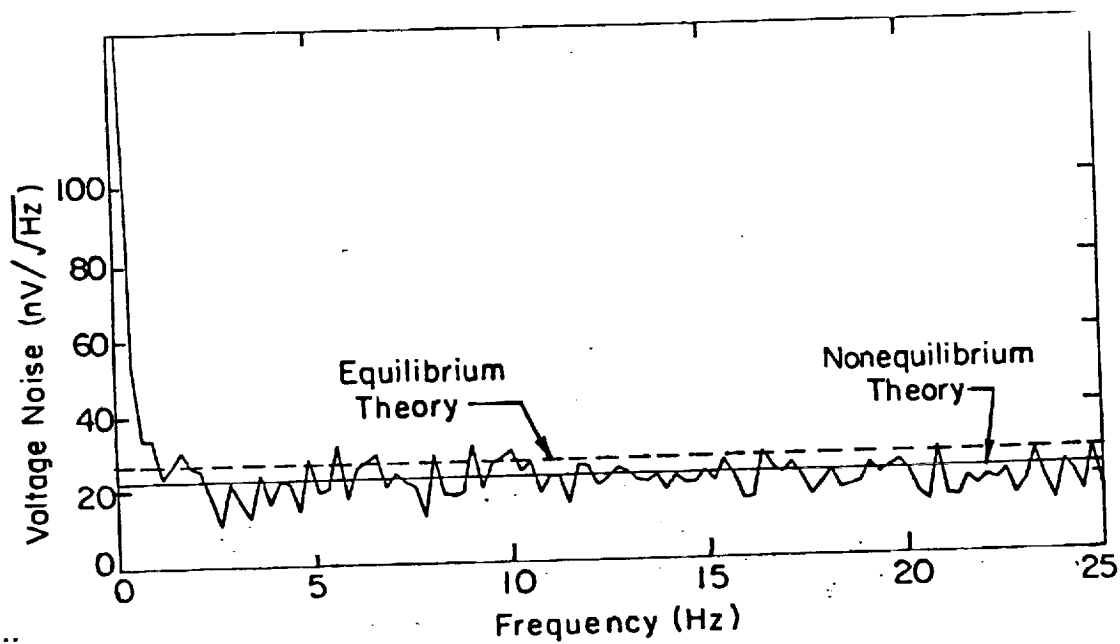


Fig. 7. Noise spectrum of a low-background composite bolometer at its optimum bias point. The dashed line indicates the noise level $V_n^2 = 4kT^2G|S|^2 + 4kTR$ expected from thermal equilibrium bolometer theory. The solid line indicates the noise level predicted by a non-equilibrium treatment of bolometer noise. The detailed characteristics of the bolometer are listed in Table I.

Characteristics of a Low-Background Composite BolometerEstimated Heat Capacities

| | |
|---|--|
| 0.4 x 0.4 x .0025 cm sapphire: | $1.6 \times 10^{-10} T^3 \text{ J/K}$ |
| 0.025 x 0.025 x 0.3 cm Ga:Ge: | $0.7 \times 10^{-10} T^3 \text{ J/K}$ |
| $1 \times 10^{-6} \text{ cm}^3$ In solder: | $1.2 \times 10^{-10} T^3 \text{ J/K}$ |
| $0.4 \times 0.4 \times 10^{-5} \text{ cm}$ Bi film: | $2.5 \times 10^{-10} T \text{ J/K}$ |
| $2 \times 10^{-7} \text{ cm}^3$ Au film: | $0.3 \times 10^{-10} T \text{ J/K}$ |
| 0.6 cm x .00125 cm brass leads: | $0.9 \times 10^{-10} T \text{ J/K}$ |
| | $(3.5 T^3 + 3.7 T) \times 10^{-10} \text{ J/K}$ |
| Bolometer resistance: | $R(T) = 616 e^{9.43/T} \Omega$ |
| Load resistance: | $R_L = 1 \times 10^7 \Omega$ |
| Temperature of heat sink and load resistor | 0.97K |
| Bolometer temperature | 1.00K |
| Thermal conductance to heat sink | $3.1 \times 10^{-8} \text{ (W/K)}$ |
| Bias current | $1.0 \times 10^{-8} \text{ A}$ |
| Measured electrical responsivity | $1.3 \times 10^7 \text{ V/W}$ |
| Calculated NEP_E (nonequilibrium theory) | $1.7 \times 10^{-15} \text{ W}/\sqrt{\text{Hz}}$ |
| Measured NEP_E | $1.6 \times 10^{-15} \text{ W}/\sqrt{\text{Hz}}$ |
| Calculated time constant | 17 ms |
| Measured time constant | 20 ms |

respectively. Applying these results to our bolometer yields a prediction of $NEP_E = 1.7 \times 10^{-15}$, in close agreement with our measured value of NEP_E .

Combining the measured value of electrical NEP with the measured value for the optical efficiency, we find the optical NEP for this bolometer system, including concentrator and cavity, to be $3.6 \times 10^{-15} \text{ W}/\sqrt{\text{Hz}}$.

Acknowledgments

This work has been supported by the Director, Office of Energy Research, Office of Basic Energy Sciences, Materials Science Division of the U. S. Department of Energy under contract No. DE-AC03-76SF00098. Support for E. E. Haller was provided by the National Aeronautics and Space Administration under grant W-14606. During various phases of this work, E. Kreysa was supported by the Deutsche Forschungsgemeinschaft, Sonderforschungsbereich 131, Radioastronomie, and P. L. Richards by the Alexander von Humboldt Foundation Senior U.S. Scientist Program.

References

1. N. S. Nishioka, P. L. Richards, and D. P. Woody, Appl. Opt. 17, 1562 (1978).
2. J. Clarke, G. I. Haffer, P. L. Richards and N-H. Yeh, J. Appl. Phys. 48, 4865 (1977).
3. F. J. Low, J. Opt. Soc. Am. 51, 1300 (1961).
4. F. J. Low, and A. R. Hoffman, Appl. Opt. 2, 649 (1963).
5. E. E. Haller, M. R. Hueschen, and P. L. Richards, Appl. Phys. Lett. 34, (8), 495 (1979).
6. P. M. Downey, Ph. D. thesis, Massachusetts Institute of Technology (1980) (unpublished).
7. Stycast 2850-FT, Emerson and Cumming, Inc., Canton, Mass. 02021.
8. R. E. Peterson, and A. C. Anderson, J. Low Temp. Phys. 11, 639 (1973).
9. L. I. Maissel and R. Glang, Handbook of Thin Film Technology (McGraw Hill, New York, 1970) pp. 18-8 to 18-12.
10. T. K. Lakshamanan Trans. 8th Nat. Vac. Symp. 1961, p. 868.
11. L. Holland, Vacuum Deposition of Thin Films (J. Wiley, New York, 1960) p. 155.
12. P. Huijter, W. T. Langendam and J. A. Lely, Phillips Tech. Rev. 24, 144 (1962).
13. G. Sidall and B. A. Probyn, Brit. J. Appl. Phys. 12, 668 (1961).
14. I. D. Gregory and D. E. Moody, J. Phys. F: Metal Physics 5, 36 (1975).
15. R. Winston, J. Opt. Soc. Am. 60, 245 (1970).
16. Nextel (TM) Velvet coating, 3M Co., St. Paul, MN 55101.
17. J. C. Mather, Appl. Opt. 21, 1125 (1982).

(Preliminary report of work to be published more completely in the International Journal of Infrared and Millimeter Waves.)

N 93 - 70638
33806

PERFORMANCE OF Ge:Ga FAR INFRARED DETECTORS

M. R. Hueschen and P. L. Richards

Department of Physics, University of California
Berkeley, California 94720

and

E. E. Haller

Department of Materials Science, University of California
and Materials and Molecular Research Division
Lawrence Berkeley Laboratory, Berkeley, California 94720

Abstract

A systematic study has been carried out of the properties of Ge:Ga photoconductive infrared detectors for wavelengths $\approx 100 \mu\text{m}$. The detectors investigated were made from Ge:Ga with acceptor concentration $N_A \sim 2 \times 10^{14} \text{ cm}^{-3}$ with both low compensation (10^{-2}) and ultralow compensation (10^{-4}). Noise measurements have been made as a function of background photon rate, bias voltage, and chopping frequency. Detective quantum efficiencies approaching unity have been observed over a wide range of experimental parameters. Photocurrent has been measured as a function of voltage and temperature. Hall mobility and lifetime have been measured to determine their effect on detector properties. A small potential drop has been observed in nominally ohmic contacts produced by implantation of B ions.

Introduction

Photoconductive detectors made from Ge:Ga are the most sensitive available infrared detectors for low background measurements at wavelengths from the 50 μm limit of Ge:Be¹ to the 115 μm edge of Ge:Ga. With the application of uniaxial stress, the response of Ge:Ga can be extended to $\sim 230 \mu\text{m}$.^{2,3} In this paper we present the preliminary results of an extensive optimization study of Ge:Ga detectors for the 50-115 μm range. The availability of techniques for producing purely doped Ge with ultralow compensation has made possible the study of photoconductive response over a wide range of compensation ratios. For this study we selected two materials. Our low compensation material was originally produced to make Li-drifted Ge detectors of ionizing radiation. It had a Ga acceptor concentration $N_A = 2.1 \times 10^{14} \text{ cm}^{-3}$ and a concentration of shallow donors of $N_D = 2 \times 10^{12} \text{ cm}^{-3}$. Our ultralow compensation material had $N_A = 2.0 \times 10^{14} \text{ cm}^{-3}$ and $N_D = 2 \times 10^{10} \text{ cm}^{-3}$. These values were determined from measurements of Hall effect and resistivity as functions of temperature. Detectors with dimensions of 1 x 1 x 3 mm were cut from each material. Electrical contacts were made on opposing 1 x 3 mm faces by boron ion implantation of a degenerate p⁺ layer followed by sputter metalization as has been described previously.² The detectors were mounted in integrating cavities with 1 mm diameter apertures.²

Experimental Techniques

The apparatus shown in Fig. 1 was devised to permit measurements of detector response to a calibrated small signal flux with a variety of modulation frequencies in the presence of a calibrated steady background flux. In order to avoid the use of multiple neutral-density filters or small apertures which require diffraction corrections, the apparatus utilizes a cold blackbody source whose temperature can be varied from 10 to 100 K. This source is located in a light-tight, LHe temperature, evacuated Cu box which is divided into three chambers with blackened walls. The

cold blackbody source and a 150 Hz tuning fork chopper are located in the left hand chamber. The exit aperture to the left hand chamber is fitted with a cold, light-tight shutter. The detector in its integrating cavity is located in the right hand chamber along with a high impedance load resistor and a MOSFET preamplifier used for the initial detector tests. Later tests were made with a JFET amplifier held at 80 K on a standoff outside of the Cu box. Each of these transistors functioned as the first stage source-follower in a conventional transimpedance amplifier.⁴ The throughput reaching the detector from the internal blackbody is $1.15 \times 10^{-5} \text{ sr cm}^2$. It is defined by the exit aperture of the left hand chamber and by the entrance to the detector integrating cavity. The purpose of the entrance aperture to the right hand chamber is to minimize stray light.

The spectral response of each detector was measured relative to that of a Golay detector by using a Fourier transform spectrometer. This spectral response was measured at the same detector temperature (3 K) used in the sensitivity measurements. It was found to be insensitive to photon flux in the range of interest. The rate \dot{N} at which photons in the detected spectral range enter the detector cavity was computed by integrating the product of the Planck curve from the internal blackbody and the measured spectral response of the detector. This allowed an absolute calibration of the detector responsivity which is not as well characterized as would be the case with a narrow band filter, but should be adequate to determine the detective quantum efficiency within a factor 2.

In many of our measurements, the internal blackbody provided a continuously variable photon background. The internal chopper was removed, and the throughput increased to $4 \times 10^{-5} \text{ sr cm}^2$. A signal with variable chopping frequency was introduced into the central chamber from an external source as is shown in Fig. 1. Multiple reflections from the black walls provided strong attenuation and low-frequency-pass filtering before the radiation reached the detector. The chopped signal photon rate from the external source within the detected spectral range was determined to be $\dot{N} \sim 10^8 \text{ s}^{-1}$ by comparison with signals from the cold blackbody. The response of the detector to this chopped signal was measured as a function of background and used to refer the detector output noise to the detector input.

Noise Measurements

The primary goal of our measurements was to determine whether photon noise limited operation could be obtained over a wide range of backgrounds. The results are shown in the form of plots of noise equivalent photon rate $NE\dot{N}$ versus photon rate for the low compensation detector in Figs. 2 and 3, and for the ultralow compensation detector in Figs. 4 and 5. The photon noise limit computed for an ideal photoconductor with responsive quantum efficiency equal to unity is shown on each plot. For the smaller values of \dot{N} , this curve is obtained from

$$NE\dot{N} = 2 \sqrt{\dot{N}} \quad (1)$$

A small correction for wave statistics (Bose factor) is included at the largest values of \dot{N} . The values of \dot{N} are calculated from the measured DC current using the initial absolute calibration of detector responsivity.

In Fig. 2 we show how the $NE\dot{N}$ at 100 Hz varies with detector bias for the low compensation detector operated at 3 K. This temperature was chosen for all detector performance measurements because it is cold enough that thermally generated carriers make no significant contribution to detector current or noise, even at the lowest backgrounds. For low bias, the detector is photon noise limited for large \dot{N} , but amplifier noise limited for small \dot{N} . At high bias it is photon noise limited for small \dot{N} , but shows excess noise at large \dot{N} . When viewed in the time domain, this excess noise has the form of current spikes whose duration is set by the response time of the amplifier. Our measured values of $NE\dot{N}$ were obtained by Fourier transformation of digitized detector output, so are relevant to measurements of steady signals. For this case the optimum bias is clearly $V \sim 200$ mV.

In Fig. 3 we show the noise in this detector with $V = 200$ mV as a function of modulation frequency. Within our experimental accuracy this detector is photon

noise (BLIP) limited at all modulation frequencies over the entire range $4 \times 10^7 < \dot{N} < 6 \times 10^{10} \text{ s}^{-1}$.

In Fig. 4 we show how the NEN at 200 Hz varies with detector bias for the ultralow compensation detector operated at 3 K. Amplifier noise has a small effect only at the very lowest values of \dot{N} and bias voltage. As is the case for the data from the low compensation detector shown in Fig. 2, excess noise in the form of current spikes appears for the highest bias at high values of \dot{N} . Unlike Fig. 2, however, excess noise also occurs for low bias and large \dot{N} . A possible cause for this phenomenon will be discussed below.

In Fig. 5 we show the noise in the ultralow compensation detector with $V = 40 \text{ mV}$ as a function of modulation frequency. Reference to Fig. 4 shows that the values of detective quantum efficiency would have been significantly better for $V = 60 \text{ mV}$. There is a systematic variation of NEN with frequency which may be related to the dielectric relaxation phenomenon which rolls off the photoconductive gain at high frequencies in low backgrounds.⁵ Related effects are visible in the data in Fig. 3, but are much less pronounced, perhaps because the DC photoconductive gain is lower in this case.

Measurements of Photocurrent

Measurements of DC photocurrent as a function of bias voltage and temperature are shown in Fig. 6 for a photon rate of $\dot{N} \sim 10^{10} \text{ s}^{-1}$ in the detected spectral range. The data for the low compensation detector at the left show a linear (ohmic) region, a superlinear region, a brief decrease in slope and then very large slope as V is increased. Optimum noise performance (for 3 K) was obtained at 200 mV, just below the voltage at which carrier multiplication takes place by impact ionization of neutral impurity sites. At this voltage the DC responsivity was $\sim 60 \text{ A/W}$ corresponding to a product of photoconductive gain and responsive quantum efficiency $G\eta = 0.8$.

The data on the right side of Fig. 6 for the ultralow compensation detector show several unusual features. The temperature dependence is larger than for the low compensation case and the low bias, low temperature region is nonlinear. The photocurrent for given bias voltage is 30 to 100 times larger than for the low compensation case in the most useful range of voltage and temperature. A bias of only 40 mV provided the optimum noise performance at low backgrounds, but was a little below the optimum at higher backgrounds. At this voltage the DC responsivity was 140 A/W corresponding to $G_n = 1.8$. This factor 2 improvement in G for the ultralow compensation detector should be useful at low backgrounds where amplifier noise is important. For both types of detectors the chopped responsivity is usually less than the DC responsivity due to dielectric relaxation rolloff, and the difference between the two detectors is smaller than in the DC case.

Hall Measurements

For a photoconductive detector with responsive quantum efficiency η , mobility μ , carrier lifetime τ , and length (between electrodes) ℓ , the photocurrent

$$I = \eta N e G = \eta N e \mu \tau V / \ell^2. \quad (2)$$

The I-V data in Fig. 6 thus reflect the temperature and voltage dependence of the $\mu\tau$ product. In order to separate these effects we have measured the Hall coefficient of both materials as a function of temperature and voltage. If we neglect the weak magnetic field dependence, the measured Hall mobility can be used as an estimate of the drift mobility $\mu(V,T)$ in Eq. (1). The temperature dependence of the Hall mobility was measured over the temperature range $2 < T < 300$ K and found to be in excellent agreement with the results of theories of scattering due to phonons, ionized impurities, and neutral impurities.⁶ We found⁶ that μ is essentially constant at $5 \times 10^5 \text{ cm}^2 \text{ V}^{-1} \text{ s}^{-1}$ for the low compensation material and

$1 \times 10^6 \text{ cm}^2 \text{ V}^{-1} \text{ s}^{-1}$ for the ultralow compensation material over the important ranges of V and T for detector operation.

Since the mobility is essentially constant, most of the nonlinearity of the I-V curves in Fig. 6 must come from voltage dependence of the carrier lifetime which, for constant \dot{N} , is proportional to carrier density. Lifetimes deduced from the Hall measurements are shown in Fig. 7, for both materials. The lifetimes have large dependences on both temperature and electric field which will be discussed in detail in a later publication.⁶ The lifetime is a factor ~ 50 longer for the ultralow compensation material because of the relative absence of recombination sites in that material.

Contact Potential

The ultralow compensation detector showed excess noise and nonlinearity in its I-V curve at small bias voltages. These unexpected features deserve further comment. During the Hall effect measurements, six ion-implanted contacts for current and potential leads were made to the sample, in the classic Hall geometry. They allowed the observation of an excess voltage drop of a few millivolts near the injecting contact on the ultralow compensation material which increased with decreasing temperature. Such an effect is expected even for ideal degenerately doped p^+ contacts. Close to equilibrium the fermi energy in the p^+ region is equal to that in the bulk material, and so is 7-10 meV above the valence band of the bulk material. Consequently there is a barrier to hole injection from the contact which is $\gg kT$ at $T = 2 \text{ K}$. Thermionic emission is not able to supply the required current unless the barrier is lowered, and a potential drop of a few millivolts develops. This effect should also be present in the low compensation material, but is a smaller fraction of the applied voltage because of the smaller mobility and much shorter lifetime. It seems likely that the nonlinearity of the ultralow compensation detector at low

temperatures and very small voltages is related to this potential barrier. It also appears that the excess noise in this detector may be related to this contact barrier and to the very high photoconductive gain which makes this detector attractive.

Acknowledgements

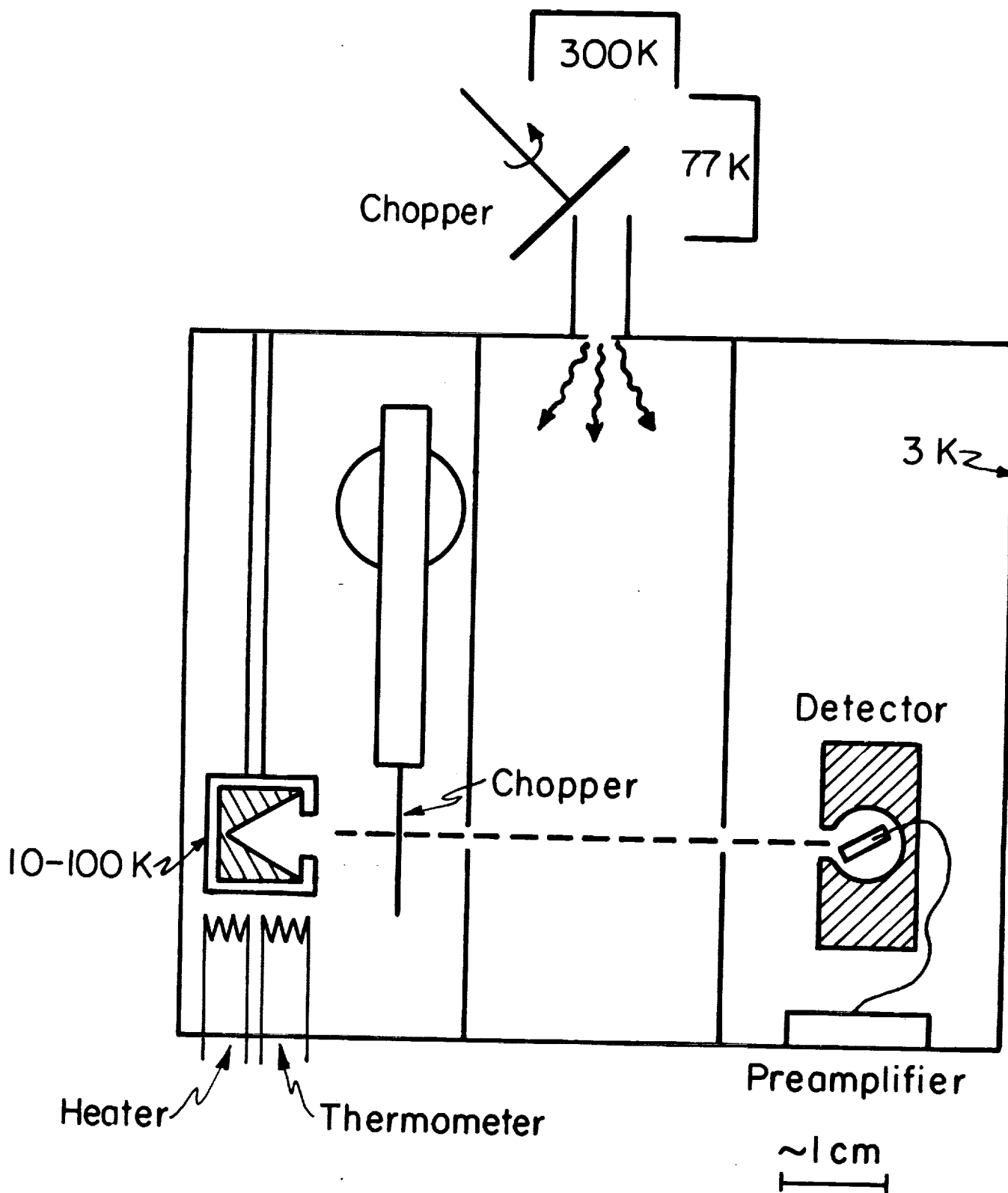
This work was supported by NASA Grant NSG-7205 and by NASA Grant W-14606 through inter-agency agreement with the U.S. Department of Energy under Contract No. DE-AC03-76SF00098.

References

1. N. Haegel and E. E. Haller (to be published).
2. E. E. Haller, M. R. Hueschen, and P. L. Richards, Appl. Phys. Lett. 34, 495 (1979).
3. A. G. Kazanskii, P. L. Richards, and E. E. Haller, Sol. State Comm. 24, 603 (1977).
4. E. L. Dereniak, R. R. Joyce, and R. W. Capps, Rev. Sci. Instrum. 48, 392 (1977).
5. A. F. Milton and M. M. Blouke, Phys. Rev. B3, 4312 (1971).
6. M. R. Hueschen, P. L. Richards, and E. E. Haller (to be published).

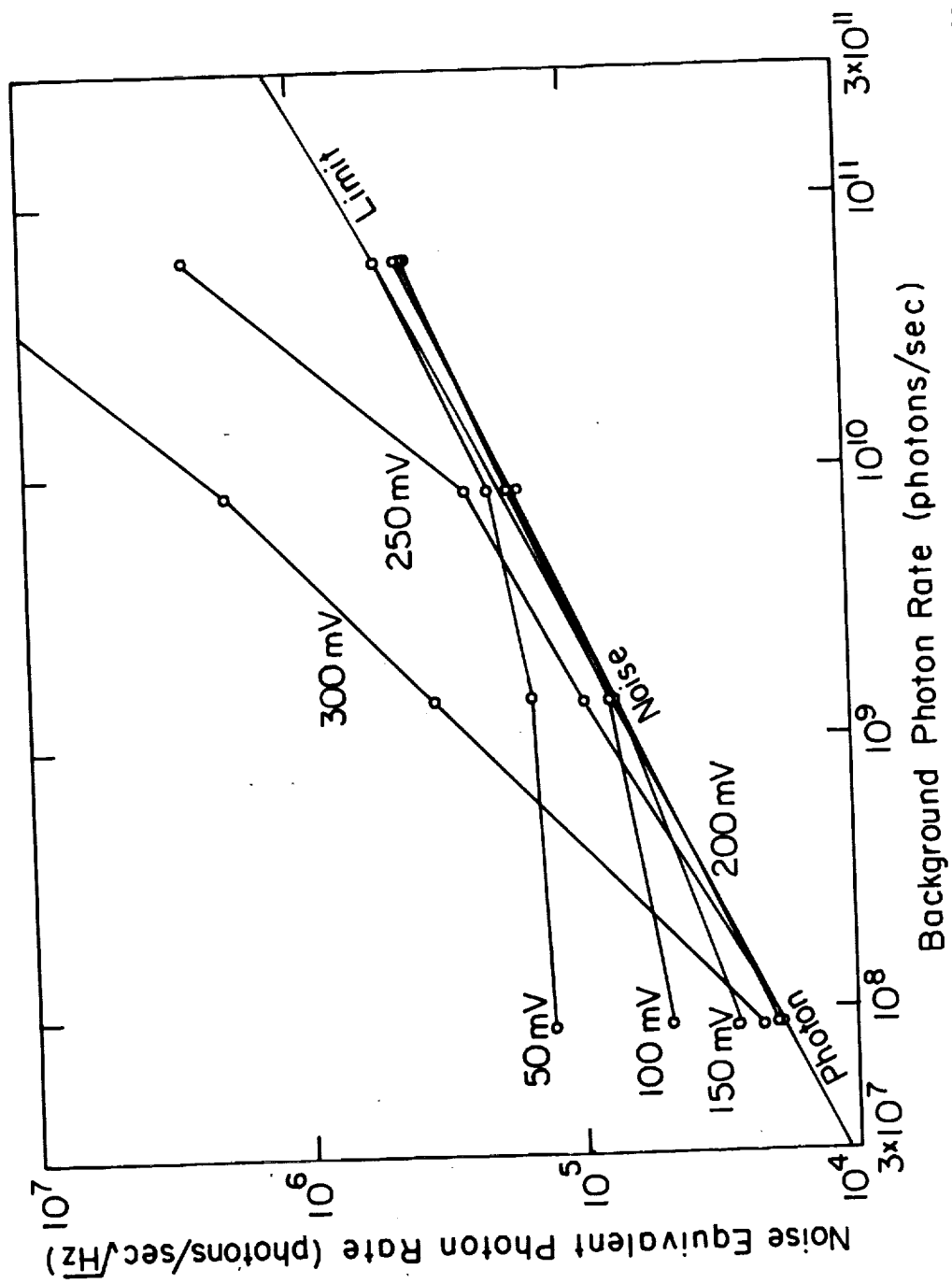
Figure Captions

1. Apparatus used for detector tests.
2. Noise as a function of photon rate with bias voltage as a parameter for the low compensation detector. The modulation frequency was 100 Hz and the temperature was 3 K.
3. Noise as a function of photon rate with modulation frequency as a parameter for the low compensation detector. The bias voltage was 200 mV and the temperature was 3 K.
4. Noise as a function of photon rate with bias voltage as a parameter for the ultralow compensation detector. The modulation frequency was 200 Hz and the temperature was 3 K.
5. Noise as a function of photon rate with modulation frequency as a parameter for the ultralow compensation detector. The bias voltage was 40 mV and the temperature was 3 K.
6. Current-voltage curves for the low compensation detector (left) and the ultralow compensation detector (right).
7. Curves of hole density (which is proportional to hole lifetime τ) for the low and ultralow compensation detectors. Most of the nonlinearity of the detector I-V curves arises from the field and temperature dependence of τ .



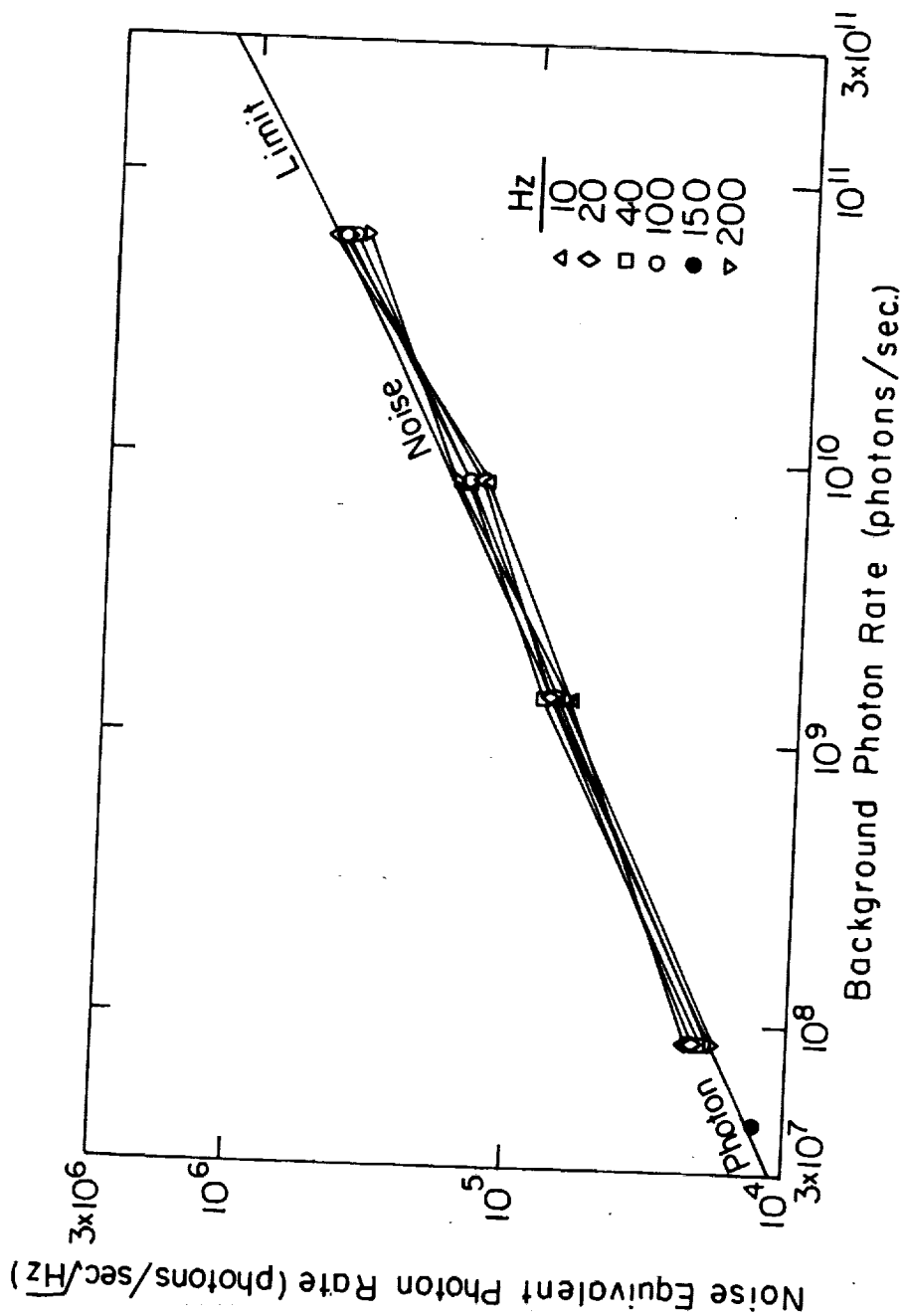
XBL 837-5981

Figure 1



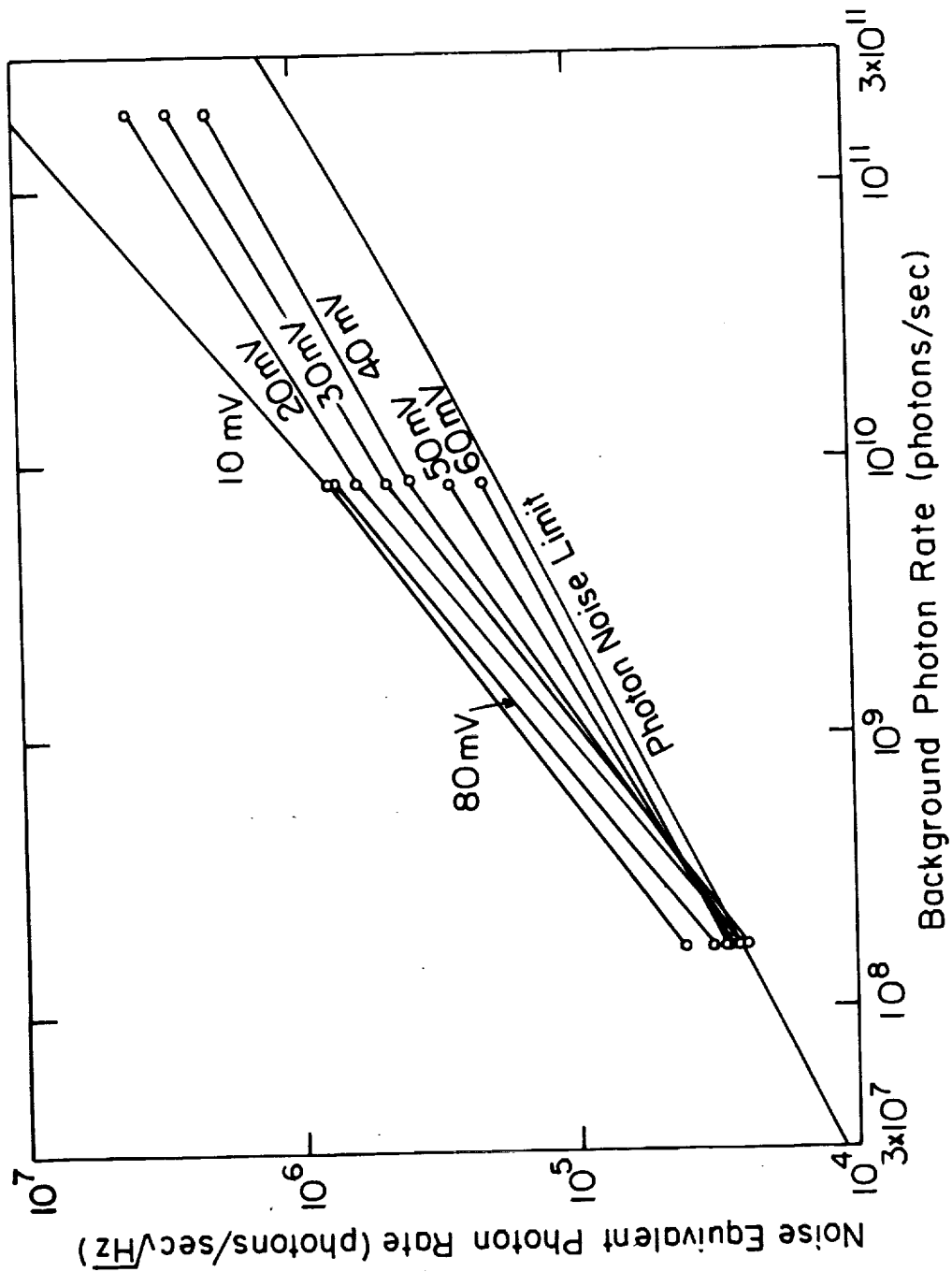
XBL 831-5152

Figure 2



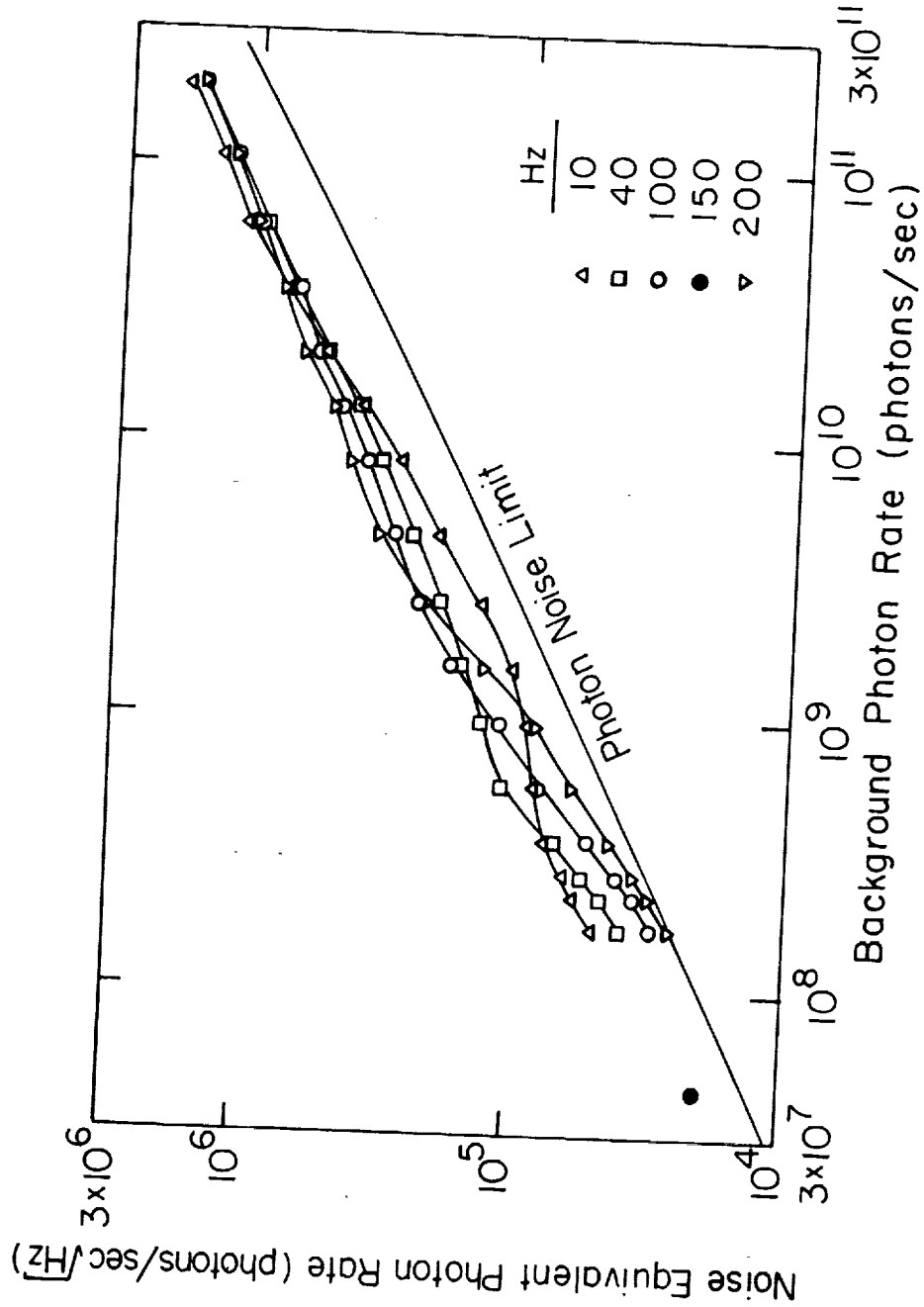
XBL 832-5197

Figure 3



XBL831-5153

Figure 4



XBL 8112-12877

Figure 5

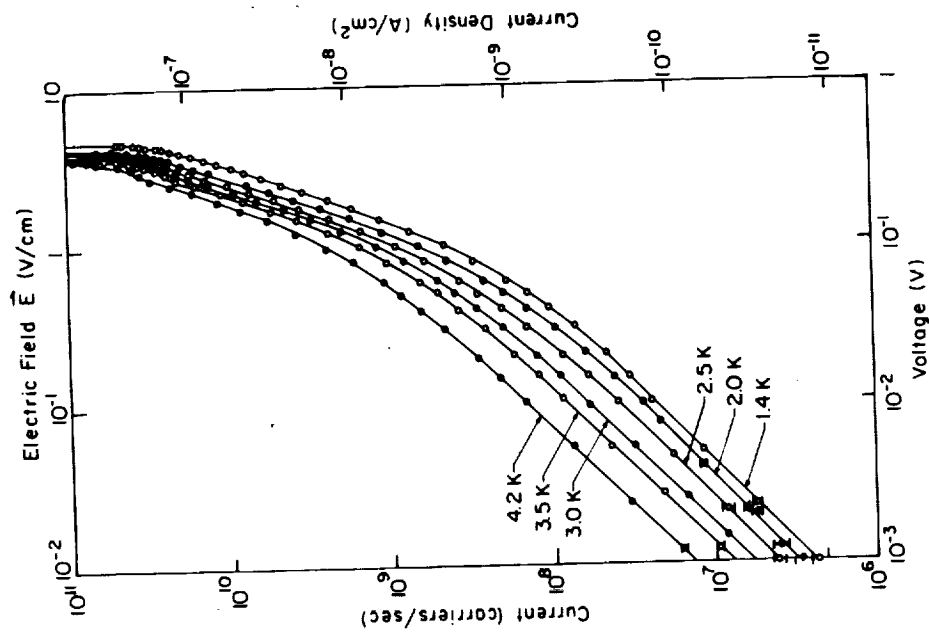
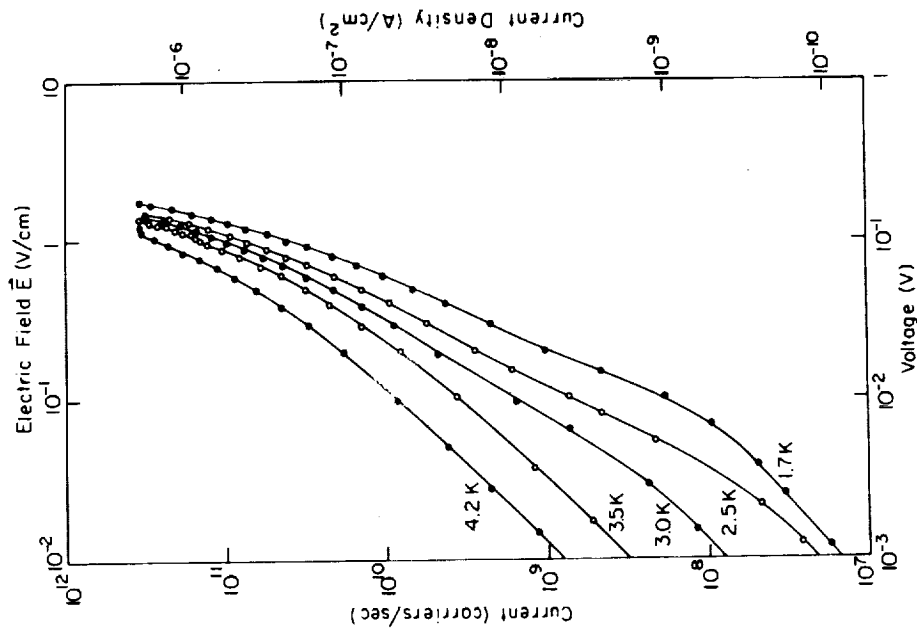


Figure 6

XBL 831-5151A

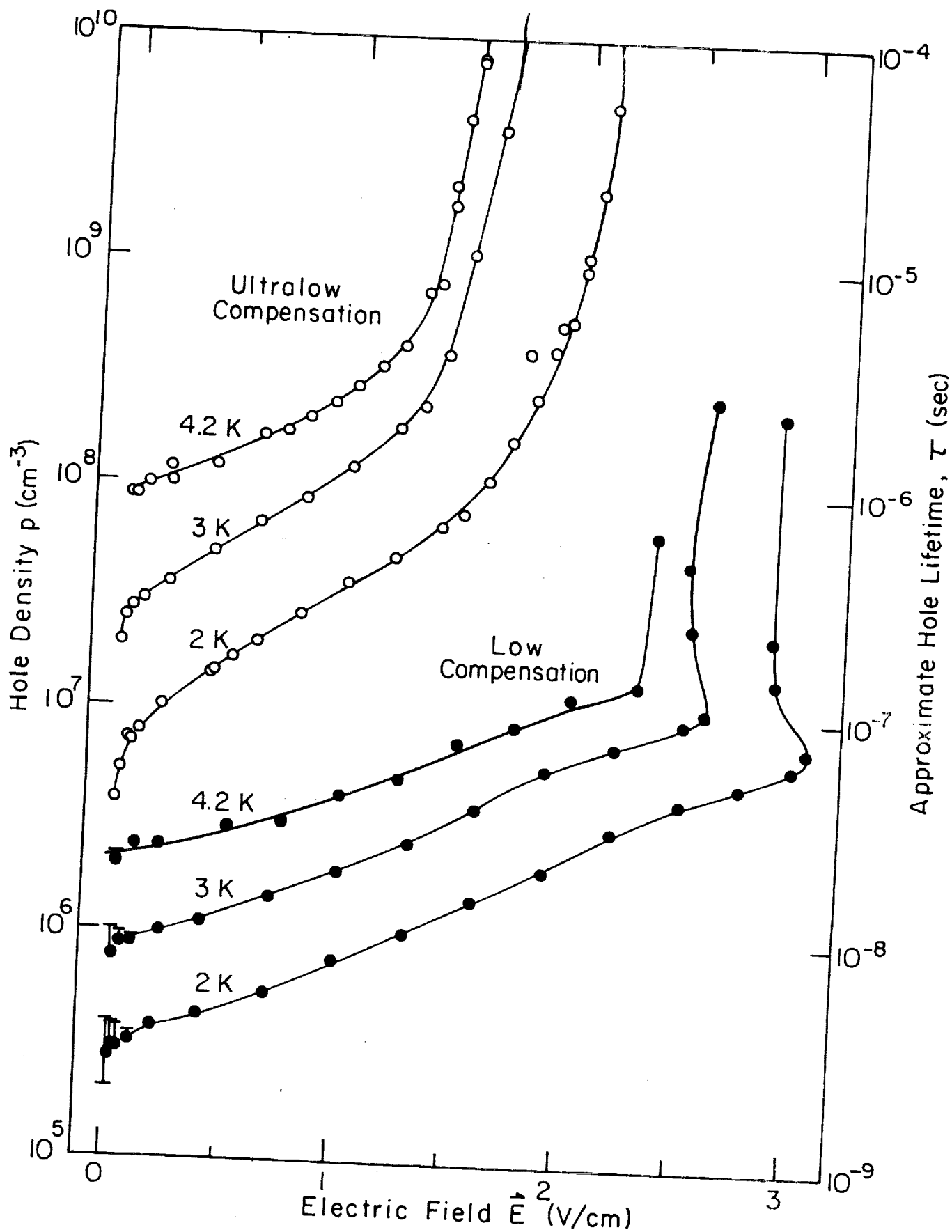
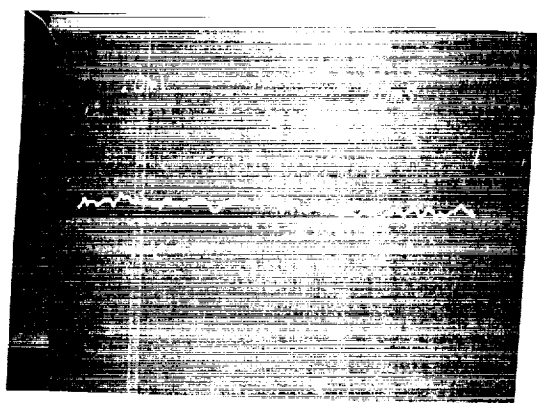


Figure 7

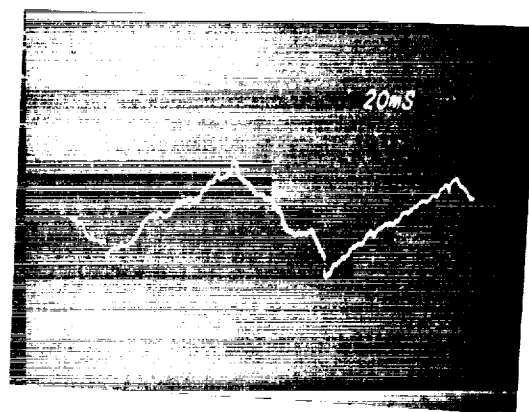
ENT

DEVELOPMENT OF INTEGRATING JFET
PREAMPLIFIERS

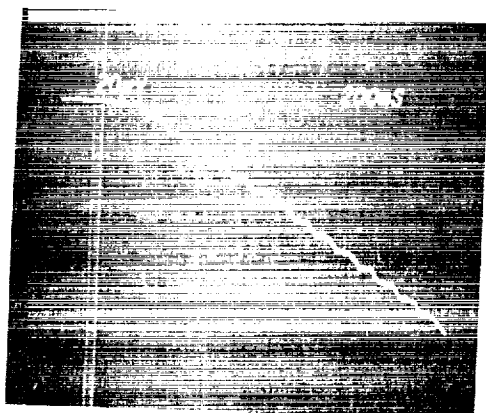
F. J. LOW, E. T. YOUNG
STEWART OBSERVATORY
UNIVERSITY OF ARIZONA
TUCSON, AZ 85721



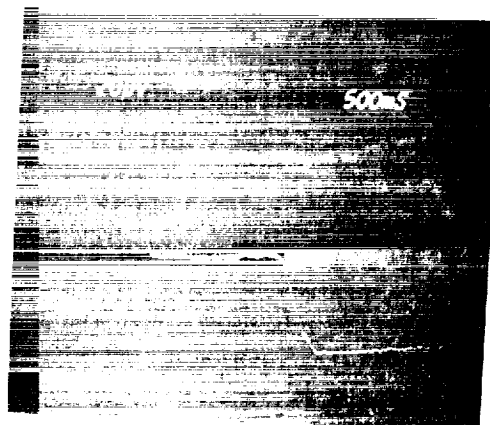
(a) 2N6484 (interf.) diode at 77°K with gate connected to all photo-diode. Preamp gain + 5000, bandwidth 1 to 100 Hz. Note ptp noise = 1.0 microvolt



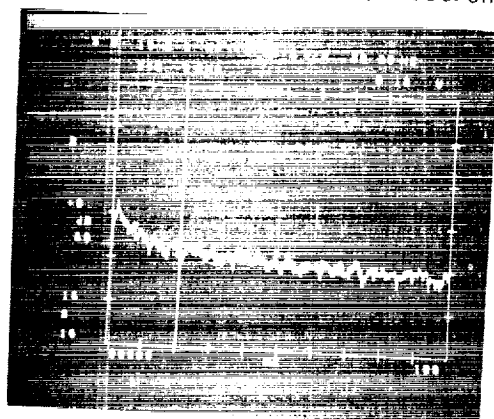
(b) As in (a) but LED source chopped on and off at 10 Hz. Intensity at photo-diode = 1×10^4 ph/sec. 1.0 microvolt + 100 photons.



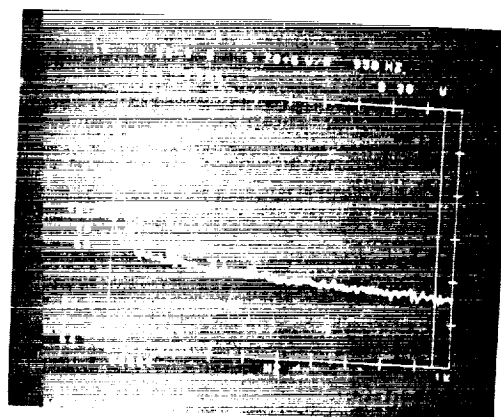
(c) Preamp gain + 10 and scope dc coupled to JFet source. Mechanical shutter opened to irradiate photo-diode as above. Note stair-step output after shutter opened. $\Delta v/\Delta t = 100$ microvolt/sec. $C = 12.5 \times 10^{-12}$ F at gate. Therefore, 15 nvolt/electron.



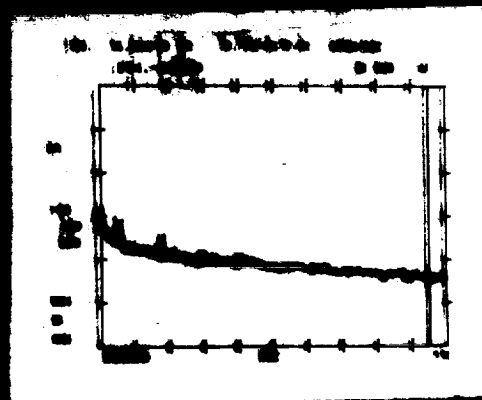
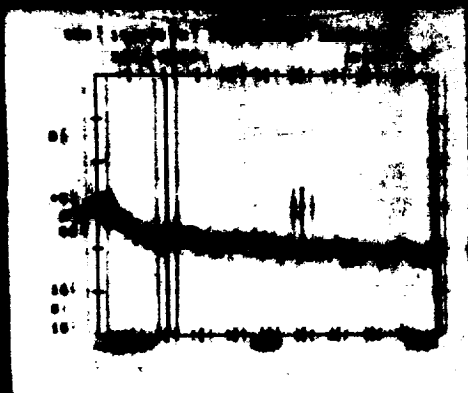
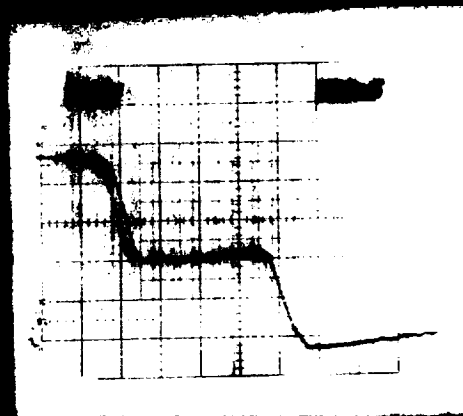
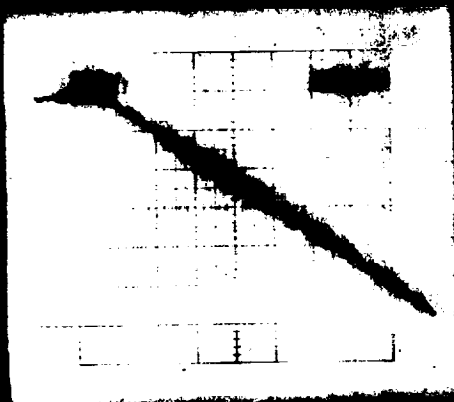
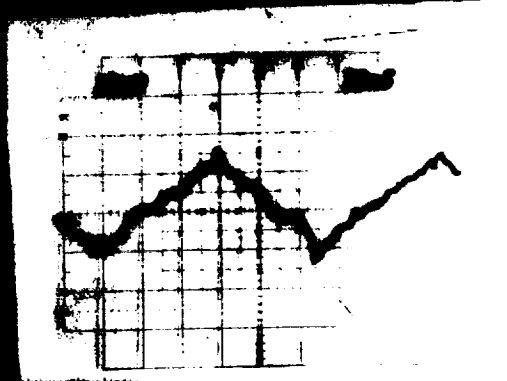
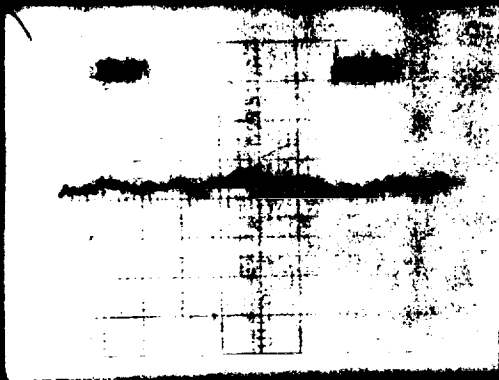
(d) Larger chopped photon flux used to show stair-step more clearly.

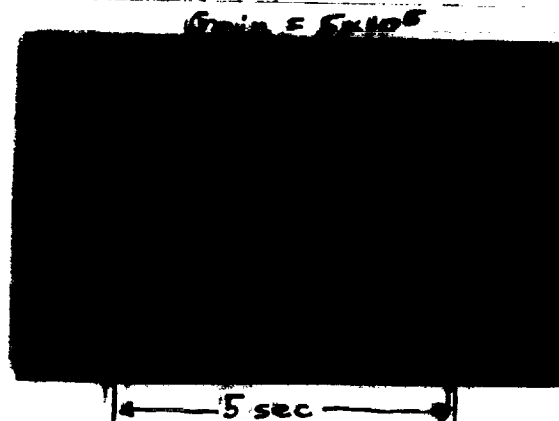


(e) Noise spectrum from 1 to 100 Hz using Nicolet Spectrum Analyzer. Noise at 20 Hz is 19.2×10^{-9} volt/Hz $^{1/2}$.



(f) Noise spectrum from 1 to 1000 Hz. Noise at 950 Hz is 5.22×10^{-9} volt/Hz $^{1/2}$.





Dark Current Measurement

Si: Sb; $V_B = +4.0$ v; $\Delta f = 0-10$ Hz

Vert. Scale = $4 \mu\text{v/cm}$

$$I = C \frac{dv}{dt} = (10E-12 \text{ f})(1.93 E-6 \text{ v/sec})$$

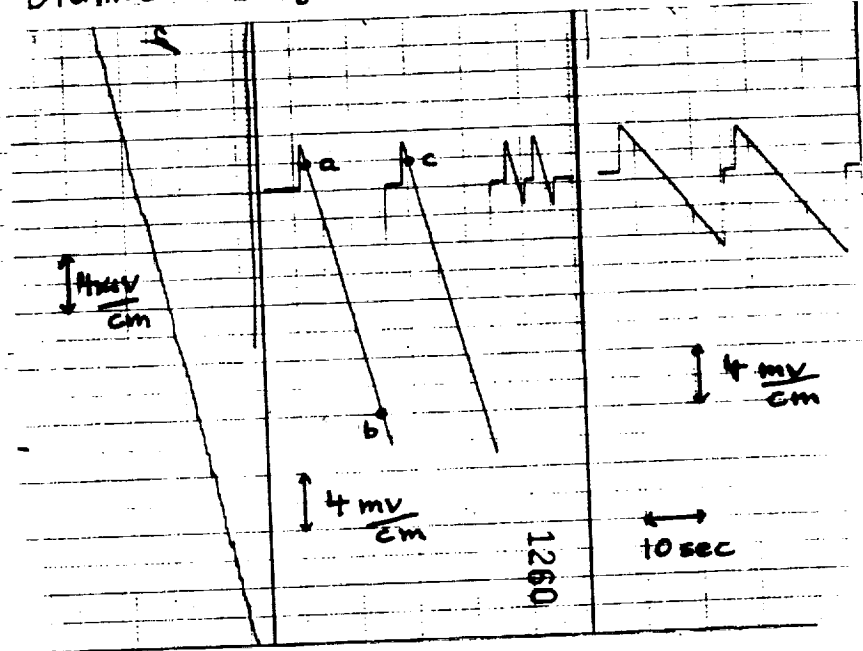
$$= \underline{1.93 E-17 \text{ amp}}$$

$$I_n = (10E-12 \text{ f})(0.15 E-6 \text{ v/sec/Hz}^{1/2})$$

$$= \underline{1.5 E-18 \text{ amp/Hz}^{1/2}}$$

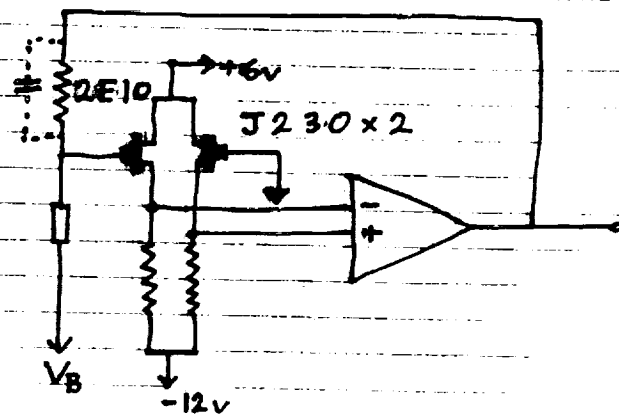
$$NEP = I_n / R = \underline{1.5 E-18 \text{ w/Hz}^{1/2}}$$

Blanked $T_b = 500\text{ C}$ $T_o = 25\text{ C}$



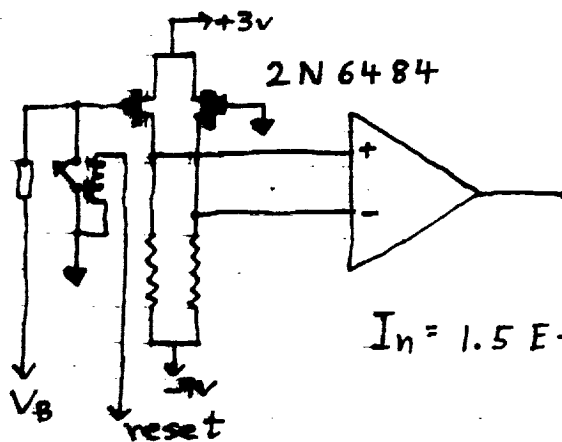
| | | | |
|----------------------------|---------------------|---------------------|--------------------|
| $\dot{V}(\mu\text{V/s}) =$ | 1.74 | 1480 | 480 |
| $I(\text{amp}) =$ | $1.74 \text{ E-}17$ | $1.48 \text{ E-}14$ | $4.8 \text{ E-}15$ |
| $P(\text{w}) =$ | 0 | $1.38 \text{ E-}14$ | $5.0 \text{ E-}15$ |
| $R(\text{amp/w}) =$ | | 1.07 | 0.96 |

IRAS TIA



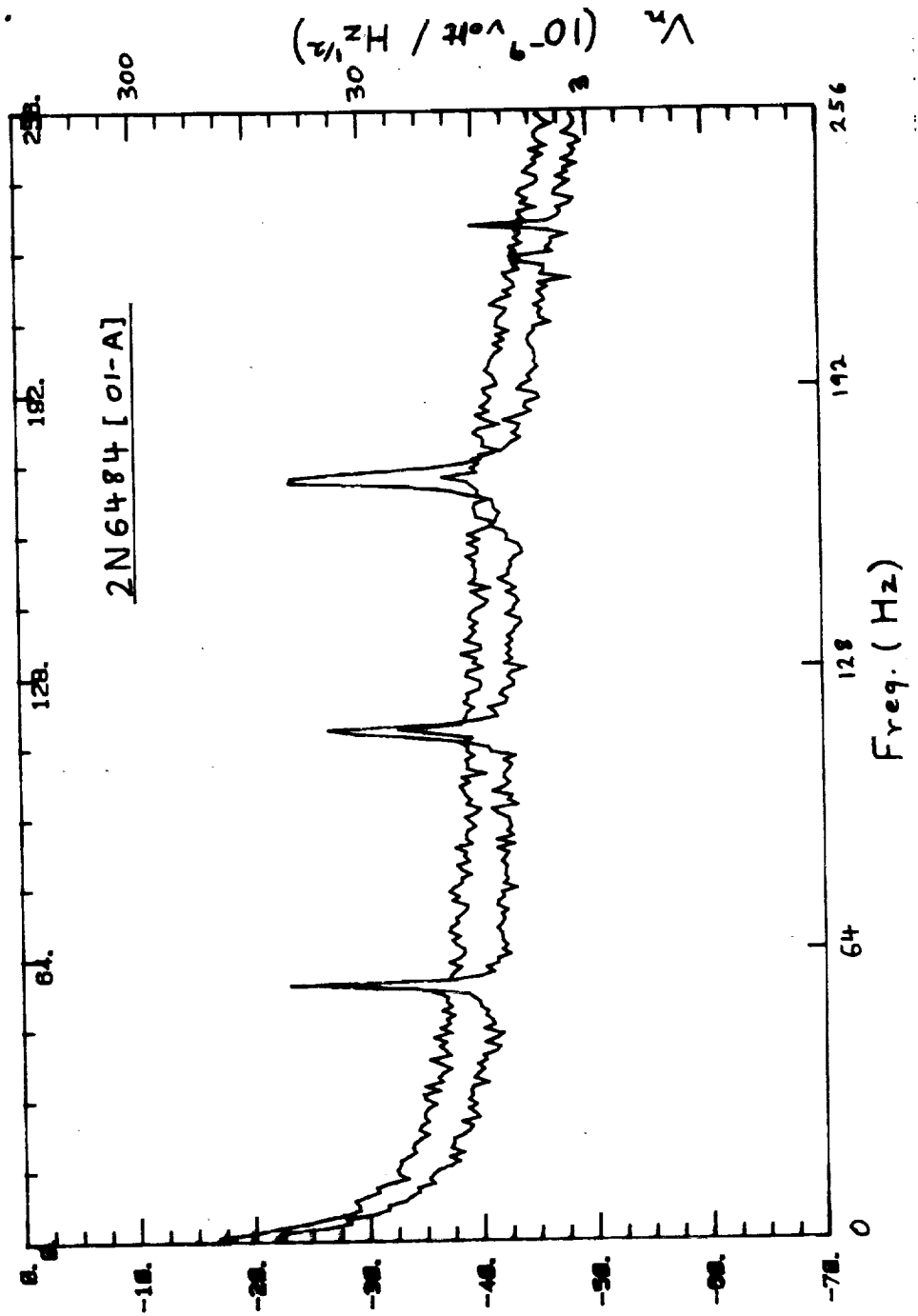
$$I_n = 1 E - 16 \text{ amp/Hz}^{1/2}$$

Integrating JFET



$$I_n = 1.5 E - 18 \text{ amp/Hz}^{1/2}$$

43 381 30 SHEETS 1 COLUMN
27 385 100 SHEETS 1 COLUMN



N 93 - 70639

IR Detector Technology Workshop
July 12-13, 1983
NASA Ames Research Center

An extended version of this material
has been submitted to the
International Journal of Infrared
and Millimeter Waves

Ge:Be FAR INFRARED PHOTOCONDUCTORS

N.M. Haegel^{1,2}

E.E. Haller^{1,2}

W.L. Hansen¹

M.R. Hueschen^{1,2,3}

P.N. Luke¹

P.L. Richards^{1,2}

C.H. Townes²

D.M. Watson^{2,4}

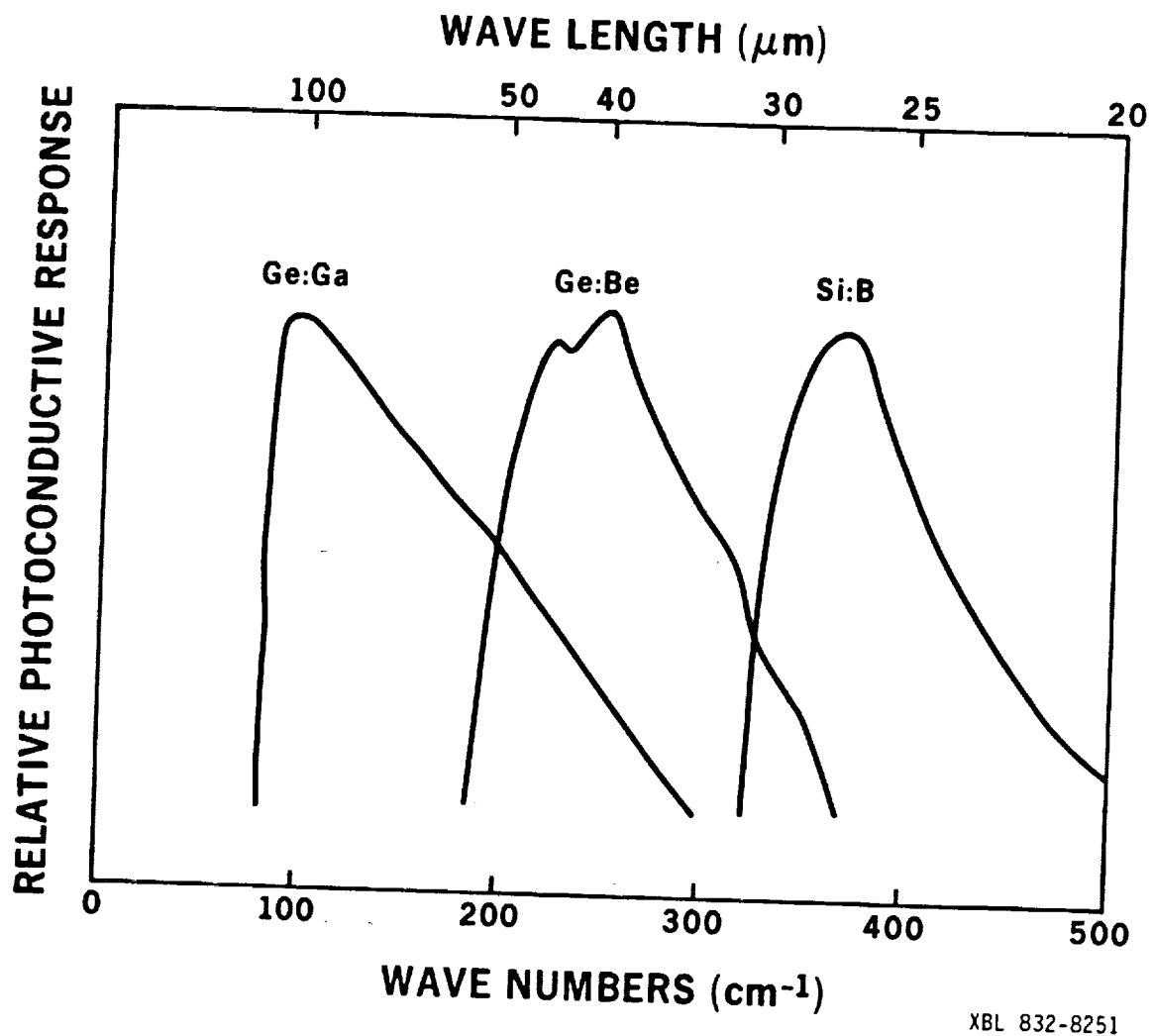
¹Lawrence Berkeley Laboratory and

²University of California, Berkeley

³Present address: Solid State
Laboratory, Hewlett Packard
Laboratories, Palo Alto CA

⁴Present address: Downs Laboratory
of Physics, California Institute of
Technology, Pasadena CA

53-74
133808
p-10
CC 787610
CC 747787
HR 912936
CB553097



XBL 832-8251

Ge:Be photoconductors can be optimized for the 30 to 50 μm wavelength range

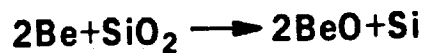
Ge:Be CRYSTAL GROWTH

Method: Czochralski

- control of shallow impurity levels ($N_A - N_D \approx 5 \times 10^{11} \text{cm}^{-3}$)
- crystallography (Dislocation density $< 1000 \text{cm}^{-2}$)

Crucible: Carbon susceptor

- avoid possible reaction with SiO_2 crucible



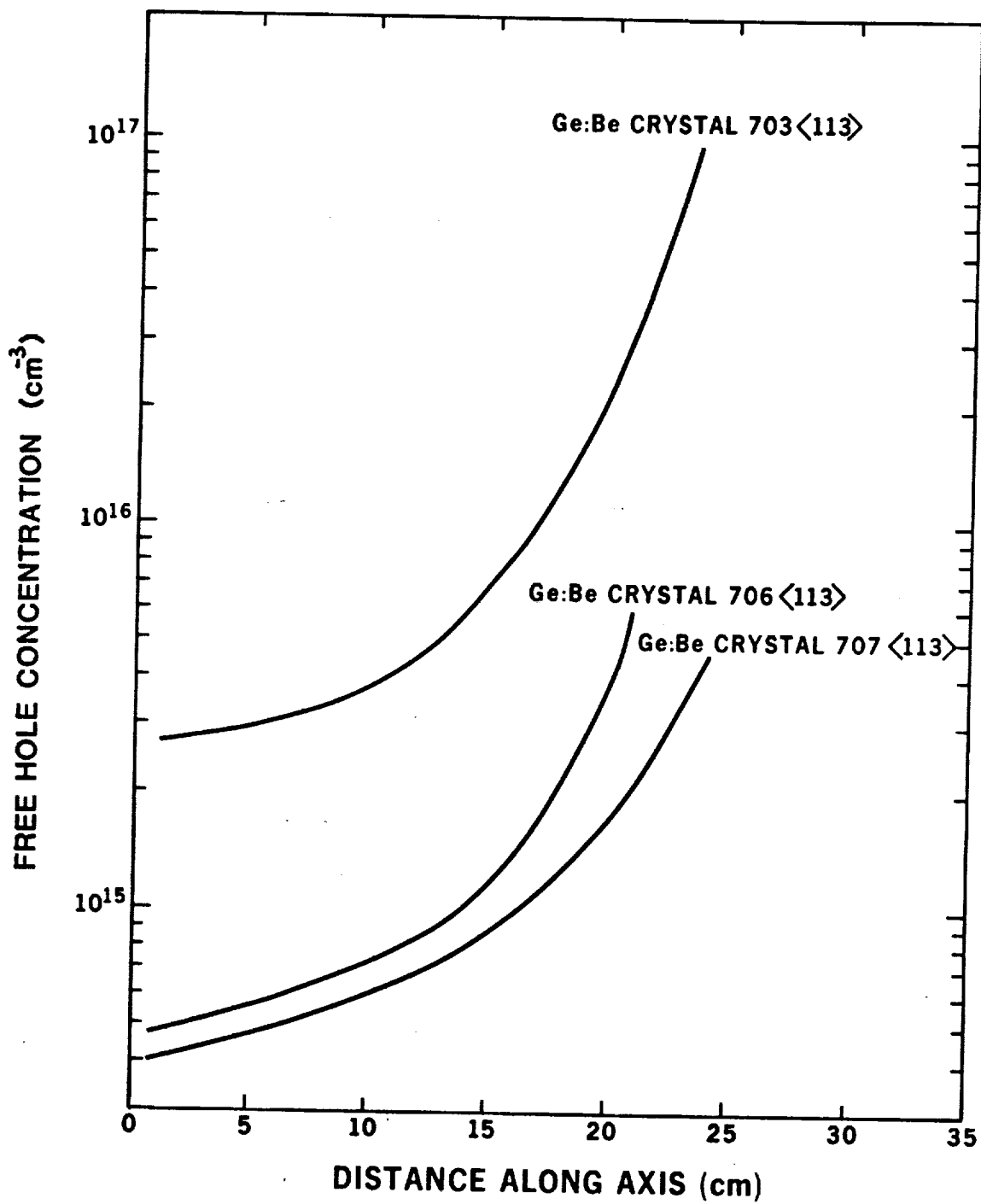
Atmosphere: Vacuum

-10^{-6} - 10^{-7} torr

- H_2O in the standard H_2 atmosphere can lead to BeO precipitation

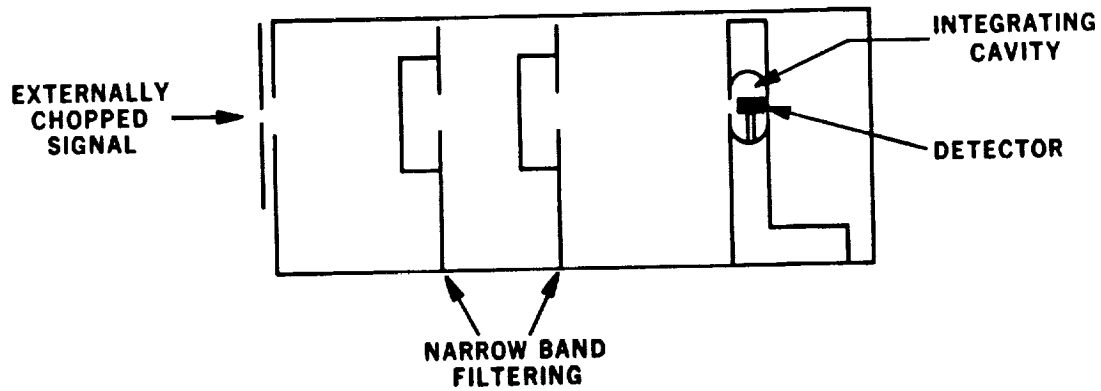


XBL 832-8256



XBL 832-8261

Ge:Be PHOTOCONDUCTOR EVALUATION



| | |
|------------------------|---|
| BACKGROUND FLUX | 1.5×10^8 PHOTONS/SEC 7.1×10^{-13} W |
| BACKGROUND LIMITED NEP | 1.15×10^{-16} W/ $\sqrt{\text{Hz}}$ |
| FILTER COMPONENTS | 42 μm FABRY-PEROT .7mm LiF .5mm KBr 2 MONOLAYERS 5-10 μm DIAMOND DUST |
| FILTER CHARACTERISTICS | λ (PEAK)=42.8 μm TRANSMISSION (PEAK)=13% Q=85 $\frac{\pi}{2} \Delta\lambda_{\text{FWHM}} = .93 \mu\text{m}$ |

XBL 832-8250

FIGURES OF MERIT

RESPONSIVITY

$$R = \text{Signal/Photon power} \\ = eG_{\eta}/h\nu$$

G = photoconductive gain

η = quantum efficiency

($\eta = 1$ assumed for all our results using an integrating cavity)

$h\nu$ = photon energy

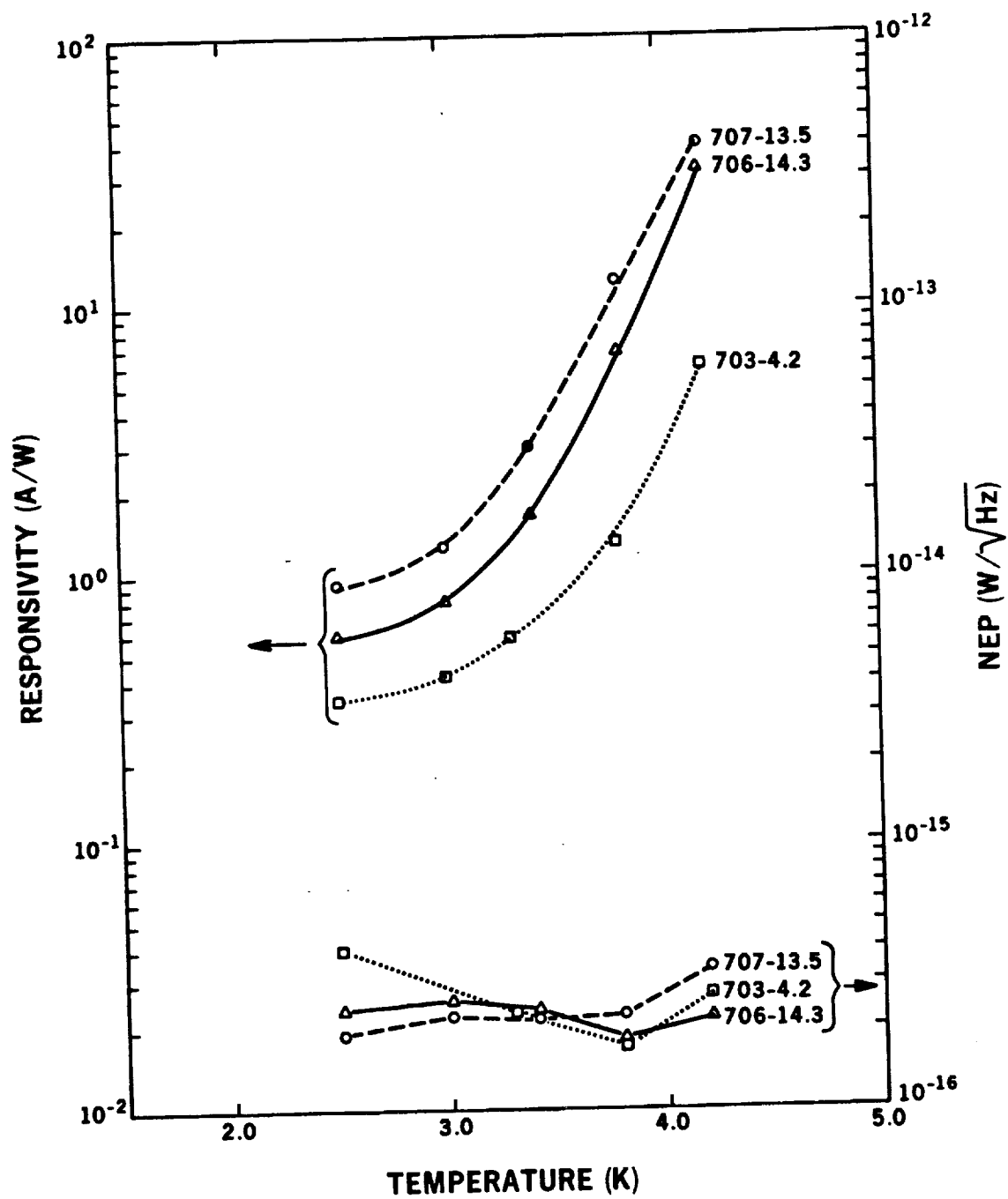
e = charge of the electron

NOISE EQUIVALENT POWER

$$\text{NEP} = \text{Noise/Responsivity}$$

Background limited:

$$\text{NEP}_{\text{BL}} = 2 \sqrt{P_{\text{Background}} h\nu}$$

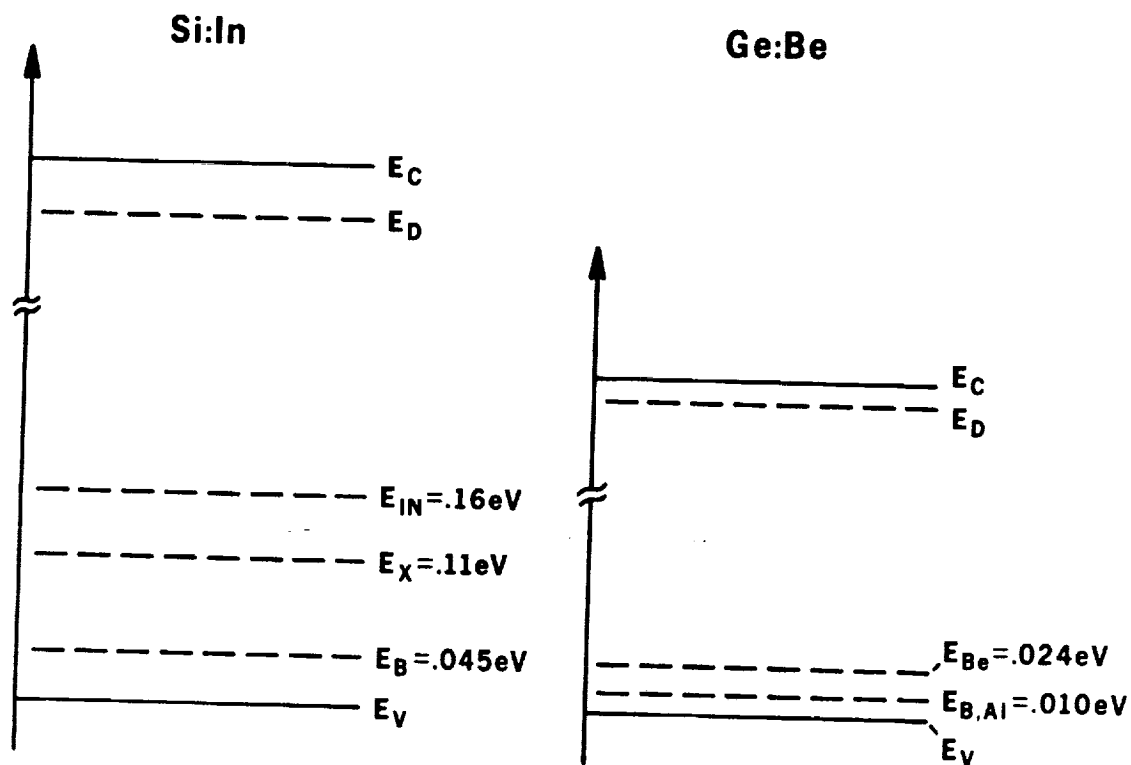


XBL 835-9788

$$NEP_{BL} = 1.1 \times 10^{-16} \text{ W}/\sqrt{\text{Hz}}$$

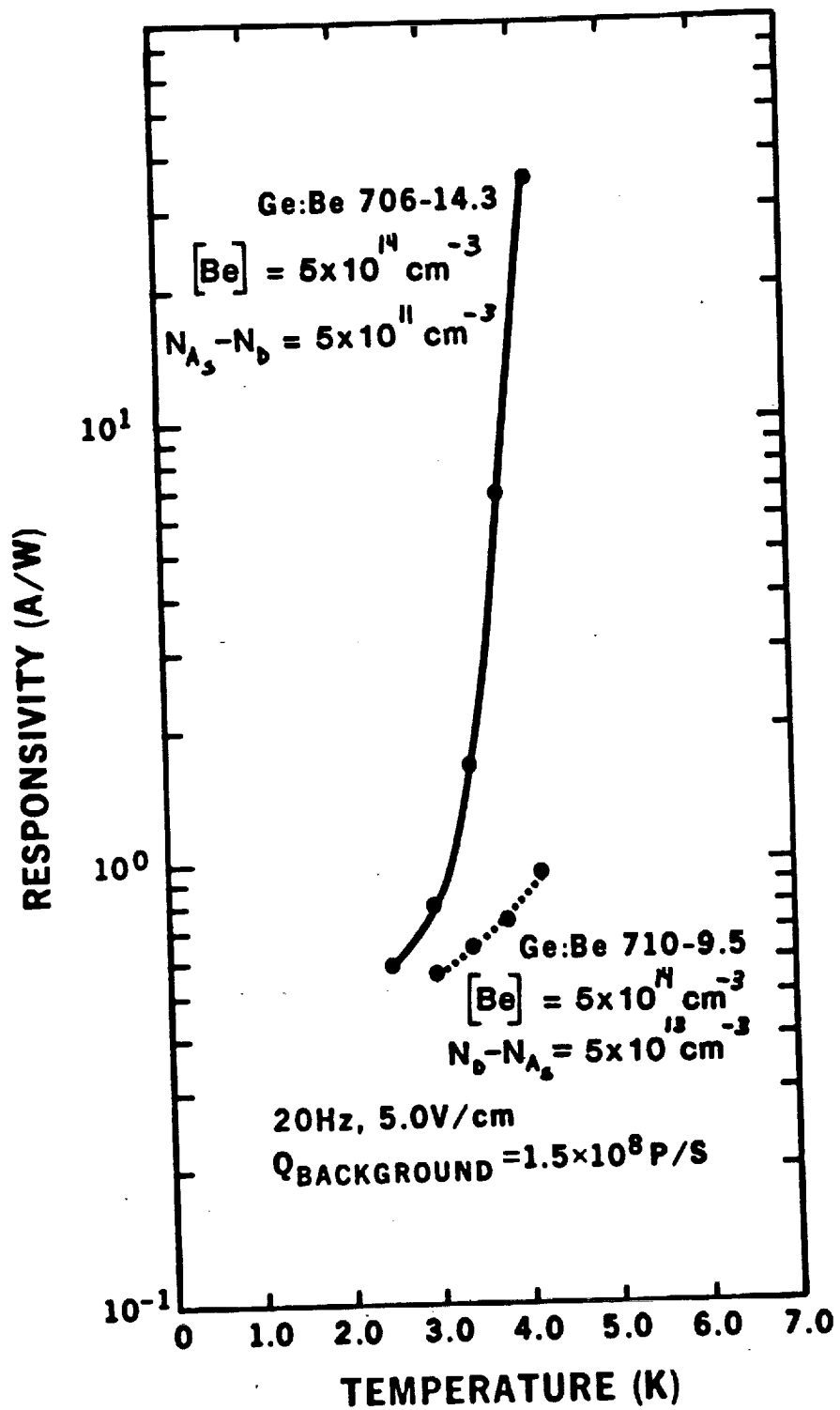
Chopping frequency 20 Hz

Bias field 5 V/cm



XBL 832-8257

See: Alexander D H, Baron R and Stafsudd O M, IEEE Trans. Elec. Dev. ED-27, No. 1, 71 (1980).



XBL 833-8803

CONCLUSIONS

- **Ge:Be detectors provide lower NEPs and higher responsivities than state-of-the-art Ge:Ga detectors at 42 μm**
- **Reliable Be doping has been achieved with Czochralski growth from a carbon susceptor under vacuum**
- **The photoconductive behavior of Ge:Be detectors is strongly influenced by the concentration of residual shallow impurities**
- **Optimization of Ge:Be detectors requires both a low concentration and precise compensation of shallow acceptors**

N 9 3 - 7 0 6 4 0

IR Detector Technology Workshop
July 12-13, 1983
NASA Ames Research Center

An extended version of this material
has been submitted to the
International Journal of Infrared
and Millimeter Waves

NEUTRON TRANSMUTATION DOPED Ge BOLOMETERS

**E.E. Haller^{1,2}
E. Kreysa³
N.P. Palaio^{1,2}
P.L. Richards^{1,2}
M. Rodder^{1,2,4}**

¹Lawrence Berkeley Laboratory and

²University of California, Berkeley

**³Max-Planck-Institute for
Radioastronomy, Bonn, FRG**

**⁴Present address: Fairchild Camera
and Instrument Corp., San Rafael CA**

*54-76
133809
P-10
CC 787610
MN 738126*

SEMICONDUCTOR BOLOMETER MATERIAL

- Resistivity-temperature dependence is controlled by dopant concentration and compensation**
- Reproducible doping technique is required**
- Optimum bolometer resistance: $1 - 20_{\text{M}\Omega}$ at operating temperature**

TRADITIONAL BOLOMETER MATERIAL

Melt doping during crystal growth



Impurity segregation and growth instabilities



Microscopic dopant striations

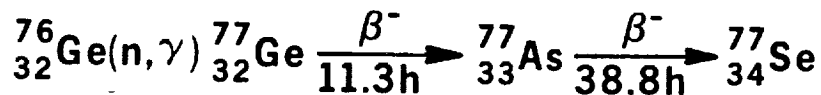
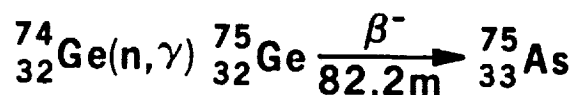
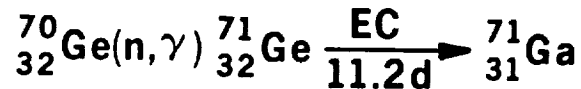


Difficulty in selecting crystal portion with optimum and uniform doping concentration

XBL 832-8253

NEUTRON TRANSMUTATION DOPED GERMANIUM

- Irradiation of Ge with thermal neutrons
- Neutron captures and decays:



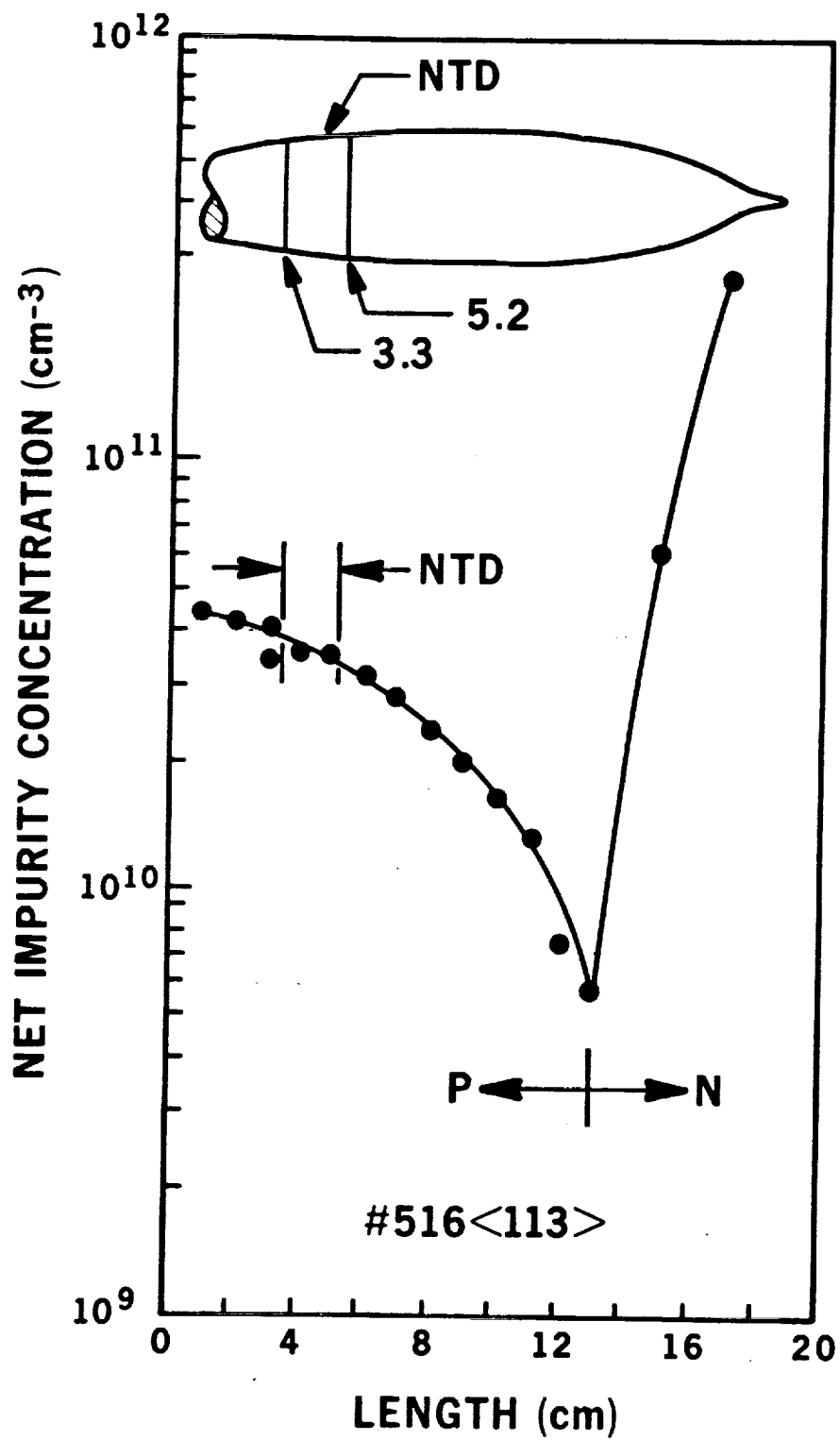
- Homogeneous impurity distribution reflects uniform neutron flux and uniform isotopic distribution
- Reproducibility: $N_{\text{Ga}} = \Phi \sigma_{70\text{Ge}} N_{70\text{Ge}}$
- Ultra-pure starting material
neutron doping levels \gg residual impurities

XBL 832-8258

SAMPLE PREPARATION

- Ultra-high purity Ge: $|N_A - N_D| < 10^{11} \text{ cm}^{-3}$
- Irradiation at Univ. of Missouri Research Reactor
(J. Meese)
- Six samples: $7.5 \times 10^{16} - 1.88 \times 10^{18} \text{ n/cm}^2$
- After six months: $750 \text{ Ga-Xrays/s cm}^3$, ~ 1 decay per
min. in a $(.3 \text{ mm})^3$ bolometer
- Radiation damage annealing: 400°C for 6 hours in
argon

XBL 832-8255



ABL 828-11253

MATERIAL CHARACTERIZATION

- Low temperature Hall Effect and resistivity measurements using Van der Pauw geometry

Berkeley (300-4.2K)

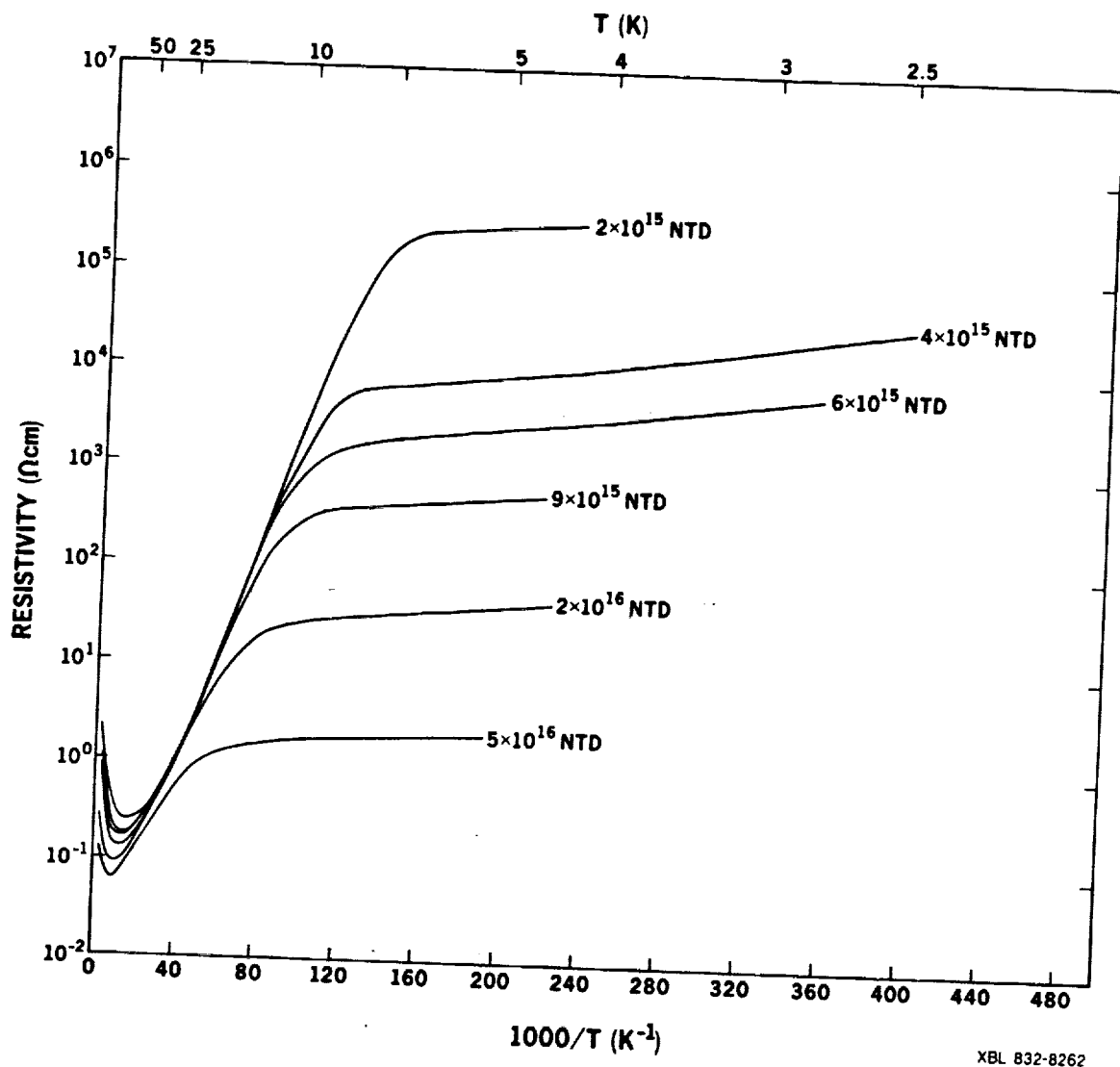
Bonn,FRG (4.2-0.3K)

- Resistivity relationship: $\rho = \rho_0 \exp(\Delta/T)$

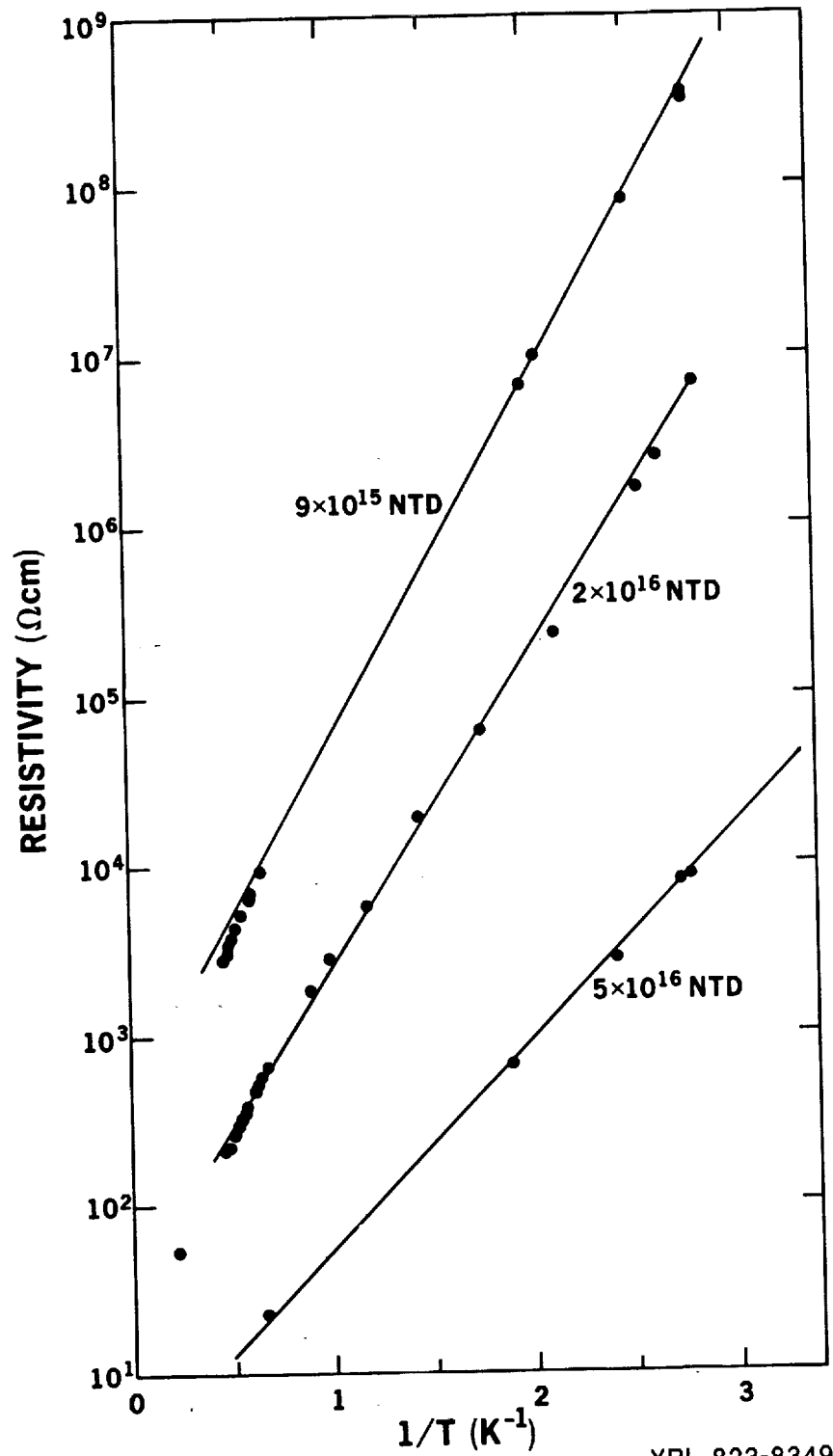
(Applies in the low temperature hopping
conduction regime $T < 8$ K)

| <u>NTD Sample</u> | <u>$\rho_0(\Omega\text{cm})$</u> | <u>$\Delta(\text{K})$</u> |
|--------------------|---|--------------------------------------|
| 9×10^{15} | 430.0 | 4.9 |
| 2×10^{16} | 34.0 | 4.4 |
| 5×10^{16} | 3.3 | 2.8 |

XBL 832-8252



Each resistivity curve is labeled with the gallium concentration per cm^3 .



XBL 823-8349

CONCLUSIONS

- NTD of high quality Ge single crystals provides perfect control of doping concentration and uniformity.**
- The resistivity can be tailored to any given bolometer operating temperature down to 0.1 K and probably lower.**
- The excellent uniformity is advantageous for detector array development.**

S5-74

133810

N93-70641

P-11

NC 473657

0.1K BOLOMETERS COOLED BY ADIABATIC DEMAGNETIZATION

| | |
|------------|------------------------|
| T. Roellig | (Ames Research Center) |
| L. Lesyna | (Ames Research Center) |
| P. Kittel | (Ames Research Center) |
| M. Werner | (Ames Research Center) |

Summary

The most straightforward way of reducing the noise equivalent power of bolometers is to lower their operating temperature. We have been exploring the possibility of using conventionally constructed bolometers at ultra-low temperatures to achieve NEP's suitable to the background environment of cooled space telescopes. We have chosen the technique of adiabatic demagnetization of a paramagnetic salt as a gravity independent, compact, and low power way to achieve temperatures below pumped ^3He (0.3K). The demagnetization cryostat we used was capable of reaching temperatures below 0.08K using Chromium Potassium Alum as a salt from a starting temperature of 1.5K and a starting magnetic field of 30,000 gauss. Computer control of the magnetic field decay allowed a temperature of 0.2K to be maintained to within 0.5mK over a time period exceeding 14 hours. The refrigerator duty cycle was over 90% at this temperature.

The cryostat was used to evaluate potential bolometer materials for ultra-low temperature use. The greatest promise was obtained from a boule of Ge:Ga with an axial concentration gradient that was purchased from Eagle-Picher. The room temperature resistivity of this material ranged from 0.05 to 0.07 Ω -cm. The boule was sliced into disks of different resistivities and tested for its ρ -T characteristics. Three of the slices yielded suitable material for 0.4, 0.2, and 0.1K bolometers. We have found that for this material the relation:

$$\rho = \rho_0 e^{A/T^{1/2}}$$

with ρ_0 and A constants (Redfield, Phys. Rev. Lett., 30, 1319, 1973) gave the best fit ρ -T curves.

Conventional bolometers were constructed out of this material and tested at 0.1 and 0.2K. In general, the bolometers behaved as theoretically expected, although electronic contributions to the system noise prevented the achievement of the theoretically ultimate NEP's. In spite of this, the

lower temperature bolometer had a measured system electrical NEP of $1.8 \times 10^{-16} \text{ W} / \sqrt{\text{Hz}}$ at 10 Hz. The success of these tests has motivated us to construct a more compact portable adiabatic demagnetization cryostat capable of bolometer optical tests and use at the 5m Hale telescope at 1mm. wavelengths.

Table Captions

Table 1: Derived parameters of the bolometer material shown in Figure 3. The resistivity has been fit to the equation $\rho = \rho_0 e^{1/T}$. Also shown is the optimum operating temperatures for bolometers made from these samples.

Table 2: Measured and derived electrical parameters of two bolometers. Both bolometers were constructed of $1 \times 1 \times 1$ mm blocks of Ge:Ga with In soldered 2mm x 20 um dia brass leads. The total noise listed in this table includes the contributions from all sources, including the pre-amplifier and measuring instrument noises.

Table 1

| <u>Sample</u> | <u>$\rho_0(\Omega\text{-cm})$</u> | <u>$A(^{\circ}\text{K})^{\frac{1}{2}}$</u> | <u>Op. Temp. ($^{\circ}\text{K}$)</u> |
|---------------|--|---|--|
| 1 | .02 | 10.3 | 0.4 |
| 2 | .03 | 7.6 | 0.2 |
| 3 | .14 | 5.1 | 0.1 |

Table 2

Bolometer Electrical Performance

| Measured Parameters: | Sample A | Sample B |
|--|-----------------------|-----------------------|
| Cold Sink Temperature ($^{\circ}\text{K}$) | 0.092 | 0.18 |
| Load Resistance ($\text{M}\Omega$) | 175 | 34 |
| Bolometer Resistance ($\text{M}\Omega$) | 1.7 | 1.7 |
| Bias Current (nA) | 11.4 | 8.5 |
| Electrical Responsivity (V/W) | 2.5×10^8 | 5.8×10^7 |
| 10 Hz Total Noise ($\text{nV}/\sqrt{\text{Hz}}$) | 45 | 38 |
| Electrical NEP ($\text{W}/\sqrt{\text{Hz}}$) | 1.8×10^{-16} | 6.3×10^{-16} |
| Calculated Parameters: | | |
| $G(\text{W}/^{\circ}\text{K})$ | 2×10^{-8} | 4×10^{-8} |
| $C(\text{J}/^{\circ}\text{K})$ | 4.5×10^{-11} | 1.1×10^{-10} |
| $\tau = C/G$ (msec) | 2.3 | 2.8 |
| Calculated Noise: | | |
| Bolometer Johnson Noise ($\text{nV}/\sqrt{\text{Hz}}$) | 3 | 4 |
| Thermal Fluctuation ($\text{nV}/\sqrt{\text{Hz}}$) | 24 | 23 |
| Load Resistor Johnson Noise ($\text{nV}/\sqrt{\text{Hz}}$) | 0.3 | 7 |
| Total Calculated Noise ($\text{nV}/\sqrt{\text{Hz}}$): | 24 | 25 |
| Theoretical NEP From Thermal Fluctuation Noise ($\text{W}/\sqrt{\text{Hz}}$): | 9.7×10^{-17} | 2.8×10^{-16} |

Figure Captions

- Figure 1: Plot of background limited noise equivalent power from two $\epsilon = 0.1$ telescopes at temperatures of 300K and 10K as a function of wavelength. Also shown are estimated NEP's of four bolometers of conventional construction operated at 1.2K, 0.3K, 0.1K, and 0.05K. The spectral bandwidth was taken to be $\Delta\lambda/\lambda = 0.1$ and the field of view was assumed to be diffraction limited.
- Figure 2: Schematic diagram of the adiabatic demagnetization refrigerator used to test bolometers.
- Figure 3: Resistivity as a function of $T^{-1/2}$ for three samples of Ge:Ga bolometer material.
- Figure 4: Load curve of a bolometer operating at 0.18K. The quantities plotted are the voltage across the bolometer (V_{out}) as a function of bias voltage across the bolometer and a 35 M Ω load resistor (V_{bias}).

Figure 1

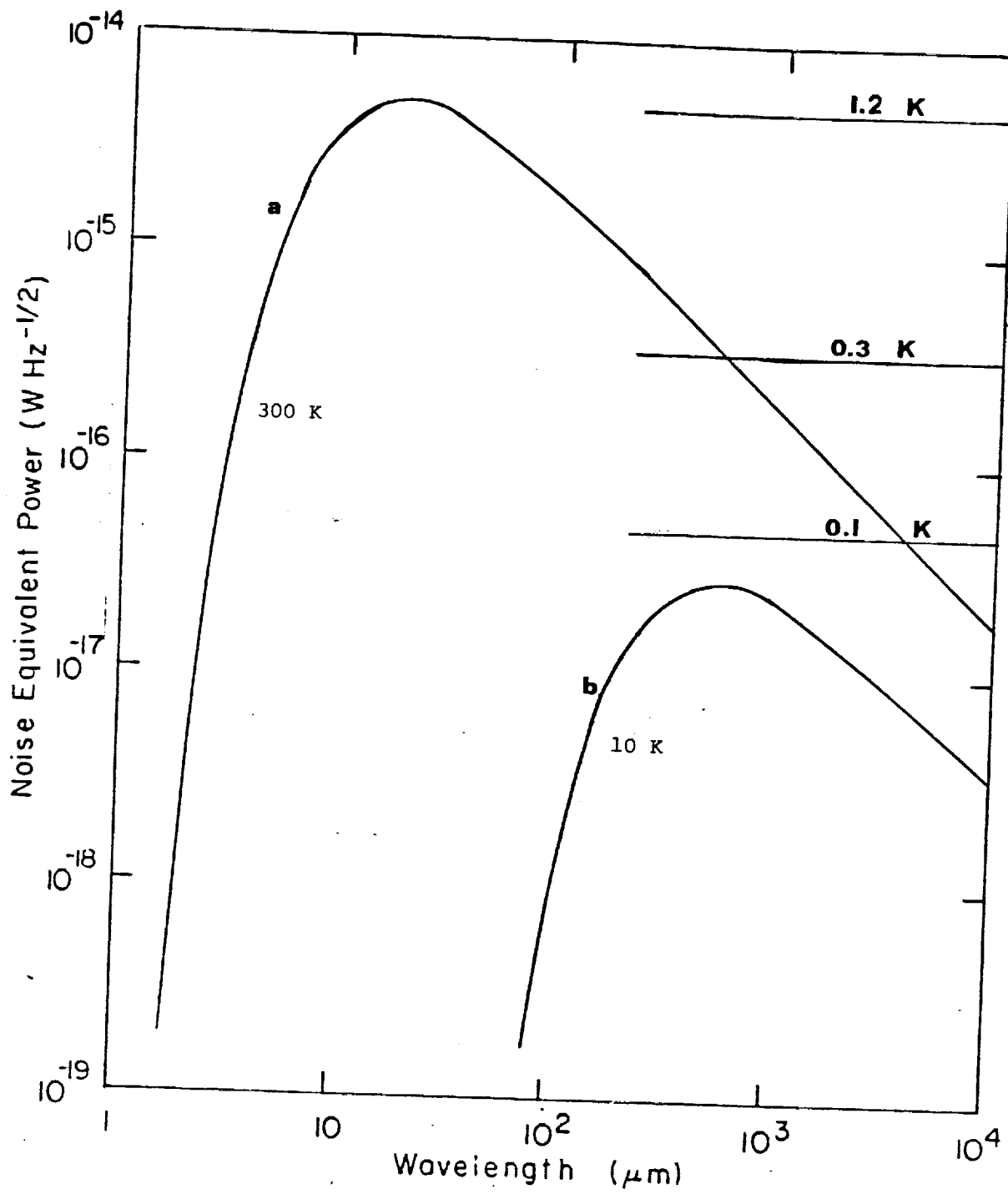


Figure 2

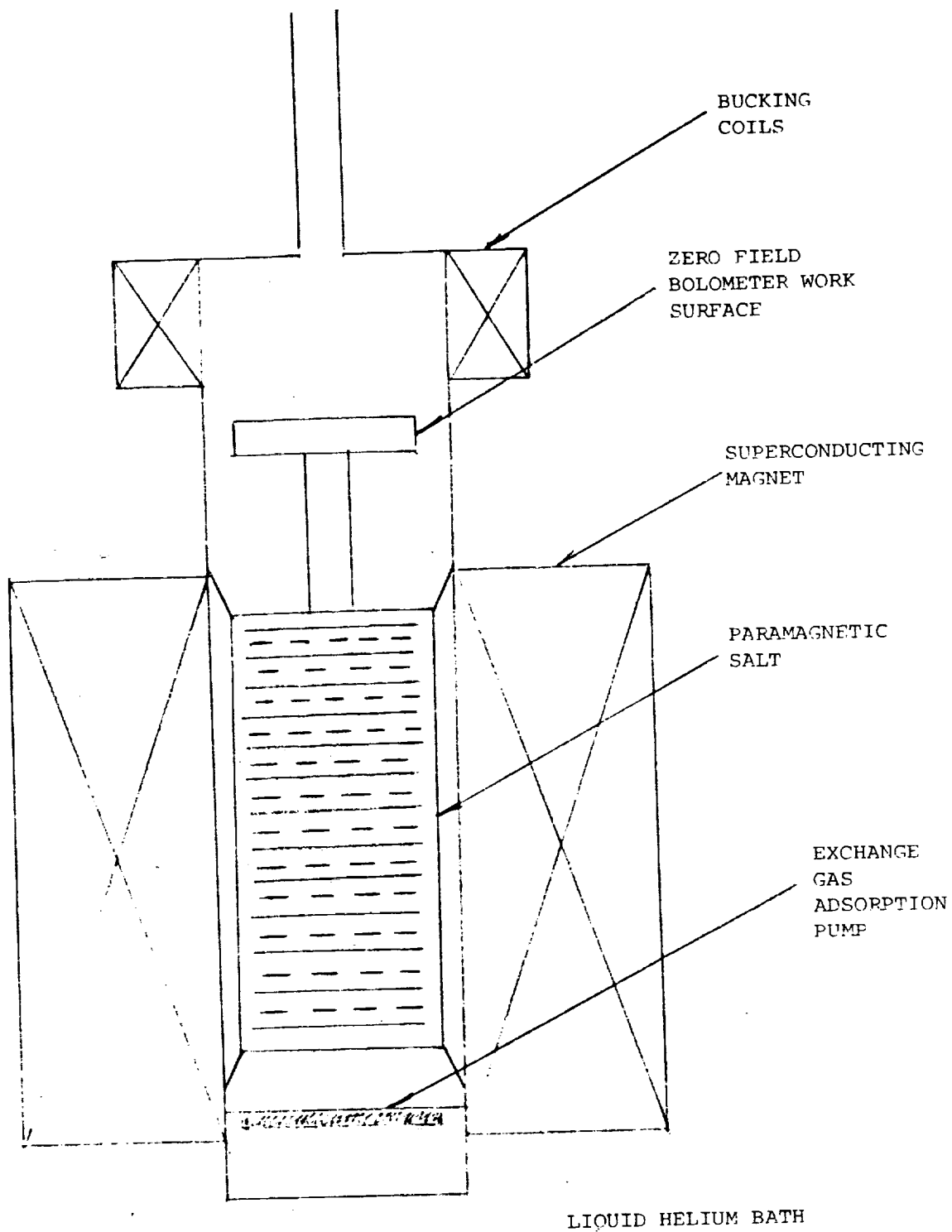


Figure 3

Ge:Ga Bolometer Material

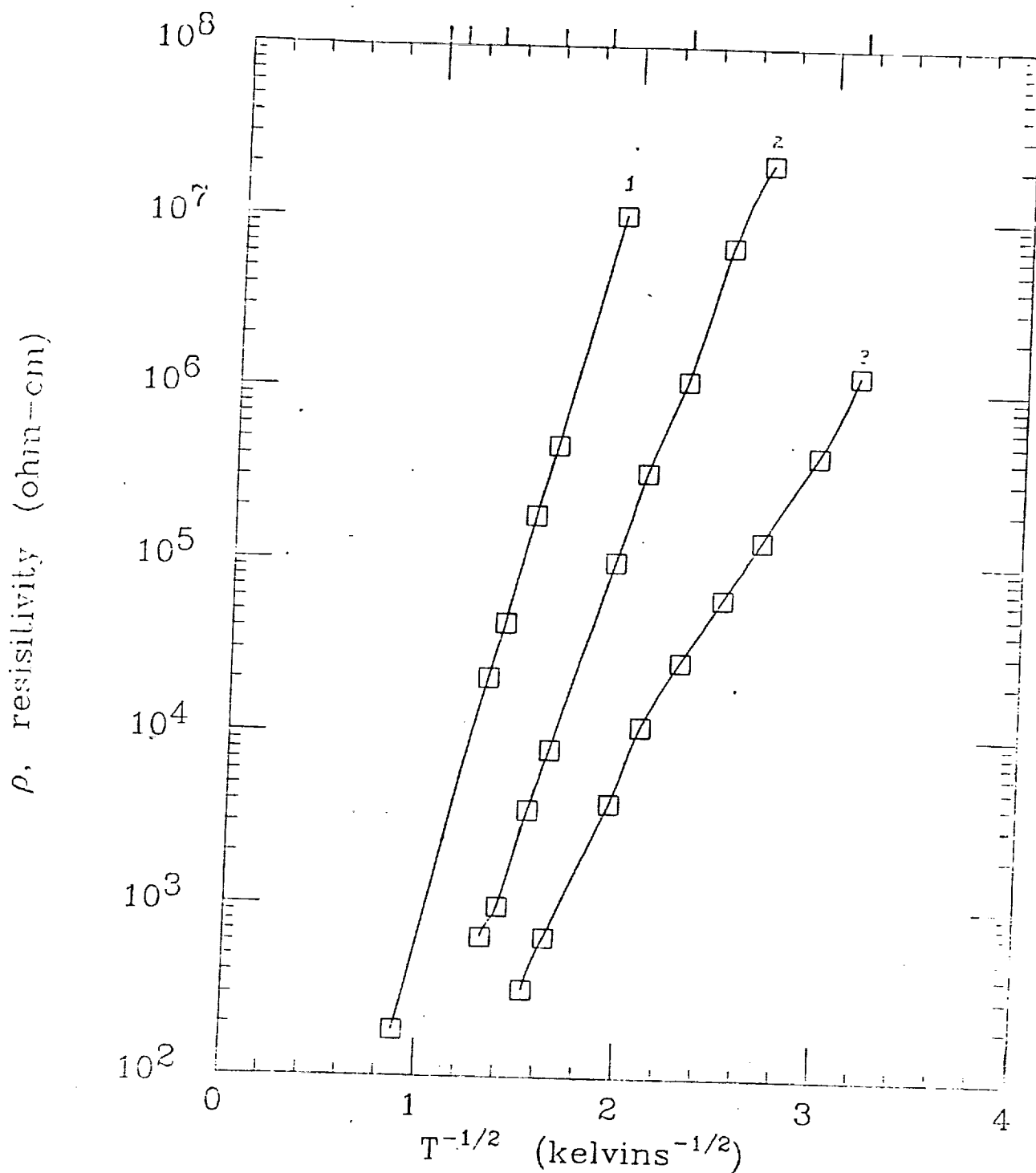
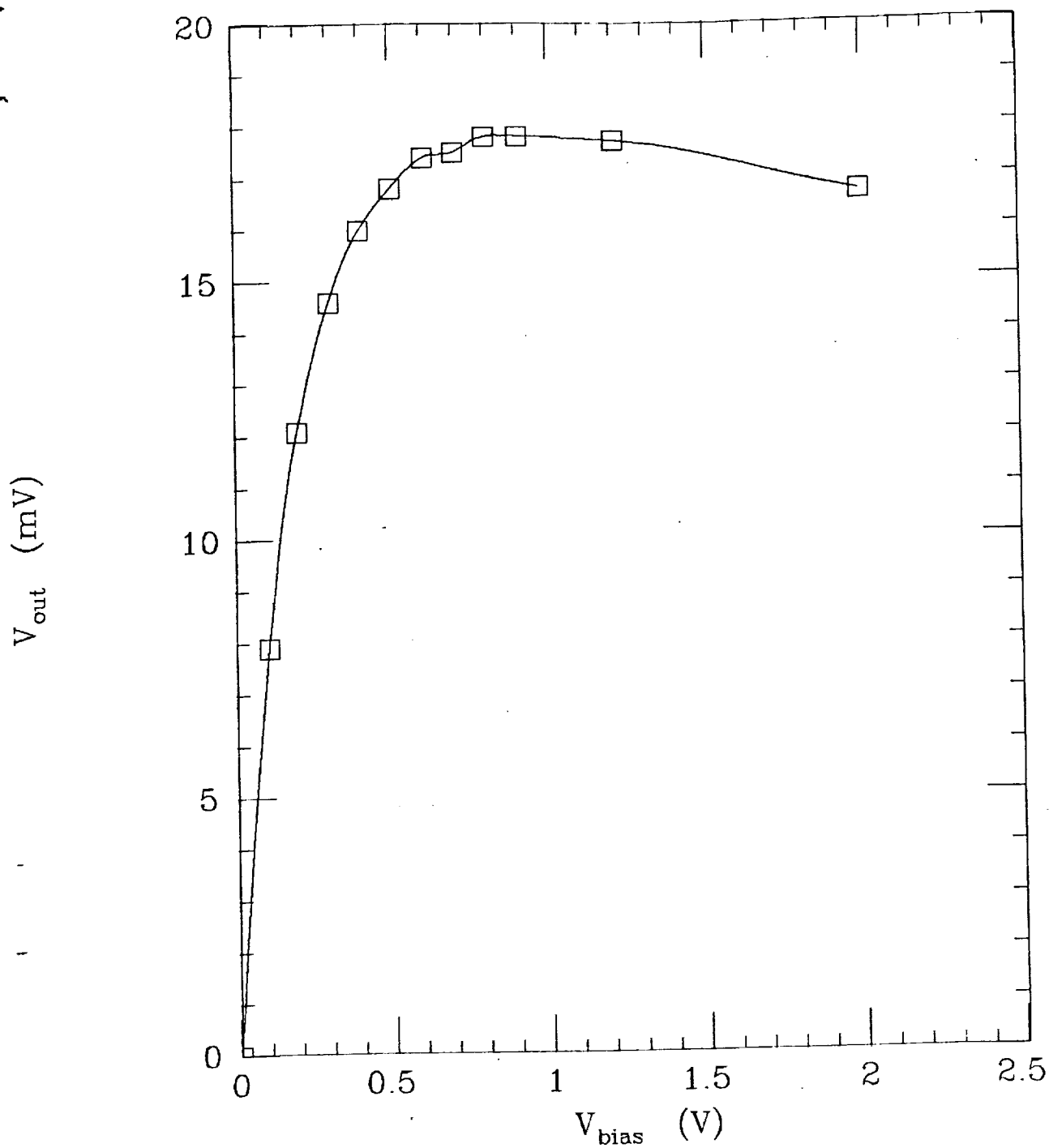


Figure 4

Bolometer Load Curve



Design Considerations for 0.1K Bolometers

Harvey Moseley

56-74
133 811 13
N93-70642

NC999967

Bolometers operating at low temperatures ($T \leq 0.3K$) are the best candidate for far infrared ($\lambda \geq 120 \mu m$) and submillimeter detection from cold orbiting telescopes. The limits of sensitivity for such devices have been studied (Mather, 1983). Based on this work, we conclude that excellent sensitivity is possible given careful detector design.

We have designed and are fabricating bolometers for operation at low temperatures. The crucial components in detector design are 1) heat capacity, 2) temperature sensing, and 3) absorption of infrared radiation. In this presentation, we discuss the choice of materials and fabrication techniques we have made in the interest of maximum sensitivity.

In order that optimization of detector performance be reasonably easy to carry out, we have attempted to use conventional fabrication techniques wherever possible (photolithography, wire bonding). The use of such procedures allows us to make design changes on short time scales, which is essential in achieving optimal performance.

In the following pages, we discuss some of the design problems presented by low temperature bolometers and indicate the solutions we have chosen.

RESEARCH SUPPORT

NASA INFRARED DETECTOR DEVELOPMENT PROGRAM (OSSA)

NASA/GSFC DIRECTOR'S DISCRETIONARY FUND

AIRBORNE ASTRONOMY PROGRAM (KAO)

COLLABORATORS

| | |
|---------------|---------------|
| M. DIPIRRO | NASA/GSFC |
| MARK DRAGOVAN | U. OF CHICAGO |
| AL HARPER | U. OF CHICAGO |
| G. LAMB | NASA/GSFC |
| JOHN MATHER | NASA/GSFC |

BOLOMETERS AS LOW BACKGROUND
INFRARED DETECTORS

ADVANTAGES:

WIDE WAVELENGTH RANGE, INCLUDING $\lambda > 120 \mu\text{m}$
STABLE IN NUCLEAR RADIATION ENVIRONMENT

PRINCIPLE OF OPERATION:

RADIATION HEAT SENSOR, TEMP RISE MEASURED BY
THERMISTER. DETAILED NOISE THEORY GIVEN BY MATHER
1982.

PERFORMANCE:

DEVICES MADE USING THE TECHNIQUES I OUTLINE ARE SHOWN
TO HAVE NOISE EQUIVALENT POWERS (NEP's) IN AGREEMENT
WITH THEORY - MOSELEY & LAMB, 1983, LANGE et al.,
1983.

PROJECTED SENSITIVITY:

BASED ON MEASURED PROPERTIES OF THE CONSTITUENT
MATERIALS, WE PREDICT $\text{NEP} < 2 \times 10^{-17} \text{ W/Hz}$ TO BE
ACHIEVABLE FOR $0.5 \times 0.5 \text{ mm}^2$ DETECTOR AT 0.1K WITH A
TIME CONSTANT $\tau \leq 5 \text{ msec.}$

REFRIGERATOR REQUIREMENTS

NEED LAUNCHABLE COOLER WHICH CAN COOL TO 100 mK WITH REASONABLE DUTY CYCLE OPERATING A 2K HEAT SINK WITHOUT EXCESSIVE POWER REQUIREMENTS.

SUCH A DEVICE HAS BEEN BUILT AT GSFC BY DR. STEVE CASTLES.
(100 mK FOR 90 MIN., 10 MIN. RECYCLE)

LABORATORY REFRIGERATOR HAS ALSO BEEN PROCURED AND IS NOW BEING SET UP. (SHE DILUTION REFRIGERATOR)

LOW TEMPERATURE BOLOMETERS

TYPICAL DESIGN PARAMETERS

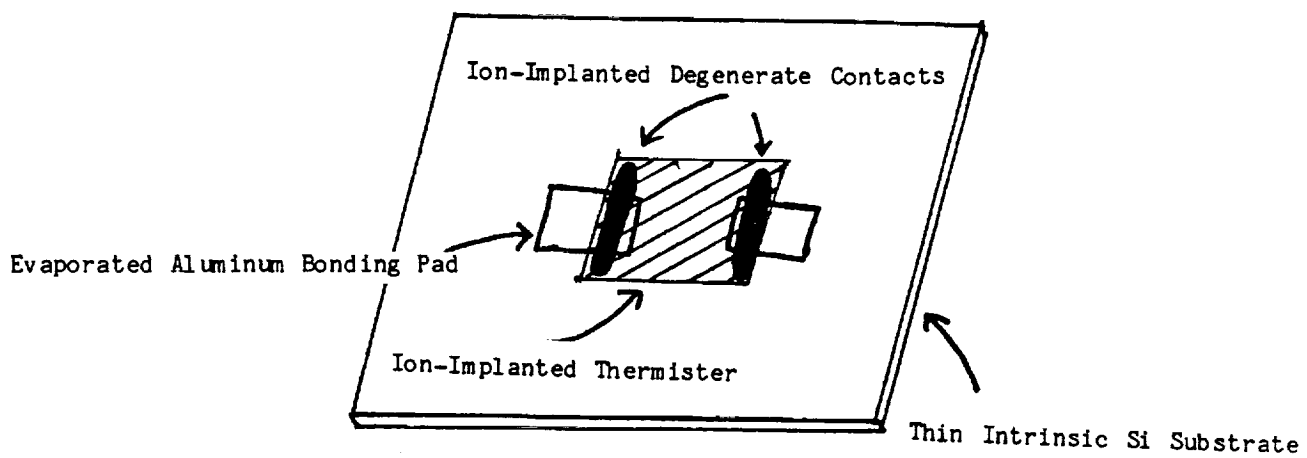
TEMPERATURE - 0.1K NOMINAL

SIZE - 0.5x0.5 mm

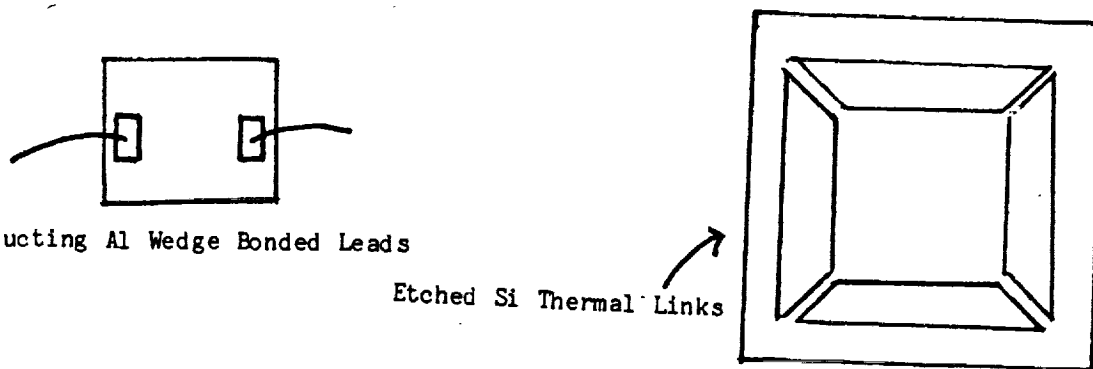
TIME CONST. - 5×10^{-3} s

NEP_{OPT} ~ 2×10^{-17} W/√Hz

BOLOMETER SCHEMATIC



Thermal Links to
Heat Sink



DESIGN CONSIDERATIONS

- MINIMIZE HEAT CAPACITY
- ACHIEVE ADEQUATE ABSORPTION OF IR RADIATION
- GET DESIRED THERMAL CONDUCTANCE
- FIND TEMP TRANSDUCER QUIET ENOUGH TO BE LIMITED BY FUNDAMENTAL NOISE PROCESSES (JOHNSON & PHONON)
- DEVELOP BIAS AND AMPLIFIER CIRCUIT WHICH DOES NOT DEGRADE SYSTEM NOISE
- DEVELOP CRYOSTAT WHOSE TEMP FLUCTUATIONS DO NOT DOMINATE NOISE OF BOLOMETER

HEAT CAPACITY CONSIDERATIONS

- o SI DESIRABLE BECAUSE OF LOW HEAT CAPACITY.
- o CONTACT AND THERMOMETER IMPLANTS HAVE HIGH HEAT CAPACITY - MINIMIZE VOL.
- o THERMAL LINK CAN DOMINATE HEAT CAPACITY: WE WILL USE EITHER SI OR AL WELL BELOW SUPERCONDUCTING TRANSITION.
- o ABSORBING FILM: WE ARE ATTEMPTING TO DEVELOP ALUMINUM GRID TO ABSORB RADIATION - LOW HEAT CAPACITY.
- o SUCCESSFUL TESTS ON GOLD ABSORBING FILMS HAVE BEEN CARRIED OUT (DRAGOVAN & MOSELEY, 1983).

NOTE: TRAPPED MAGNETIC FIELDS IN SUPERCONDUCTORS CAN CAUSE SUBSTANTIAL PORTIONS TO BE NORMAL, THUS HAVE HIGH HEAT CAPACITY. SHIELDING OF FIELDS DURING COOLDOWN IS CRITICALLY IMPORTANT.

THERMAL CONDUCTANCE

- o ALUMINUM LINKS - BELOW $\sim 0.15\text{K}$, AL IS DOMINATED BY PHONON TRANSFER. CONDUCTION CAN BECOME LOW ENOUGH TO BE USEFUL.
- o SI LINKS - CONDUCTION DEPENDENT ON MEAN FREE PATH. CAN PROBABLY BE TAILORED WITHIN CERTAIN RANGES, BUT DIFFICULT TO MAKE VERY LOW.

DESIRED $G \sim 1 \times 10^{-12}$ W/K
FOR DESIGN BOLOMETER

$$\tau = \frac{C}{G}$$

TEMPERATURE SENSOR

- o ABSENCE OF "CURRENT NOISE" CRITICAL; SENSOR SHOULD BE LIMITED BY JOHNSON NOISE.

- o HIGH $\alpha = \frac{d \ln R}{d \ln T}$ DESIRABLE

MATHER'S (1983) RESULT. NEP PROPORTIONAL TO $\frac{1}{\sqrt{\alpha}}$

- o DOPED Si & Ge ARE CONVENIENT THERMOMETERS. WITH ION IMPLANTED CONTACTS, NOISE CAN BE NEAR THAT PREDICTED BY THEORY.

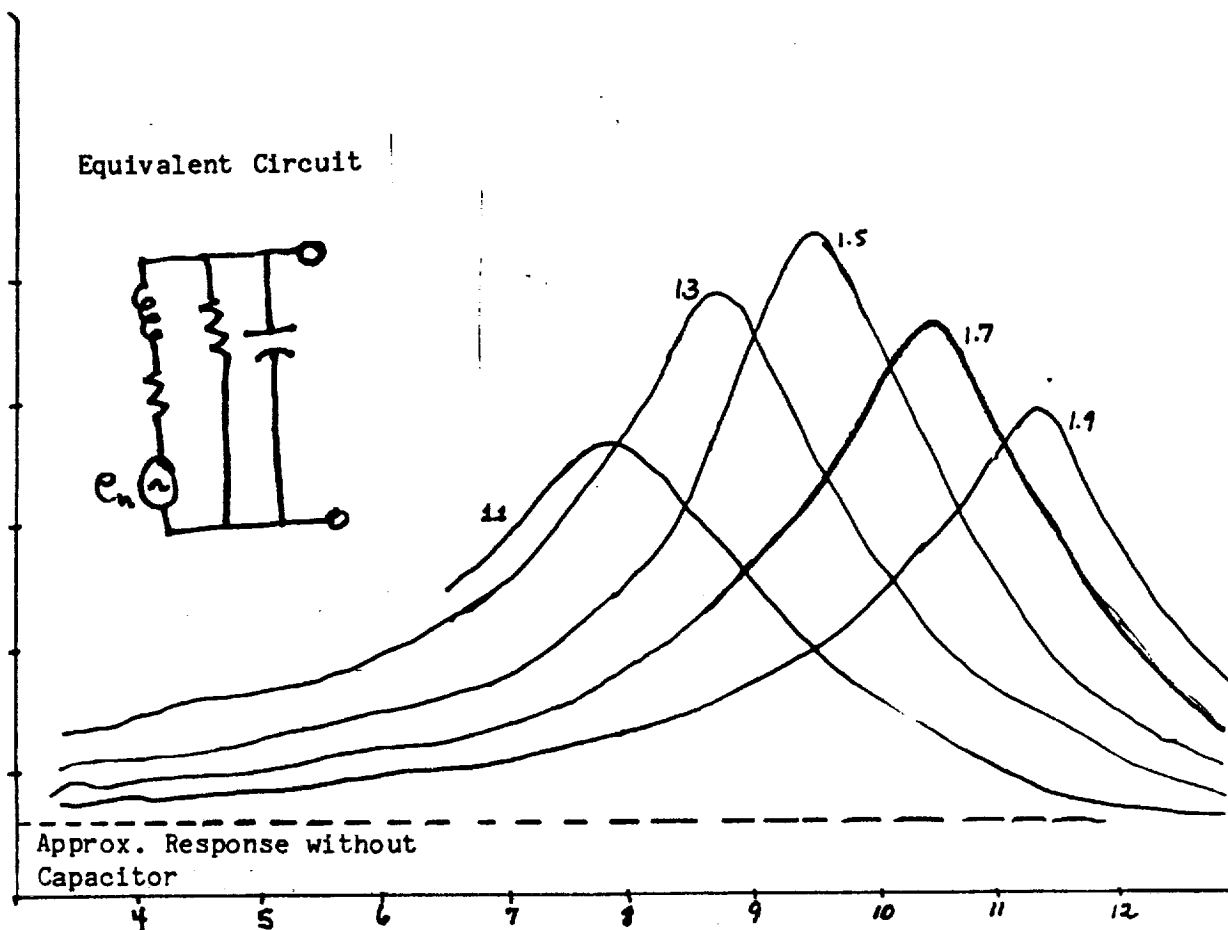
REFERENCES: MOSELEY & LAMB, 1983
LANGE et al., 1983
WEISS (priv. comm.)

- o DEVICE IMPEDANCES CAN BE SELECTED TO MATCH NOISE CHARACTERISTICS OF AMPLIFIERS.

AMPLIFIERS AND BIAS CIRCUITS

- JFET's CAN BE VERY GOOD - NOISE TEMPERATURE $T_N \sim 10 \text{ mK}$
 $R_{\text{noise}} \sim 100 \text{ M}\Omega$ BASED ON OUR MEASUREMENTS.
- QUIET LOAD RESISTORS CAN BE MADE USING BOLOMETER
PROCESS IF NECESSARY.
- SINCE BOLOMETERS HAVE $T_{\text{noise}} > T_{\text{phys}}$ AMPLIFIERS PRODUCE
NO PROBLEM FOR OPERATING TEMPERATURES NEAR 0.1K.
- RESONANCE EFFECTS WITH CAPACITORS CAN BE USED IF NECESSARY.
- MICROPHONICS REPRESENT PRACTICAL PROBLEMS BUT NO
FUNDAMENTAL DIFFICULTY. RECENT TESTS SHOW THAT MICROPHONICS CAN
BE SUFFICIENTLY SUPPRESSED.

Frequency Response for Various Biases



Resonant enhancement of bolometer signals using a shunting capacitor. As predicted by Mather (1983), both amplitude and Q of enhancement are functions of detector bias. Use of the capacitive resonance can be useful in improving the performance of detectors in amplifier noise limited systems.

CRYOSTAT TEMP FLUCTUATIONS

- o FOR FIXED τ , $G \propto C$

τ = TIME CONST., G = THERMAL CONDUCTANCE, C = HEAT CAPACITY
IN A PROPERLY DESIGNED BOLOMETER $C \propto T^3 + G \propto T^3$

- o TEMPERATURE FLUCTUATIONS IN THE CRYOSTAT CAUSE BOLOMETER FLUCTUATIONS. THESE CAN BE RELATED TO AN EQUIVALENT POWER FLUCTUATION.

$$\delta P = G \delta T \propto T^3 \delta T$$

$$\text{HOWEVER, NEP} \propto T^{5/2}$$

THUS, AS $T \rightarrow 0$ THE TEMPERATURE FLUCTUATION POWER DECREASES FASTER THAN DETECTOR NOISE, AND IS LESS IMPORTANT THAN AT HIGHER TEMPERATURES.

TYPICAL TEST PROCEDURE

- o NOISE vs. FREQUENCY
- o I, V PLOTS
- o $Z(\omega)$ MEASUREMENTS (CAN BE RELATED TO THERMAL TIME CONST.
(MATHER, 1982))
- o INDEPENDENT INFRARED ABSORPTANCE MEASUREMENT - (TRANSMISSION
AND REFLECTION MEASUREMENTS ON SPECTROMETER)
- o COMPARISON OF MEASURED PARAMETERS TO THEORY

EXCELLENT AGREEMENT HAS BEEN OBTAINED BETWEEN MEASUREMENT AND THEORY IN OUR ION IMPLANTED SILICON BOLOMETERS. THUS THE TESTS OUTLINED ABOVE ARE SUFFICIENT TO ALLOW US TO PROJECT PERFORMANCE OF THESE DEVICES AS INFRARED DETECTORS.

REFERENCES:

Dragovan, M. and Moseley, H., Preprint (1983).

Lange, A. E., Kreysa, E., McBride, S. E., Richards, P. L., and Haller, E. E.,
Preprint (1983).

Mather, J. C., Appl. Opt. 21, 1125 (1982).

Mather, J. C., Preprint (1983).

Moseley, H. and Lamb, G., Preprint (1983).

57-74 44

133812

N93-70643

AE 261302

REVIEW OF AMCID TECHNOLOGY

C. M. PARRY

AEROJET ELECTROSYSTEMS COMPANY

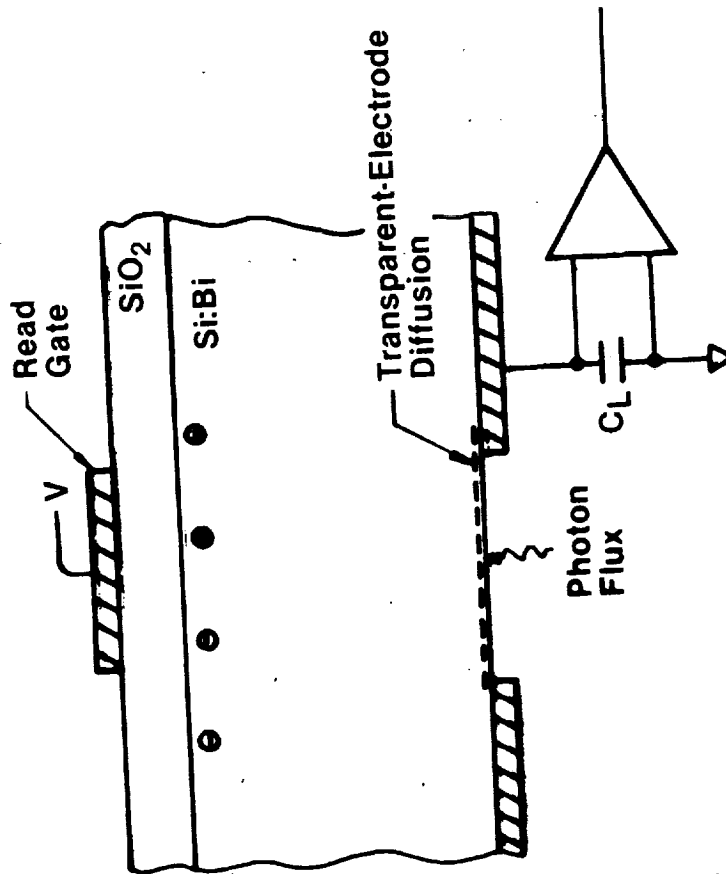
BOX 296

AZUSA, CA. 91702

REVIEW OF
AMCID TECHNOLOGY

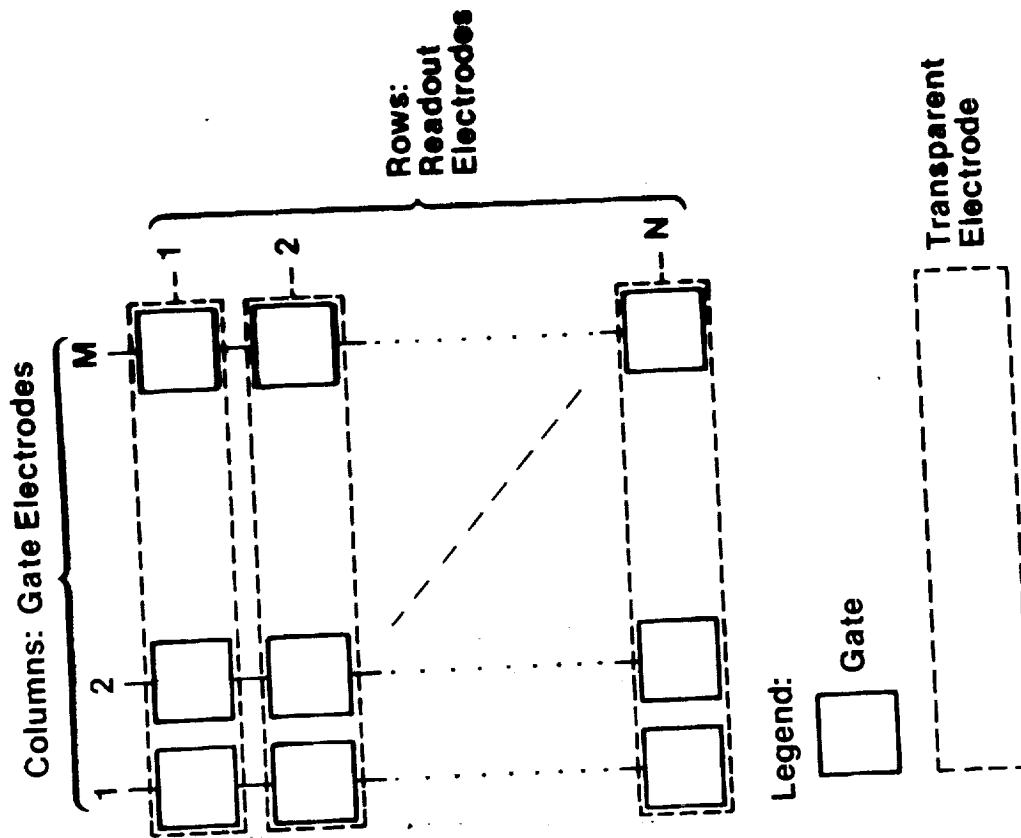
July 12 1983

BASIC AMCID CONFIGURATION

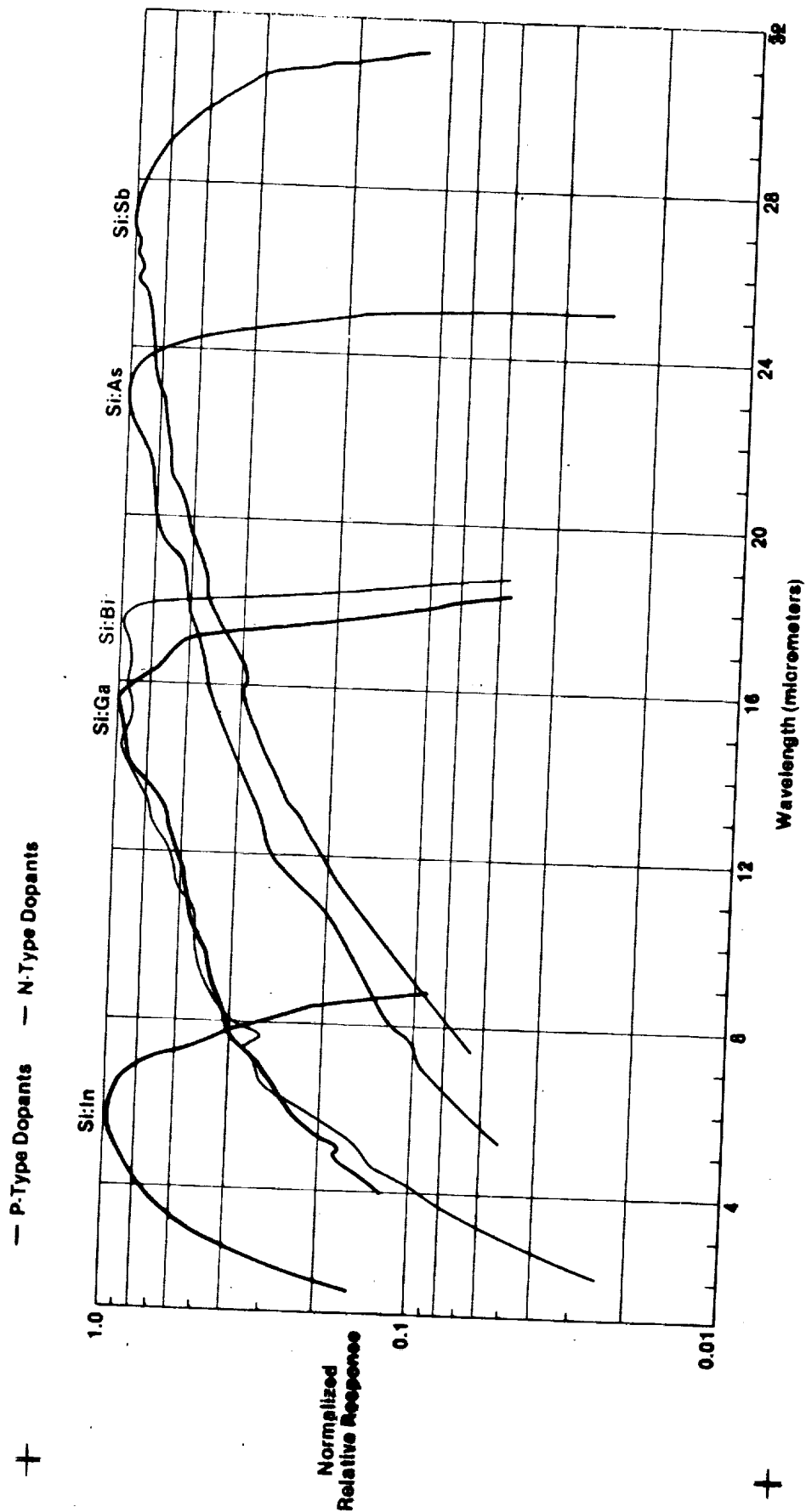


| ADVANTAGES |
|---|
| <ul style="list-style-type: none"> • Simple Design • Random Access • High Uniformity • Simple Drive Circuit |

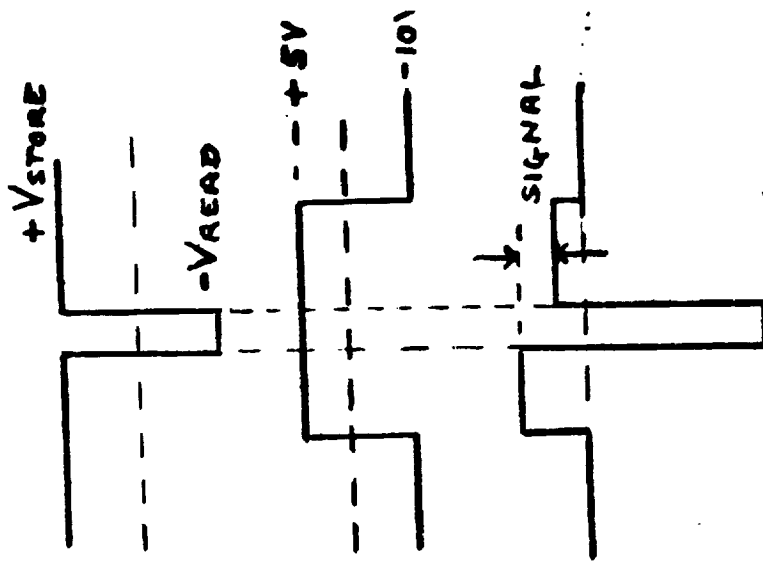
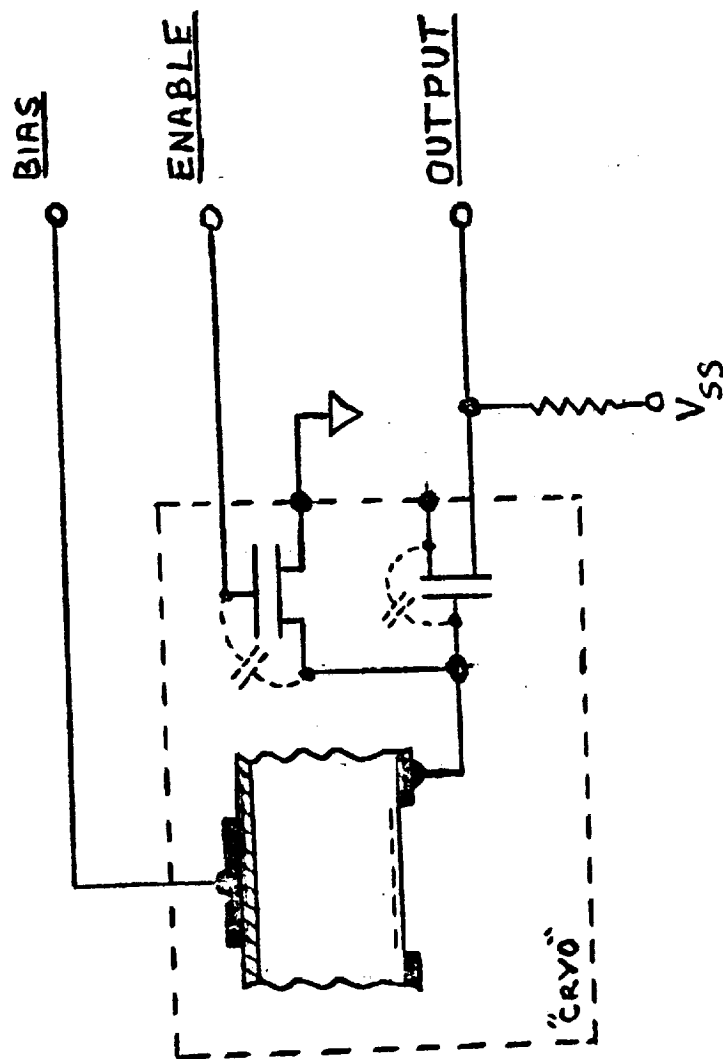
MxN AMCID MOSAIC



Spectral Response of Doped Silicon Detectors



ENABLE READOUT



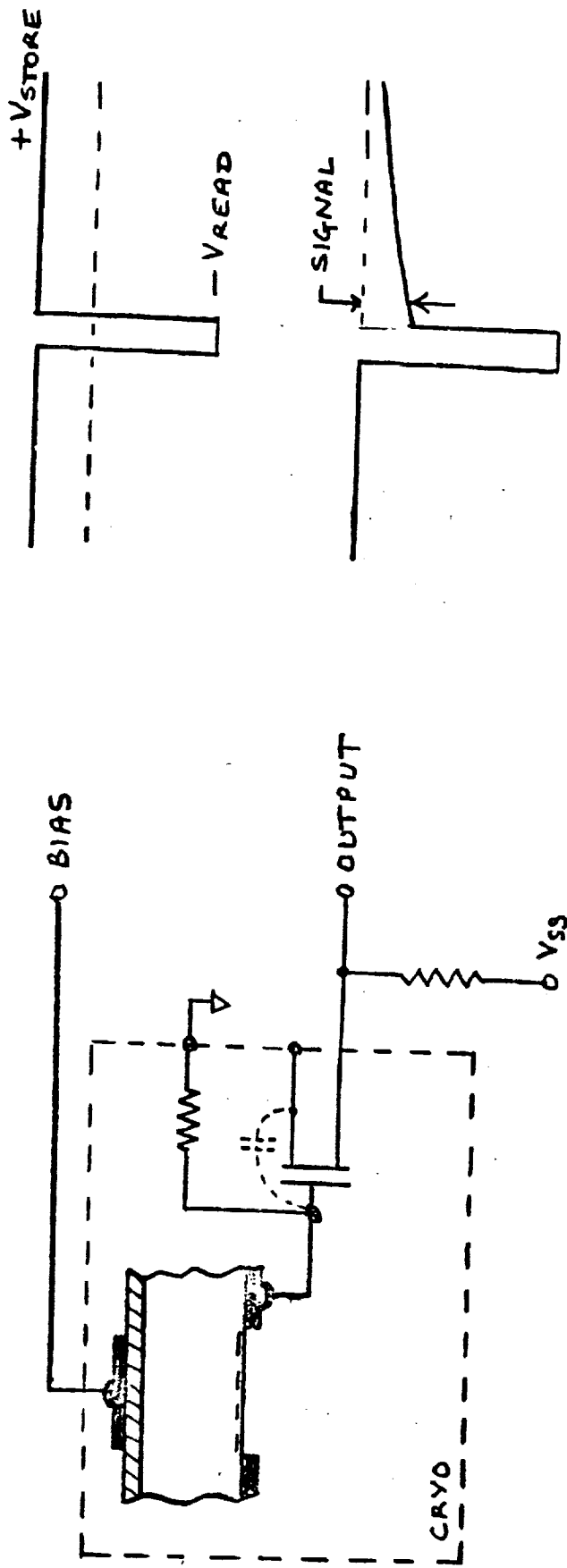
DEFICIENCIES:

- DYNAMIC RANGE PROBLEM
- DISPLACEMENT TRANSIENTS \gg SIGNAL

- ENABLE SWITCH CAPACITANCE

$$\Delta V_{OUT} = Q / [C_{AMP} + C_{SWITCH}]$$

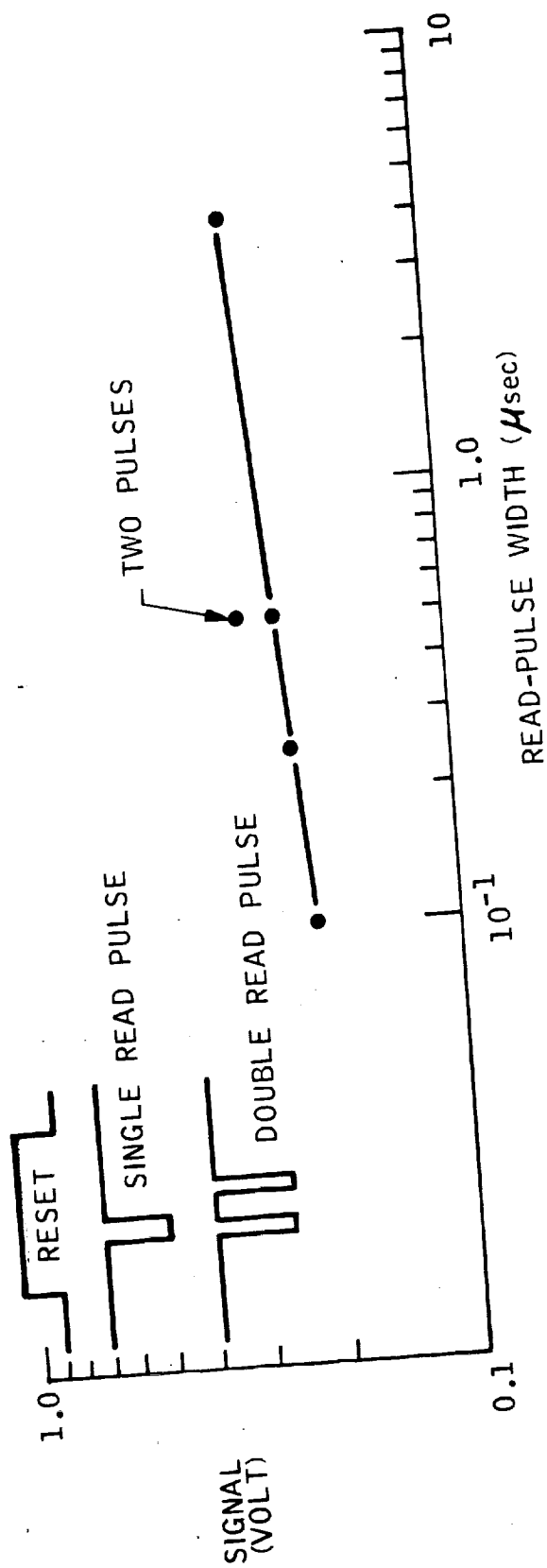
RESISTIVE READOUT



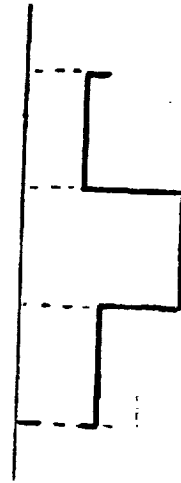
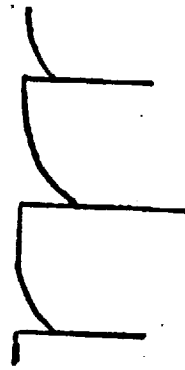
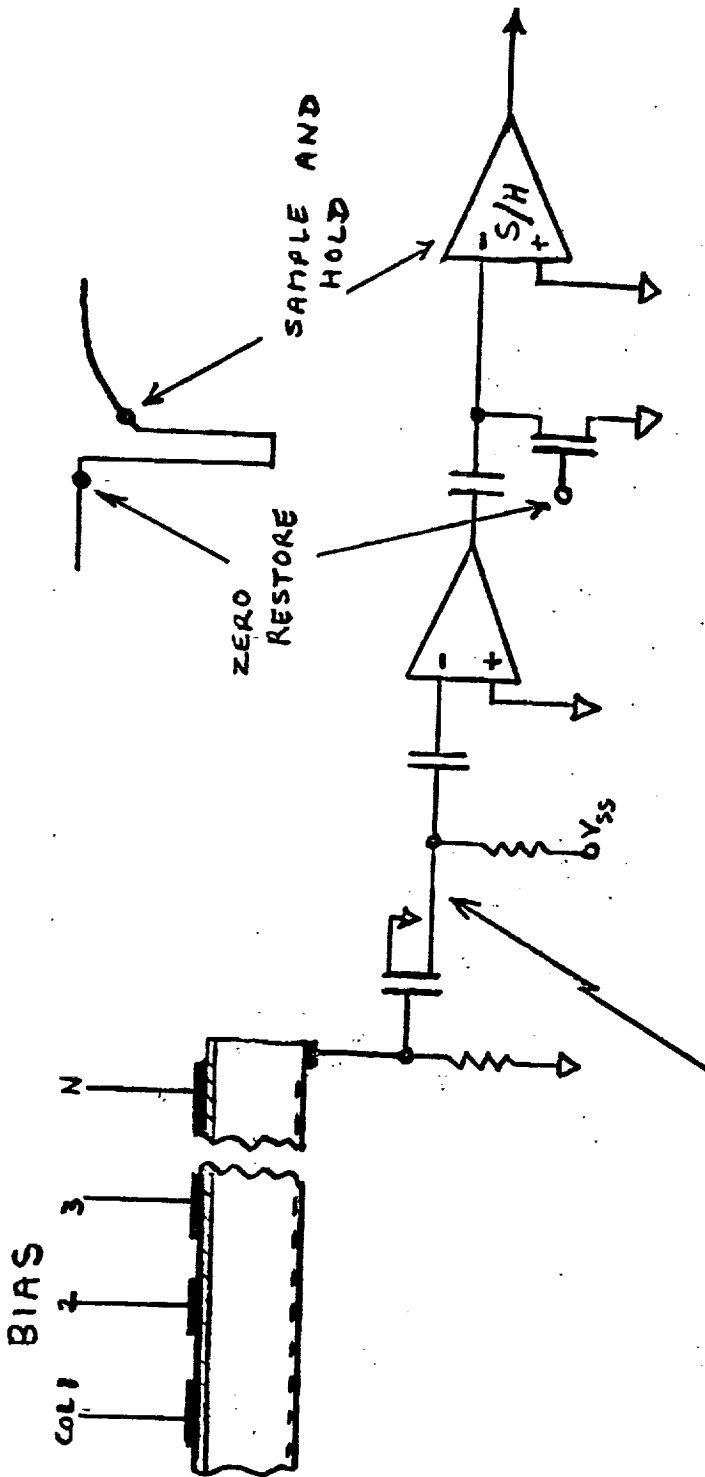
REQUIREMENTS:

- PIXEL READ INTERVAL $\gg R_L C_{FET}$ \gg READ TIME ($\sim 10 \mu\text{sec}$)
($T_{\text{FRAME}} / N_{\text{DETECTORS}}$)
- $R_L \ll R_{\text{DETECTOR}}$

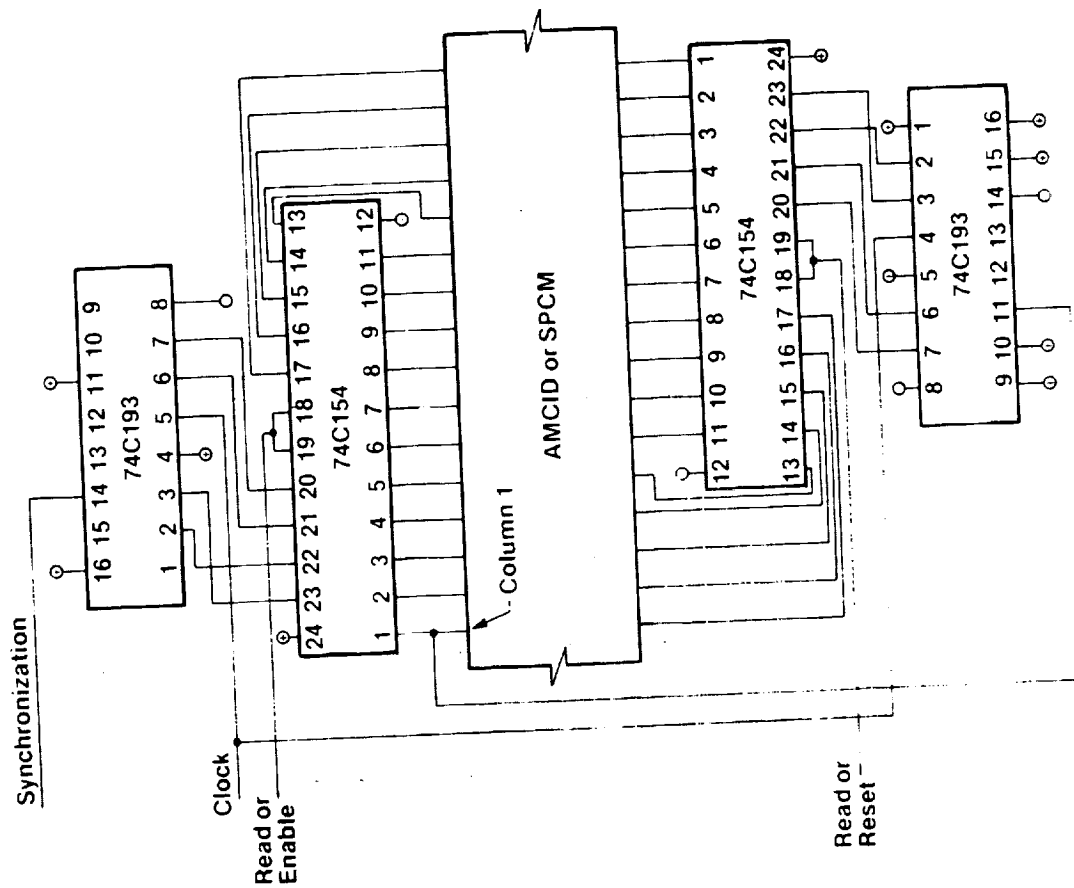
SIGNAL VERSUS READ-PULSE WIDTH



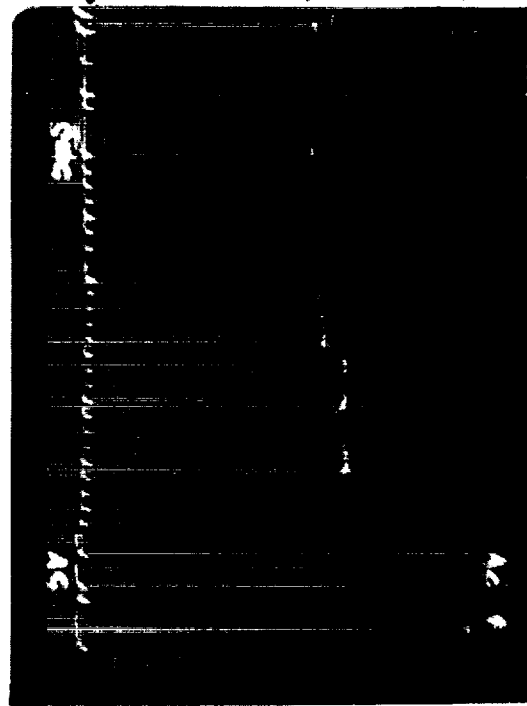
DELTA-RESET SAMPLING



On-Focal Plane Scanning Electronics



AMCID OUTPUT



Input to signal processor from one "on focal plane" FET source follower. Contains 32 detector signals multiplexed on one row output line. Shape of signal is shown below.

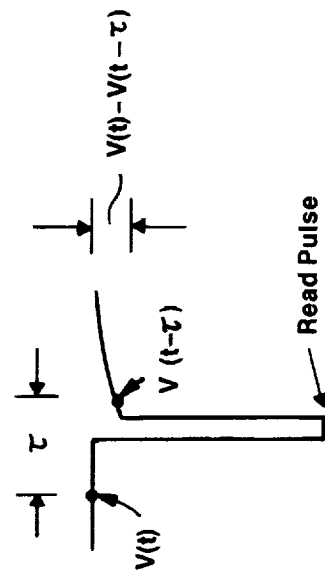
Output from signal processor. Column 1 detector shows largest output. Columns 3,5,23,31, and 32 do not respond.

Output signal baseline

UNCLASSIFIED

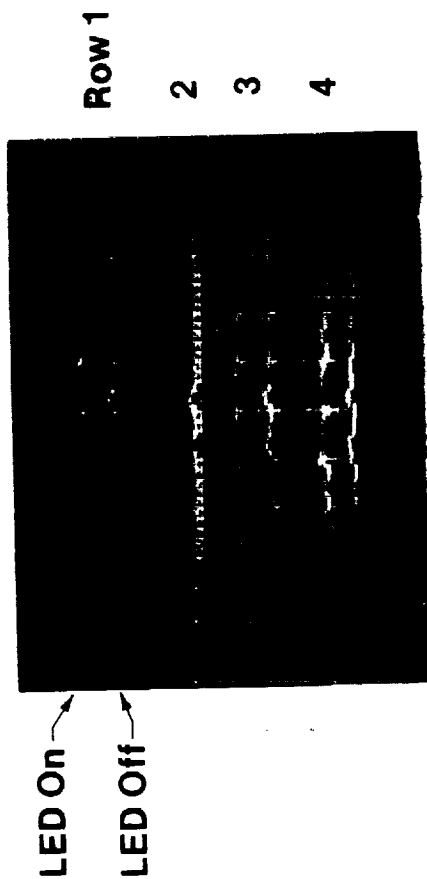
Column 1

Input Signal Shape



1081-3141

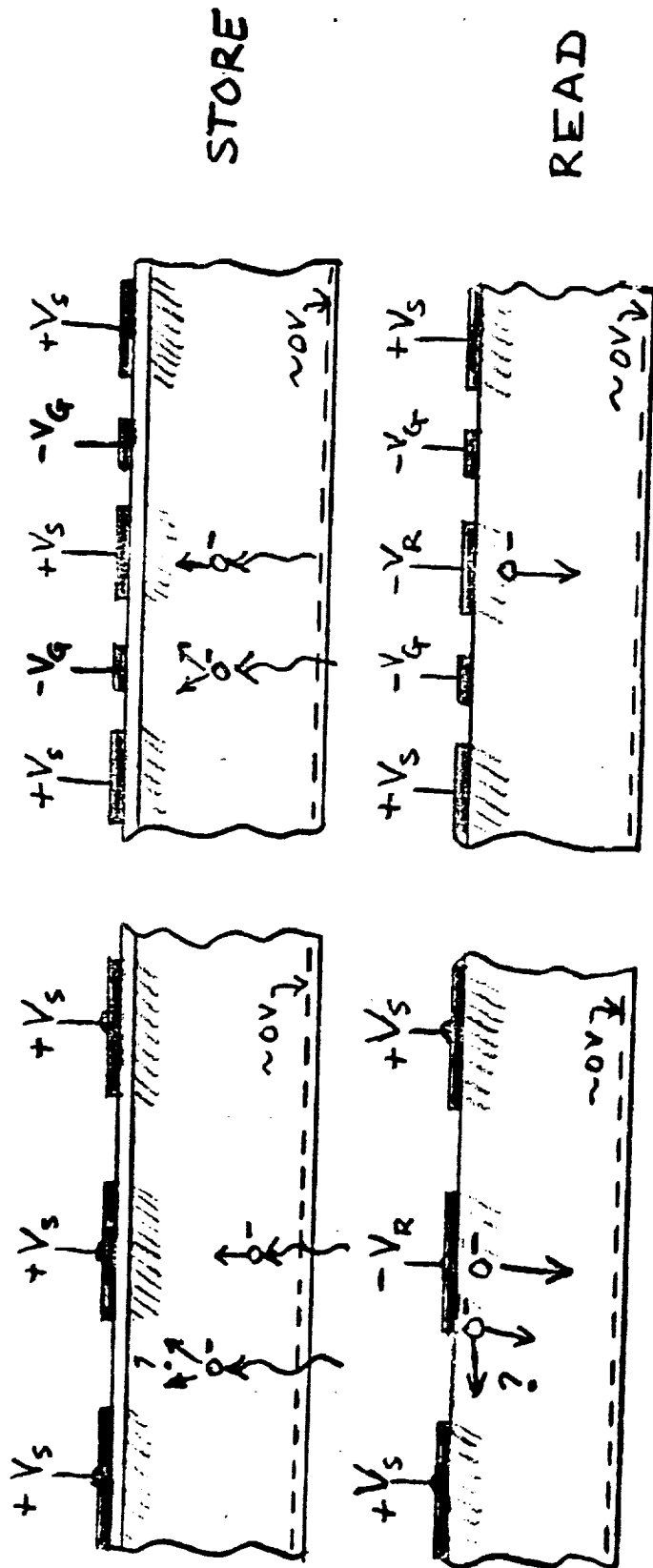
Multiplexed Row Output



1 ms/division

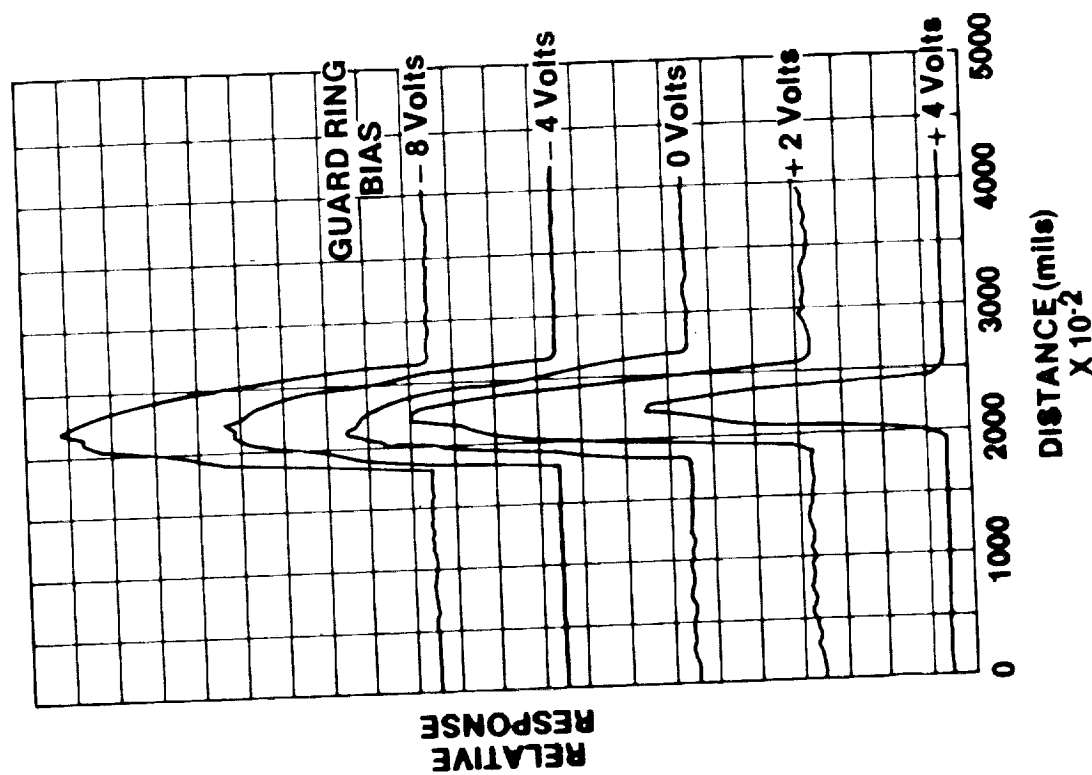
ORIGINAL PAGE IS
OF POOR QUALITY

GUARD ELECTRODE



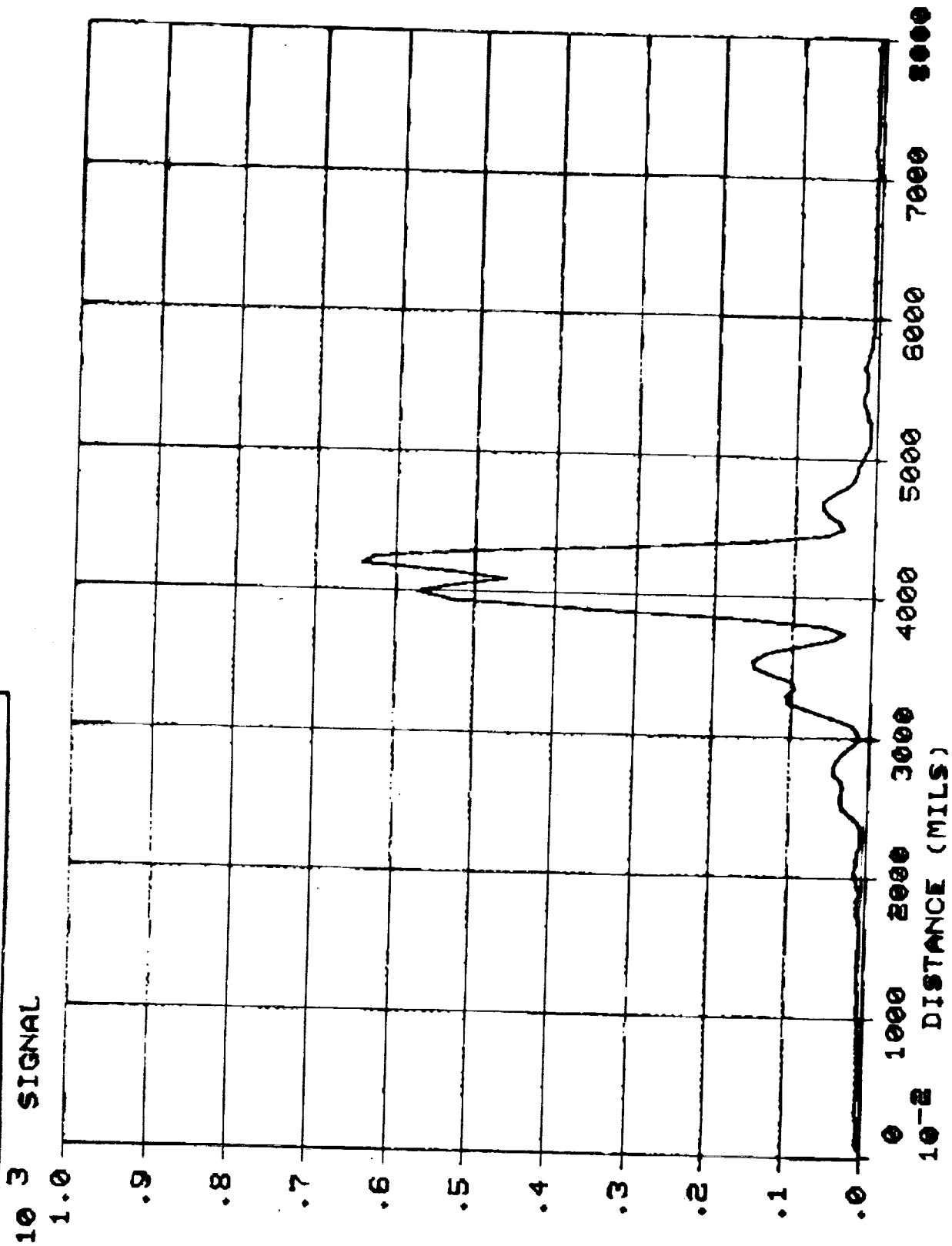
- DEFINES DETECTORS
- DIMINISHES CROSSTALK
- REDUCES YIELD

DEPENDENCE OF RESPONSE ON GUARD RING BIAS ROW SCAN

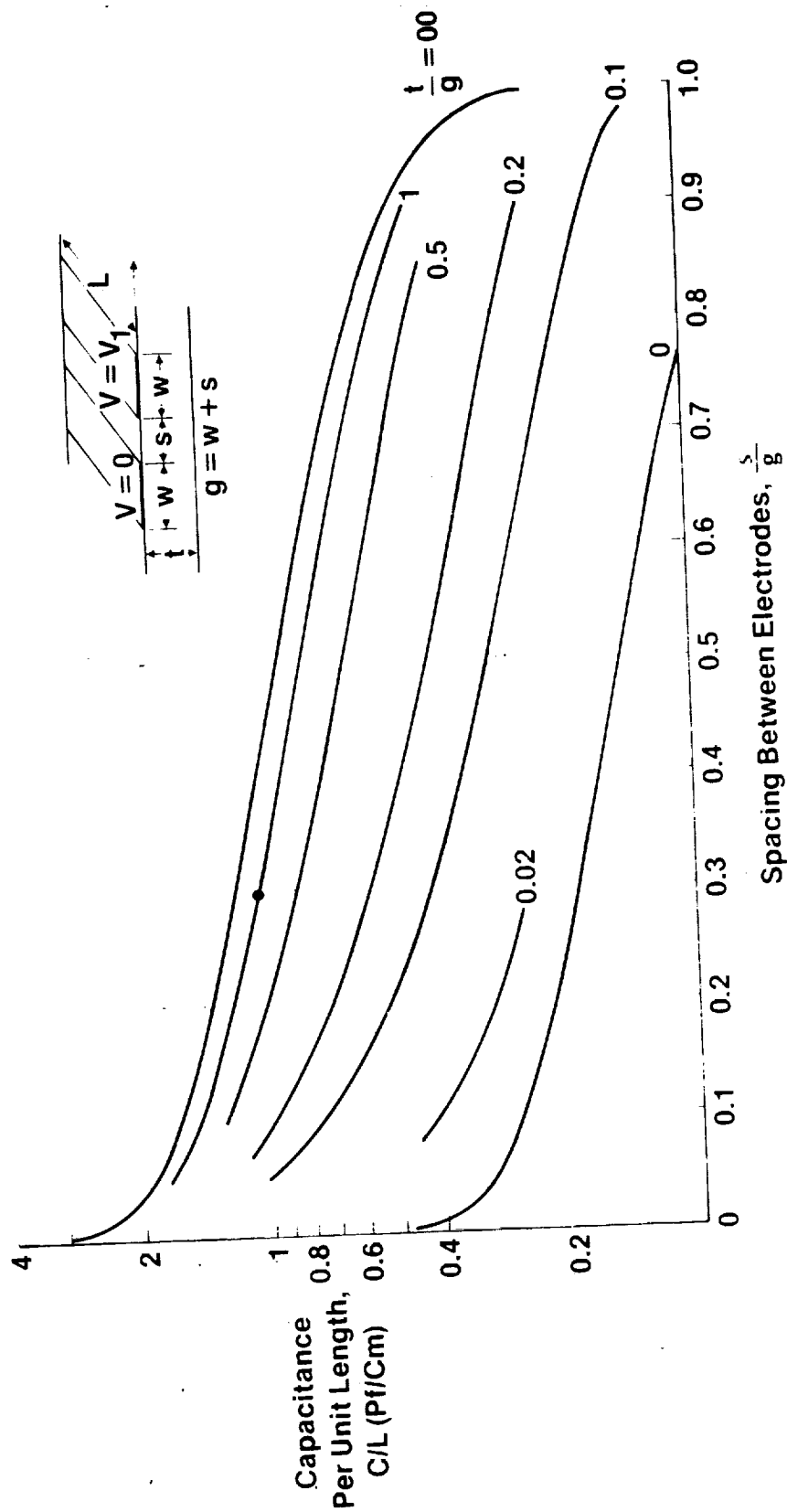


Scan: Row 13
Output: Col 11
Temperature: = 10.5K

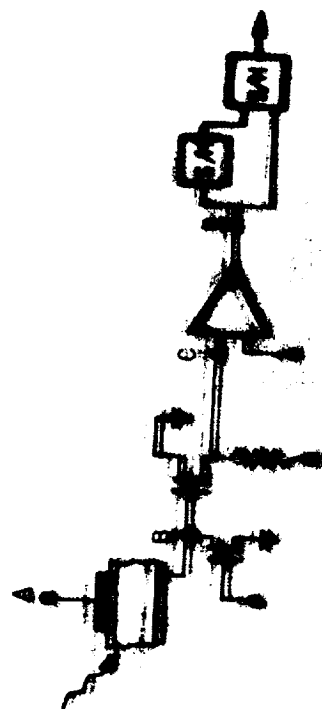
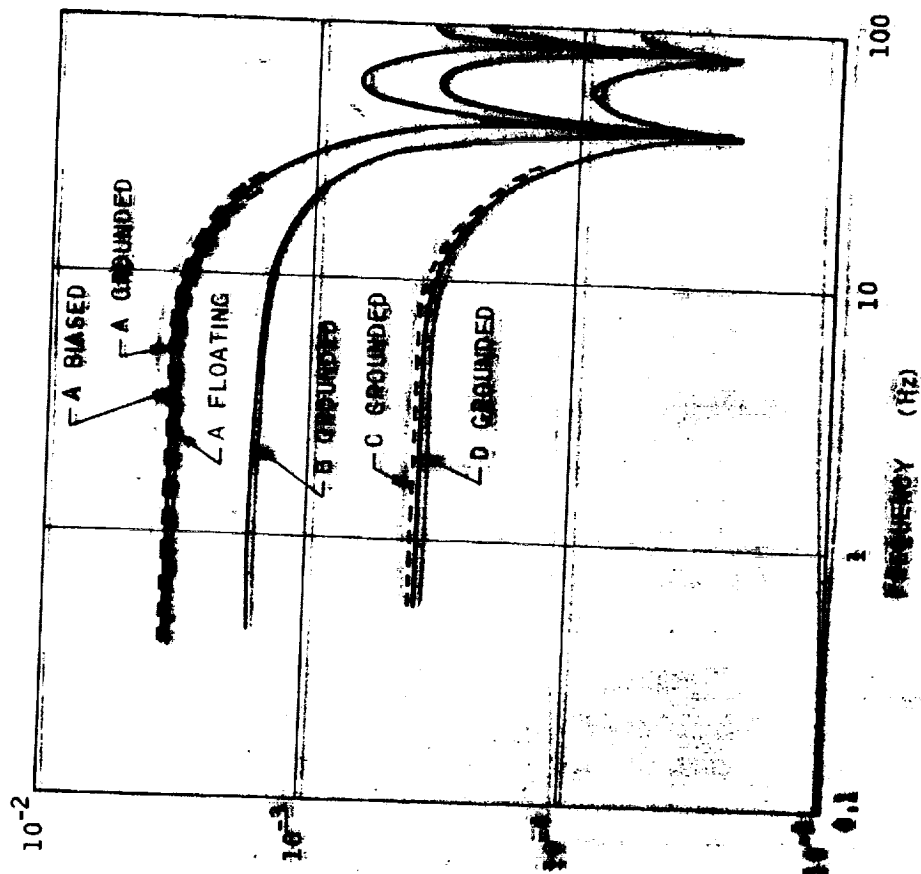
Typical Column Spot Scan



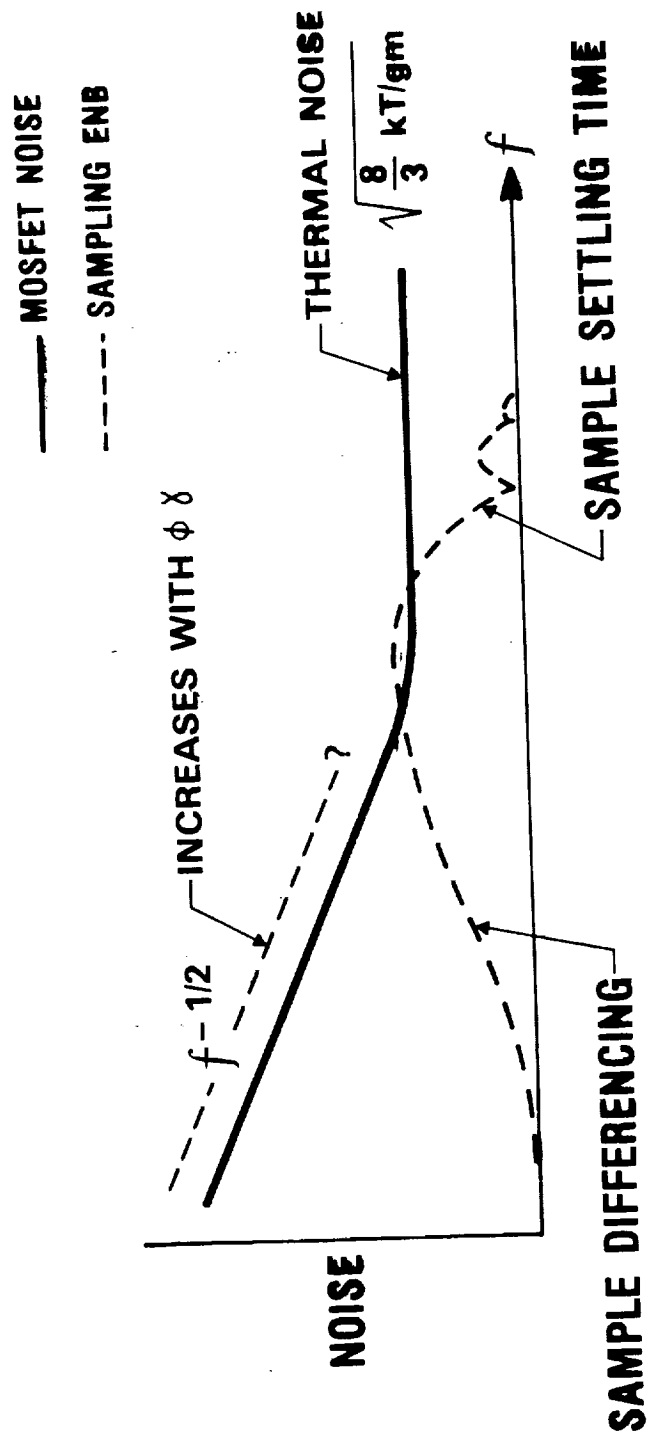
Capacitance of Two Coplanar Electrodes On A Silicon Wafer ($\epsilon_r = 11.6$)



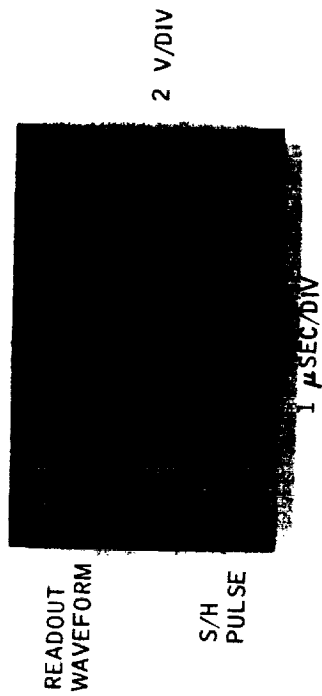
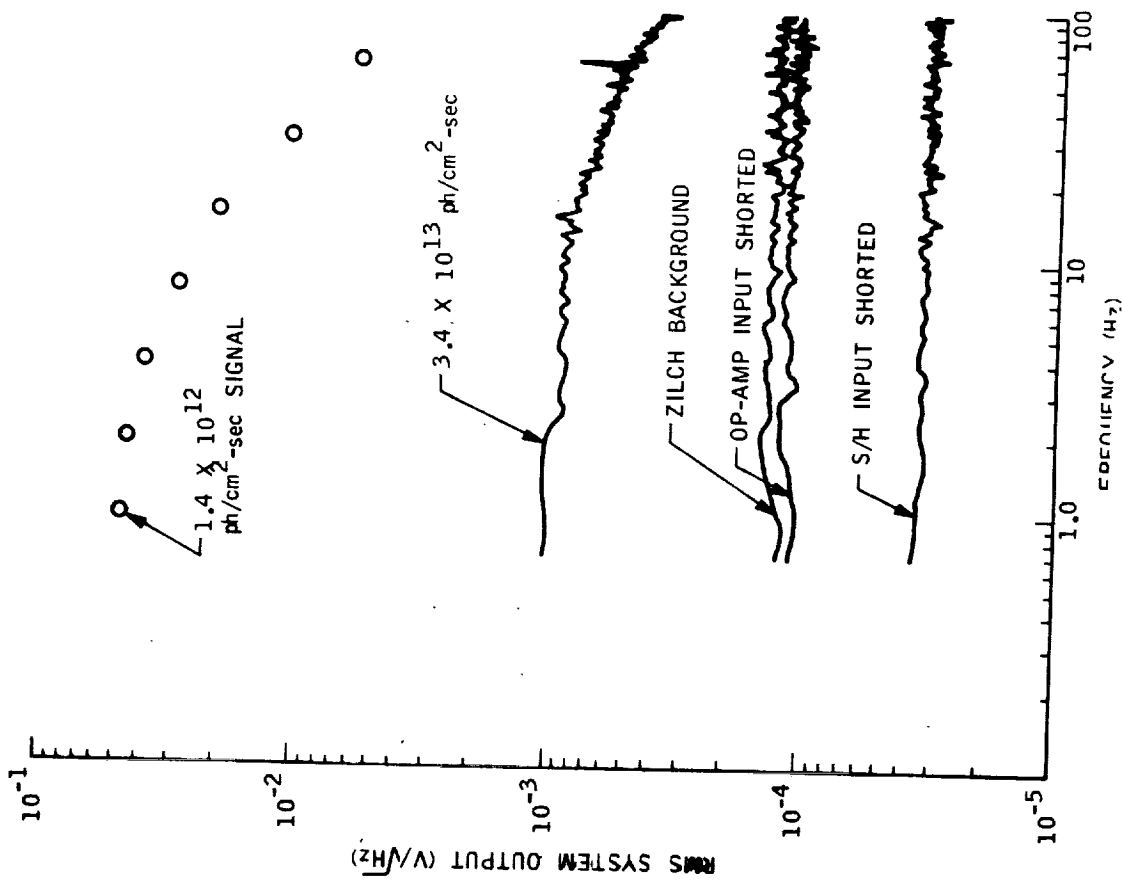
CID SYSTEM IS PREAMP-NOISE LIMITED



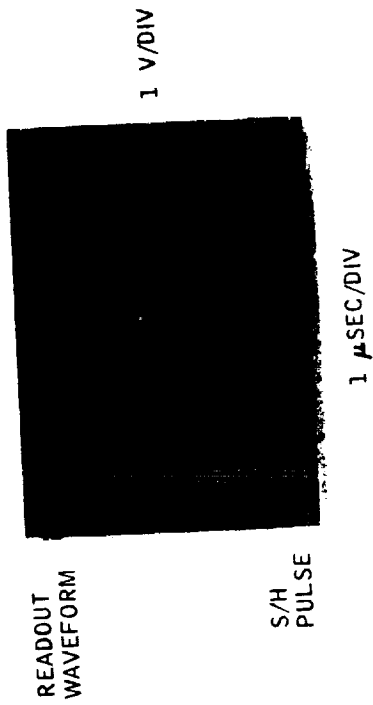
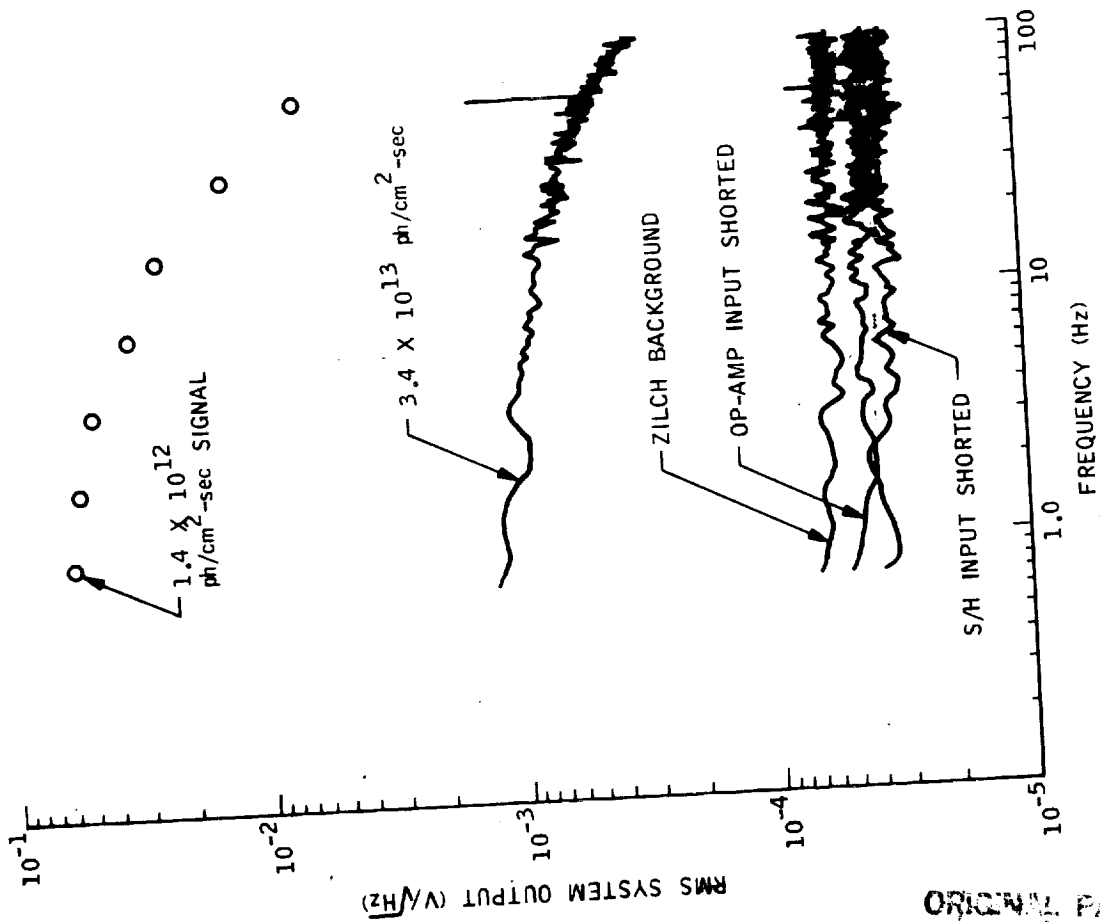
CRYOPREAMP NOISE CONTRIBUTION



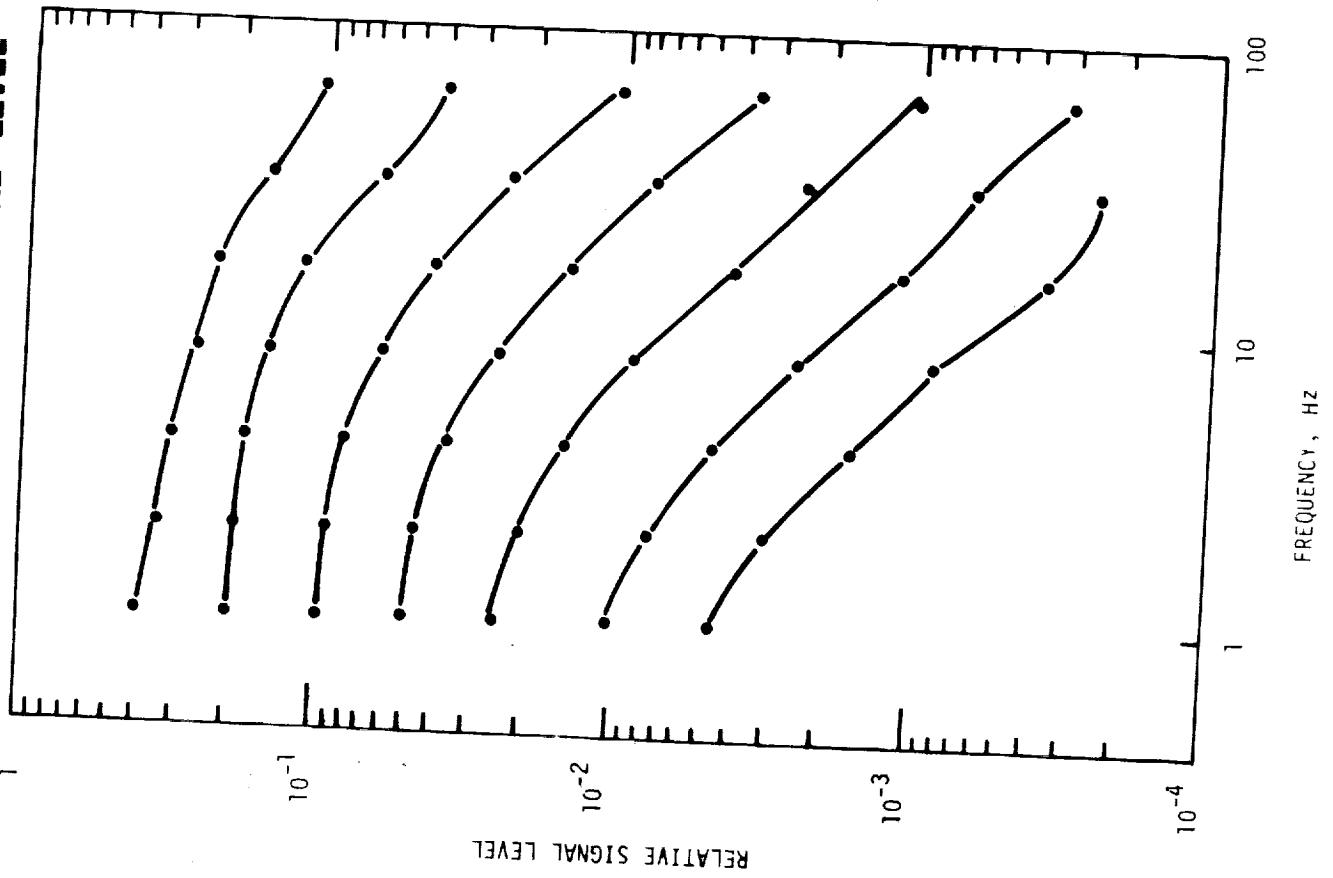
AMCID OUTPUT, 530-KHz BANDWIDTH



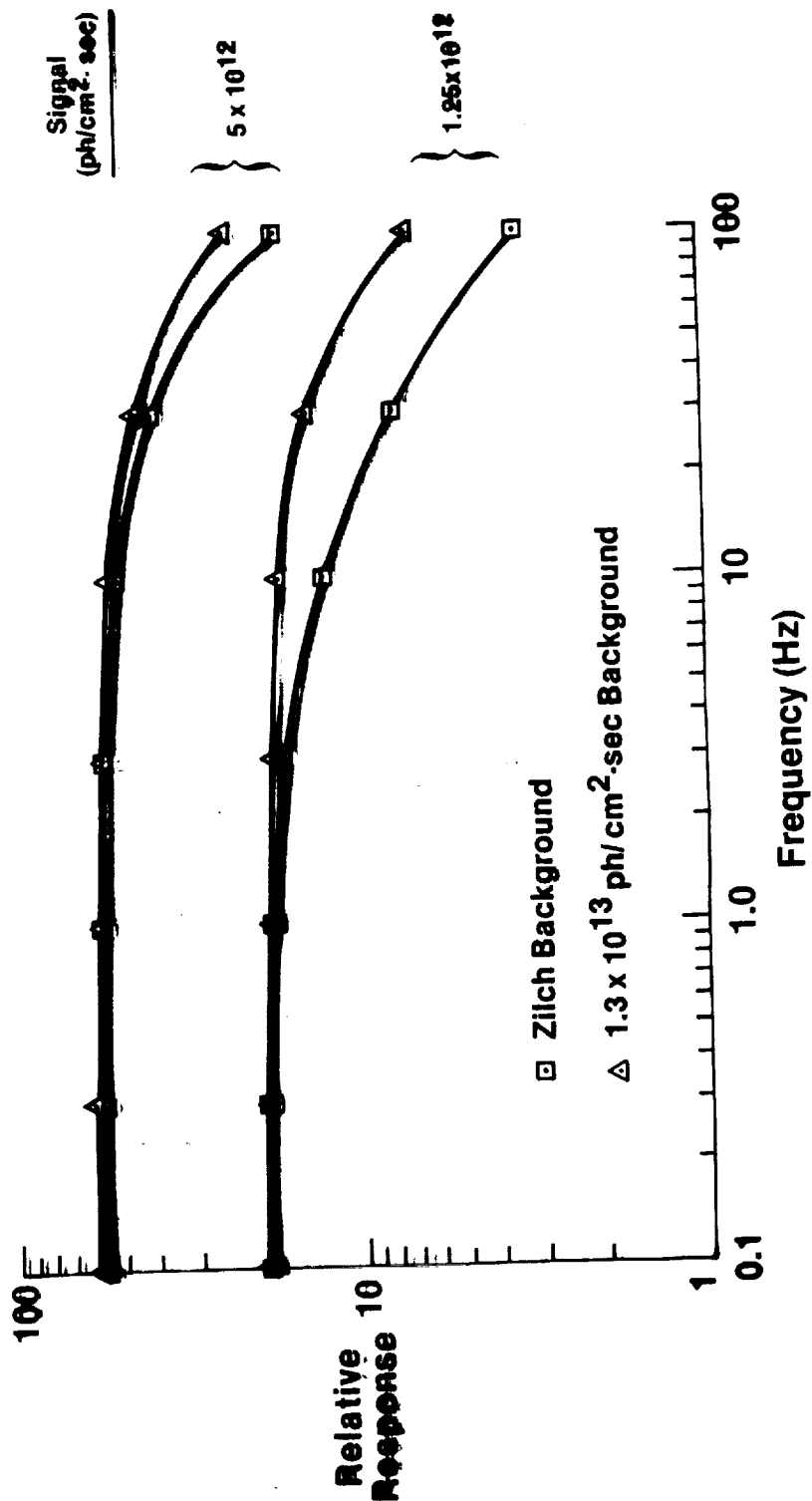
AMCID OUTPUT, 65-KHz BANDWIDTH



FREQUENCY RESPONSE VERSUS SIGNAL LEVEL

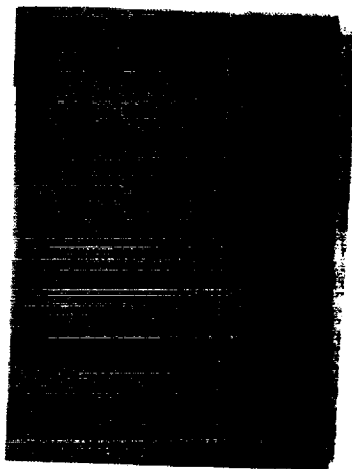


Effect of Background on Frequency Response

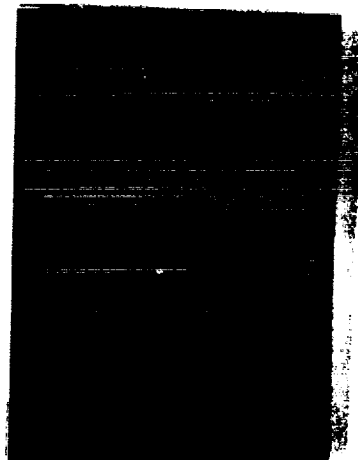


TIME CONSTANT VERSUS FLUX LEVEL

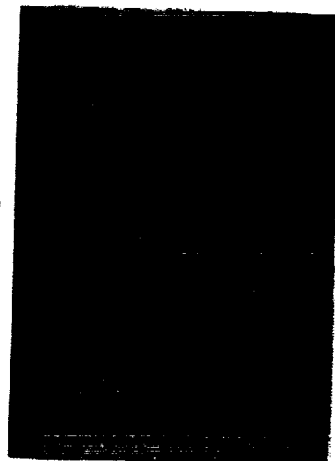
ϕ = PHOTON FLUX
N = INTEGRATED PHOTON FLUX



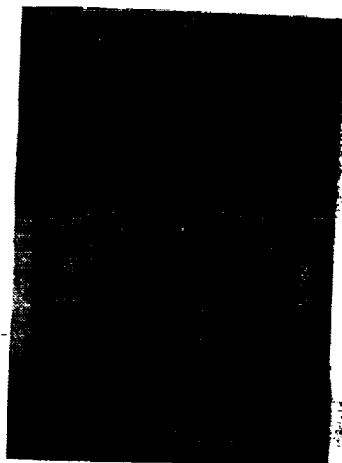
$N = 1.5 \times 10^{10}/\text{cm}^2$



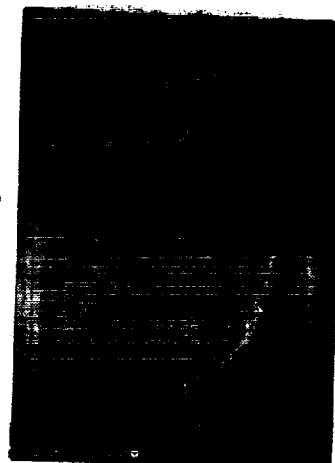
$N = 1.5 \times 10^9/\text{cm}^2$



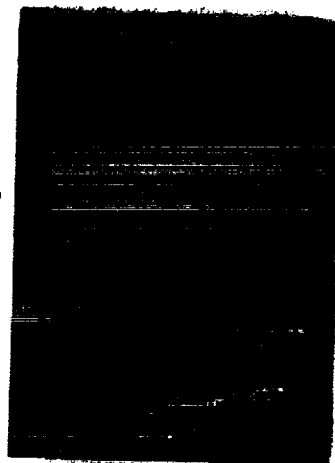
$N = 1.5 \times 10^8/\text{cm}^2$



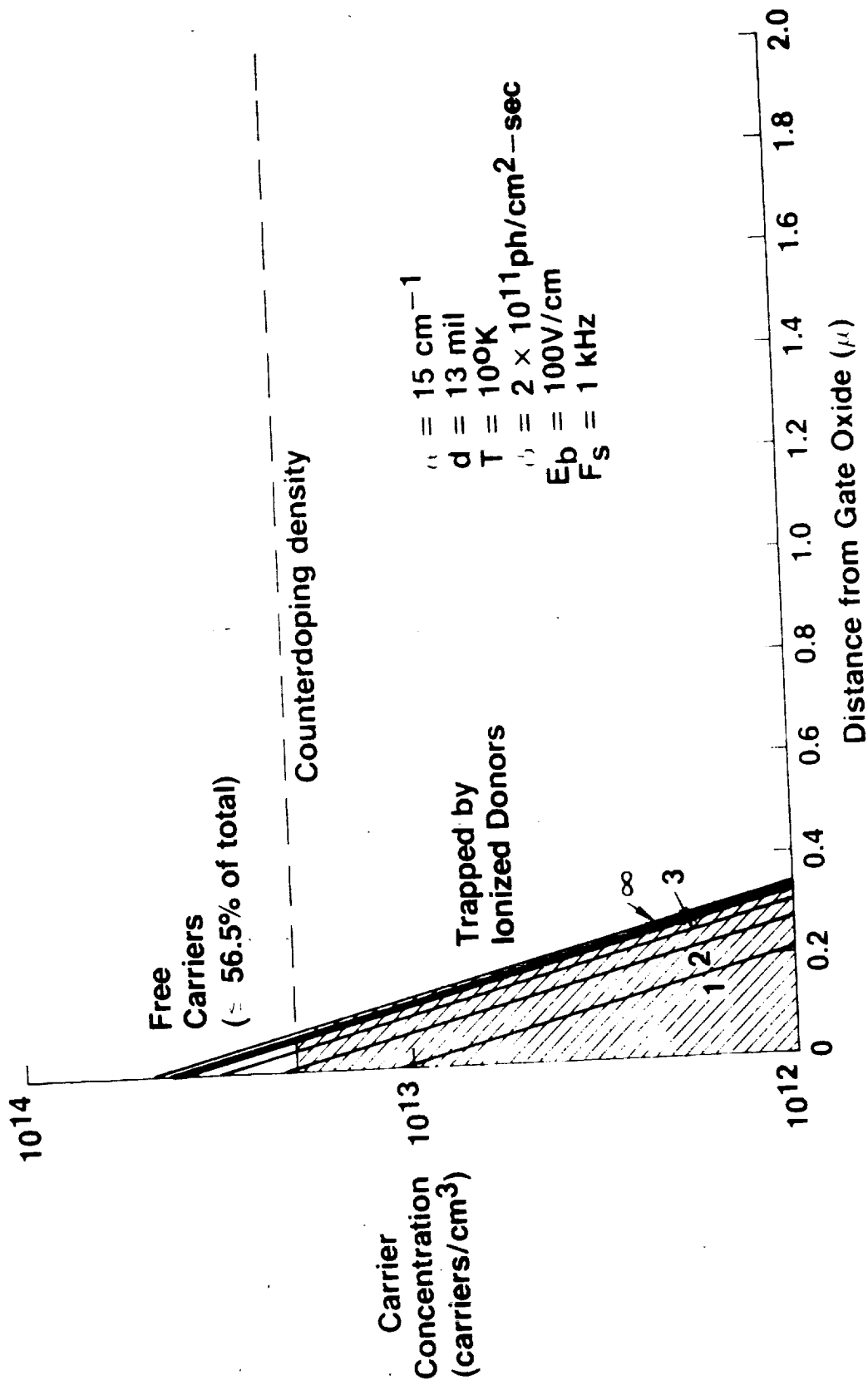
$\phi = 8 \times 10^{10}/\text{cm}^2\text{-sec}$



$\phi = 9 \times 10^9/\text{cm}^2\text{-sec}$

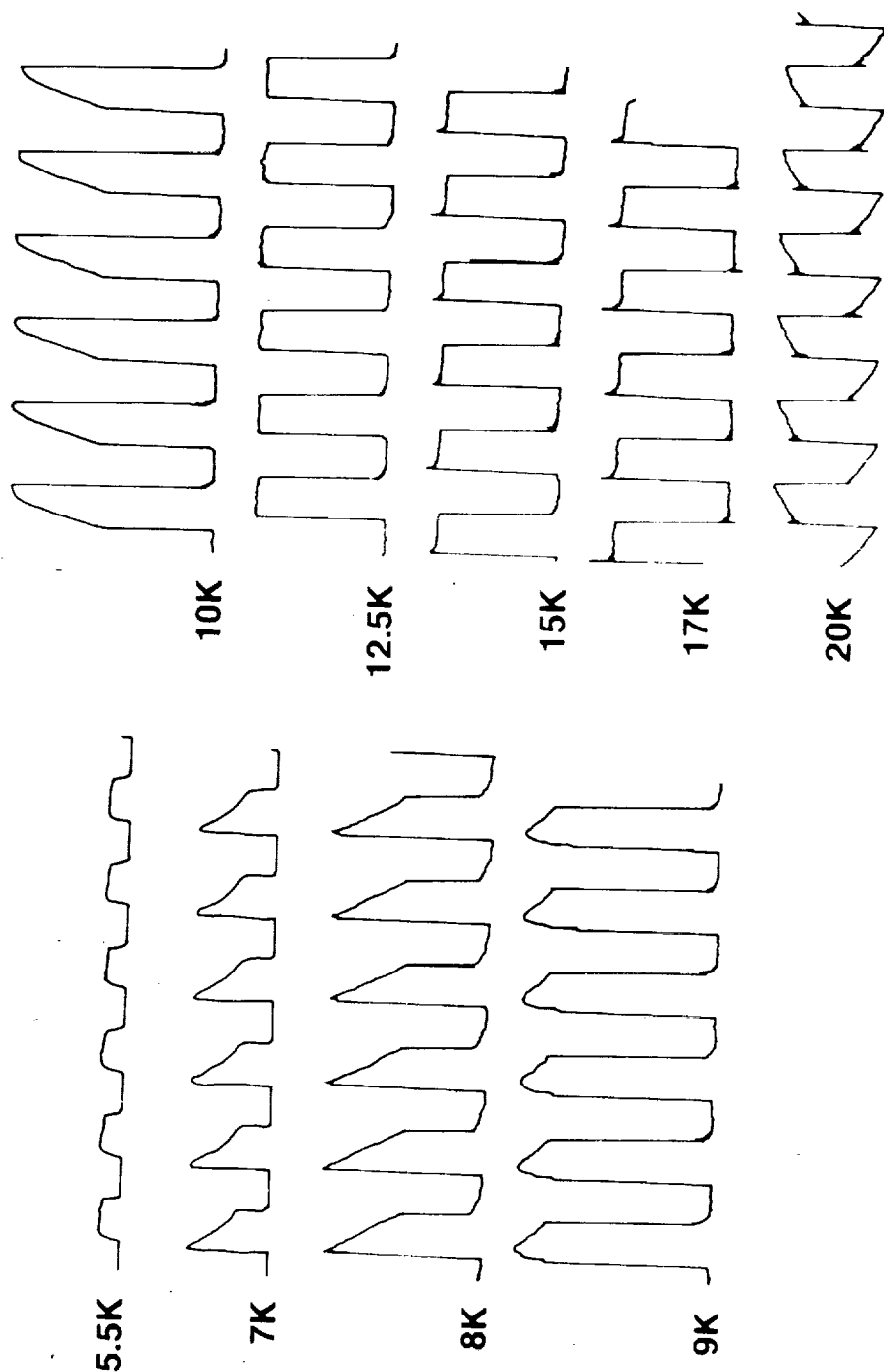


Bulk-Trap model of CID Performance



Dependence of Signal Shape On Temperature

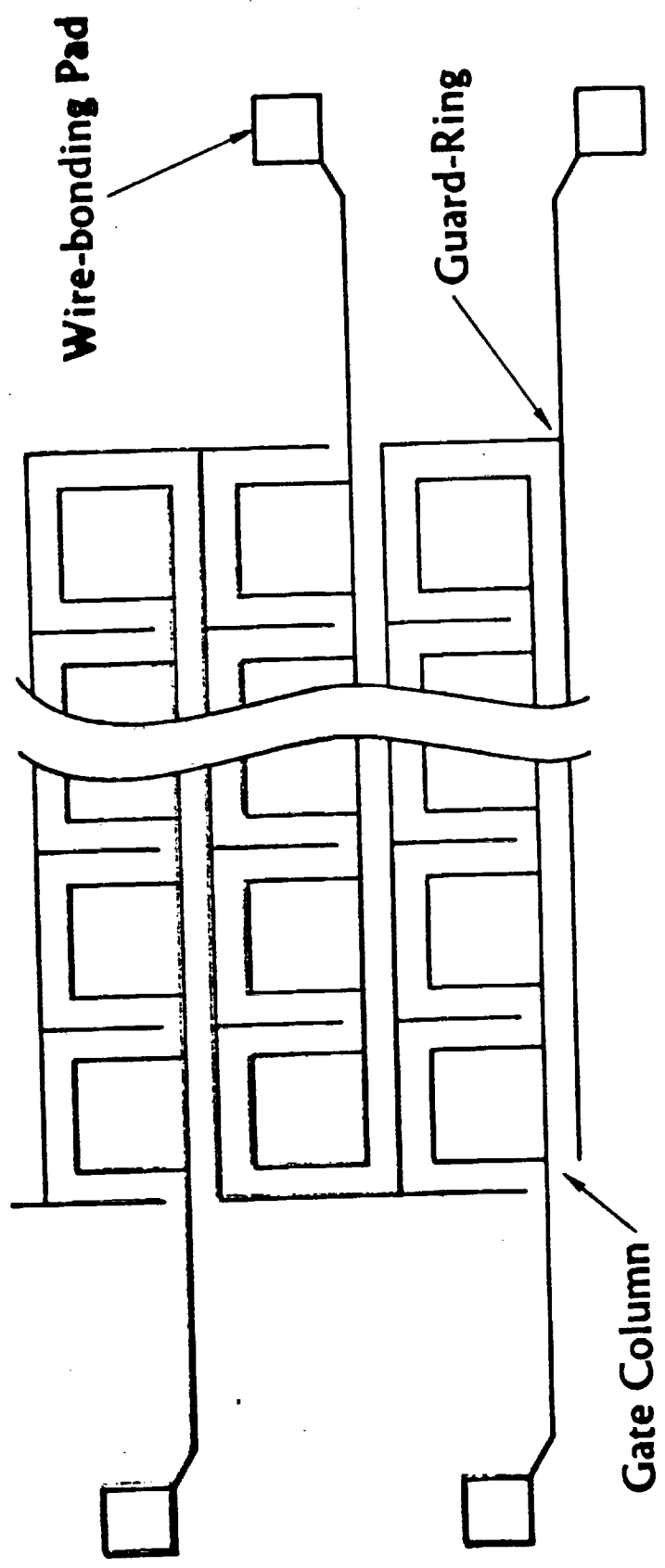
Si:Bi AMCID II Row 1 Col 12
(X226) $V_s = +6\text{ V}$, $V_r = -8\text{ V}$
Signal 2 Hz, $F_s = 500\text{ Hz}$
 $V_g = -10\text{ V}$



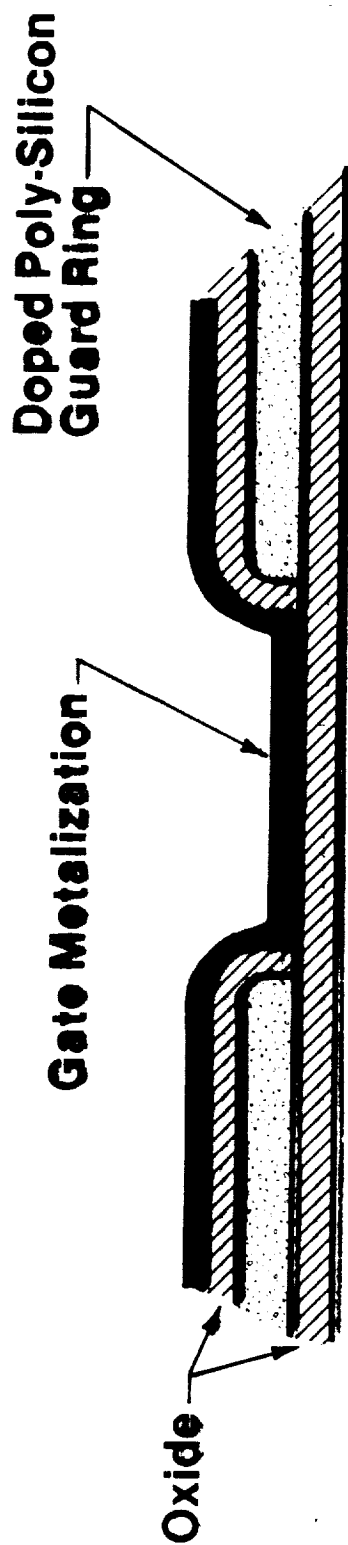
600-1070

First-Generation 32 x 32 AMCID Guard Ring

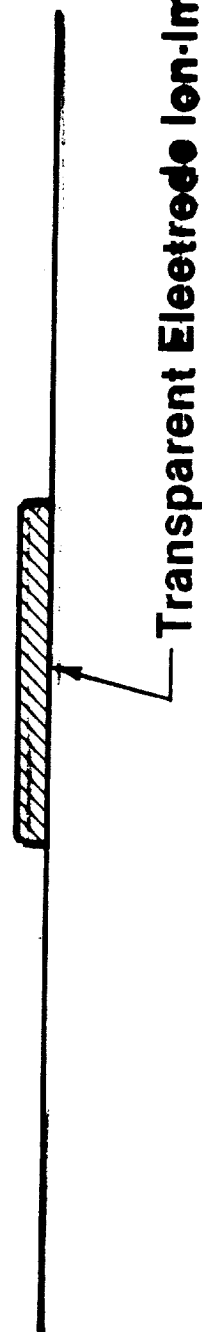
- Single-Level Interconnect For Gates and Guard Ring



Second Generation AMCID Configuration



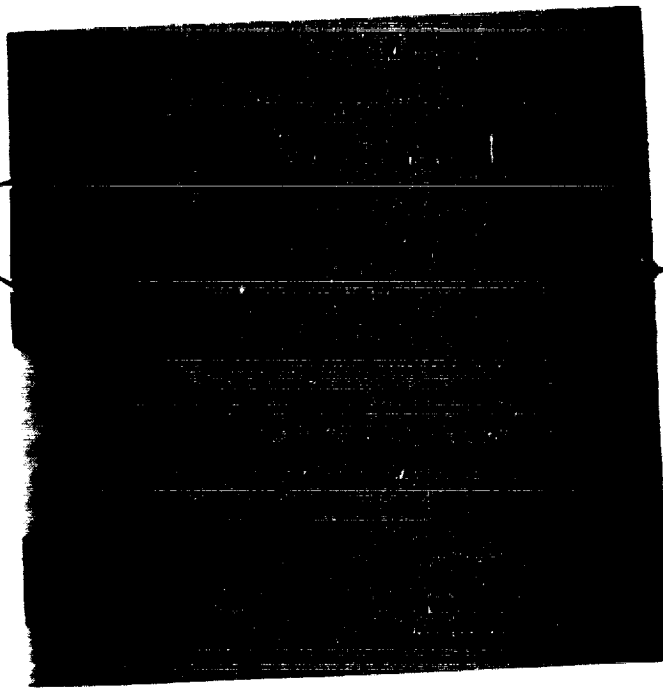
Si:Bi



**Aerojet
Electro
Systems**

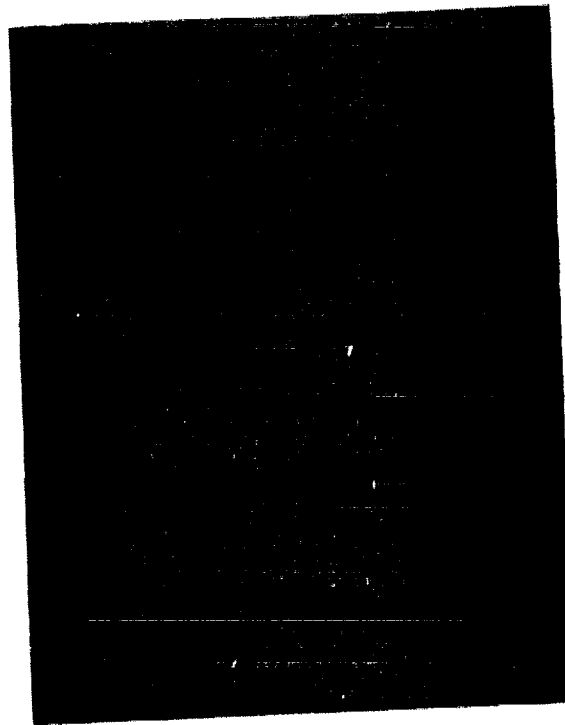
AMCID Metalization Pattern (Revised)

Wire Bonding Pads



Polysilicon
Guard Ring

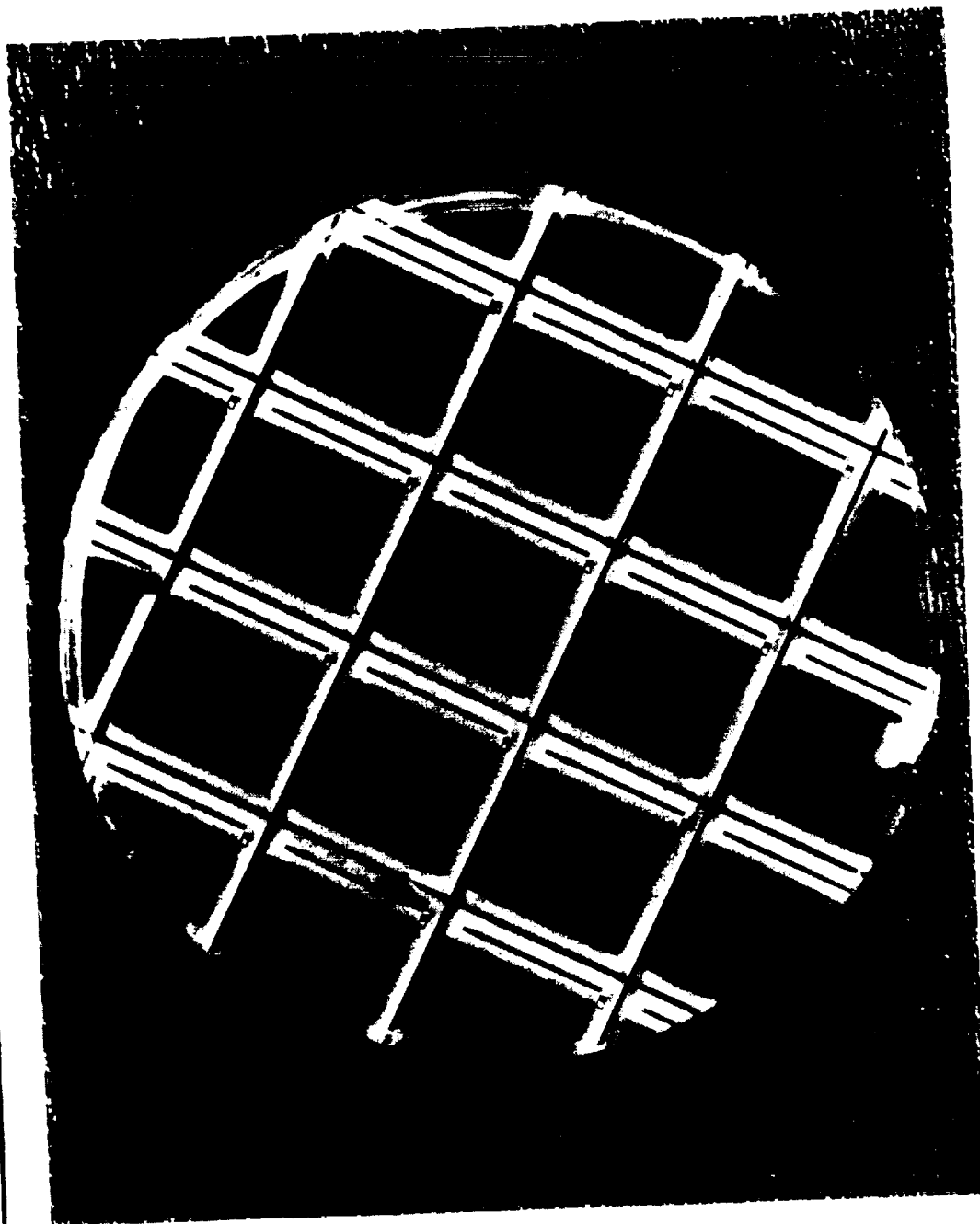
Gate



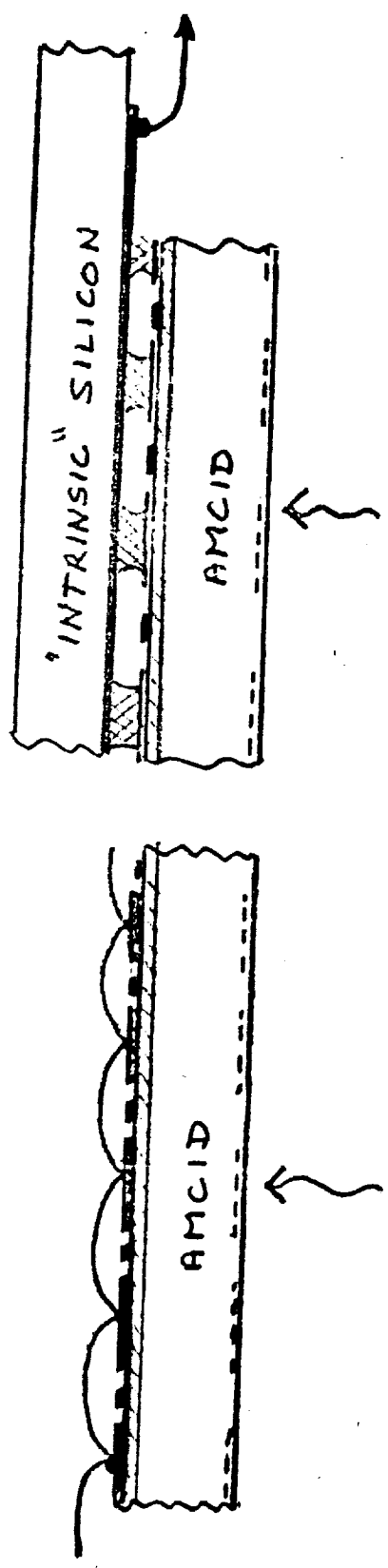
Second - Generation Amcid, Gate Side



Second - Generation Amcid, Readout Side



STITCH INTERCONNECT



GOLD WIRE
TC/TS STITCH BONDED

HYBRID Si ON Si
INDIUM-BUMP BONDED

- PLANAR PROCESS
 - CLEAN & SIMPLE
 - AVOIDS CROSSOVER DEFECTS
- HIGH YIELDS AT WAFER LEVEL

58-74
133813
P-12
N93-70644
AE261302

CONCEPTUAL DESIGN OF A MULTIPLEXED
Ge:Ga DETECTOR ARRAY

C. M. PARRY

AEROJET ELECTROSYSTEMS COMPANY

BOX 296

AZISA, CA. 91702

REQUIREMENTS

- 50 (OR MORE) DETECTORS - MOSAIC

- 80% FILL

- NEP $\leq 10^{-16}$ W/ $\sqrt{\text{HZ}}$ AT 100 μm , 5fps

$$= 1.6 \times 10^{-16} \text{ RMS WATTS (WB)}$$

$$= 8 \times 10^4 \text{ RMS PH/SEC (AT 100 } \mu\text{m)}$$

$$= 1.6 \times 10^4 \text{ PH/SAMPLE (AT 5fps)}$$

- ASSUMING 5 TO 10 A/W $\dagger 5 \times 10^5$ p/sec/pixel

$$n_s \lesssim 1000 \text{ e/s}$$

- "STRESSABLE" - UNIAXIAL TO 90 Kpsi

(DI)STRESSING ALTERNATIVES



THERMAL CONTRACTION

$$\frac{\Delta L}{L}(M_1) \gg \frac{\Delta L}{L}(Ga) > \frac{\Delta L}{L}(M_2)$$

- LACK OF MATERIALS [W]
- DATA BASE POOR
- REQUIRES HIGH PRECISION

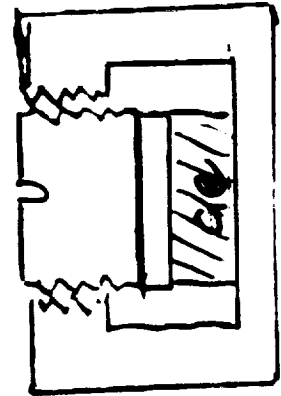
PRELOADED BELVILLE OR SPRING

- MATERIALS "DO NOT EXIST"
-



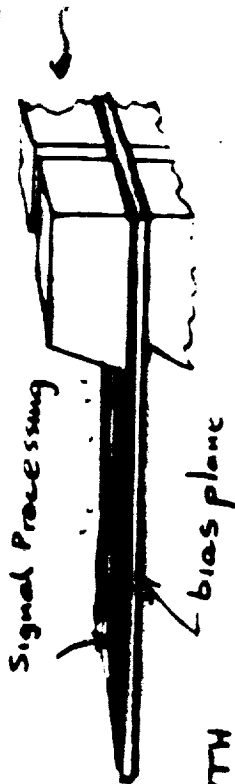
PRELOADED ANVIL

- NEEDS CALIBRATION OR CRYO STRAIN GAUGE



CONFIGURATION CHOICES

• ROW MODULES



- SEGMENTING LIMITS X-TALK
- BEVEL MULTIPLIES OPTICAL DEPTH
- SYSTEM IS EXTENSIBLE
- MODULAR TESTING & SELECTION
- DISASSEMBLABLE FOR SERVICE & REPAIR
- 80% FILL AT 1mm MATRIX

• MONOLITHIC

- COLUMN INSTABILITY FOR $L/W \geq 7$
- NO CONTROL OF CROSSTALK
- DEMANDS UNIFORM BIAS
- LOW YIELD



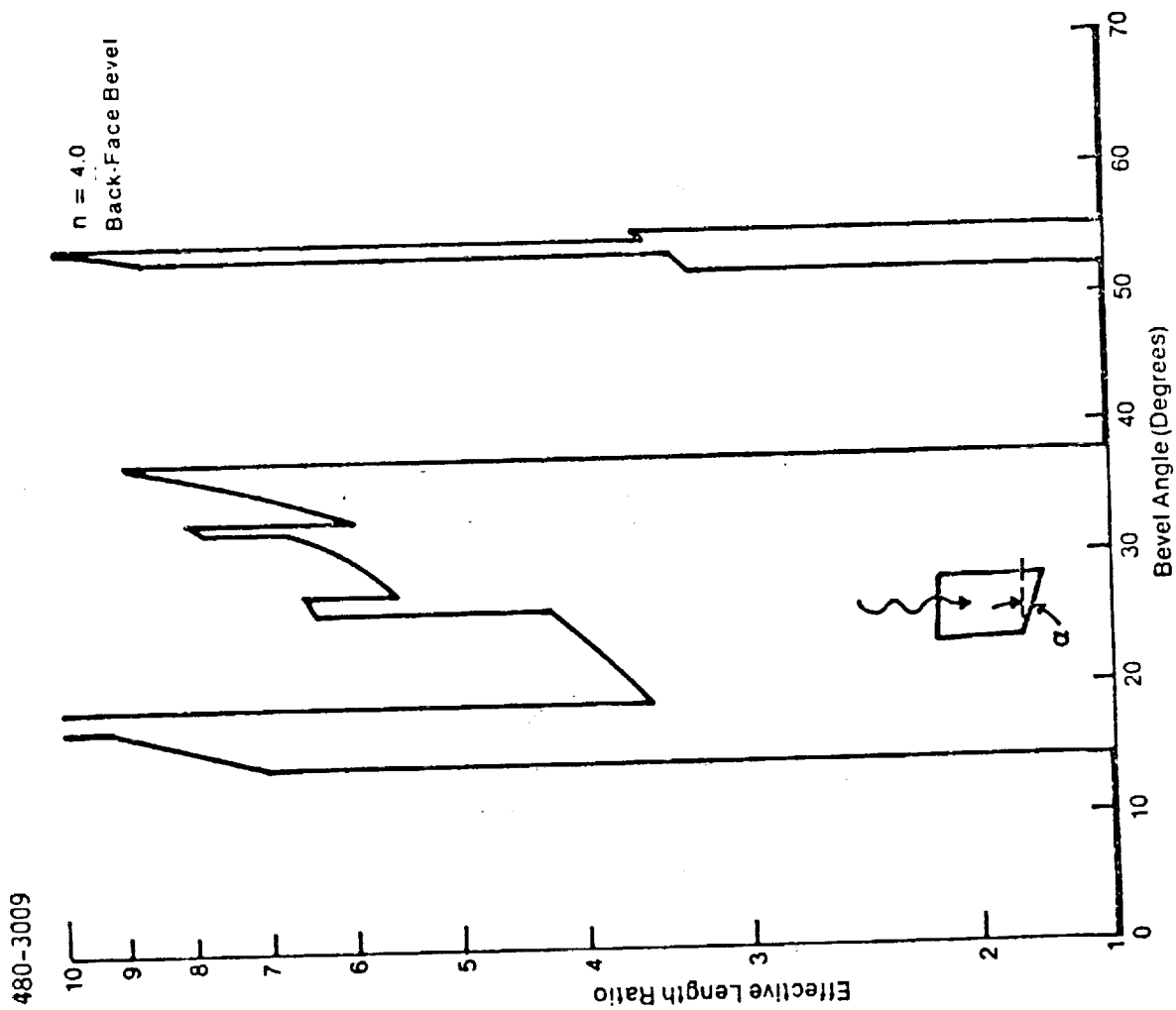
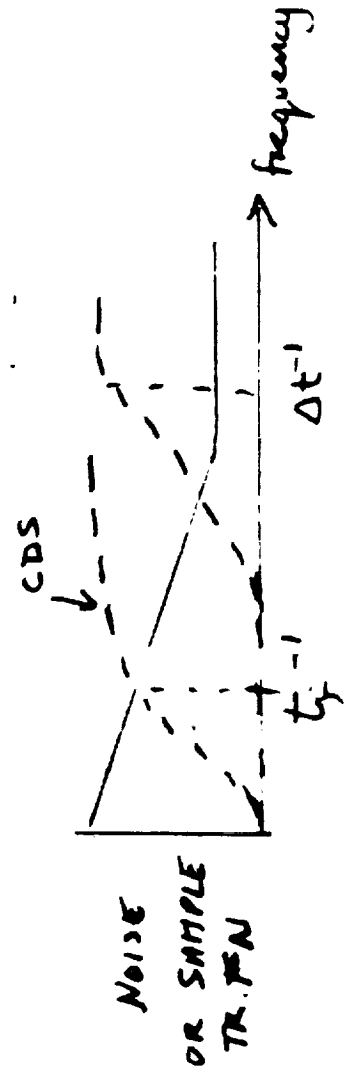
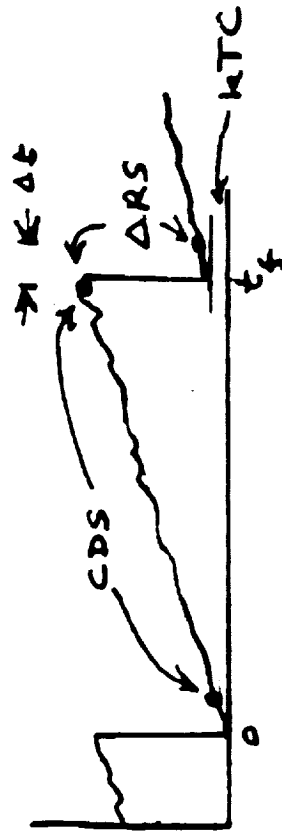


FIGURE 2-7 EFFECTIVE ABSORPTION DEPTH VS BEVEL ANGLE

READOUT CHOICES

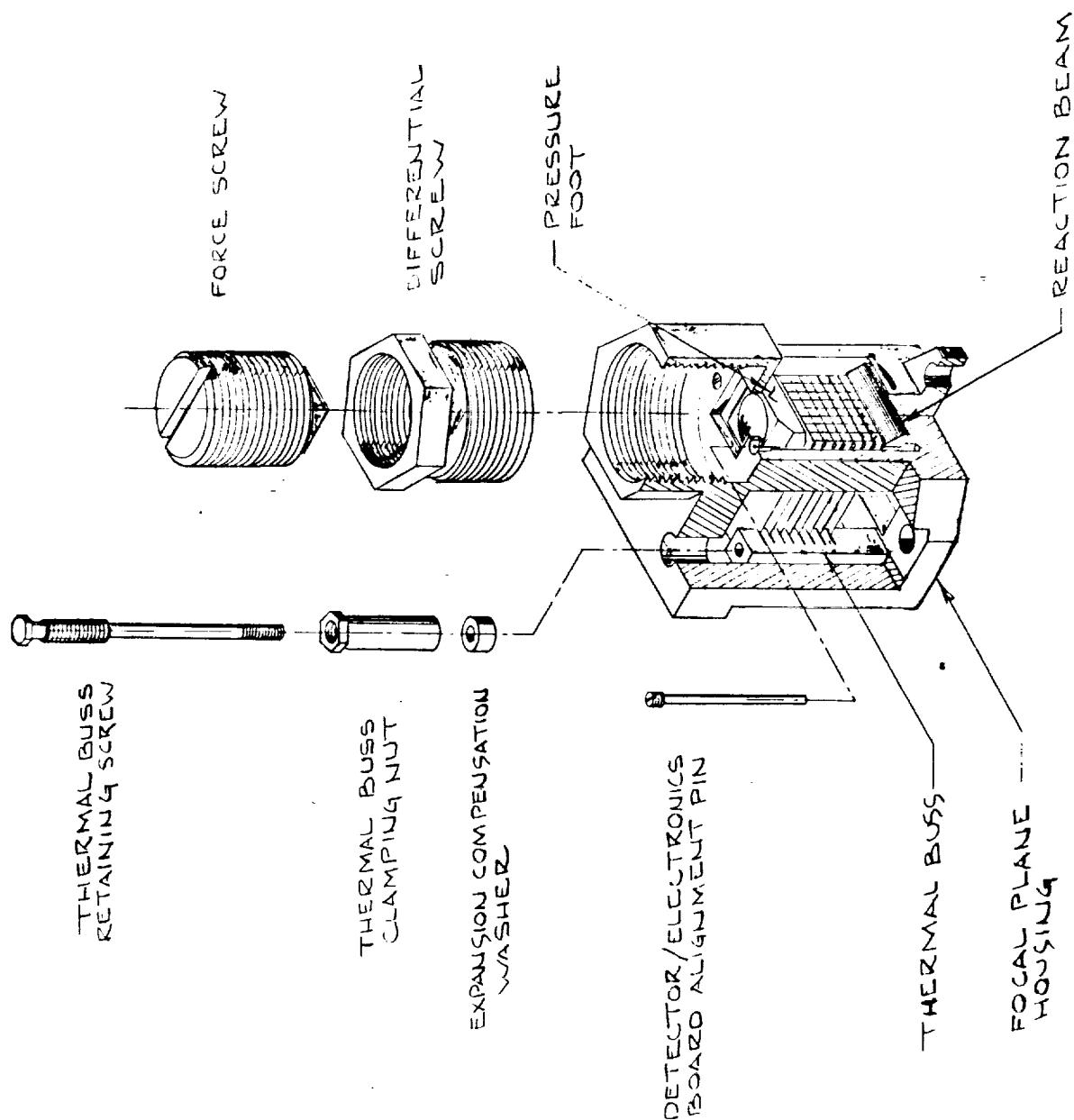
- DISCRETE CRYOFET + TIA
- CCD - INTEGRATE & MUX
 - TRANSFER NOISE \gg 500 e/sample IN SURFACE CHANNEL DEVICES
- MOS SWITCH - INTEGRATE & MUX USING Δ RESET



PARTICLE IONISATIONS

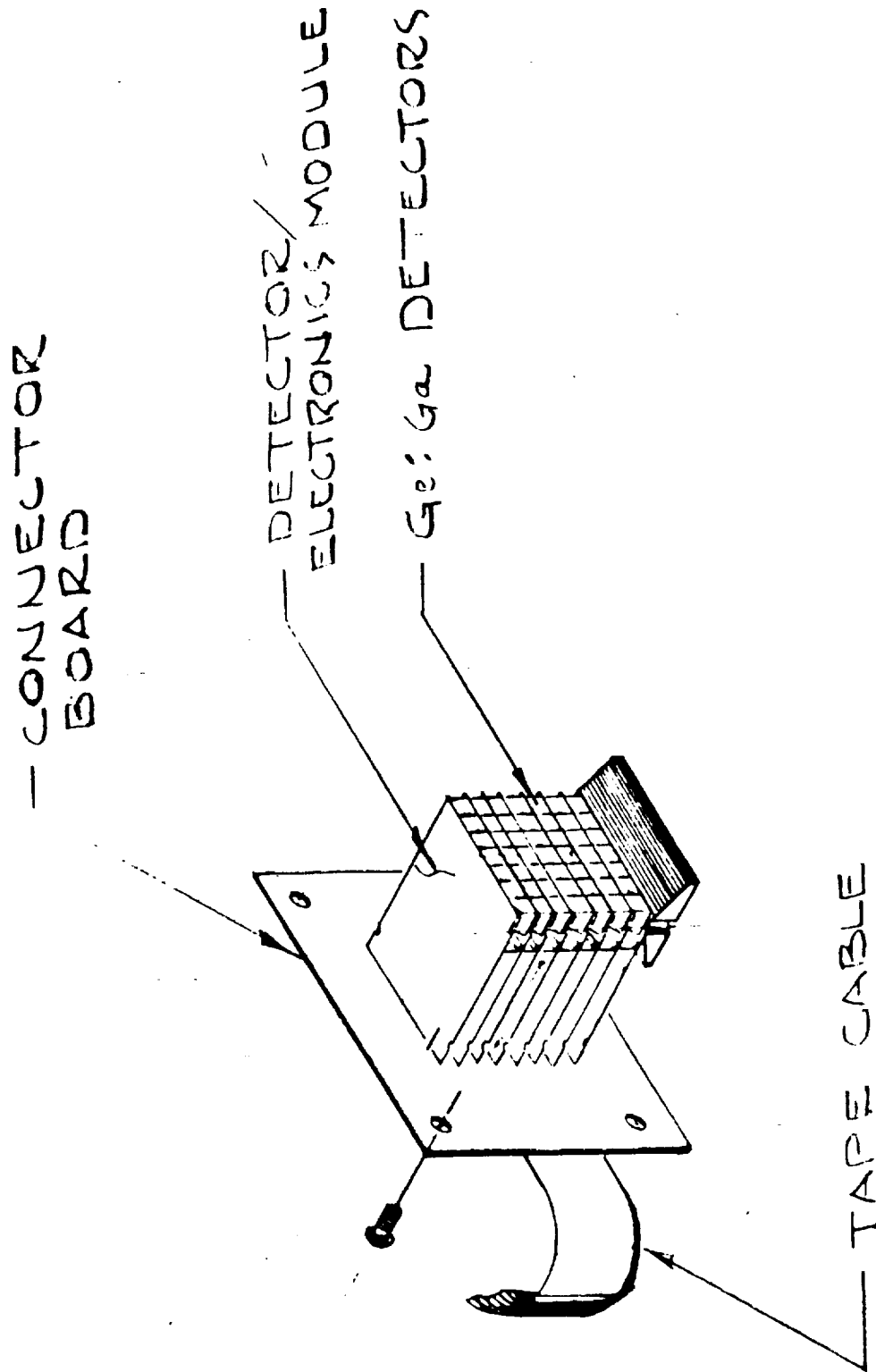
1mm CUBE OF GERMANIUM

| ALT | PARTICLE | FLUX | E_{MeV} | $\dot{N} sec^{-1}$ | \bar{h}_{crrr} |
|-----------------|-----------|------------------------------------|--------------|--------------------|------------------|
| 460 Km 233°S | PROTONS | 1×10^3 | > 50 | 4 | 10^6 |
| | EL & BR. | 2×10^5 2×10^4 | > 0.5 > 5 | .03 75 | 10^5 |
| 300 Km 233°S | PROTONS | | | 1.1 | 10^6 |
| | ELECTRONS | | | 11 | 10^5 |



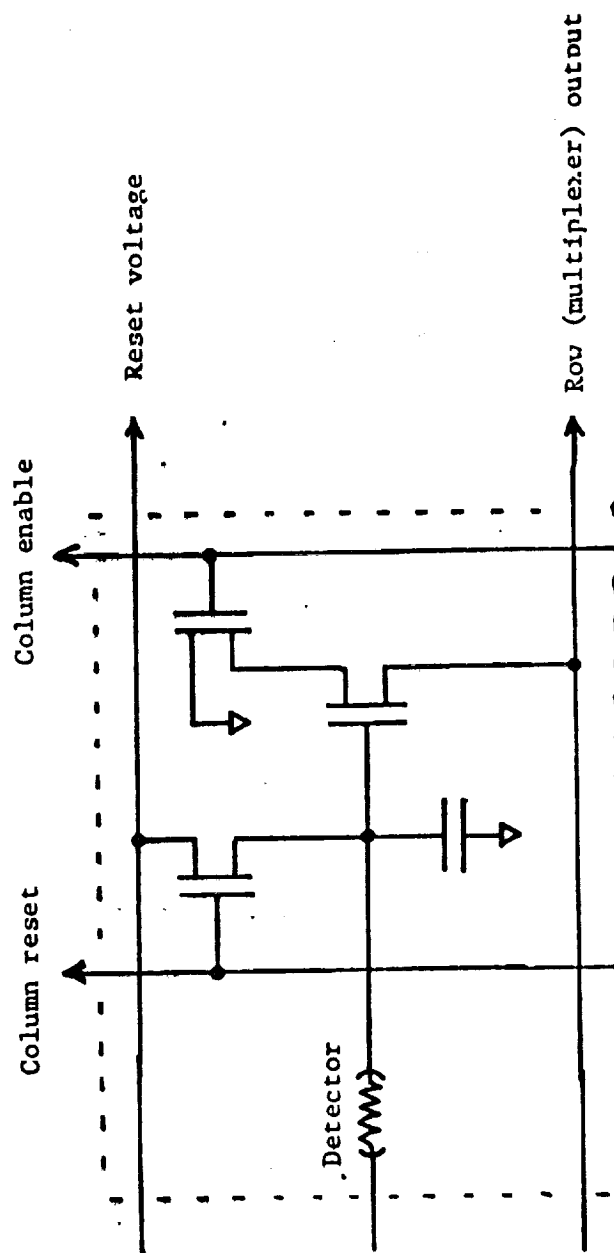
NASA

NAME _____ NO. _____



ELECTRONIC ISSUES

- CAN MOSFETS TURN ON/OFF AT LOW TEMP. ?
 - TURN ON $\sim 0.5 \mu s$ AT 2.8K (RC LIMITED)
 - FOR P-CHAN 3N163, M-CHAN 4 & N-CHAN 3N169
 - AMP (200pA) \uparrow LOW POWER AMP ($\sim 50 \mu A$)
- CAN LOW DRS NOISE BE ACHIEVED ?
 - USING DISCRETE FETS ($C \sim 2 pF$ NET, P-CHAN)
 - $n_s \lesssim 200$ RMS e/SAMPLE FROM 1s TO 30,000 sps
 - $\Delta Q = \Delta V_N \cdot C$
 - WILL CMOS MUX DRIVERS WORK COULD ?
 - RING OSCILLATOR STAGE DELAY DECREASES
 - ~ 3.3 (2ns DELAY AT 4.0K)
 - SWITCHING POINT (N-P BALANCE) & INDEPENDENT OF T
 - FOR 5V SUPPLY (CD4049 INVERTER)
 - LOW-CLOCK-RATE POWER MINIMIZATION
 - 2 BINARY COUNTERS (74C193) ~ 15 mW
 - + 3 DECODERS (74C15A) @ 50 kHz



SPCC UNIT CELL

STATUS SUMMARY

- AMCID OPERATION DEMONSTRATED
 - Si:Bi , Si:As , Ge:Hg
- Si:Bi RESPONSE UP TO $5A/W$ @ $16 \mu m$
 - $\eta \approx 0.4$, $q \approx 1$
- CAN BE ADDRESSED IN $\leq 10 \mu sec$
 - 3Kf.p.s for 32 pixel row
- RESPONSE-TIME FLUX DEPENDENT
 - INTERPRET DATA WITH CAUTION
- YIELDS (\$ COST) MAY NOW BE ACCEPTABLE

59-74
133814
p.33
NC 473657
N98-70645

LOW BACKGROUND IR DETECTOR AND DETECTOR ARRAY EVALUATIONS

J. H. Goebel, D. A. Jared, J. H. Lee, C. R. McCreight
M. E. McKelvey, and P. S. Stafford
NASA Ames Research Center
Moffett Field, CA 94035

Introduction

A technology program has been underway at Ames since 1978 to develop and evaluate detectors and integrated detector arrays for low-background astronomical applications. The approach is to evaluate existing ($<24 \mu\text{m}$) array technology under low-background conditions, with the aim of adapting and optimizing existing devices. For longer wavelengths, where the technology is much less mature, development is sponsored and devices are evaluated, in both discrete and array formats, for eventual applications. The status of this program has been reported previously.^{1,2}

We rely on industrial and university sources for the detectors. Typically, after a brief functionality check in the supplier's laboratory, we work with the device at Ames to characterize its low-background performance. In the case of promising arrays or detectors, we conduct ground-based telescope testing to face the problems associated with real applications.

A list of devices tested at Ames is given in Fig. 1. In the array category, accumulation-mode charge-injection-devices (CIDs) appear repeatedly; this reflects our recent experience with the 2×64^3 and 16×16^4 arrays. Results from the $1 \times 16 \text{ CID}^5$ and InSb CCD^6 have been reported. The status of our tests of the discrete Ge:x detectors from Lawrence Berkeley Laboratory (LBL) are described below. Tests of a 1×2 switched sample photoconductor

array⁷ are just beginning. A 32-channel CMOS multiplexer has been tested at 10 K.⁸ Low-temperature silicon MOSFETs⁹ and germanium JFETs¹⁰ have also been tested, primarily at Ball Aerospace.

This paper describes results to date on three elements of this program: CID arrays, discrete Ge:Ga detectors, and Ge JFET preamplifiers.

2 x 64 Si:Bi CID Arrays

Three 2 x 64-element CID arrays were developed by Aerojet ElectroSystems Company as a means of evaluating extrinsic silicon detector technology under low-backgrounds.³ Fig. 2 shows the layout of the array, which was packaged in a 32 mm-square butterfly case. Two long transparent electrodes, with read gates and an oxide layer on the opposite face of the Si:Bi substrate, run vertically through the center of the figure. Four 74C154 CMOS decoders, and a 74C193 counter, are mounted on the left; these provide the sequential read and store pulses to the 64 pairs of detectors. In the upper right are the two 3N163 FETs and 40 M Ω load resistors. Resistors for thermometry and heating are also included.

A detailed view of the pixel is shown in Fig. 3. In laying out the array, the two rows of pixels (175 μ m square on 220 μ m centers) were separated by 250 μ m, so that one row could be illuminated by sky, and the other by object-plus-sky. The two row outputs can be read out separately, or differenced directly to provide "front end" background subtraction.

Most of our testing on these arrays has actually been done at a "moderate" background, which we estimate to be 4E7 ph/s (= 6E-13 W), to match conditions in the Lick Observatory cryogenic spectrometer, in which observing runs were made in October 1982 and July 1983. Recently, by use of an attenuation filter, we have obtained data in the low-background range. This background is

estimated at $3E5$ ph/s ($= 5E-15$ W). The optical system used in earlier testing of the 1×16 CID was also used in these tests.

Our recent 2×64 results show both similarities to and differences from the 1×16 array data summarized in Ref. 5. The 2×64 data were taken at moderate background, except where noted; the similarities will be discussed first.

Our measurements of responsive quantum efficiency are all consistent, and in the range of slightly below 0.20 to about 0.25. This corresponds to a responsivity in the range 2.5 to 3.2 A/W. Although some adjustments in read and store voltages and sampling locations were necessary and we observed some variability from day to day, these results are typical of good performance. Very recently, we measured a low-background responsive quantum efficiency of 0.20, which is consistent with earlier results. Other characteristics which apply to both arrays are input capacitance (4.3 pF measured 2×64 average vs. 3.8 pF in Ref. 5) and 2 Hz low-background 3 dB-limit to frequency response. An array temperature in the range 11 ± 2 K produced optimum signal/noise results in all cases.

A number of differences in performance were also observed. Fig. 4 shows the limit of mid- 10^5 to 1×10^6 electrons for well capacity, which we measured at both moderate and low backgrounds. This is a factor of about 50 lower than one would predict on the basis of the areal capacitance of SiO_2 layers, and this significant discrepancy is not understood. Another difference is that while the absolute difference between optimum 2×64 read and store voltages (about 12 V) is comparable to the 1×16 difference (about 9 V), the midpoint of the 2×64 voltage swing was significantly displaced from ground. That is, we find an optimum (V_{store} , V_{read}) pair of (+1 V, -11 V), compared to the previous (+4 V, -5 V) setting.

Other 2×64 parameters were different, in a positive sense. We have regularly achieved read noise levels below 200 e^- rms in the laboratory, and measured 157 e^- rms (Fig. 5) while the analog

system was mounted to the 120" telescope at Lick Observatory. This result is a factor of four better than the 1 x 16 average, the latter being limited by the drive and sample/hold circuitry. Furthermore, the 2 x 64's were much more uniform. Fig. 6, which shows signal for each channel after offset correction, indicates standard deviations about 10% of the average, vs. about 25% for the 1 x 16. The latter result was high due to the large number of inactive pixels in the sample array, and the tendency for photoelectrons created in the "dead" sites to be swept into and read out from the neighboring active pixels. Finally, it was found that frequency response was significantly enhanced at moderate backgrounds. Fig. 7 illustrates moderate-background signal response at 30 Hz; our data show a 3 dB point at or greater than 20 Hz at moderate background.

Based on our experience and incomplete results, the following general assessment of Si:Bi CID technology is offered. While significant and unexplained differences were found between the 1 x 16 and 2 x 64 arrays, the three 2 x 64 arrays are similar. It seems that within the same generation of devices, at least, one can assume common performance characteristics. The processing and production technology is not yet highly developed, as evidenced by the delayed deliveries and inactive pixel pairs which resulted on our contract. (The three delivered arrays had 2, 3, and 8 pairs of inactive pixels.) Although we have not studied possible trapping effects in sufficient detail, at a signal level of 3900 ph/integration at a $3E5$ ph/s background, we did not observe a significant signal lag. The character of the moderate-background signal response in Fig. 7 (i.e. two or three readouts to reach full signal amplitude, with the first sample significantly above the 50% level) applies to low-background conditions as well. This character can be interpreted as being caused by dielectric relaxation within the device.⁵ Note, however, that this picture is not completely satisfactory, since we find that at moderate background and extended (>1 s) integration times, the device takes

many reads to reach full signal amplitude. Also, we do not have good dark current data yet, but can report that, viewing the cold shutter, the array could integrate for >30 s without coming close to saturation. A final comment is that we have no data on CID response in a radiation environment; this would clearly be critical in an orbital application.

In summary, many aspects of CID performance appear promising for low-background applications. With a 20% responsive quantum efficiency and 200 rms e^- of read noise, one calculates a $1.8E-17$ W/ \sqrt{Hz} NEP in 1 s of integration time, indicating a very good inherent sensitivity. Low-background radiation and trapping effects are among the key CID characteristics which we have not yet established.

16x16 Si:Bi CID array

This array⁴ is a contiguous subarray of a 32x32 chip with all 256 pixels active. While its row electrodes have been connected with metallized traces, the read gates in the columns have been stitched together with a gold ball bonder (Fig. 8). This approach improved production yield and probably array uniformity as well. Two CMOS scanner chips address the columns with a maximum frame rate of about 1 kHz, and each row is read out by a 3N163 MOSFET.

The array has been evaluated under low backgrounds in the same test setup described in detail in Ref. 5. Testing was performed at a variety of temperatures, and 10 to 11 K was found to be an optimum temperature range. Blackbody radiation was filtered by an 11.0 ± 0.03 μm narrow bandpass filter and neutral density filters. Table 1 shows the average performance parameters across the array. Fig. 9a shows a sample row readout (row 7) with the blackbody illumination on and off. Fig. 9b shows temporal response of a single pixel to chopped external blackbody radiation. The blackbody signal is about $6E6$ ph/s and the chopper blade signal is about $2E5$ ph/s.

Typical noise levels achieved are presently in the 600 electron/readout range. This noise is higher than that for the 2x64 arrays reported above; we find the 16 x 16 drive electronics are limiting, and are currently constructing an improved version.

Note a significant response lag is not present in this array at these backgrounds to the extent reported in other CID arrays. However, there is an interesting asymmetry in the amount of response lag upon increasing and decreasing illumination. There is less lag present when flux is decreased (up on the oscillograms in Fig. 9b) than when flux is increased.

Fig. 10 gives the output of a typical row (Row 8). The average responsivity is 4 A/W, corresponding to an average responsive quantum efficiency of 27%. The variation is about 10% of the mean. The well capacity of $\sim 3E5$ electrons is lower than expected on the basis of device electrode capacitance, and limits the array's applicability in moderate- and high-background experiments.

At moderate backgrounds we have found the device's characteristics to remain nearly unchanged. At these backgrounds one is driven to the fastest readout rates, which can lead to extra noise due to clocking problems. But the quoted well capacity, quantum efficiency, and uniformity numbers apply from photon rates of $1E5$ to $1E10$ per second.

To acquire data from large arrays of this type, it is essential to have a computer-based automatic data acquisition system. We have designed and constructed such a system based upon an industry standard MULTIBUS architecture.¹¹ The system is low cost, compact and portable. Fig. 11 shows its architecture. The interesting features are the use of commercial 12-bit, 125 kHz A/D 16k RAM dual-port data acquisition boards, and co-processor boards, which do real-time digital signal integration. This allows the CPU to be more productively employed during data acquisition. Two 1.2 Mbyte floppy discs and a high-resolution color graphics monitor provide the storage and display functions.

This system is more susceptible to noise than desired, and we cannot go below 600 e⁻ read noise without major modifications.

The second version of the data system is shown in Fig. 12. It retains the co-processor concept to reduce data storage requirements through real time signal averaging, but relocates the A/D and co-processor boards in the array drive electronics box, and does not connect them to the MULTIBUS. This architecture significantly reduces the complexity of the electronic exerciser/computer interface, and improves interference and clock-pickup immunity. Of all interference problems, synchronous clock pickup is the most serious. It cannot be reduced by averaging or subtracting frames, but can be avoided by careful shielding and grounding design.

With the first version of the data system, we have been able to take images of a 250 μm spot. The pixels are approximately 165 μm center-to-center, so the reimaged spot is predominately in one display pixel with some small amount in each of the surrounding pixels. There is very little response beyond the adjacent pixels in a given row, indicating low crosstalk between columns. Between rows, however, significant crosstalk is seen. A sample of the monitor output is shown in Fig. 13. The system's portability and durability have been tested in the field, where successful operation has been demonstrated.

Ge:Ga and Ge:Be Testing

An apparatus has been constructed at Ames for the evaluation of long-wavelength infrared detectors, and sample extrinsic germanium photoconductors have been tested. Preliminary responsivity and noise-equivalent power (NEP) results show good agreement with evaluations of the same detectors by N. Haegel at LBL.

The test system is built within an extra-long Infrared Laboratories HD-3(8) dewar. Included in the assembly are a low

temperature (5 - 150 K) internal radiation source and a galvanometer-type chopper as well as provision for the use of radiation sources external to the dewar. Modulation frequencies with the internal chopper are variable from 0.1 to about 70 Hz with various waveforms.

Gallium- and beryllium-doped germanium photoconductors have been provided by Dr. E. Haller of LBL. The gallium-doped detectors (gallium concentration = $2 \times 10^{14} \text{ cm}^{-3}$) have shown a best NEP at zilch background of about $6 \times 10^{-17} \text{ W}/\sqrt{\text{Hz}}$. Responsivity at the best NEP is 5 A/W, with responsivities up to 30 A/W achievable before breakdown. These responsivity numbers are in agreement with LBL results to within 10 - 20%. Fig. 14 is a typical plot of response and NEP vs. bias field.

The strong dependence of responsivity on detector temperature observed at LBL¹² for the beryllium-doped detectors (Be concentration = $1 \times 10^{15} \text{ cm}^{-3}$) has also been seen in our laboratory. Ge:Be signal response decreases by 70% and noise by 90% as detector temperature is reduced from 4.2 K to 3.6 K. The best NEP (see Fig. 15) is about $2 \times 10^{-16} \text{ W}/\sqrt{\text{Hz}}$, measured at 3.8 K and negligible background.

The test system is ultimately slated for the evaluation of prototype Ge:Ga photoconductor arrays currently under study.

Ge JFET Testing

The germanium JFET represents a dormant semiconductor technology which was supplanted by silicon technology nearly two decades ago. For cryogenic applications it has long been known that cooled Ge JFETs behave quite well at high frequencies, particularly for nuclear particle detectors. At low electronic frequencies where IR photoconductors operate, little work has been done. Together with R. Arentz and D. Strecker of Ball Aerospace, we have evaluated their applicability to the source follower and TIA configuration using 20-year-old Texas Instruments Model XM12

Ge JFETs.¹⁰ Table 2 presents our qualitative assessment of the devices which were tested at 1.8K. When cooled, the thermalized gate channel leakage current vanishes, and the diode is well behaved with a broad reverse-bias flat-band region. Fig. 16 shows the transconductance curves at room and pumped liquid helium temperatures. The transconductance increases at cryogenic temperatures, and Fig. 17 shows that the source follower gain can be tuned to near unity at 1.8 K, where the input capacitance is near 4 pF.

The noise behavior is of critical importance in the TIA application. Fig. 18 shows that Johnson-noise-limited performance can be achieved with a $1\text{E}10\ \Omega$ feedback resistor between 1 and 1000 Hz when the pair of Ge JFETs are operated at 4K with about 100 μW of dissipated power. Fig. 19 indicates that the TIXM12's have noise performance in the source-follower mode that is a) superior to that of the ZK-111 MOSFET at 4K and b) comparable at frequencies above 10 Hz to a J230 Si JFET self-heated to 80K in a 4K enclosure.

The potential applications of Ge JFETs, with their good noise performance, are in hybrid and monolithic focal planes of long-wavelength doped germanium, or in other single-temperature focal planes. Renewed development efforts on this type of device are clearly desirable.

Acknowledgement

The continued support for this program from NASA's Office of Aeronautics and Space Technology is gratefully acknowledged.

References

1. C. R. McCreight and J. H. Goebel, Proc. SPIE 331, 9 (1982).
2. C. R. McCreight, Proc. SPIE 304, 187 (1981).
3. J. F. Yee, "Final Report, Multiplexed Extrinsic Silicon Detector Arrays," Aerojet ElectroSystems Company Report 6184, NASA CR-166,323, March 1982.
4. M. H. Sweet, "16 x 16 Element Extrinsic Silicon Detector Array," Aerojet ElectroSystems Company Report 6152, NASA CR-166,285, December 1981.
5. C. R. McCreight and J. H. Goebel, Appl. Opt. 20, 3189 (1981).
6. J. D. Bregman et al., "Low Background Performance of a Monolithic InSb CCD Array," NASA TM-84216, January 1982.
7. J. F. Yee, "Si:Bi Switched Photoconductor Infrared Detector Array," Aerojet ElectroSystems Company Report 6372, NASA CR-166,439, January 1983.
8. J. H. Lee, "Ambient and Cryogenic Temperature Testing of a 32-channel CMOS Multiplexer," NASA TM-84385, July 1983.
9. N. Sclar, "Design, Production, and Testing of Field Effect Transistors," Rockwell International Report SC5299.13, NASA CR-166,321, February 1982.
10. R. F. Arentz et al., Proc. SPIE 364, (1982). (In press)
11. P. S. Stafford and D. A. Jared, "Infrared Astronomical Imaging Using a Microcomputer Data System," paper 83-2377CP, to be presented at AIAA Advanced Software Concepts: Sensor and Signal Processing Concepts Meeting, Hartford, CT, October 1983.
12. N. M. Haegel, E. E. Haller, and P. N. Luke, "Performance and Material Aspects of Ge:Be Photoconductors," LBL-15409, presented at the 7th International Conference on Infrared and Millimeter Waves, Marseilles, France, February 1983.

TABLE 1

16 x 16 Si:Bi CID Array Performance
Measurements at Ames

$\lambda = 11 \mu\text{m}$ at low (about $1\text{E}6$ ph/s) background

| | |
|-----------------------------------|--|
| Responsive quantum efficiency | ~ 0.25 |
| Well capacity | $\sim 3\text{E}5$ electrons |
| Read noise | < 600 electrons |
| Responsivity ($17 \mu\text{m}$) | ~ 4 A/W |
| NEP | $< 1\text{E}-16$ W/ $\sqrt{\text{Hz}}$ or BLIP |
| Uniformity of responsivity | 10% |

Table 2

TIXM12 SUMMARY

- WILL OPERATE WELL TO AT LEAST 1.8K IN INFRARED DETECTOR CIRCUITS
 - ORDERLY I-V CHARACTERISTICS AT 1.8K
 - LOW POWER
 - LOW NOISE
 - LOW INPUT CURRENT
 - LOW INPUT CAPACITANCE
 - HIGH GAIN
 - HIGH TRANSCONDUCTANCE
 - ESD PROTECTED
 - SMALL CROSS SECTION AND RELATIVELY INSENSITIVE TO RADIATION EFFECTS
- IMMEDIATE APPLICATION IN DISCRETE ARRAYS
- INDICATE THAT LARGE SCALE INTEGRATED-ARRAY LONG-WAVELENGTH MONOLITHIC GERMANIUM FOCAL PLANES ARE FEASIBLE

Figure Captions

- Fig. 1 Devices Tested at Ames
- Fig. 2 2 x 64 element Si:Bi CID array assembly mounted in butterfly case
- Fig. 3 Close-up of 2 x 64 array, showing pixel geometry and scanner chips
- Fig. 4 Well capacity measurement for 2 x 64 CID array
- Fig. 5 Noise spectrum for 2 x 64 CID array
- Fig. 6 Uniformity of responsivity of 2 x 64 array
- Fig. 7 2 x 64 response to 30 Hz chopped blackbody signal
- Fig. 8 16 x 16 element Si:Bi CID array. To the left are 74C193 and 74C154 CMOS scanner chips
- Fig. 9 a) Full frame, and b) single pixel readouts from 16 x 16 array
- Fig. 10 Uniformity in responsivity of 16 x 16 array
- Fig. 11 Z80-based microcomputer data acquisition system
- Fig. 12 Improved version of data acquisition system
- Fig. 13 Images of 250 μ m spot obtained with data acquisition system. Clockwise from upper left are shown: image of spot after background was subtracted; image before subtracting background (note elevated fixed-pattern noise); image of weak source in presence of strong background; and display of random noise. Note that each output has been separately scaled.

- Fig. 14 Ge:Ga responsivity and NEP as functions of bias at 3.0 K
- Fig. 15 Ge:Be responsivity and NEP as functions of bias at 3.8 K
- Fig. 16 TIXM12 I-V curves
- Fig. 17 TIXM12 gain and input capacitance as a function of gate-to-drain voltage
- Fig. 18 TIXM12 noise spectral density curves
- Fig. 19 Noise characteristics for various FETs in grounded-gate, source-follower configurations

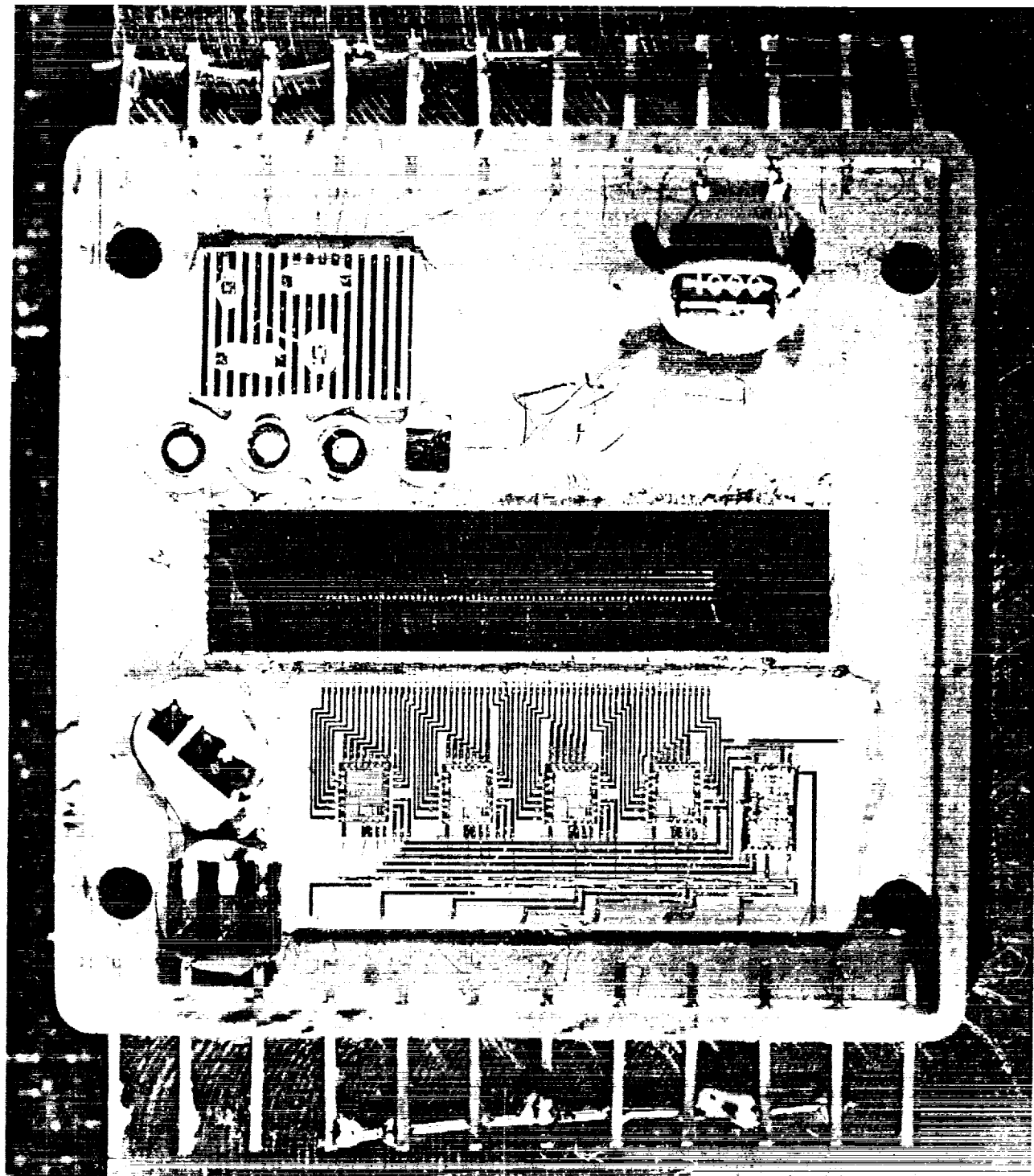
DEVICES TESTED AT AMES

| | DEVICE | QUANTITY | MATERIAL | SOURCE |
|--------------|--------------------------------------|----------|--------------|--|
| A. ARRAYS | 1 x 16 SAMPLE CID | 1 | Si:Bi | AEROJET |
| | 2 x 64 CID | 3 | Si:Bi | AEROJET |
| | 16 x 16 CID | 2 | Si:Bi | AEROJET |
| | 1 x 10 BLOCKED IMPURITY BAND | 1 | Si:As | ROCKWELL |
| | 1 x 20 MONOLITHIC CCD | 1 | InSb | SANTA BARBARA RESEARCH CENTER, VIA LANGLEY |
| B. DISCRETES | 1 x 2 SWITCHED SAMPLE PHOTOCONDUCTOR | 1 | Si:Bi | AEROJET |
| C. OTHER | LONG-WAVELENGTH PHOTOCONDUCTORS | — | Ge:Ga, Ge:Be | LAWRENCE BERKELEY LABORATORY |
| | 32-CHANNEL CMOS MULTIPLEXER | 3 | Si | IRVINE SENSORS |
| | JFET* | 7 | Ge | TEXAS INSTRUMENTS, VIA HUGHES |
| | CRYOGENIC MOSFETs* | 3 | Si | ROCKWELL |
| | COMMERCIAL FETs AND CAPACITORS, ETC. | — | Si | (VARIOUS) |

*TESTED PRIMARILY AT BALL AEROSPACE

Figure 1

Figure 2



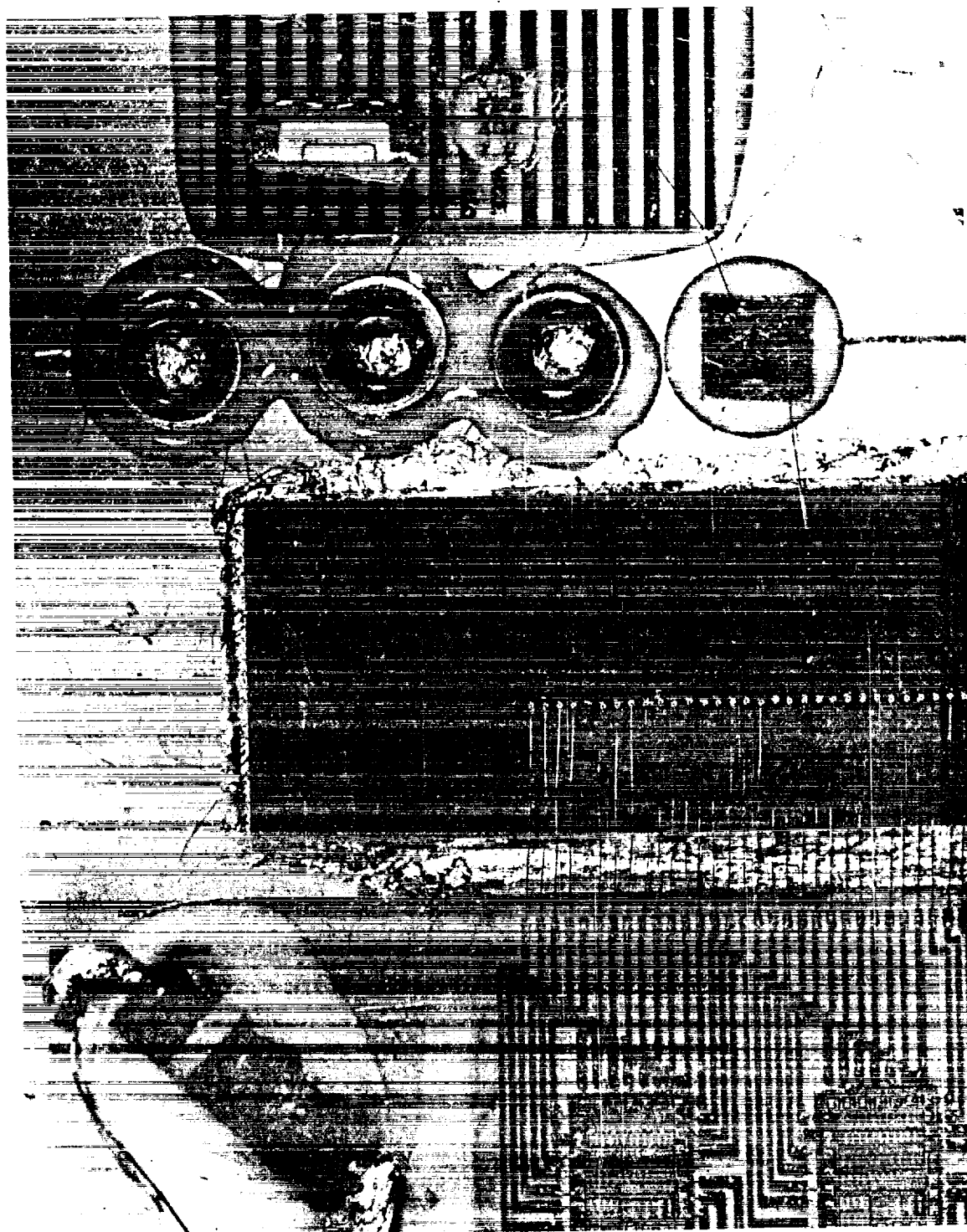


Figure 3

ORIGINAL PAGE IS
OF POOR QUALITY

WELL CAPACITY MEASUREMENT

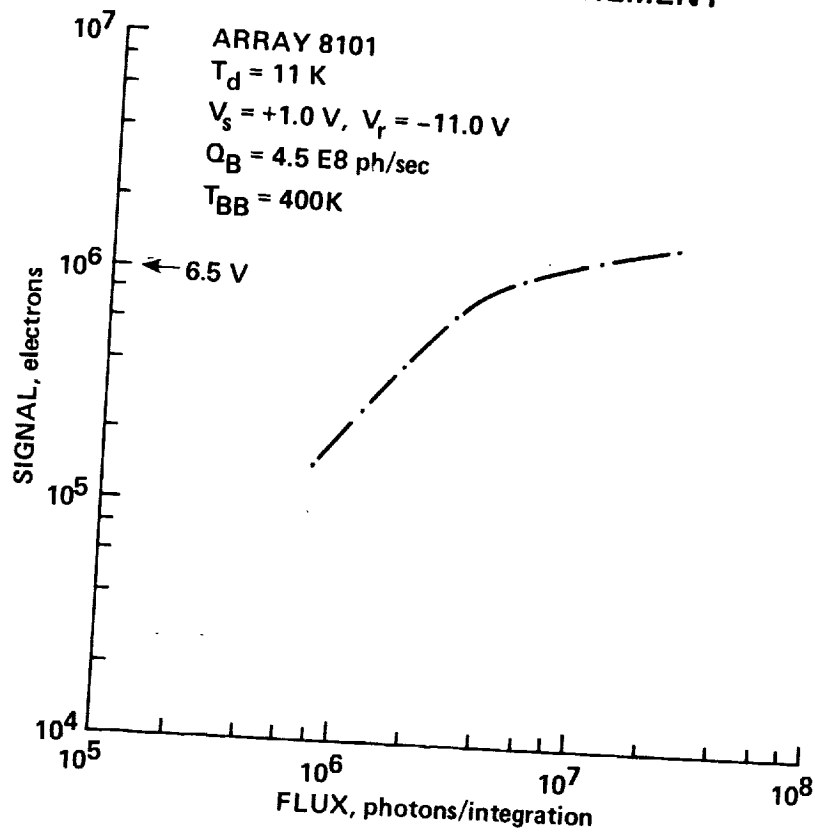


Figure 4

2 x 64 NOISE SPECTRUM

$T_d = 10.8 \text{ K}$
PIXEL 43, CH. 1
 $V_s = 0.15 \text{ V}$, $V_r = -10.5 \text{ V}$
NOISE = $6.3 \mu\text{V}$
= $157 e^- \text{ rms}$

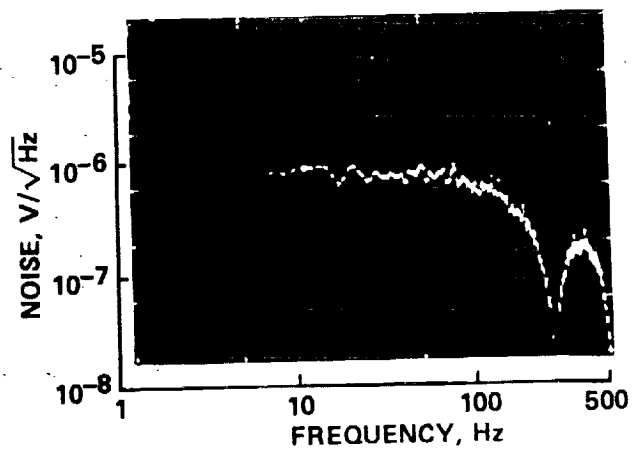


Figure 5

2 x 64 UNIFORMITY

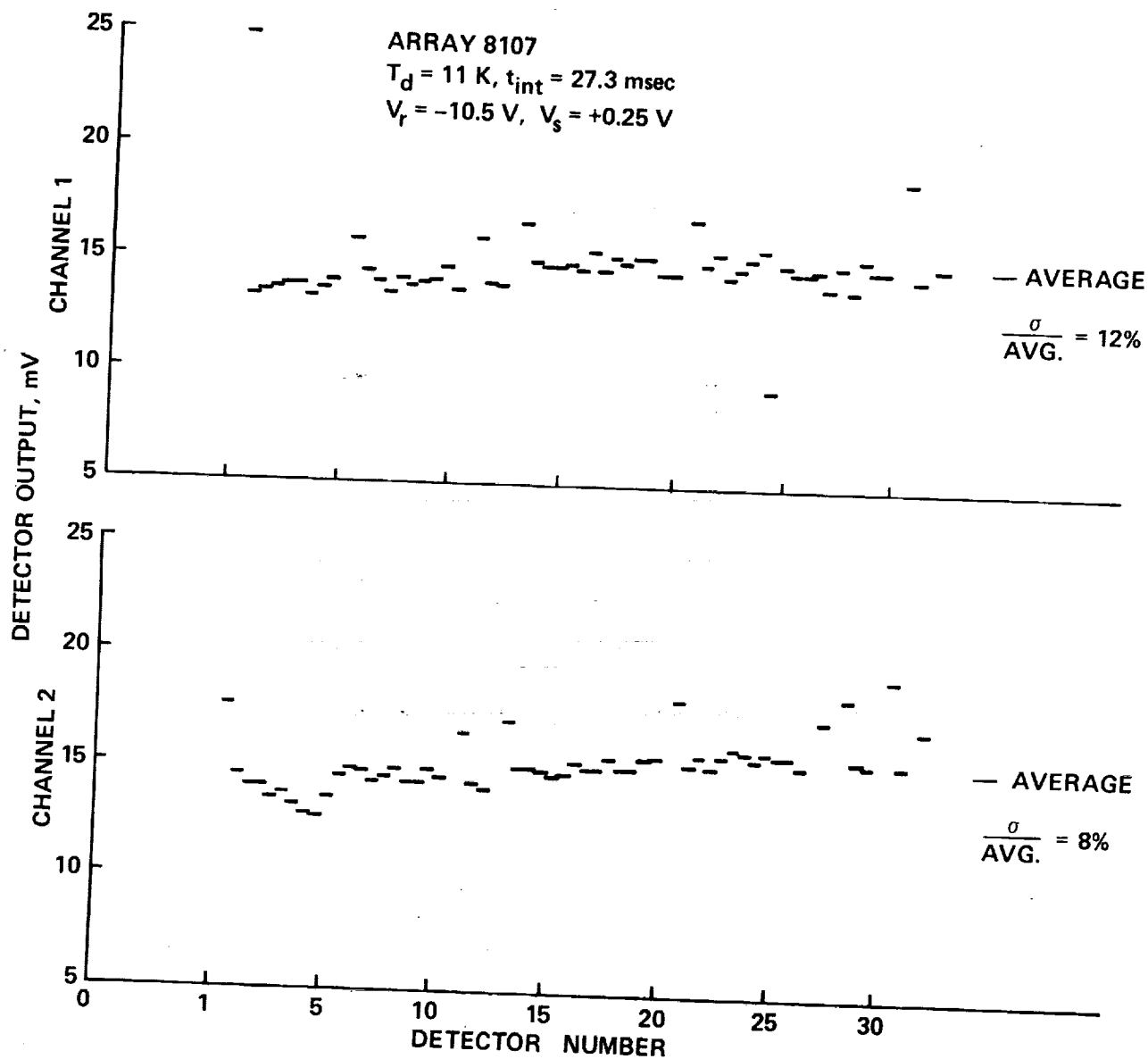
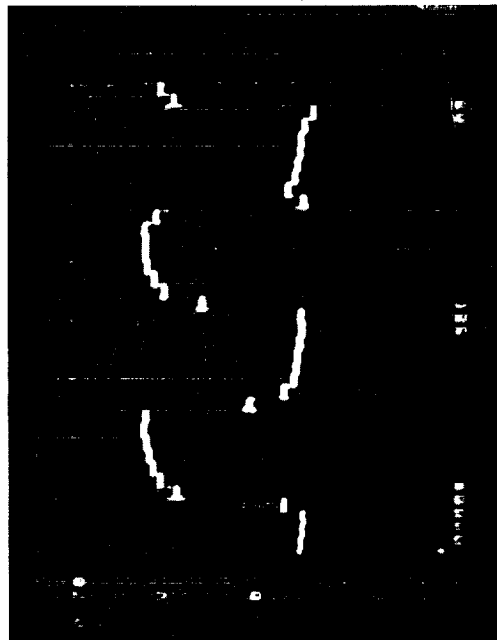


Figure 6

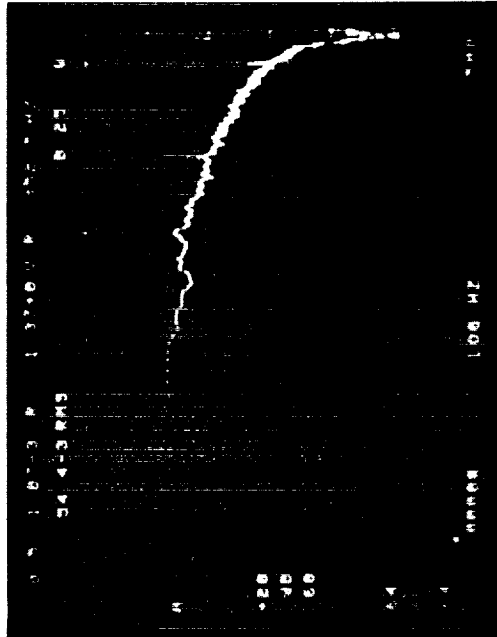
Ames Research Center
2 x 64 Si:Bi CID ARRAY DATA

TEMPERATURE = 11 K
INTEGRATION TIME = 2 msec
BACKGROUND = 8×10^{-13} W

SIGNAL



NOISE



CHOPPING FREQUENCY = 30 Hz
QUANTUM EFFICIENCY ~ 0.2

rms READ NOISE ~ 300 e^-

Figure 7

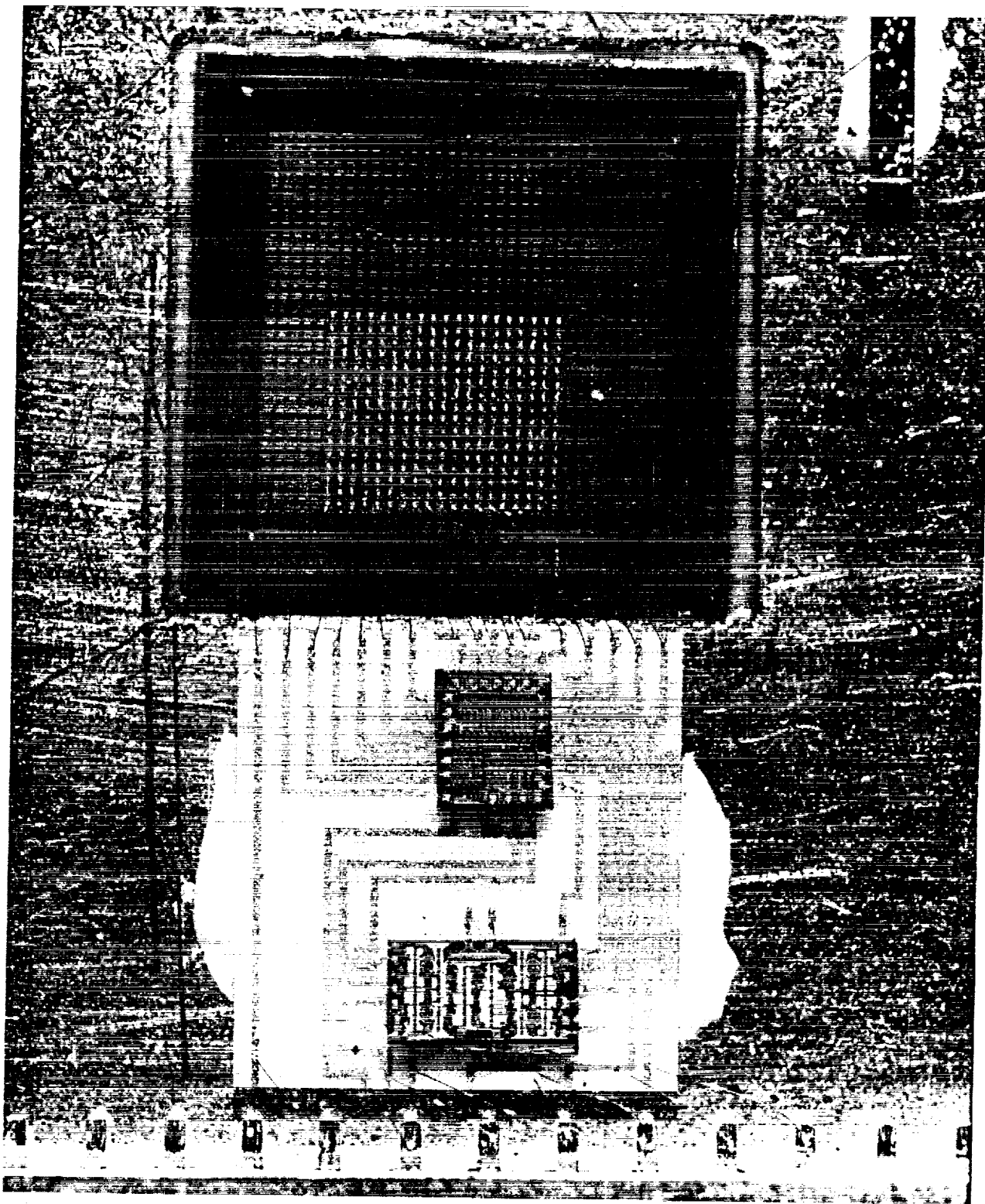
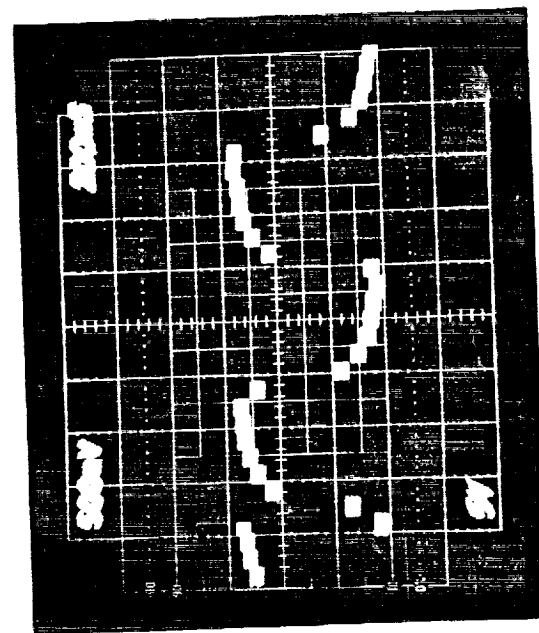
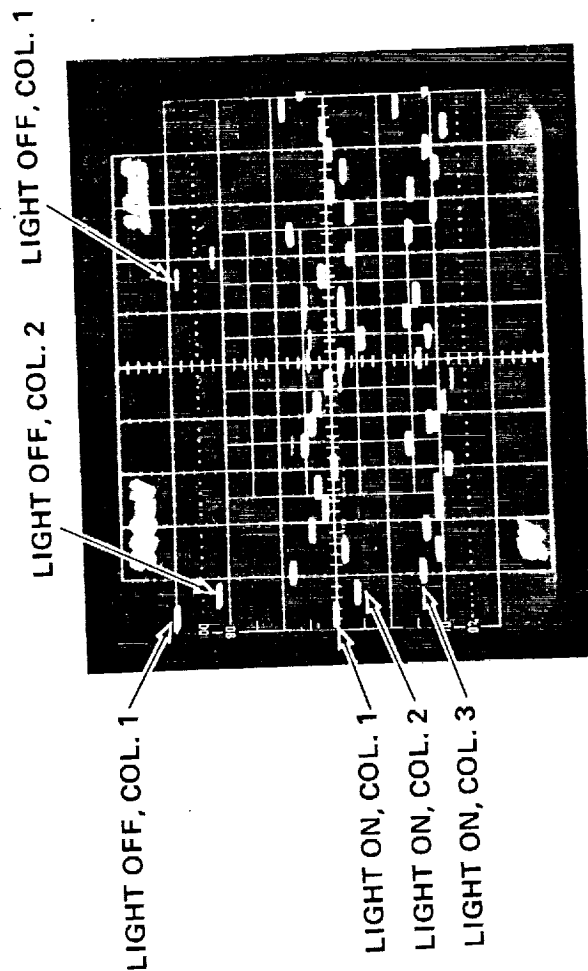


Figure 8

16 x 16 Si:Bi CID TEST RESULTS AT AMES OCTOBER 29, 1981

DETECTOR TEMP = 11 K
INTEGRATION TIME = 64 msec
SIGNAL FLUX = $1.1 \text{ E} - 13 \text{ W}$
ESTIMATED BACKGROUND = $3.2 \text{ E} - 15 \text{ W}$

FULL FRAME, SHOWING ALL 16 PIXELS
IN ROW 7 WORKING



ONE PIXEL (COL. 1, ROW 7) ONLY,
SHOWING RESPONSE TO CHOPPED (1 Hz)
ILLUMINATION. ESTIMATED
RESPONSIVITY = 2.4 A/W

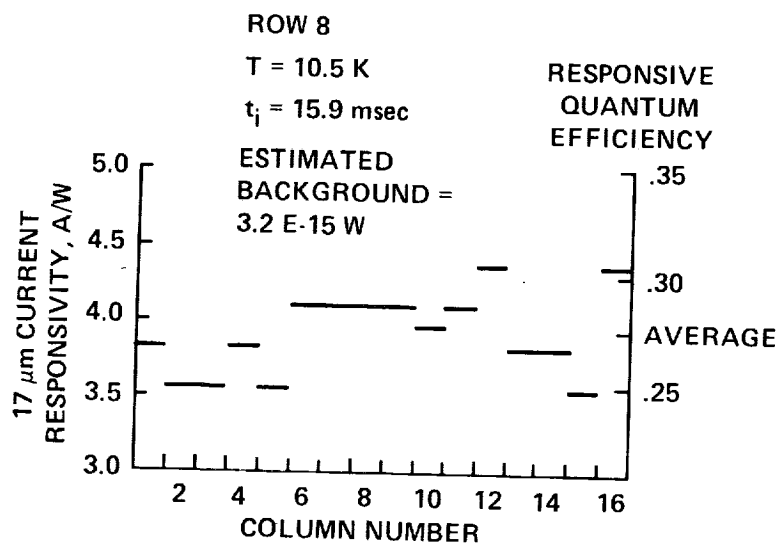


Figure 10

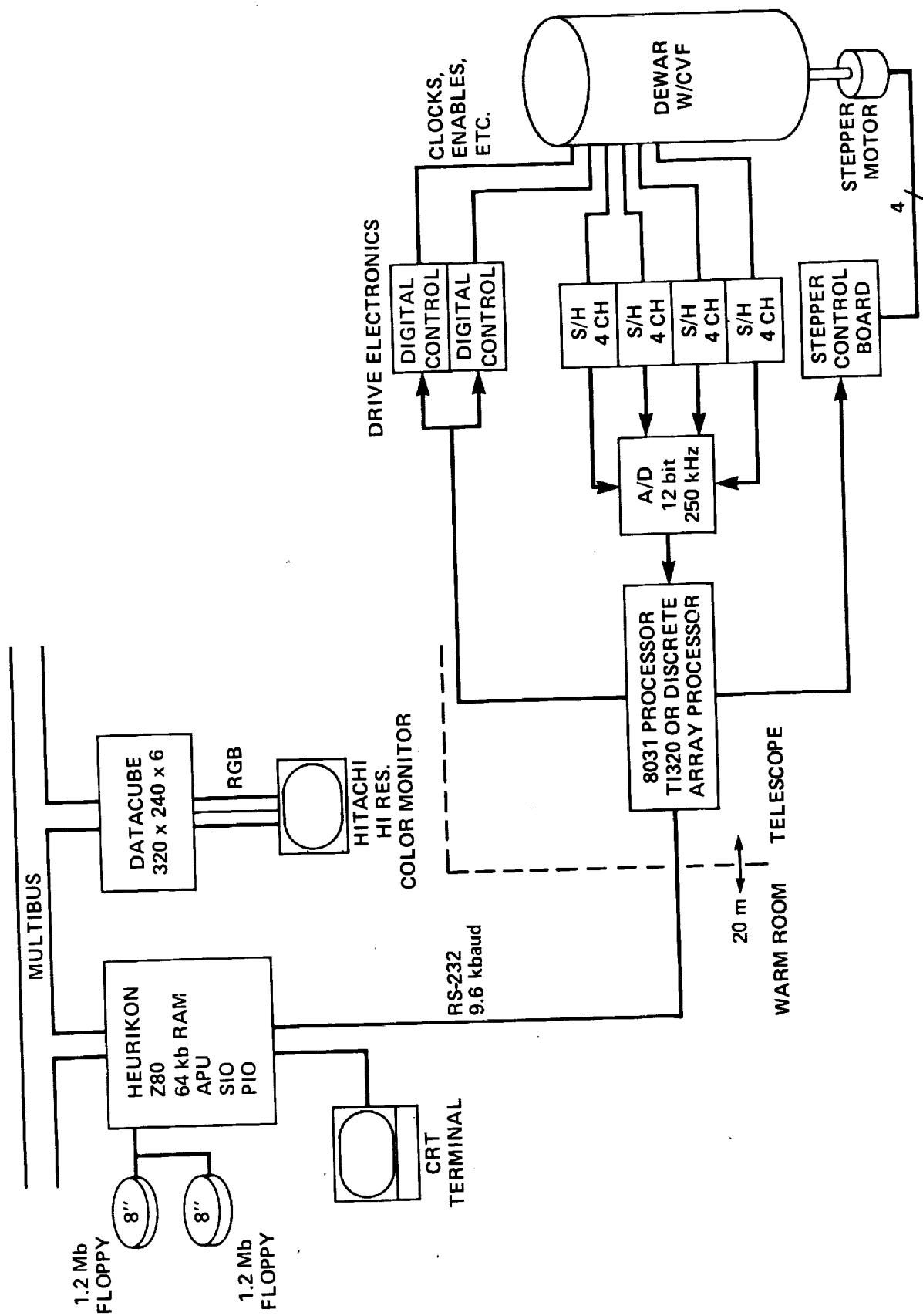


Figure 11

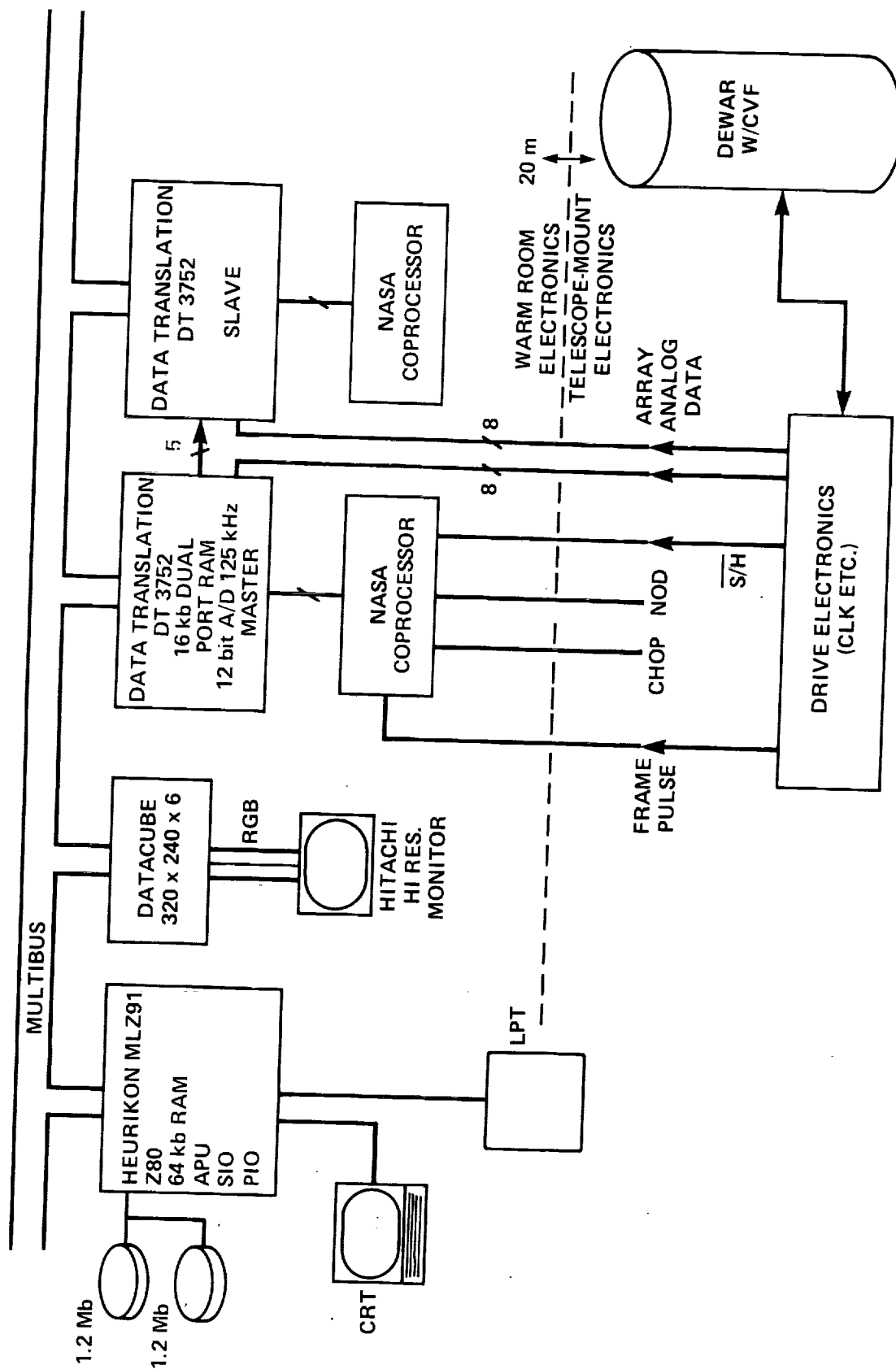


Figure 12

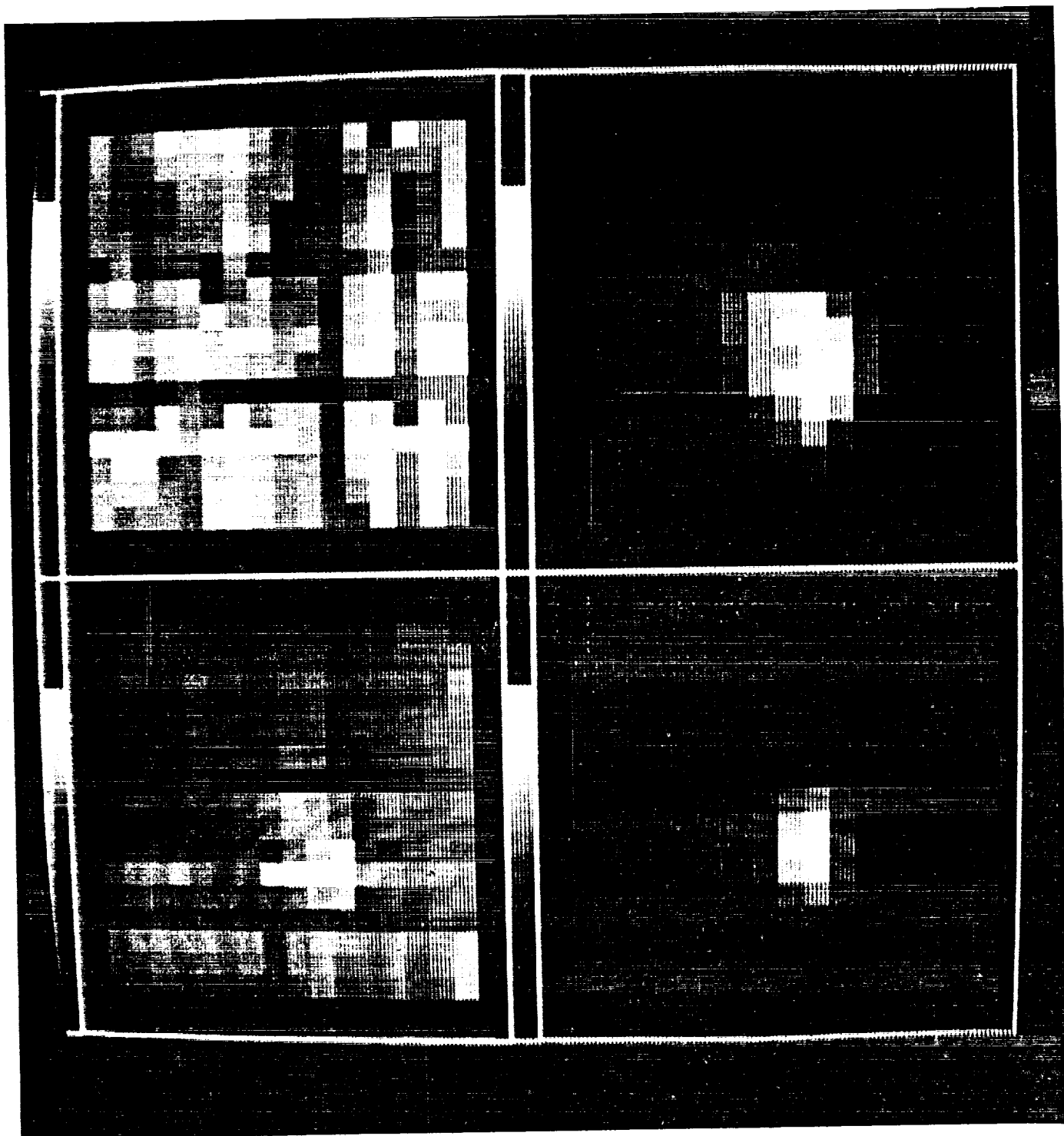


Figure 13

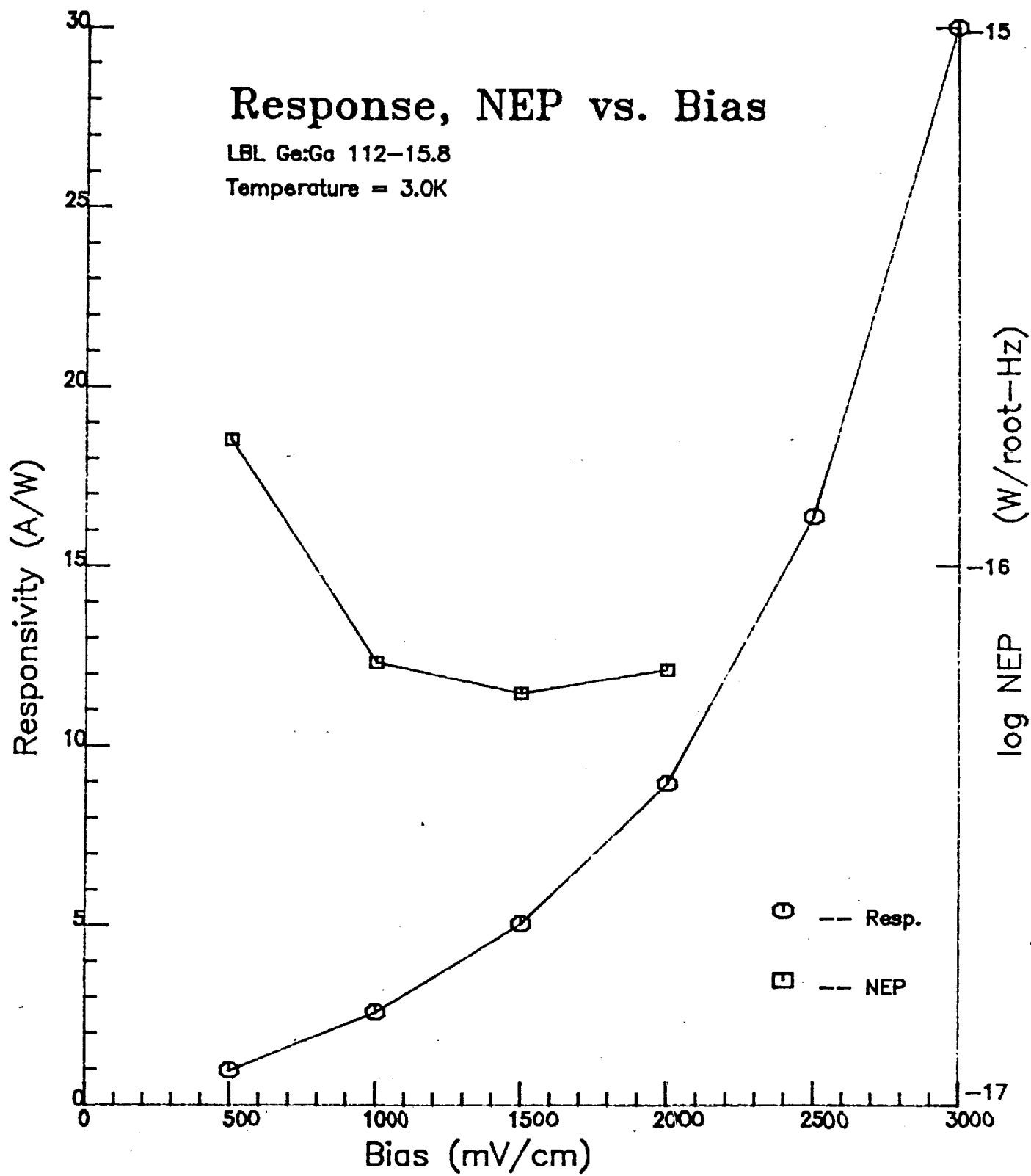


Figure 14

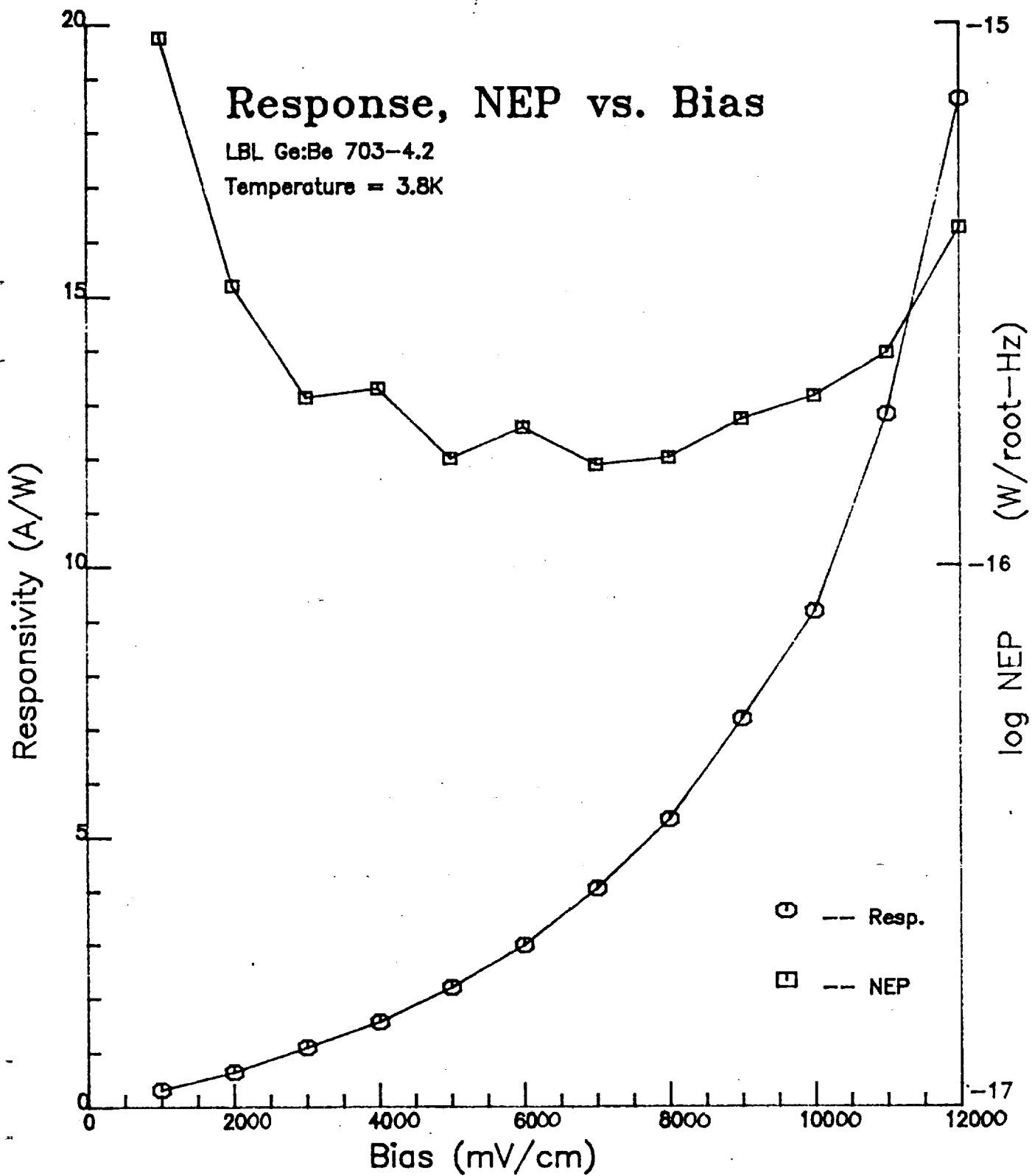
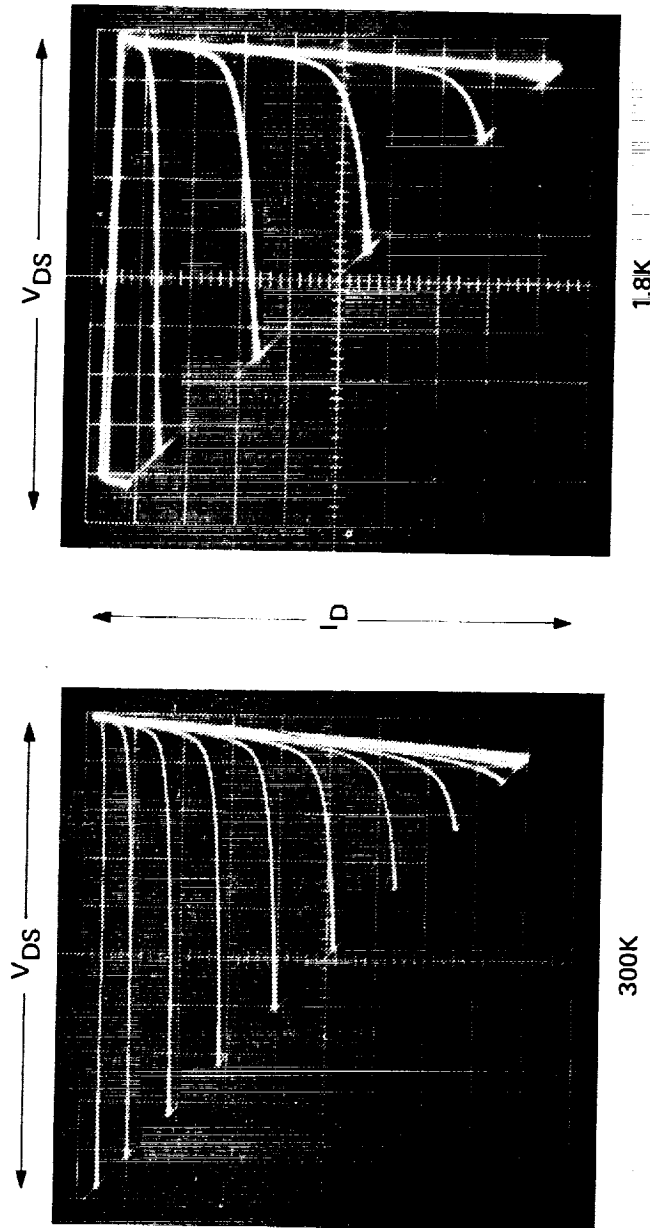


Figure 15

TIXM12 I-V CURVES

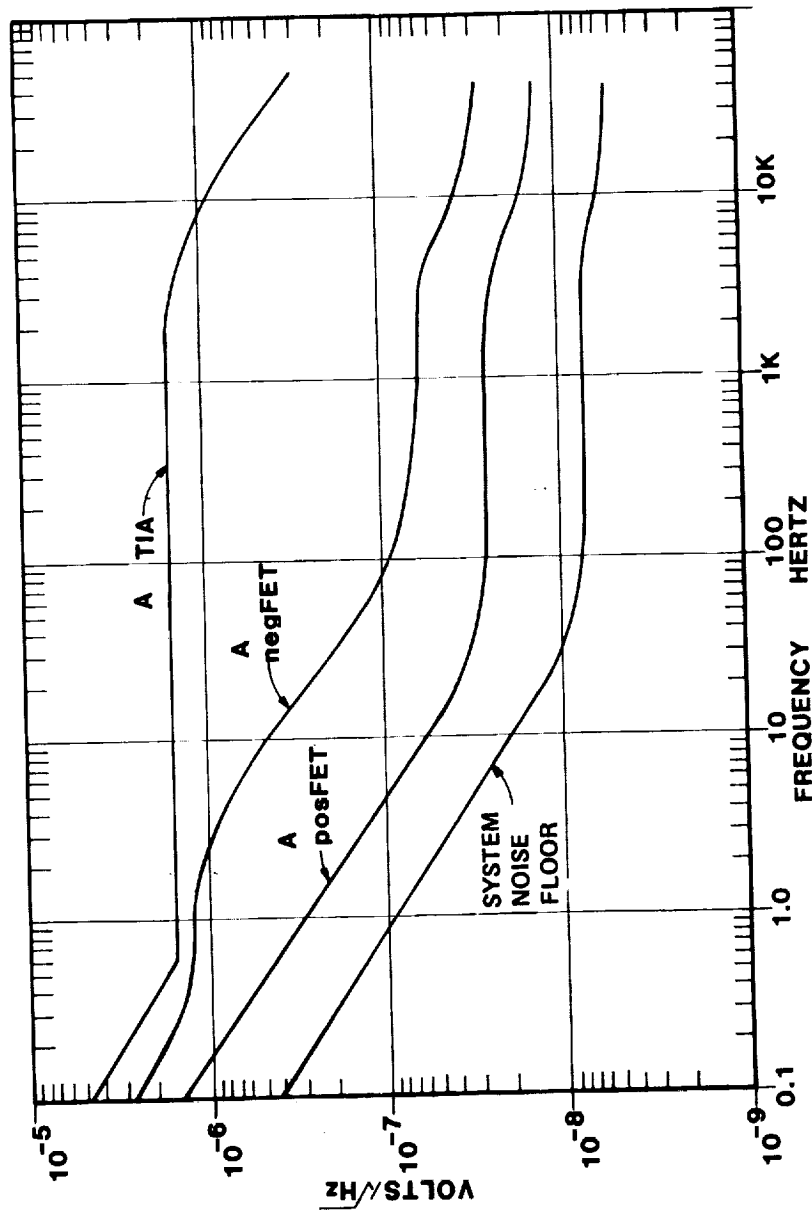
COMMON SOURCE MODE



HORIZONTAL SCALE = 2 V/MAJOR DIVISION
 VERTICAL SCALE = 1.0 mA/MAJOR DIVISION
 GATE CHANGES = 200 mV/STEP

Figure 16

TIXM12 NOISE SPECTRAL DENSITY CURVES



TEMP = 4K "A" CURVES DRAIN CURRENT = 68.7 μ A FET POWER = 93.2 μ W (EACH)

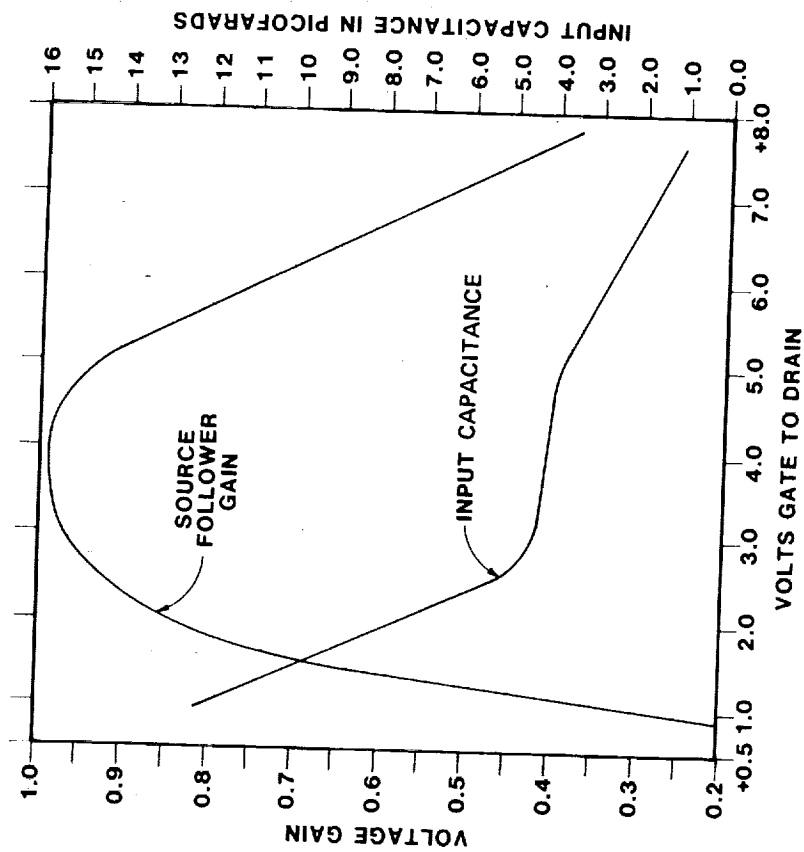
RI = 1.2E10-OHM

JOHNSON NOISE = $1.6 \mu\text{V} / \sqrt{\text{Hz}}$

A/N 2655

Figure 17

TIXM12 GAIN AND INPUT CAPACITANCE AS A FUNCTION OF GATE-TO-DRAIN VOLTAGE



TEMP=4K, DRAIN CURRENT=65 μ A, FET POWER DISSIPATION=116 μ W

A/N 2655

Figure 18

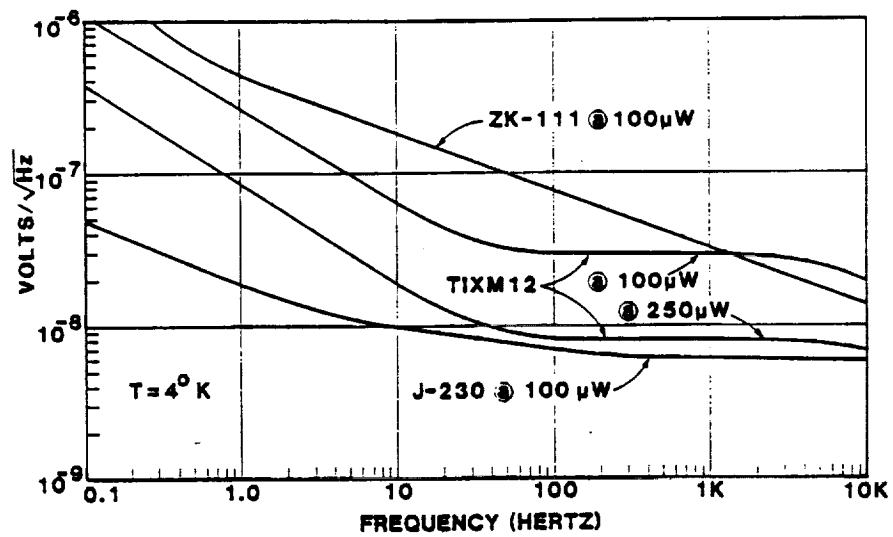


Figure 19

510-74 47
133815
p 6
cc 986725
N93-70646

UCSD IR DETECTOR DEVELOPMENT PROGRAMS

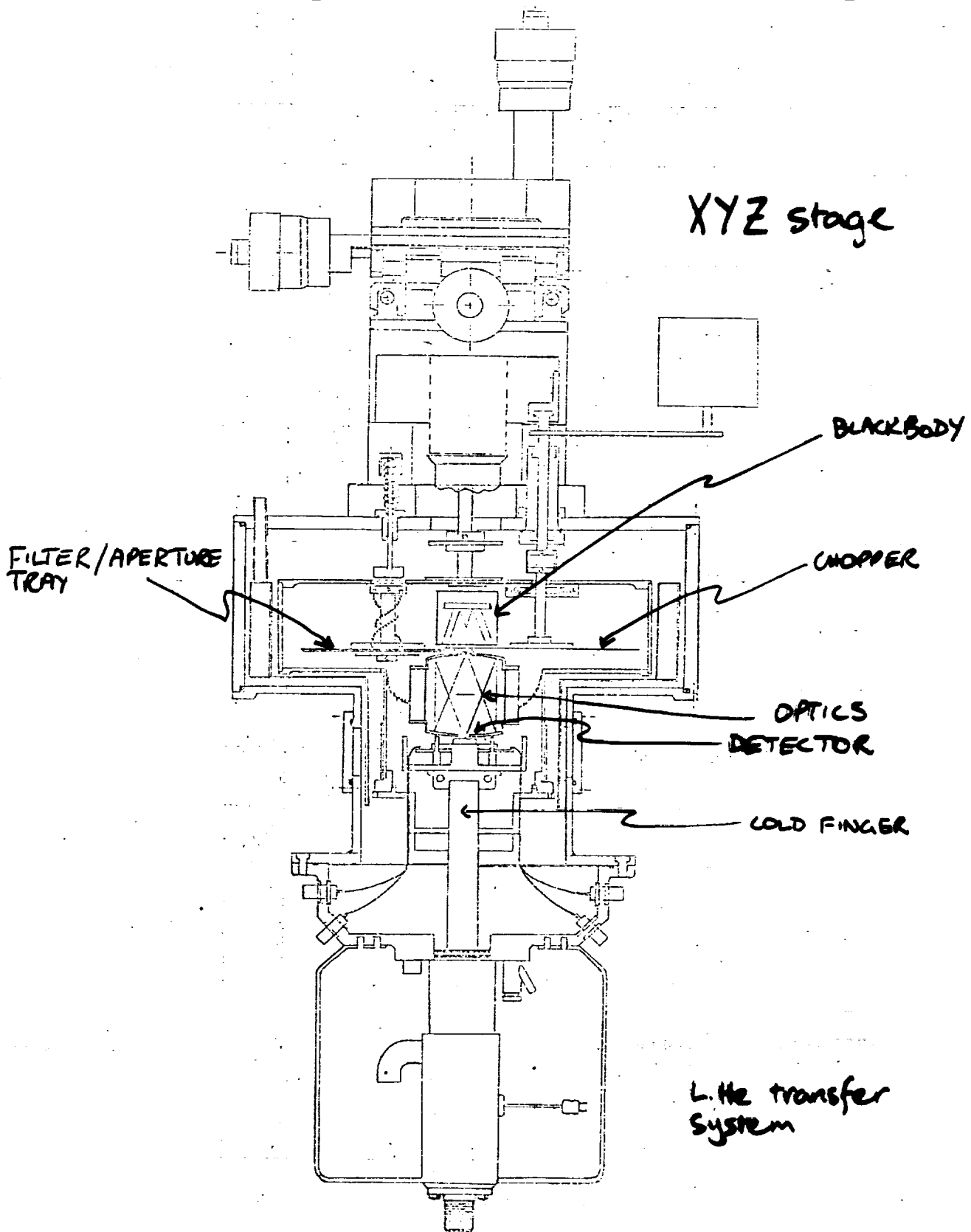
B. JONES, R. PUETTER, R. HEIR, A. SCHMIDT,
J. CASLER, S. NELSON, J. HUJSAK

CENTER FOR ASTROPHYSICS
AND SPACE SCIENCES

UNIVERSITY OF CALIFORNIA
MAIL CODE C-011
LA JOLLA, CA 92093

Funding:
NASA
University of California
MICRO
CALSPACE
Aerojet ElectroSystems Company

UCSD Low Background IR spot scanner



SPOT SCANNER PARAMETERS

- Independent control of 3 temperatures
 - ① Detector 2.7 \rightarrow 20 K NOM.
 - ② Optics/background 20 - 50 K NOM
 - ③ Blackbody 50 - 250 K NOM
- Stability ± 0.1 K
- Motion of on-axis optics $\left. \begin{matrix} X \\ Y \\ Z \end{matrix} \right\} \pm 12.5 \text{ mm}$
 $Z \pm 2.0 \text{ mm}$
- Reproducibility of motion $\pm 2.5 \mu\text{m}$
- Spot size ≤ 3 mil to 0.25 inch
- Chop frequency 0 - 500 Hz
- Filters 24 filter/aperture combinations
- Operation XYZ stage, chopper & temperature computer controllable
- 68 pin leadless carrier with 68 solid stainless steel micro triax feedthru's

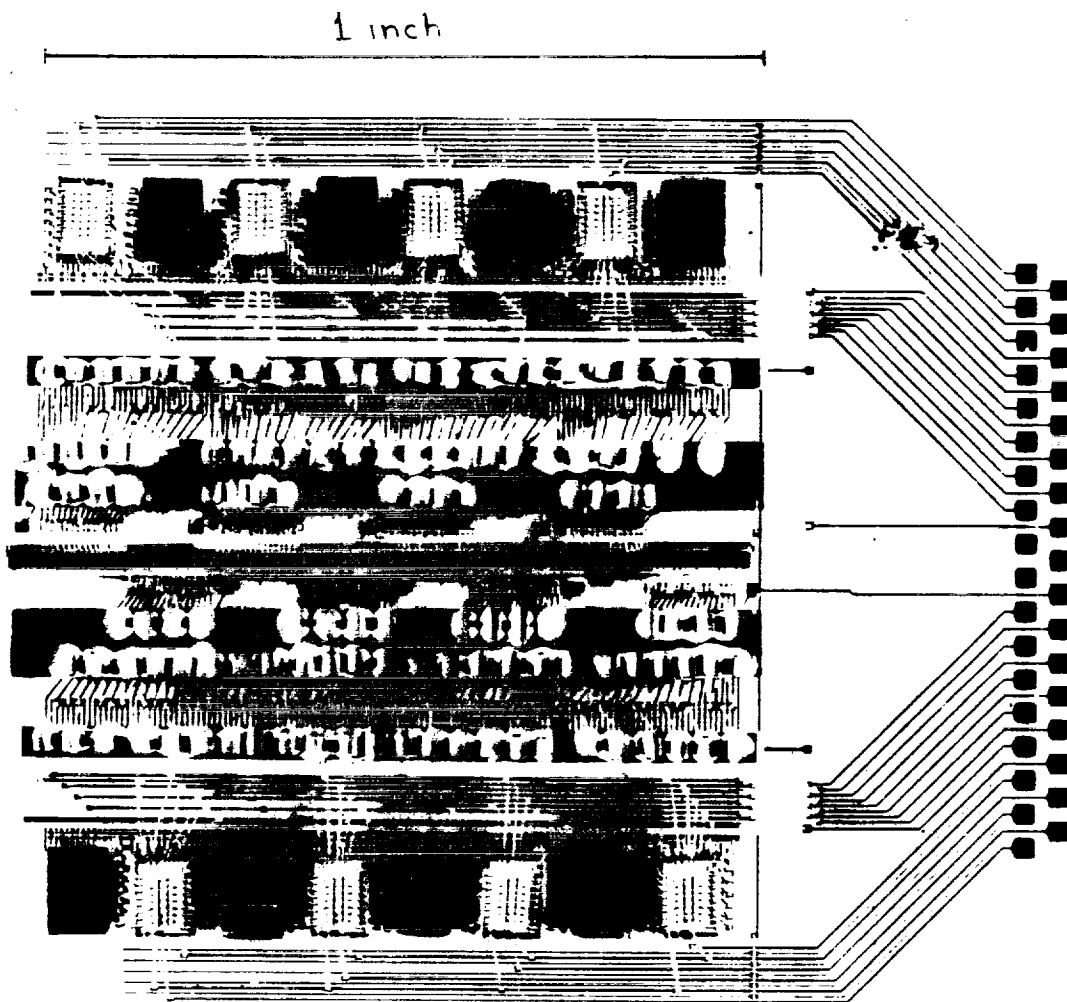
Planned CID testing

Full characterization including

- detector temperature
- pixel uniformity
- response nonlinearity as fn. of
 - background
 - frequency
 - bias
 - etc
- quantum efficiency
- read out noise as fn. of
 - bias voltages
 - clock timing
 - clock voltages
 - etc
- well size

Aerojet linear 128 element array

- material - silicon-bismuth
- geometry - detectors 6×20 mils, 8 mil centers
- read out - 8 MUX each 16 channel, CMOS, on focal plane, power $\leq 100 \mu\text{W}$ per MUX
- capacitance - 100 pf = well size $10^{10} e^-$ at 10v
- quantum eff - $\sim 40\%$
- temperature - $\sim 10\text{K}$
- noise - background noise lt under good ground based conditions at $R = \lambda/\Delta\lambda \sim 100$
- readout time - $\sim 25 \mu\text{s}$ per pixel.



511-35
133 816
P-12

Si:Bi ARRAY DETECTORS AND ASTRONOMICAL
APPLICATIONS OF THE GODDARD 10 MICRON CAMERA

Gerald Lamb, Daniel Gezari, and Peter Shu
NASA/Goddard Space Flight Center

Richard Tresch-Fienberg and Giovanni Fazio
Harvard-Smithsonian Center for Astrophysics

William Hoffmann
Steward Observatory, University of Arizona

N93-70647

NC94975

HG695612

A7852975

I. INTRODUCTION

An improved 4 - 18 micron array camera system has been developed at NASA Goddard Space Flight Center for astronomical photometry, using an Aerojet ElectroSystems Corp. 16 x 16 Si:Bi accumulation mode charge injection device (AMCID) which could be suitable for eventual low-background spaceflight applications. An astronomical observing program using this device has been carried out as a collaboration between NASA Goddard Space Flight Center (Infrared and Radio Astronomy Branch and Micro Electronics Branch), the Harvard-Smithsonian Center for Astrophysics, and Steward Observatory of the University of Arizona.

In 1983 the camera system was revised, and a new Aerojet Si:Bi array with 16 x 16 active pixels was obtained from NASA/Ames Research Center as part of a new scientific collaboration between the Ames and Goddard infrared array research groups. The 16 x 16 device had sufficiently good sensitivity, uniformity and noise characteristics to be used for successful observations at the Mt. Lemmon 60 and 61-inch telescopes in May 1983. Complete laboratory characterization of the 16 x 16 array will be carried out in summer of 1983. Initial results indicate that this detector has sensitivity and noise characteristics comparable to other devices from the same generation of Aerojet arrays.

II. ARRAY CAMERA SYSTEM DESCRIPTION

Si:Bi AMCID detector array characteristics and performance have been discussed in general by McCreight and Goebel (1981), in technical reports prepared by Aerojet for NASA Ames Research Center, and by Parry (1983). Prior to 1983, the detector used extensively in the Goddard camera was an Aerojet Si:Bi array with an 8 x 10 pixel active area, and several additional functioning rows and columns. A description of that system was given by Arens, Lamb, and Peck (1981).

The array, cryogenic MOSFET preamplifiers, focusing optics, and filter wheel mechanisms are housed in a liquid helium dewar and maintained at a temperature of approximately 10K. The detector operating temperature may be adjusted to optimize detector performance with a small heater attached to the array housing.

Operation of a single detector of the array and its associated cryogenic preamplifier is as follows. Infrared radiation incident on a detector element

is converted into a charge flux in the extrinsic semiconducting crystal. This charge flux is integrated in the detector accumulation capacitance and read out by a clock voltage pulse to the cryogenic MOSFET preamplifier. The MOSFET devices presently used have about $80 \text{ nV Hz}^{-1/2}$ voltage noise at 1 KHz.

The Goddard array camera system architecture is shown in Figure 1. The array is read out by clocking individual columns and scanning output signals from each row as follows. Each of the 16 parallel array detector output channels (one for each row) feeds a source follower MOSFET. When a column of pixels is read out by applying a -8.5 volt pulse to the read gate electrode, the charge generated by incident radiation during the integration is deposited onto the input capacitance (approximately 2 pF) of the appropriate MOSFET, yielding about 0.1 microvolt signal per electron. The signal goes to the correlated double sampler (CDS), a switching filter with the unique property of reducing the $1/f$ noise, the dominant noise source in the readout electronics. The output of the CDS is then digitized by a 12-bit analog-to-digital converter.

The pixels are sampled at a variable frame rate as high as 1000 Hz, generating thousands of individual frames of data for typical integrations of a few seconds. Motorola 68000 microprocessors sort and co-add these frames at each chopper sky position, and send the final summed images to an LSI 11/23 microcomputer for flat-fielding and other array processing operations. The LSI 11/23 also controls telescope chopping and nodding during astronomical observing. Image data and operational software are stored on a Winchester hard disk with floppy disk backup.

Optics to focus an image onto the array consist of paired field and relay lenses and appropriate aperture stops which create a well-defined beam. Lens pairs have been selected for use with f/27, f/35, and f/45 telescopes. The optics magnify or demagnify the image to place 2×2 pixels within the Airy diffraction disk at 10 microns. The size of each detector unit cell is $0.2 \times 0.2 \text{ mm}$, yielding pixels less than 1 arcsec on a side on telescopes with apertures greater than 2 meters. Two filter wheels permit the use of a variety of interference filter/blocker combinations. A tunable circular variable filter (CVF) with 5% bandwidth can also be installed in one of the filter wheel housings. The astronomical observations done to date have utilized four bandpass filters with effective wavelengths 8.3, 9.6, 11.2, and 12.4 microns and bandwidths between 0.25 and 0.9 micron. Wider bandpass filters are not used on warm, high background ground-based telescopes, since the detector wells fill faster than they can be read out.

Data acquisition during observing is controlled by system software programs which include a real-time display mode, which allows the observers to view bright infrared sources in real-time with the 10 micron camera for source acquisition, telescope pointing, focusing, etc. Individual images can be combined during the observations for background subtraction, gain matrix correction, and integration. Images are displayed as gray-scale pictures, with signal/noise statistics provided in real-time. This permits evaluation of the results as the observations progress. Spatial registration to reduce image blur when combining successive images of the same object is accomplished with a cross-correlation program, and smoothed images or contour maps are generated. Photometric calibration is done by comparison with images of IR standard stars.

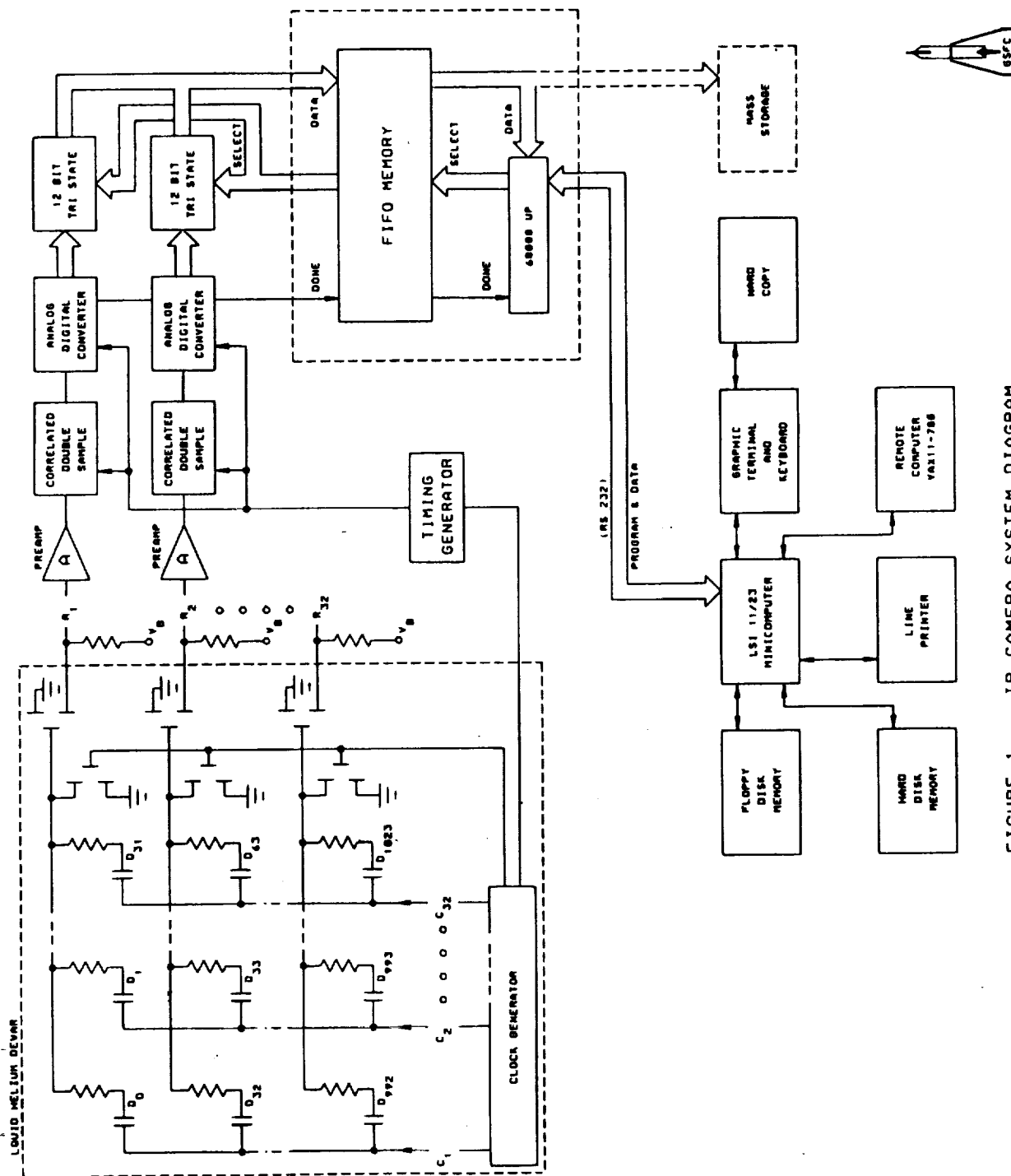


FIGURE 1. IR CAMERA SYSTEM DIAGRAM

III. DETECTOR AND CAMERA SYSTEM PERFORMANCE

Most of the laboratory or observational data we have obtained on the Goddard array camera system performance were obtained under high background conditions. Some of this discussion applies to laboratory testing of "sister" arrays of the same generation manufactured by Aerojet. These devices were not selected for optimal sensitivity, so the characteristics described in the following paragraphs should be taken as average (but not limiting) performance of present Si:Bi AMCID technology. For a general description of the testing program at Ames, and a discussion of Si:Bi AMCID array characteristics at low background, see McCreight and Goebel (1981).

Si:Bi is sensitive to infrared radiation at wavelengths between about 4 and 18 microns (Figure 2). This entire spectral range would be accessible from space; from the ground, atmospheric absorption limits the camera to observations between about 8 and 13 microns.

As the accumulation layer capacitance fills with photo-generated charge there is a gradual saturation seen as a decrease in small signal response and as a limit on DC level with increasing integration time. For the 16 x 16 Si:Bi array described here the limit appears at about 2×10^5 charges.

Table 1: Goddard Camera "16 X 16" Si:Bi Array Characteristics

Well Capacity = 2×10^5 electrons

Dark Current = 200 electrons sec^{-1}

Quantum efficiency = 5%

Responsivity = 0.5 Amp W^{-1}

Noise Equivalent Power = $4 \times 10^{-17} \text{ W Hz}^{-1/2}$ (zero background)

Optical Frequency Response = 200 Hz ($@ 10^9 \text{ photons sec}^{-1} \text{ pixel}^{-1}$)
 25 Hz ($@ 10^7 \text{ " " " "}$)

The net observed noise equivalent power (NEP) of any array detector element (not considering electronic readout noise) during operation is the sum of the incident background radiation noise and the detector dark current shot noise.

$$\text{NEP} = \frac{hc}{\lambda} \frac{1}{\eta} [2(\eta\phi + \phi)]^{1/2} \text{ W Hz}^{-1/2}$$

where h = Planck's constant, c = speed of light, η = quantum efficiency, ϕ = flux (photons/sec), ϕ = dark current (charge/sec), and I = integration time.

The camera system responsivity is approximately 0.5 Amp W^{-1} , based on observations of infrared standard stars. This is about a factor of 10 lower than the responsivity of an ideal system (McCreight and Goebel 1981) and can be accounted for by non-optimum operating conditions (detector temperature, read and store voltages, clock rate, etc.) and the low quantum efficiency of these specific devices (estimated to be about 5% between 8 and 13 microns).

The quantum efficiency η for our case is calculated as follows:

$$\eta(\lambda) = \frac{(\text{Charge collected})}{(\text{Photons incident})}$$

$$= \frac{(\Delta B_{\text{out}} G_{\text{cds}} C e^{t/\tau}) / (G_{\text{MOS}} G_{\text{pa}} q)}{T A \Omega \Phi I}$$

where ΔB_{out} = output bin difference (signal level), G_{cds} = CDS Gain, $C = -19$ detector capacitance, G_{MOS} = MOSFET gain, G_{pa} = preamp gain, $q = 1.6 \times 10^{-19}$ Coulomb, τ = MOS gate time constant, t = clamp sample time, T = system transmission, A = detector area, Ω = solid angle, Φ = flux (photons $\text{sec}^{-1} \text{cm}^{-2} \text{Sr}^{-1}$), and I = integration time.

The well capacity of the detectors, which impacts noise performance and dynamic range, is about 10^5 electrons. Si:Bi detector responsivity and signal/noise are functions of detector operating temperature, read and store voltages, sampling frequency, chopping frequency, and wavelength and level of incident illumination. The relative response of Si:Bi detector material and the present 16 x 16 array camera system is shown plotted vs. wavelength (Figure 2), detector temperature (Figure 3), frame rate (Figure 4) and chopping frequency (Figure 5).

Based on our observations of NGC 7027 at the 90-inch telescope with typically 10% bandwidth interference filters, the noise equivalent flux density of the camera system was about NEFD = 2.5 Jy in 2 minutes (1 Jy = $10^{-26} \text{ W m}^{-2} \text{ Hz}^{-1}$). In this case the system is background noise limited by the warm telescope and sky at just above the MOSFET noise limit. The MOSFET noise is kept below the background noise by choosing an appropriate sampling rate. At low background, dark current limited detector NEP for this generation of Aerojet arrays was found to be as low as a few times $10^{-17} \text{ W Hz}^{-1/2}$.

Detector gain varies by no more than 15% among pixels in a row, but by as much as a factor of 2 between rows in the array, reflecting differences in input capacitance of the MOSFET preamplifiers and the total amplifier gain associated with each channel. Since at least one gain matrix is generated for each filter band each night, uniformity and stability do not significantly constrain the photometric accuracy attainable with the array camera system.

Si:Bi AMCID array technology poses some detector performance problems which are not yet fully understood. These include: 1) poor frequency response at low backgrounds (not necessarily a fundamental problem for space telescope applications except those measurements involving time-fluctuating signals) due to trapping at low light levels (photo-electrons being preferentially absorbed by bulk or interface trapping rather than being read out), 2) limited well capacity (present maximum about 10^6 electrons, not a problem for low background applications), 3) inherent cross-talk between columns of as much as 20% (can be corrected in data analysis or possibly with new guard ring technology), 4) cryogenic FET noise (can be reduced in readout noise limited cases by selection of alternate FET technology and appropriate operating temperature), and 6) image persistence or "response lag" (we observe 1% residual signal in images on and off source at high background; others have found several 10's of percent, c.f. Fowler 1983).

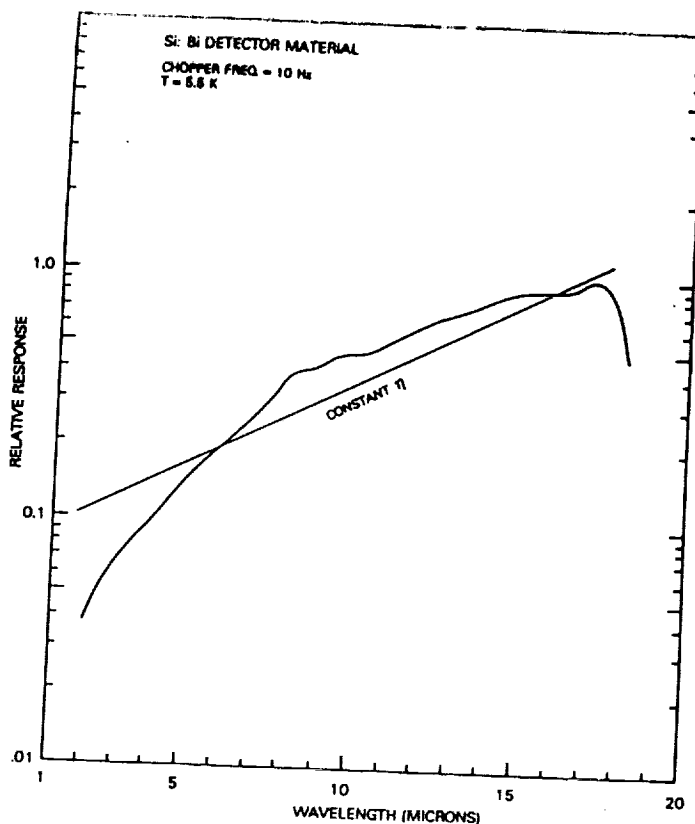


Figure 2: Relative response of Si:Bi detector material vs. wavelength. The sample is not one of the arrays used in the Goddard 10 micron camera, but is characteristic of this detector material. The "constant η " line indicates constant detector response per photon vs. wavelength, normalized for incident photon energy.

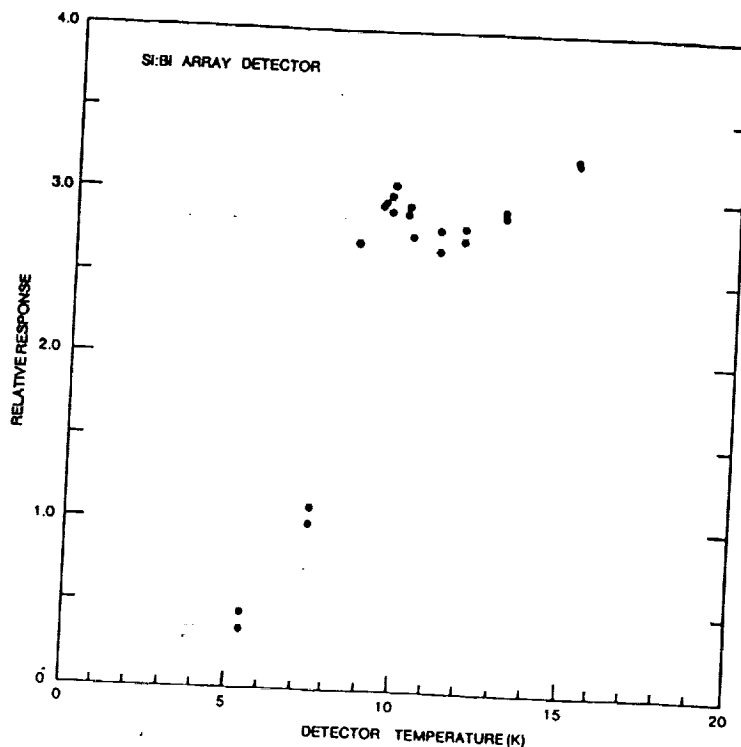


Figure 3: Relative response vs. detector temperature of an early 3 x 3 pixel Aerojet array used in the Goddard 10 micron camera. This dramatic temperature dependence has not been reproduced in initial tests of the 16 x 16 array.

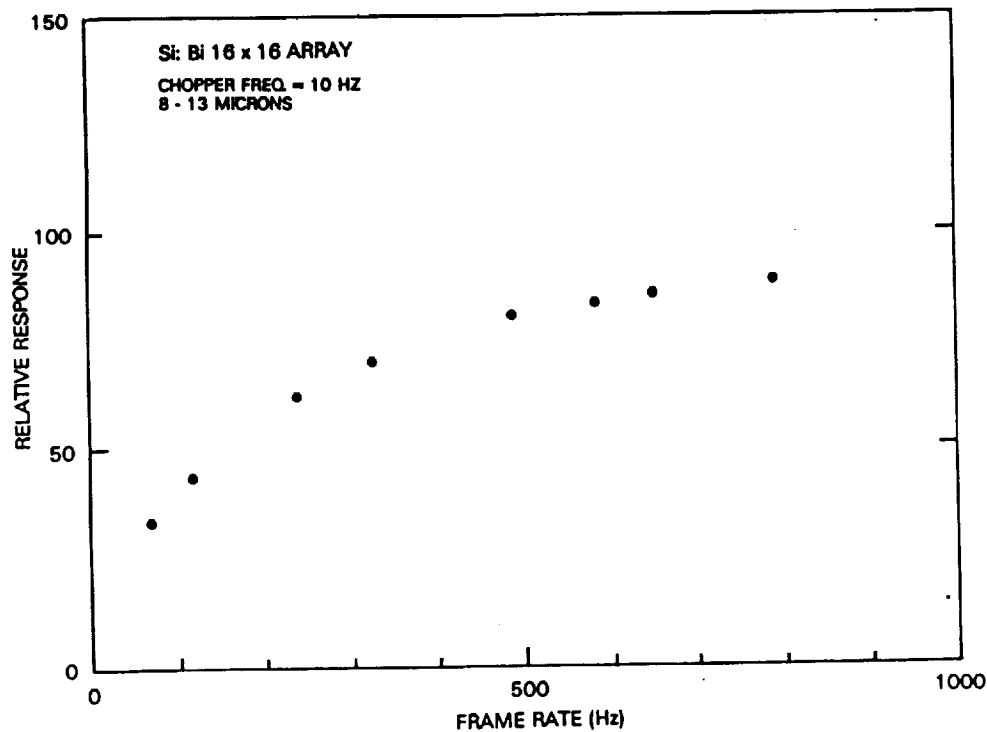


Figure 4: Relative response vs. frame rate for the 16 x 16 pixel array as measured in the laboratory. Typically, the camera system is operated at frame rates between 400 and 800 Hz.

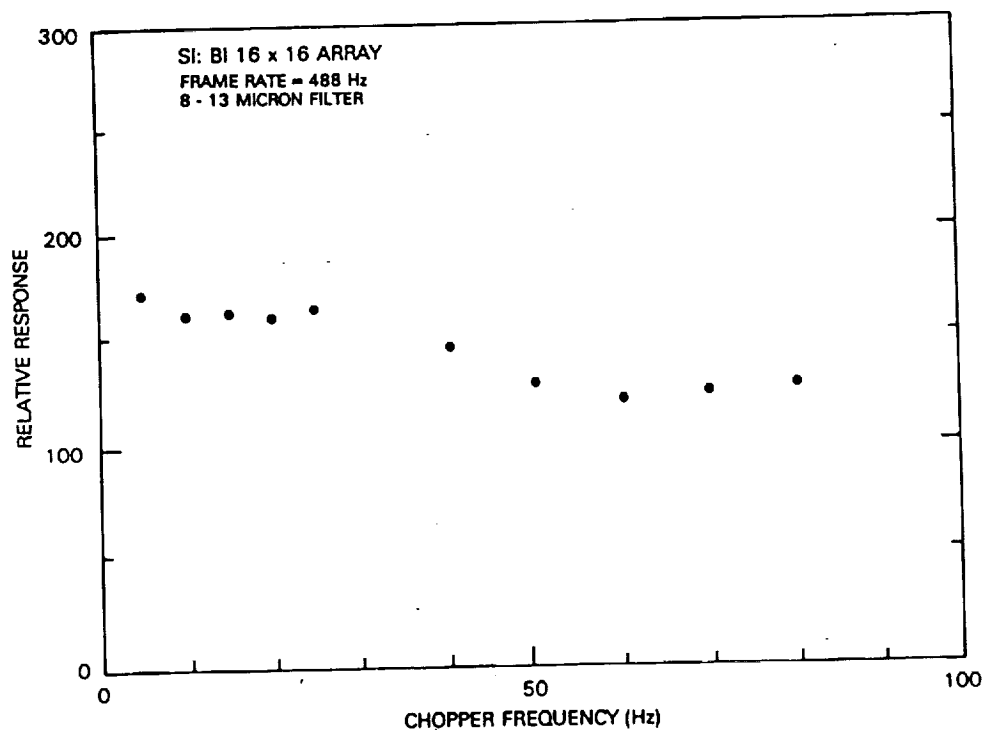


Figure 5: Relative detector response vs. chopper frequency for the 16 x 16 pixel array as measured in the laboratory. Typically, the camera system is operated during astronomical observations with the telescope secondary mirror oscillating in a square wave pattern at 5 to 10 Hz.

IV. OBSERVATIONAL APPLICATIONS AND ASTRONOMICAL RESULTS

The first astronomical observations with the Goddard array camera were made in March 1981 on the Mt. Lemmon 61-inch telescope. At that time, the largest group of contiguous active pixels was 2×10 in size. The successful operation of the camera was demonstrated, and images of Orion BN/KL, IRC+10216, Jupiter, and several stars were obtained (Arens *et al.* 1981).

In November 1981, the 8×10 array was used successfully at the Infrared Telescope Facility (IRTF) on Mauna Kea. The Orion BN/KL region was mapped at 12.4 microns; our images had better relative positional accuracy and showed more detail than the earlier map from Mt. Lemmon (Figure 6). Images of Orion IRC2 at 8.3 and 9.6 microns were also obtained. Our results are very similar to those obtained with a single detector published by Downes *et al.* (1980), both in the number and arrangement of compact sources and their relative intensities, demonstrating that the new CID technology could be used to make reliable astronomical measurements. The nucleus of Seyfert galaxy NGC 1068 was detected (Figure 7), but there was insufficient spatial resolution to resolve any of the features seen in a recent radio map from the Very Large Array (Van der Hulst, Hummel, and Dickey 1982). The brightest planetary nebula in the infrared, NGC 7027, was observed at 12.4 microns at the IRTF. However, spatial coverage of the central 10 arcsec of the nebula was incomplete.

In May 1982, the 10 micron camera was taken to the Steward 90-inch telescope at Kitt Peak National Observatory. NGC 7027 was imaged at 8.3, 9.6, and 12.4 microns (Tresch-Fienberg *et al.* 1983, Arens *et al.* 1983). Due to an electronic problem in the dewar, the largest contiguous block of pixels during these observations was 5×10 pixels. In order to cover NGC 7027 adequately, a composite of 12 images was generated. We have compared the infrared images (Figure 8a) to a high resolution radio map (Figure 8b) and to optical images (Figure 8c) taken with a charge-coupled device (CCD) camera (Figure 9). The dust and gas distributions in the ionized zone (the HII region) are found to be similar on a scale as small as 2 arcsec, confirming and extending earlier findings on the extent to which the dust and gas are mixed (Becklin, Neugebauer, and Wynn-Williams 1973).

By studying the radio, infrared, and optical intensity distributions, we find that two distinct populations of dust are required to explain the properties of the infrared radiation from NGC 7027. The depth of an apparent absorption trough in the spectrum of this object at 9.6 microns is anti-correlated with local enhancements in extinction, while the intensity of 9.6 micron radiation is greatest in these same regions. As suggested by an earlier investigation into the variation of the 8-13 micron spectrum with position in the nebula (Jones *et al.* 1980), and by measurements which imply that NGC 7027 is carbon-rich (Perinotto *et al.* 1980), we believe that the dip in the spectrum of this object at 9.6 microns is not caused by the silicate absorption seen in many nebulae. Instead, we propose that our results may be understood in terms of two populations of non-silicate grains. One is a patchy distribution which contributes to the local variation of extinction across the nebula, while the other is more uniformly distributed and responsible for unidentified emission features near 8 and 11 microns.

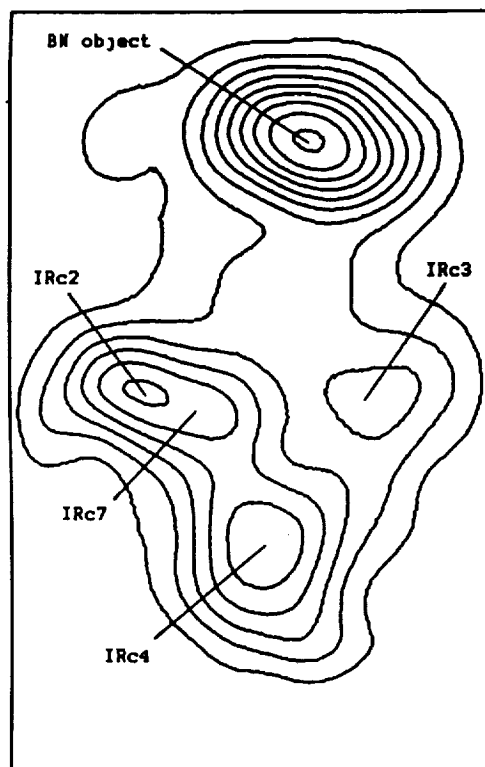


Figure 6: Smoothed intensity contours of the Orion BN/KL star-formation region at 12.4 microns. This map is a composite of ten 8 x 10 pixel images obtained on the 3-meter IRTF in November 1981. The area shown is 21.2 x 13.4 arcsec in size (NS x EW). North is at the top; east is at the left.

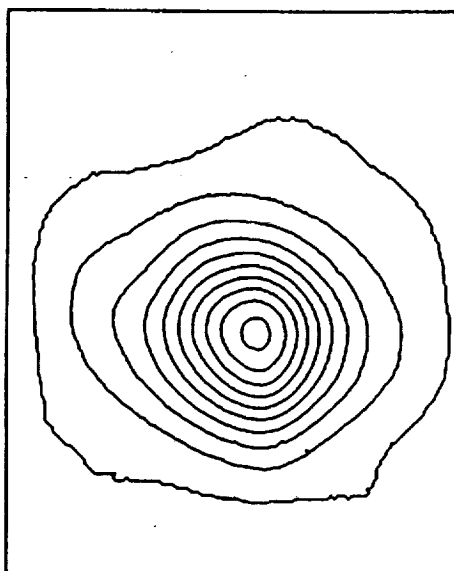


Figure 7: Smoothed intensity contours of the nucleus of Seyfert galaxy NGC 1068 at 8.3 microns. This 8 x 10 pixel image was obtained on the IRTF in November 1981, and the contour levels are 10%, 20%, ... 100% of peak intensity. The area shown is 7.9 x 6.3 arcsec (NS x EW). The orientation is the same as that of Figure 6.

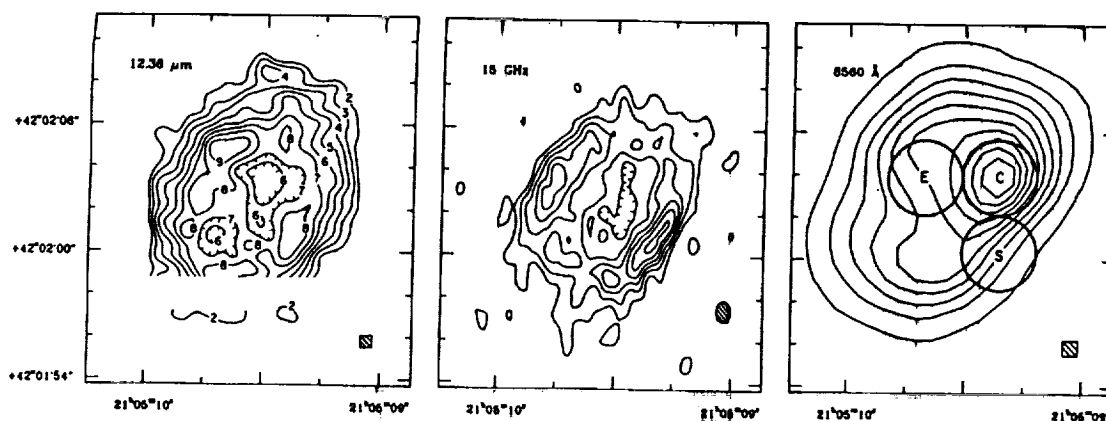
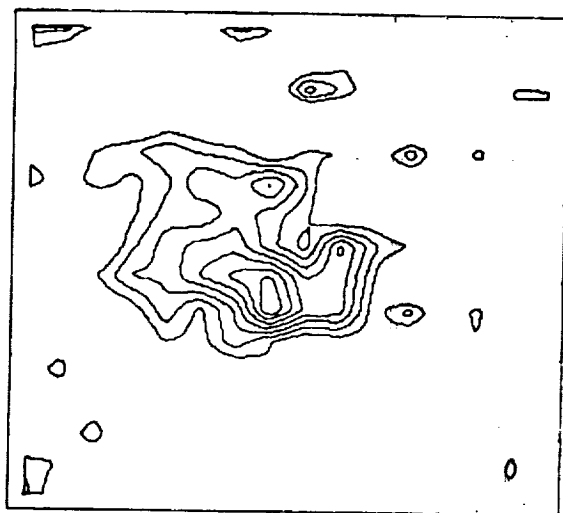


Figure 8(a): Planetary nebula NGC 7027 image at 12.4 microns taken with the Goddard array camera. The infrared map is a composite of twelve 5 x 14 pixel images obtained at the Steward Observatory 90-inch telescope in May 1982. The contours are labeled in units of $3 \times 10^{-18} \text{ W m}^{-2} \text{ Hz}^{-1} \text{ sterad}^{-1}$. The hatched square represents one 0.58×0.58 arcsec pixel.

Figure 8(b): 15 GHz, radio map obtained with the synthesized beam shown in the hatched oval, is taken from Harris and Scott (1976). The contour interval is 290K (brightness temperature).

Figure 8(c): 8560 Angstrom optical image obtained in September 1982 with the Center for Astrophysics CCD camera on the 24-inch telescope of the F. L. Whipple Observatory. The contours represent 10%, 20%, ...100% of peak intensity. The hatched square represents one 0.73×0.73 arcsec CCD pixel.

BD30_144 BD30_144.GEOM.1



BD30_221 BD30_221.GEOM.1

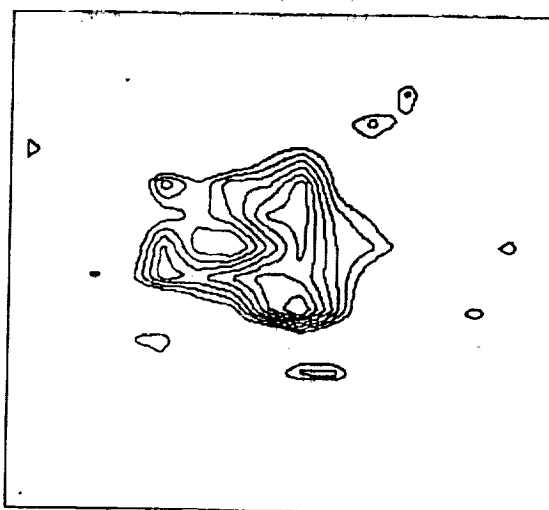


Figure 9: Planetary nebula BD+30 3639 at 8.3 and 12.4 microns. These images are the average of eight pictures each obtained with the 16 x 16 pixel Goddard camera in May 1983 on the LPL 61-inch telescope on Mt. Bigelow. The images are not yet flat-fielded, nor have the pictures been cross-correlated to minimize blur during the averaging process. Each pixel subtends 1.3×1.3 arcsec on the sky.

In April and May 1983, the new 16 x 16 pixel array was first used for astronomical observations at the Mt. Lemmon 60 and 61-inch telescopes. All but 2 of the 256 pixels in this array are active. Diffraction limited images of planetary nebulae BD+30 3639 (Figure 9) and NGC 6790 were obtained at the 61-inch telescope in our four filter bands between 8.3 and 12.4 microns. A series of laboratory tests are presently underway at Goddard to optimize the performance of this device under both high and low background conditions. Photometric accuracy, spatial uniformity, and stability of the camera system are of particular interest to astronomers. Photometric accuracy is estimated by comparing observations of many standard stars in each filter band. Results from the May 1982 90-inch run, for which we have the most standard star data, indicate a relative photometric accuracy of 10%, limited by variations in battery voltages used to power the readout clock. Since more stable low-noise supplies are available, this is not a limiting value.

Uniformity and reproducibility are found by studying flat-field (gain) matrices for the array detectors, which are generated during the observations each night for each filter by taking several integrations on source-free regions of the sky at 1 and 2 airmasses. Integrations at each position are averaged, and the 1 airmass matrix is subtracted from that at 2 airmasses. The difference matrix is normalized to a reference pixel. The result is an array of numbers representing differences in gain among the detector's pixels. An image produced with the appropriate background subtraction is then multiplied by the gain matrix and is ready for absolute calibration.

The Goddard array camera system will be evaluated under low background conditions in the laboratory to rigorously determine the dark current, readout noise, quantum efficiency, dynamic range, linearity, cross-talk, and uniformity of response. The camera electronics system will be further upgraded to provide more resolution in the analog-to-digital conversion and more compact and rugged instrument packaging. Other areas of concern for future space applications include array reliability, radiation hardening, mechanical durability, and electronic packaging for space qualification. Techniques of array fabrication have been developed and applied in the Goddard Micro Electronics Laboratory, and we expect to have several in-house fabricated custom arrays operational within the next year.

ACKNOWLEDGEMENTS

Craig McCreight is a primary collaborator in the technical development and astronomical application of the new 16 x 16 array in the Goddard camera. John Arens and Michael Peck, both now at the Space Sciences Laboratory of the University of California, Berkeley, were leading members of the group which developed the original Goddard 10 micron camera and made astronomical observations with it in 1981 and 1982. We thank Chris Parry and Aerojet ElectroSystems Corp. for cooperation in obtaining array detectors. Harvey Moseley has provided many useful suggestions. Ramesh Sinha and Jeffrey Bowser of Systems and Applied Science Corp. have contributed actively to the development of the camera system software. During the initial development of the Goddard 10 micron camera, we obtained valuable assistance from Bob Pernic at Yerkes Observatory, Matt Greenhouse, Marcia Rieke, and the staff of the Steward Observatory 90-inch telescope, and Charlie Telesco, Eric Becklin, and the staff of the NASA Infrared Telescope Facility.

REFERENCES

- Arens, J. F., Lamb, G. M., Peck, M. C., Fazio, G. G., and Hoffmann, W. F. 1981, abstract, B. A. A. S., 13, #2.
- Arens, J. F., Lamb, G. M., and Peck, M. C. 1981, Proc S.P.I.E., 280, 61.
- Arens, J. F., Lamb, G. M., Peck, M. C., Moseley, H., Hoffmann, W. F., Tresch-Fienberg, R., and Fazio, G. G. 1983, (submitted to Ap. J.).
- Becklin, E. E., Neugebauer, G., Wynn-Williams, C. G. 1973, Ap. Lett., 15, 87.
- Downes, D., Genzel, R., Becklin, E. E., and Wynn-Williams, C. G. 1980, Ap. J., 244, 869.
- Fowler, A., 1983, Proc. Infrared Detector Workshop, NASA Ames Research Center, (C. McCreight, ed.).
- Harris, S. and Scott, P. F. 1976, M.N.R.A.S., 175, 371.
- Jones, B., Merrill, K. M., Stein, W., Willner, S. P. 1980, Ap. J., 242, 141.
- McCreight, C. R. and Goebel, J. H. 1981, Appl. Optics, 20, 3189.
- Parry, C., 1983, Proc. Infrared Detector Workshop, NASA Ames Research Center, (C. McCreight, ed.).
- Perinotto, M., Panagia, N., and Benvenuti, P. 1980, Ast. & Ap., 85, 332.
- Tresch-Fienberg, R., Fazio, G., Arens, J. F., Peck, M. C., Lamb, G. M., Moseley, H., Hoffmann, W. F., 1983, B. A. A. S., 14, #3.
- Van der Hulst, J. M., Hummel, E., Dickey, J. M. 1982, Ap. J. Letters, 261, L59.

A MOSAIC INFRARED SENSOR FOR SPACE ASTRONOMY

PRINCIPAL INVESTIGATOR: DR. ASHOK K. SOOD

NASA PROGRAM MANAGER DR. NANCY BOGGESS

CONTRACT NO. NASW-3688

512-74 48
133817
p. 29.
N93-70648 856

PROGRAM OBJECTIVES

- THEORETICAL/EXPERIMENTAL EVALUATION OF HgCdTe DETECTOR ARRAYS (1 TO 5 μm) FOR SPACE ASTRONOMY APPLICATIONS
- ANALYZE LOW BACKGROUND HgCdTe/CCD COUPLING SCHEMES FOR LOW TEMPERATURE SPACE ASTRONOMY
- TEST AND EVALUATE EXISTING SILICON CCDs AT TEMPERATURE BELOW 77 K

F 6336

PROGRAM TEAM

ASHOK SOOD
PRINCIPAL INVESTIGATOR

DETECTOR
DEVELOPMENT

DR. PETER ZIMMERMANN
DR. HO CHUNG

LOW TEMPERATURE
DETECTOR/CCD
COUPLING SCHEMES

DR. SATO IWASA
DR. NEAL BUTLER
MR. JIM STOBIE
MR. CHIP MARSHALL

F 6344

DETECTOR PERFORMANCE STATUS

F 3408

MW DETECTORS

- THEORETICAL LIMITATIONS
- MEASURED PERFORMANCE

SW DETECTORS

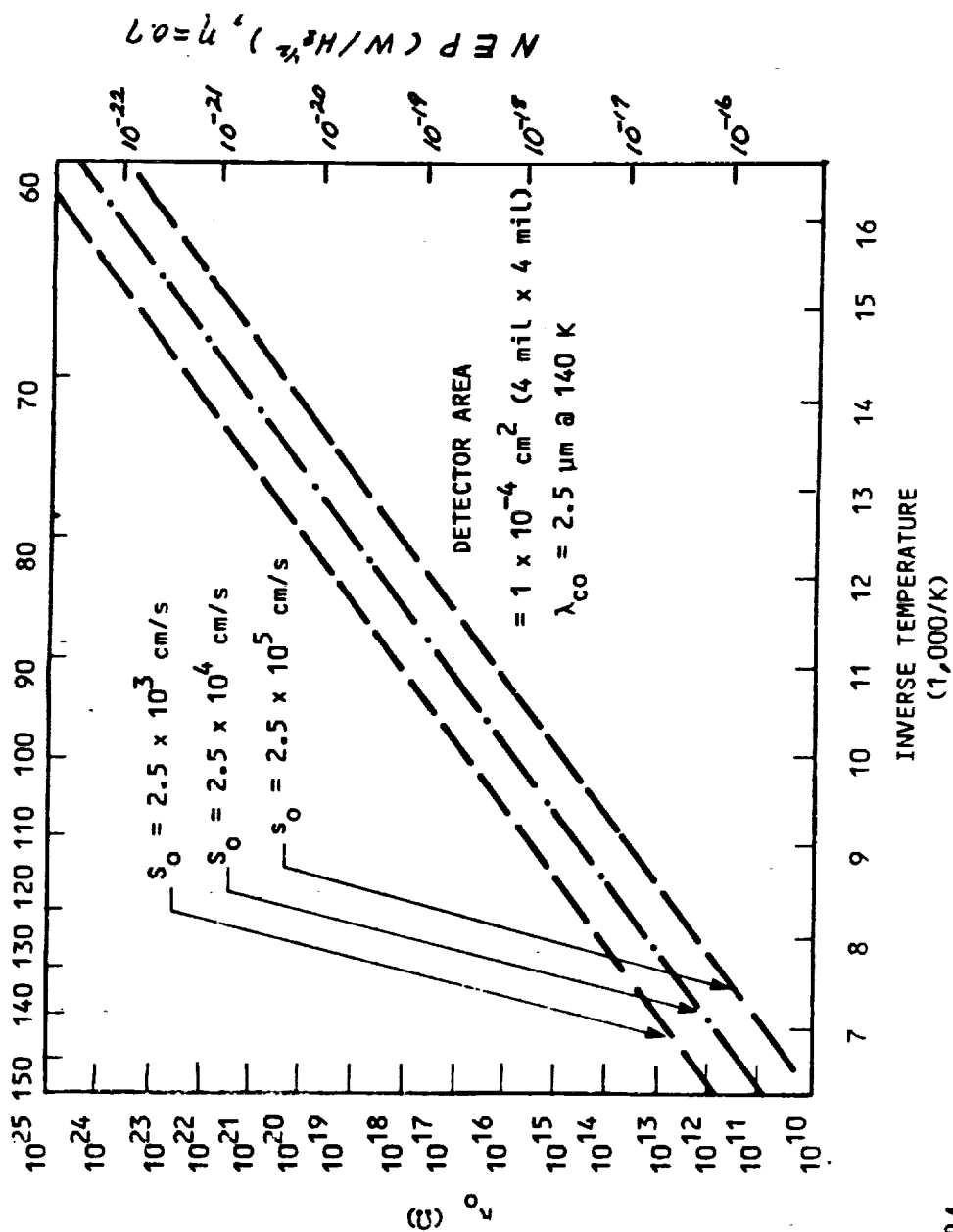
- THEORETICAL LIMITATIONS
- MEASURED PERFORMANCE

PREAMPLIFIER DEVELOPMENT

SUMMARY

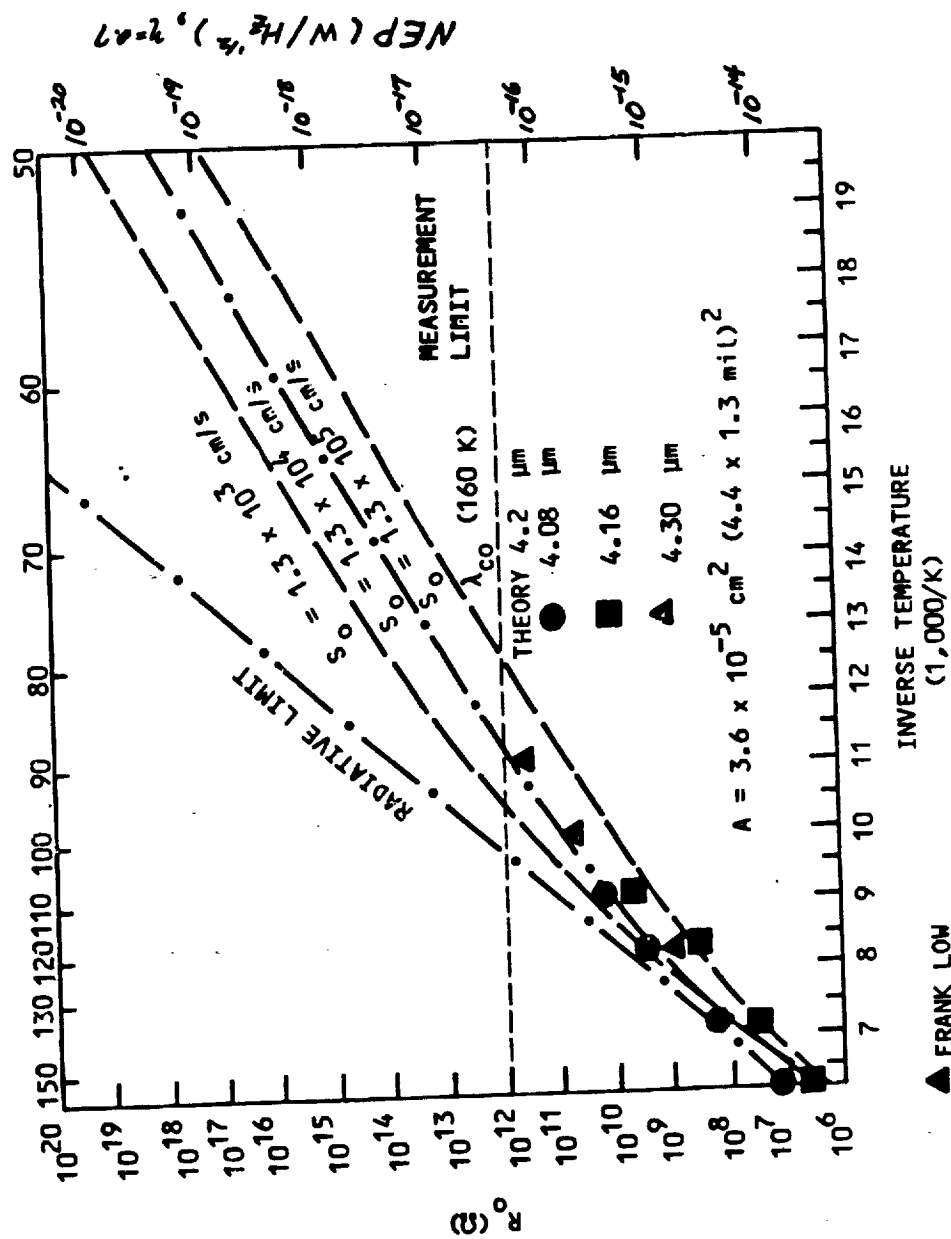
PLANS

HIGH R_0A PRODUCTS ARE PROJECTED FOR SW HgCdTe DIODES AT LOW TEMPERATURES

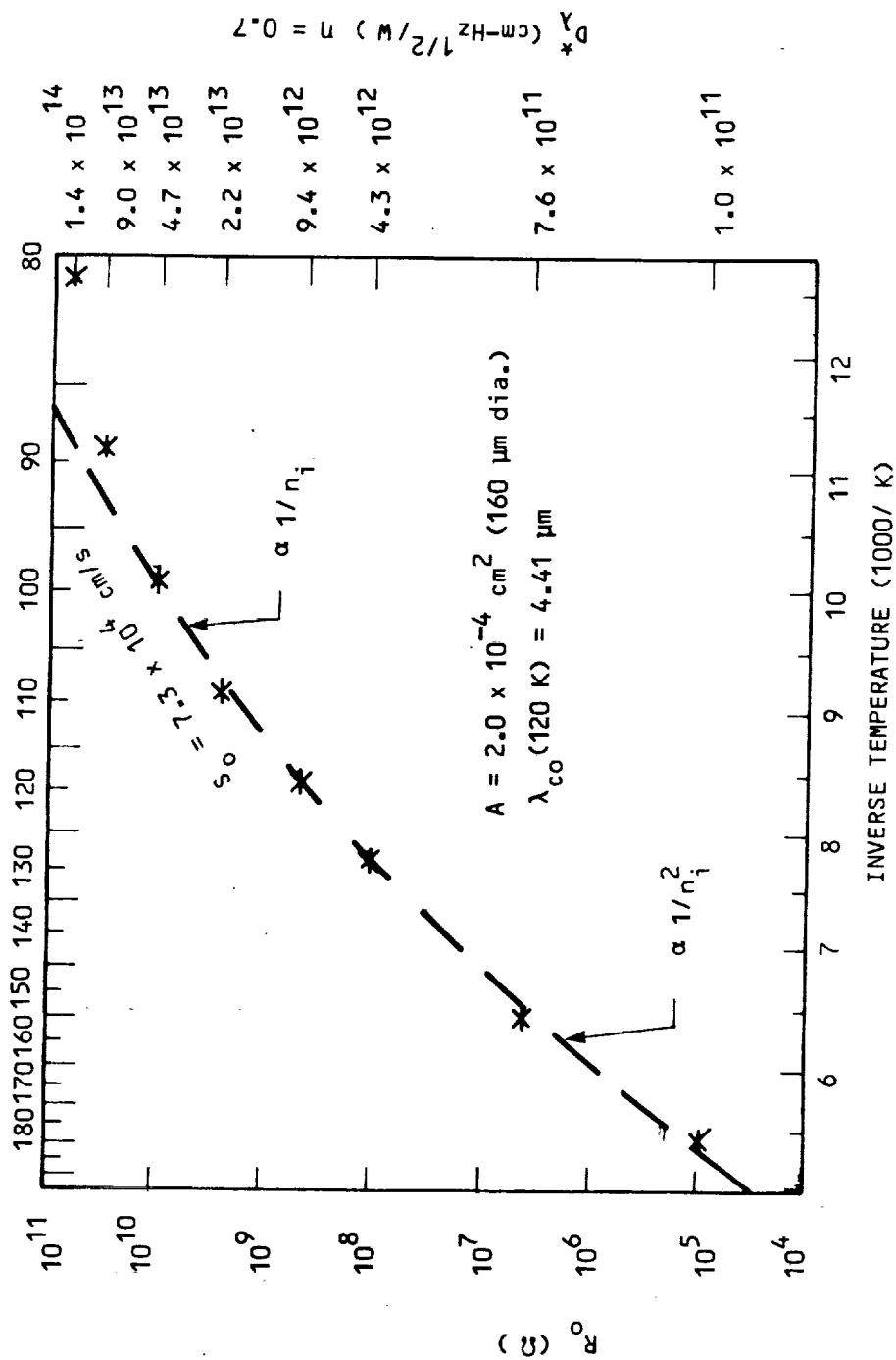


F 6204

THEORETICAL AND PRACTICAL MW HgCdTe PV PERFORMANCE
SHOW HIGH R_{0A} PRODUCTS ACHIEVABLE AT LOW TEMPERATURES

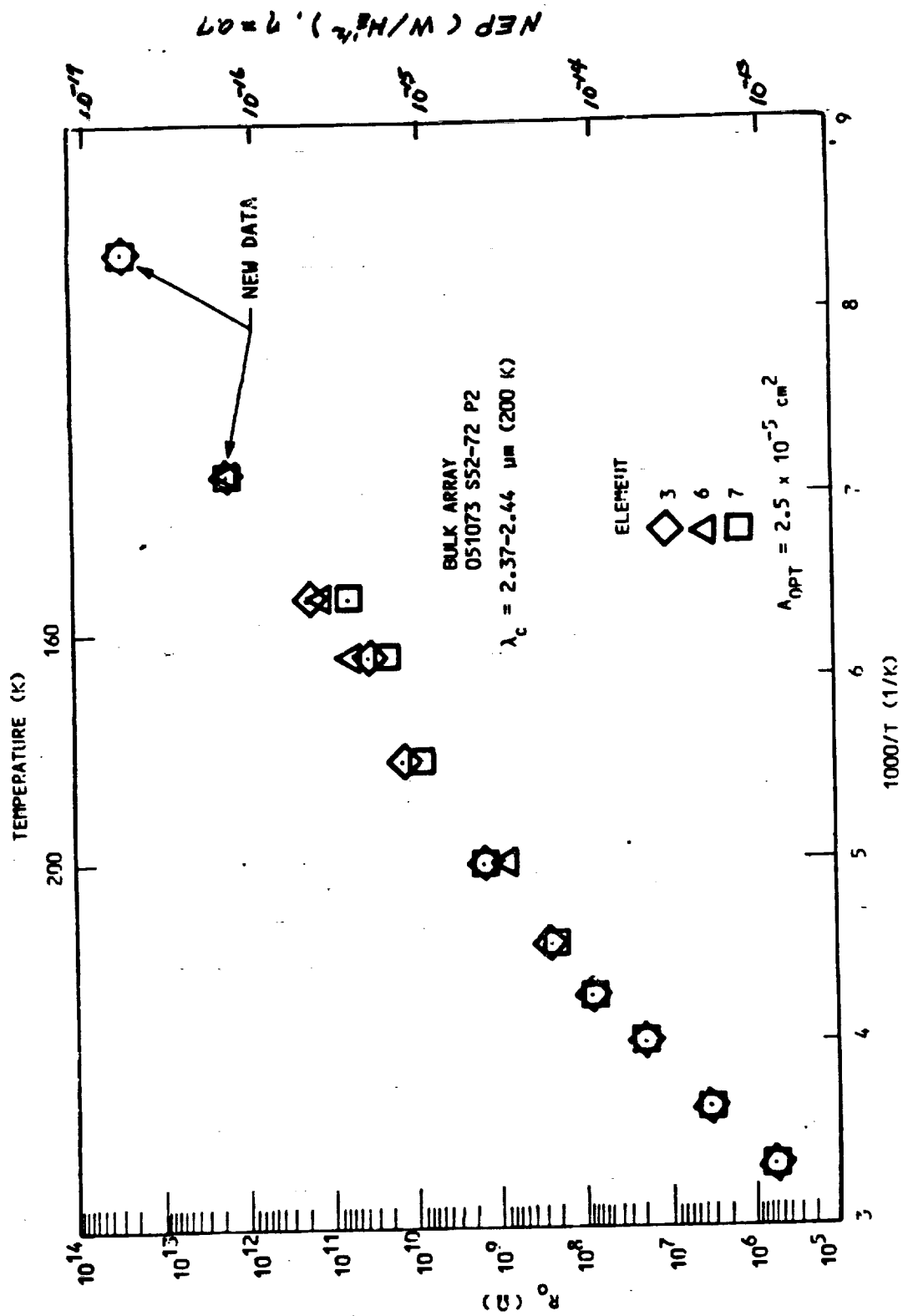


ZERO BIAS IMPEDANCE VS TEMPERATURE FOR A MW HgCdTe PV DETECTOR

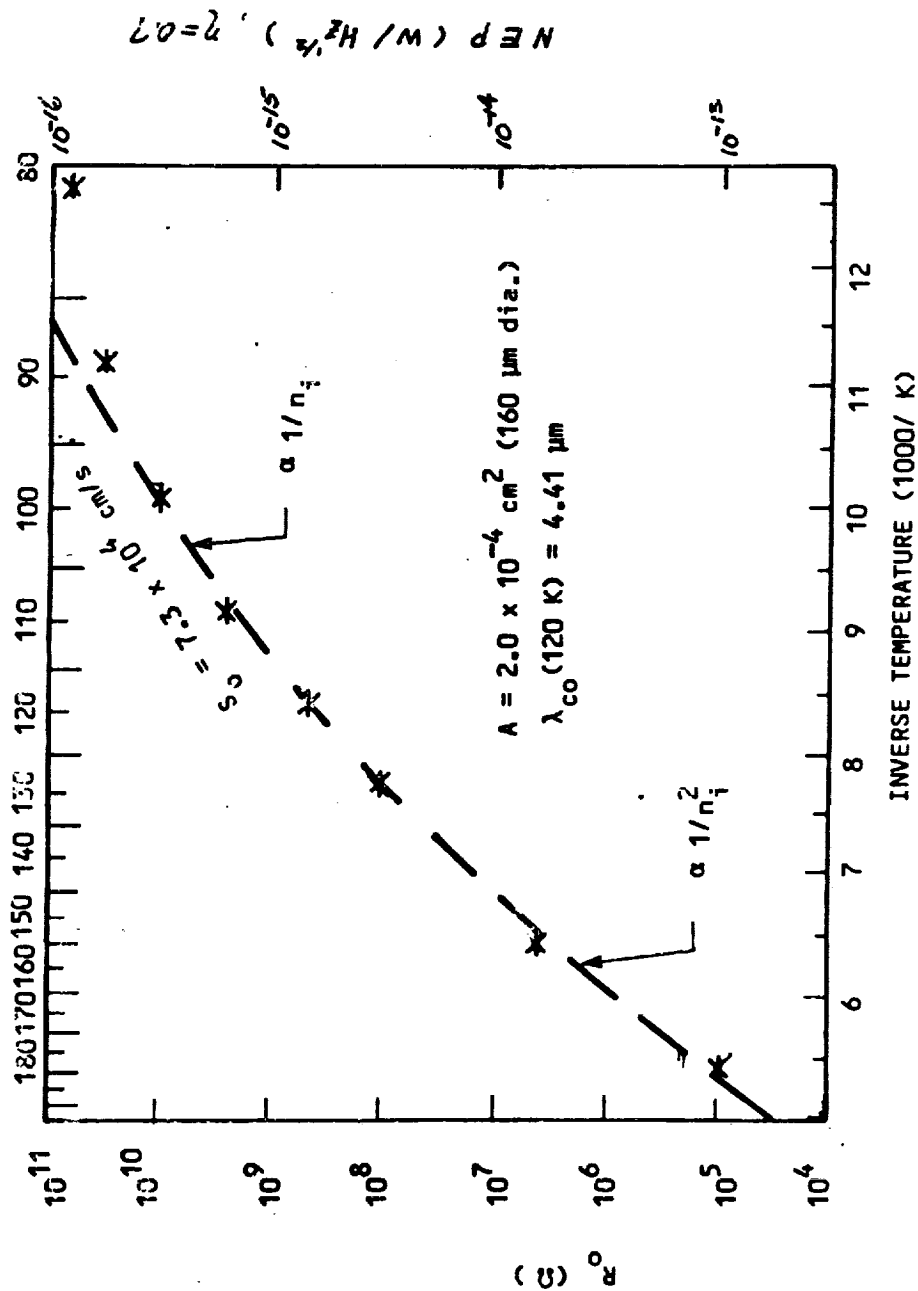


F 6199

ZERO BIAS IMPEDANCE VS TEMPERATURE FOR THREE SWIR DETECTORS

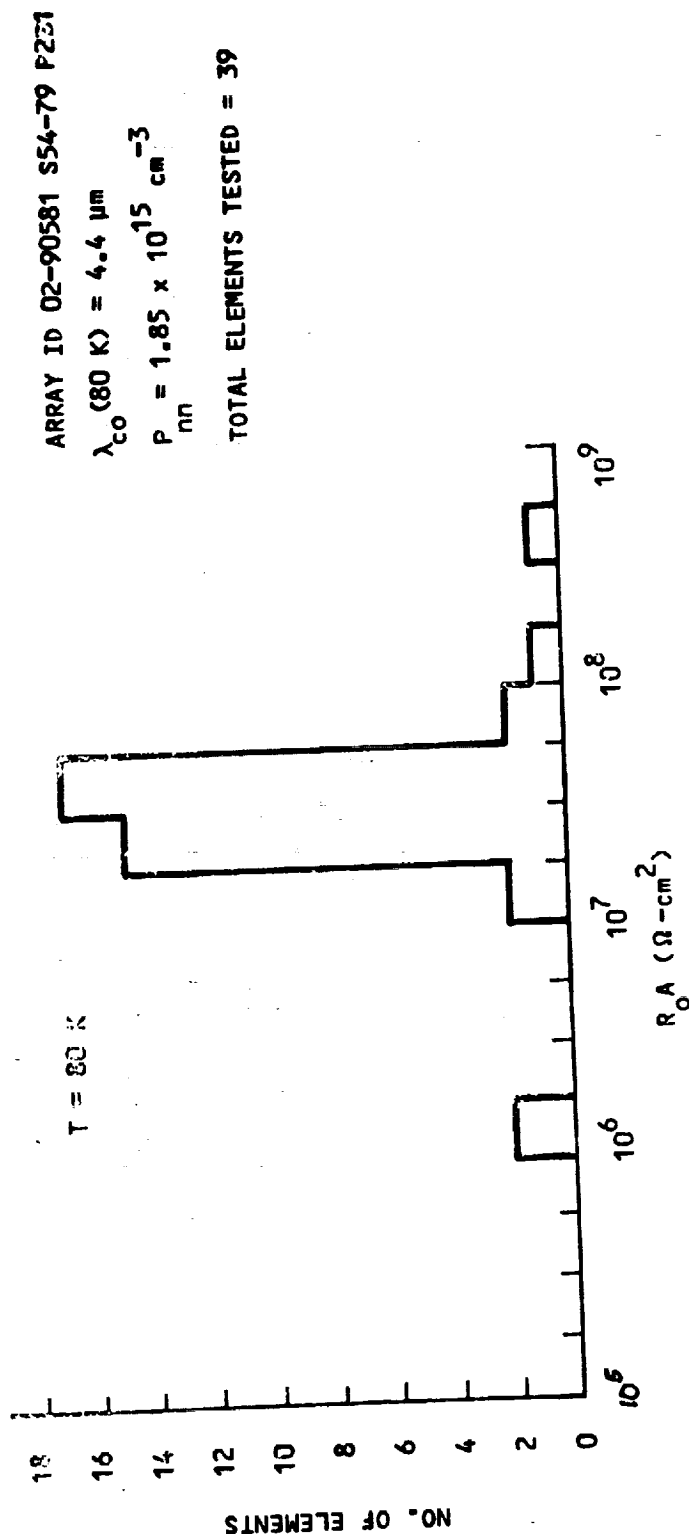


ZERO BIAS IMPEDANCE VS TEMPERATURE FOR A MW HgCdTe PV DETECTOR



F 6199

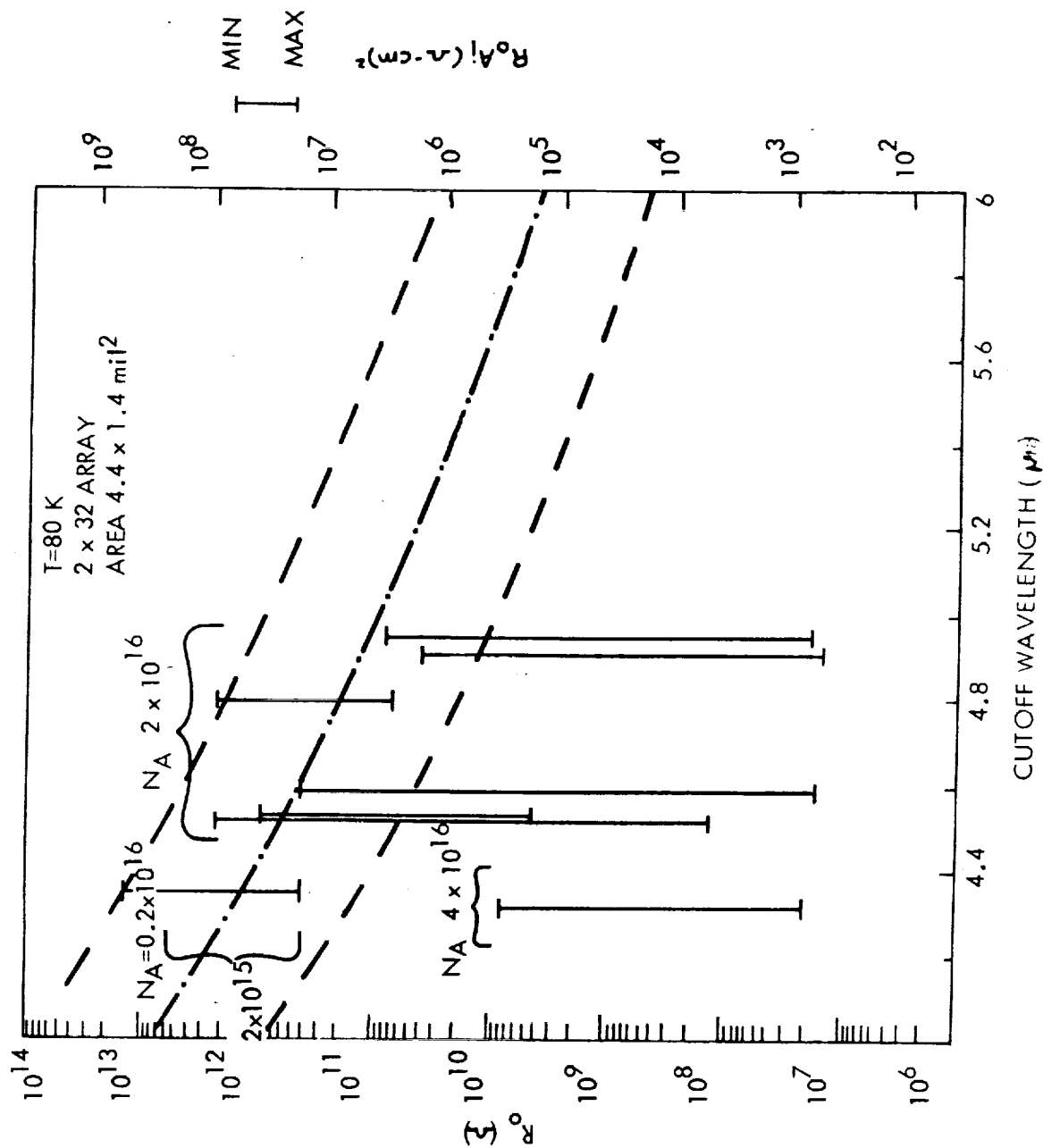
ROA DISTRIBUTION SHOWS GOOD MM PERFORMANCE
UNIFORMITY HAS BEEN ACHIEVED AT 80 K



$NEP (W/H_z^{1/2}), \eta = 0.7$

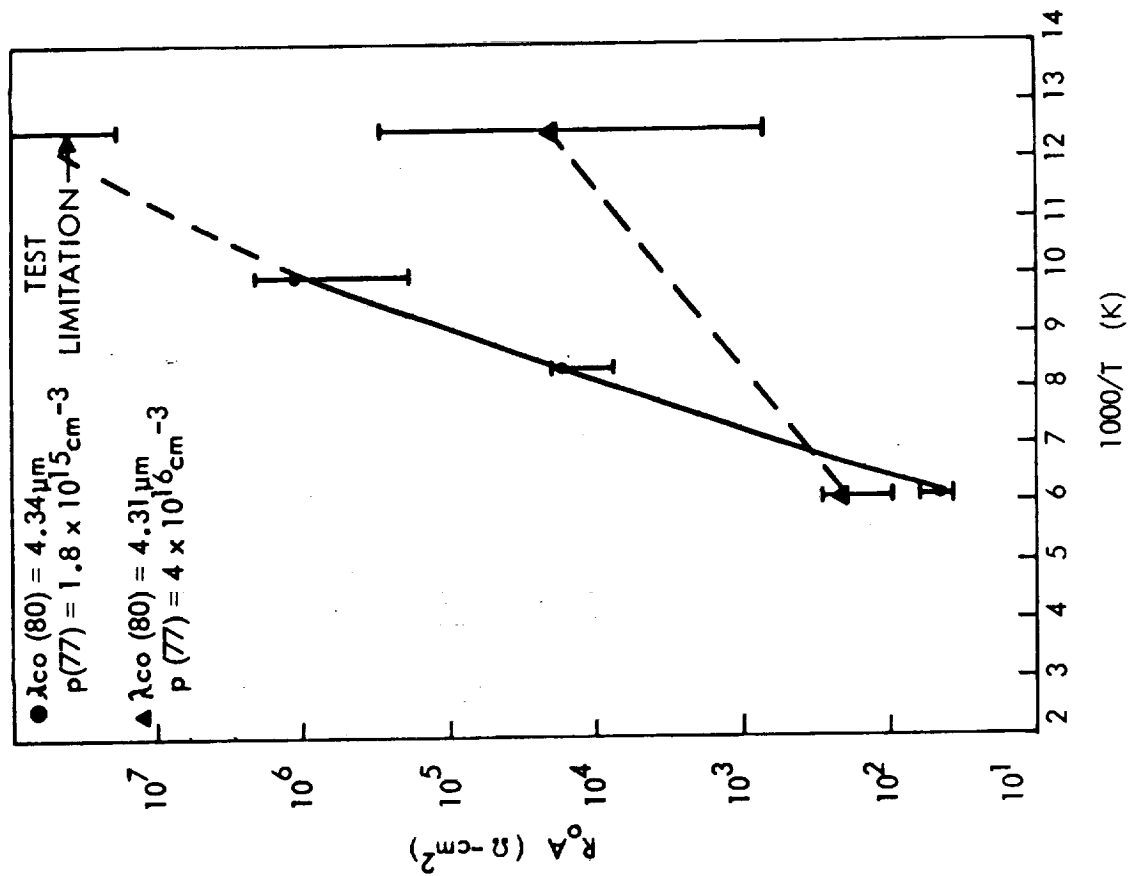
F 6296

HgCdTe MW ARRAY DATA SHOWS UNIFORMITY AND PERFORMANCE IMPROVEMENT OBTAINED BY LOWERING DOPING LEVEL



F 3518

LOW CARRIER CONCENTRATION IS OPTIMUM FOR MW PV DETECTORS OPERATING AT LOW TEMPERATURES



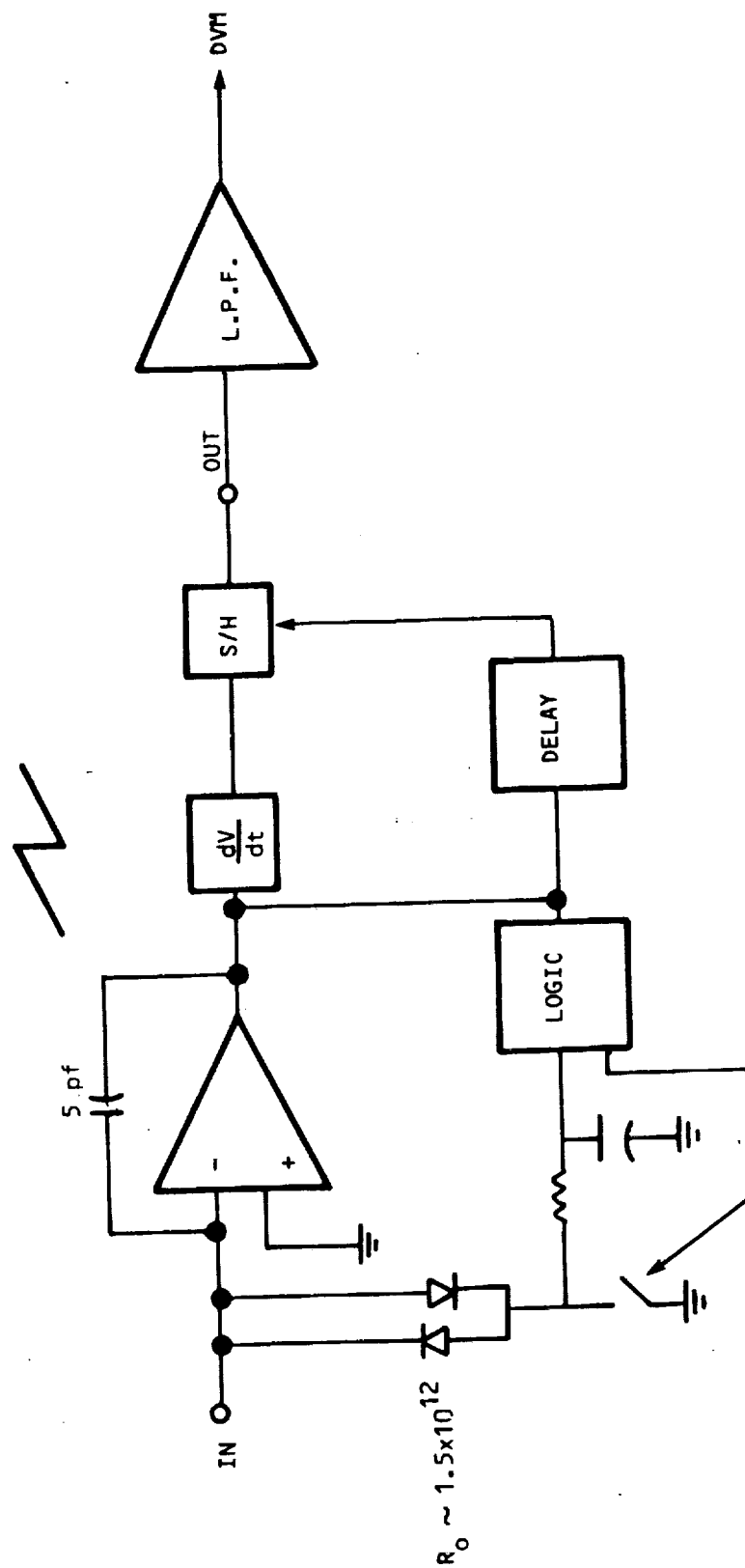
F 2904

PREAMPLIFIER DEVELOPMENT

- PREAMP FOR MEASURING $R_0 \leq 5 \times 10^{13} \Omega$ DEVELOPED
 - LOW TEMPERATURE PREAMP CONFIGURATION DESIGNED AND TESTED
- (PREAMP NOISE IS LIMITED BY CAPACITIVE LOSSES)

F 3417

LOW NOISE PREAMPLIFIER SCHEMATIC



- CAPACITIVE FEEDBACK ELIMINATES JOHNSON NOISE OF FEEDBACK RESISTOR.

F 3419

PLANS

- FABRICATE DETECTORS WITH LOW DOPING FOR IMPROVED LOW TEMPERATURE PERFORMANCE
- EXTEND TEST CAPABILITY TO LIQUID HELIUM TEMPERATURES
- TEST AND EVALUATE MOSAIC ARRAY PERFORMANCE AT LOW TEMPERATURES

**FOCAL PLANE ANALYSIS AND TEST
FOR
ASTRONOMICAL APPLICATIONS**

14-17

F 6323

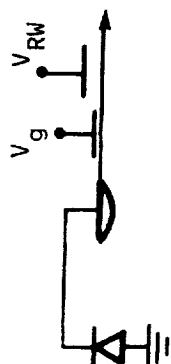
FOCAL PLANE REQUIREMENTS FOR SPACE APPLICATIONS

| <u>REQUIREMENTS</u> | <u>IMPORTANCE</u> |
|------------------------------|-----------------------|
| LOW TEMPERATURE OPERATION | FUNCTIONAL DEPENDENCE |
| LONG INTEGRATION TIMES | DARK CURRENT |
| MODERATE TO SLOW CLOCK RATES | TRANSFER EFFICIENCY |
| LOW READ OUT NOISE | TRANSFER NOISE |

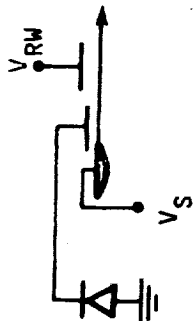
1. LOW ϕ_B IR/CCD COUPLING SCHEMES
 - SELECTION PROCESS
 - RESETTABLE GATE COUPLING ANALYSIS
 - OPTIMUM SYSTEM CONFIGURATION
2. LOW TEMPERATURE CCD DATA
 - DARK CURRENT
 - TRANSFER EFFICIENCY
 - NOISE

CCD INPUT COUPLING SCHEMES

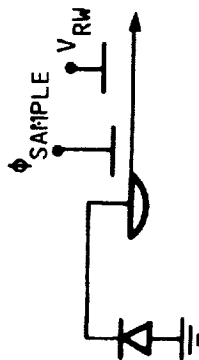
1 DIRECT SOURCE INJECTION



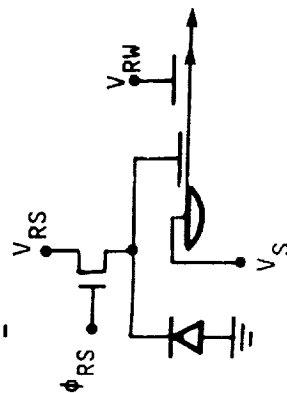
2 DIRECT GATE COUPLING



3 SAMPLED SOURCE INJECTION



4 RESETTABLE GATE COUPLING



F 6189

RELATIVE PERFORMANCE OF COUPLING SCHEMES

| COUPLING SCHEME | COMMENTS | NOISE FIGURE |
|--------------------------|---|---|
| DIRECT SOURCE INJECTION | REQUIRES OPTICAL BIAS CURRENT FOR GOOD COUPLING EFFICIENCY | POOR NOISE FIGURE AT LOW Φ_B LIMITED BY CCD TRANSFER NOISE AND BIAS SHOT NOISE |
| DIRECT GATE COUPLING | REQUIRES VERY LONG OBSERVATION TIMES AND GOOD DETECTOR UNIFORMITY | MODEST NOISE FIGURE LIMITED BY CCD 1/F NOISE |
| SAMPLED SOURCE INJECTION | ELIMINATES CCD 1/F NOISE BUT ADDS KTC RESET NOISE | POOR NOISE FIGURE LIMITED BY CCD TRANSFER NOISE AND KTC NOISE |
| RESETTABLE GATE COUPLING | NONDESTRUCTIVE READOUT ALLOWS KTC NOISE REMOVAL BY DIFFERENCING | BEST NOISE FIGURE LIMITED BY CCD 1/F NOISE |

CCD TEST VEHICLES

| <u>CCD</u> | <u>TYPE</u> | <u>REGISTER LENGTH</u> | <u>BIT LENGTH (μM)</u> | <u>CHARGE CAPACITY (ELECTRONS)</u> |
|------------|----------------------------|----------------------------|--|--|
| 2178 | 2-PHASE BURIED CHANNEL | 128 BITS | 50 | 18×10^6 |
| 3027-R381 | 3-PHASE SURFACE CHANNEL | 20 BITS | 26 | 6×10^6 |

F 6278

**FACTORS AFFECTING TRANSFER EFFICIENCY
AND TRANSFER NOISE**

● **CCD PROCESS-DEPENDENT FACTORS**

- **TRAP DENSITY**
- **TRAP TIME CONSTANTS**

● **CCD DESIGN PARAMETERS**

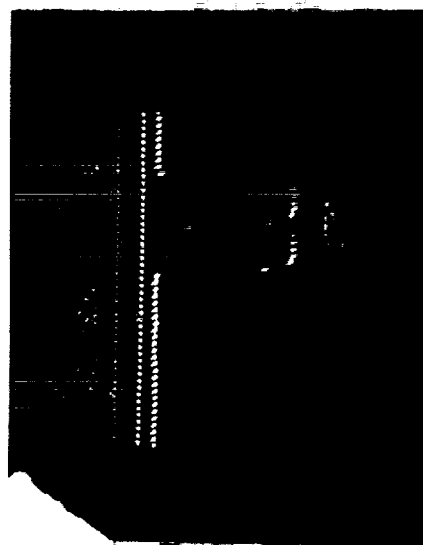
- **GATE LENGTHS**
- **REGISTER TYPE: SURFACE OR BURIED**
- **NUMBER OF TRANSFERS PER BIT**

● **CCD OPERATIONAL PARAMETERS**

- **CLOCK FREQUENCY**
- **OPERATING TEMPERATURE**
- **CLOCK WAVEFORMS**
- **FAT ZERO BIAS CHARGE**

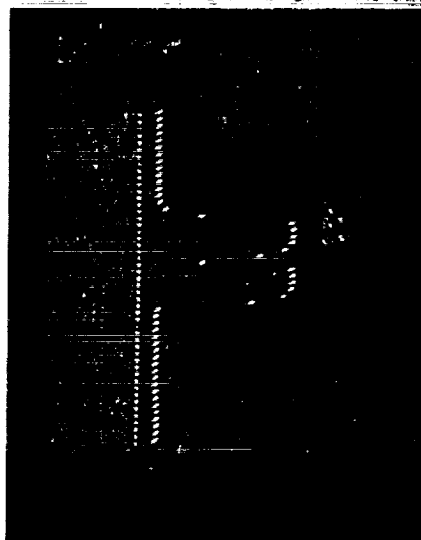
BURIED CHANNEL TRANSFER EFFICIENCY DATA (10% FAT ZERO)

$f_c = 50 \text{ kHz}$



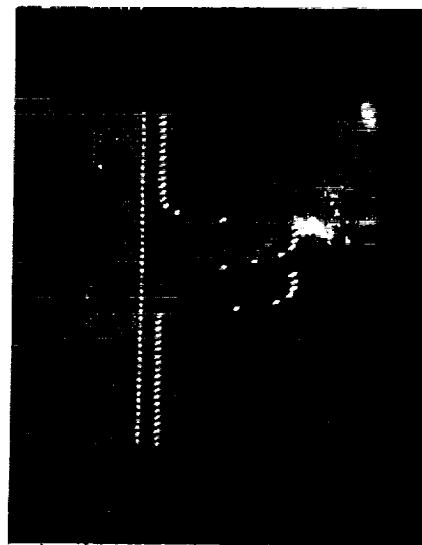
60 K →

$\epsilon = 0.9993$



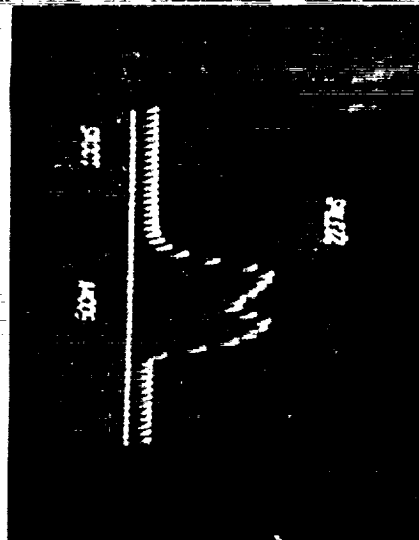
← 55 K

$\epsilon = 0.996$



50 K →

$\epsilon = 0.999$

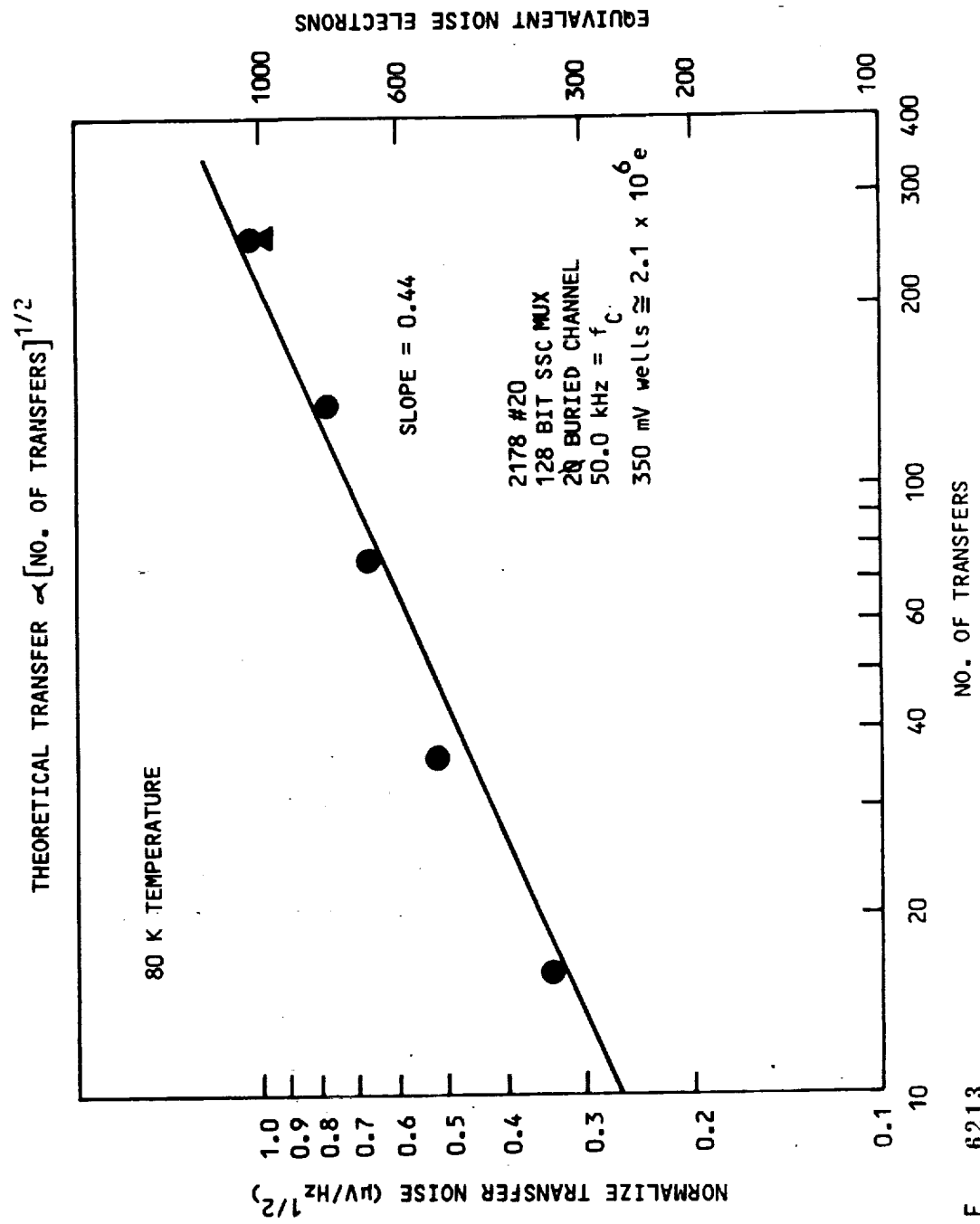


← 35 K

$\epsilon = 0.997$

F 5976

2♦ BURIED CHANNEL TRANSFER NOISE



F 6213

TRANSFER EFFICIENCY DATA

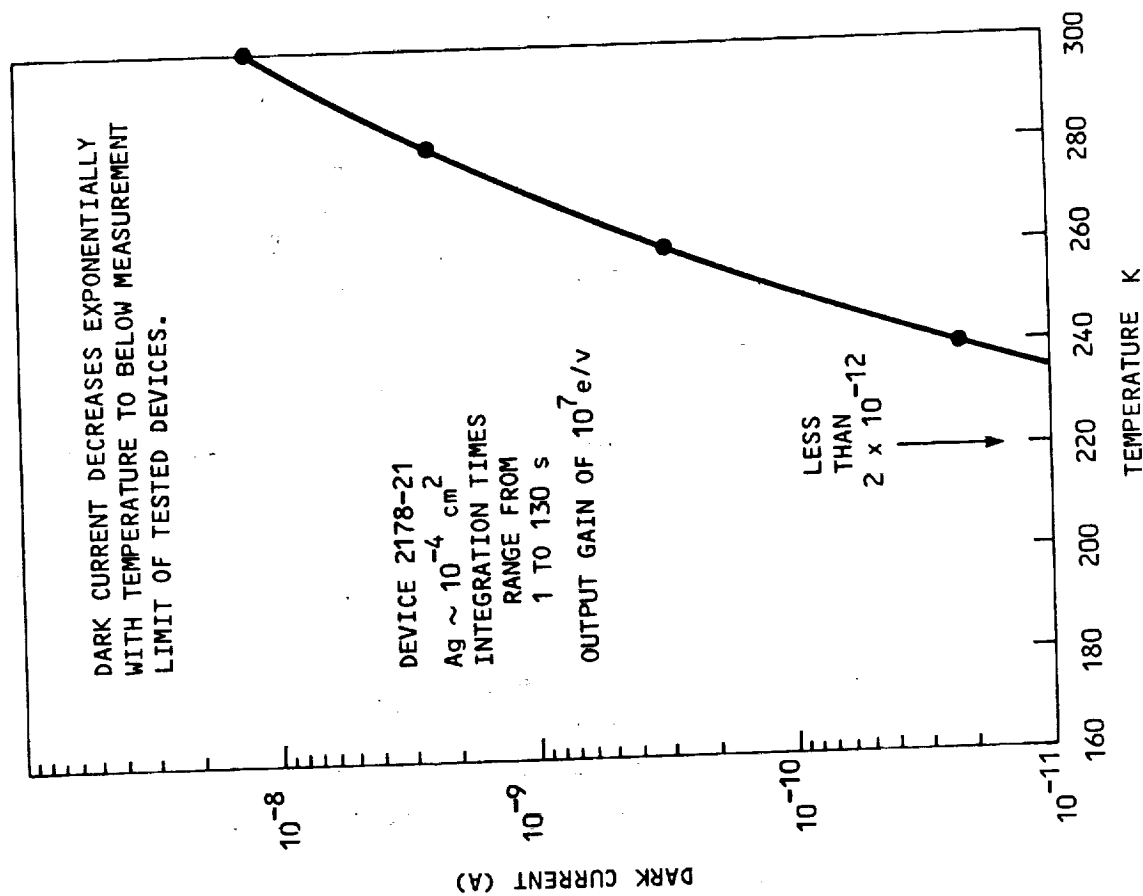
CONCLUSIONS

- FUNCTIONAL CCD OPERATION OBTAINED DOWN TO 35 K
- USE OF FAT ZERO CHARGE IMPROVES TRANSFER EFFICIENCY AT ALL TEMPERATURES
- TRANSFER EFFICIENCY FOR BOTH SURFACE AND BURIED CHANNEL DEVICES DECREASES WITH TEMPERATURE BELOW 80 K
- BURIED CHANNEL DEVICES ARE PREFERRED FOR OPERATION AT 80 K AND ABOVE
- SURFACE CHANNEL DEVICES ARE PREFERRED FOR OPERATION AT 50 K AND BELOW
- BEST TRANSFER EFFICIENCY AT 50 K ON TESTED DEVICES IS 0.9996 AT

$$F_c = 500 \text{ Hz AND } 10\% \text{ FAT ZERO}$$

F 6291

DARK CURRENT MEASUREMENTS



NOISE CONCLUSION

- DETERMINED CCD NOISE DOWN TO 35 K
- TOTAL READOUT NOISE CONTRIBUTION OF LESS THAN 600 ELECTRONS IS EXPECTED FOR A 64 x 64 ARRAY AT 60 K
- READOUT NOISE IS INSIGNIFICANT WHEN R6C IS USED DUE TO INHERENT CURRENT GAIN AT THE INPUT

F 6298

ACCOMPLISHMENTS

- THEORETICAL TRADE-OFFS FOR PV-HgCdTe DETECTORS COMPLETED AT LOW TEMPERATURES
- CHARACTERIZED EXISTING PV-HgCdTe DETECTOR ARRAYS (1-5 μm) AT LOW TEMPERATURES
 - LOW TEMPERATURE PERFORMANCE EXCEEDS MEASUREMENT CAPABILITY
 - PREAMPLIFIER DESIGNED/BUILT
 - LIMITING DETECTOR CURRENT MECHANISMS ANALYZED
- EVALUATED VARIOUS DETECTOR/CCD COUPLING APPROACHES
 - RESETTABLE GATE COUPLED APPROACH CHOSEN FOR LOW BACKGROUND
- LOW TEMPERATURE CCD TEST/ANALYSIS
 - MEASURED CCD PERFORMANCE AT 50 K SHOWS COMPATIBILITY WITH ASTRONOMICAL REQUIREMENTS

49
7/3-74
N93-70649.8
P-9
RY232914
HI782556
A785297

HYBRID SILICON
FOCAL PLANE ARRAYS

D. Pommerrenig, D. Enders and L. Trousil
(Rockwell International)

R. Capps, E. Irwin and E. Tollestrup
(University of Hawaii)

E. Dereniak
(University of Arizona)

Presented at the Infrared Detector Technology Workshop, NASA Ames Research Center,
July 12-13, 1983

This work was supported in part by NASA Ames Grant No. NAG2-165.

The Shuttle Integration and Satellite Systems Division of Rockwell International and the University of Hawaii's Institute for Astronomy have undertaken a joint project to demonstrate applications for hybrid silicon infrared CCD arrays in both ground and space based astronomical instrumentation. The primary goal is to provide a point of departure for both instrument designs and further development of the device. The test device is an indium doped silicon (Si:In) version of the 32x32 Rockwell 30331 surface channel hybrid silicon IRCCD. The 30331 devices form a family of two-dimensional infrared CCD's which are fabricated by hybrid interconnection of a highly standardized direct injection surface channel silicon CCD multiplexer with any of a potentially large selection of extrinsic silicon or germanium photoconductive detector arrays. The device structure and a typical instrument interface are shown in Figure 1.

The motivation for further study of this technology is contained in the following summary of both its positive and potential negative aspects. It is noteworthy that there is considerable room for technical improvement in all of these areas through better understanding of processing requirements and application related design changes.

- + Independent detector and multiplexer optimization
- + Operation at temperatures below 15K
- + Wide selection of detector material
- + Easily expandable size
- + Reasonable production yield
- + Standardized drive and interface electronics
- Possible interface state noise
- Fat zero injection required for high CTE

A few of these issues will be discussed in detail, followed by a summary of the demonstrated performance of the test devices.

The hybrid silicon family tree has two primary branches. The first extends in the direction of variations in the choice of detector material as suggested previously. This branch is shown in Figure 2. The second branch involves the spatial expandability of this technology. Several 32x32 multiplexers can be interconnected to sub-zones of a larger detector chip. Each multiplexer services part of the total array and provides redundancy in event that one multiplexer fails. For instance, four 32x32 multiplexer chips could be used to read-out a single 64x64 detector chip. This semi-redundant modular structure is the basis for expansion of the current hybrid silicon devices into very large focal plane arrays. A concept of this type is shown in Figure 3 and has already been demonstrated by Rockwell.

The presence of interface states can degrade the operation of surface channel devices. The degradation takes the form of reduced charge transfer efficiency and increased noise. The CTE can be recovered by injection of fast zero electrons; but the noise floor may remain high. This is the trade off which is currently required to achieve operation below approximately 40k. Buried channel devices eliminate this problem but freeze out at temperatures which are not compatible with the detectors required for SIRTf. Fortunately, the density of interface states is a strong function of the wafer processing technique and, therefore, further processing improvements could effectively eliminate this problem in optimized surface channel devices.

The demonstrated performance of the test devices is summarized in Table 1. The experience gained through characterization of the IRAS detectors suggests that considerable effort must be invested in order to understand how these data relate to the requirements of extremely low background space applications. It is already clear that performance improvement may be achieved through trade offs between related operating parameters. Additional test data obtained from the test devices are shown in Figures 4 and 5. In general, the existing information is very encouraging but does not yet extend into the SIRTf environment.

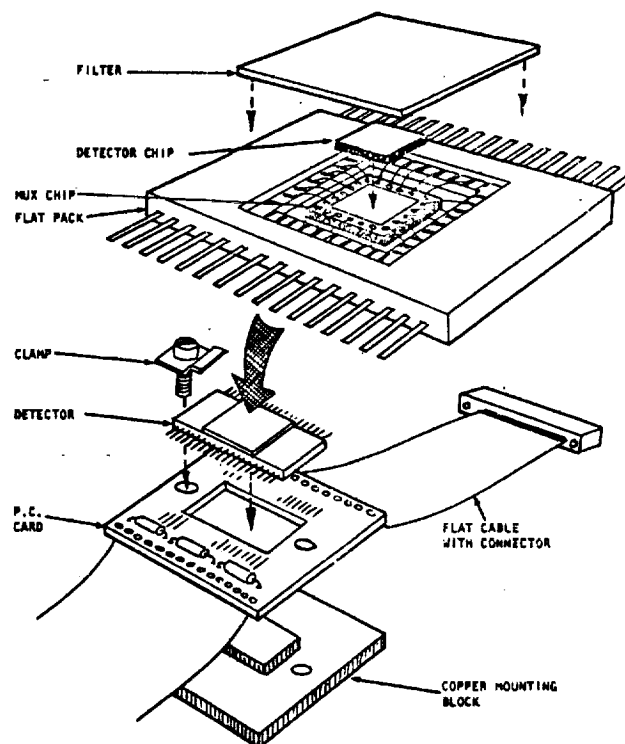


Figure 1 Rockwell Proprietary Focal Plane Assembly

Table 1. Typical 32x32 IRCCD Performance

| Parameter | Minimum | Typical | Maximum |
|---|----------------------|------------------|---------|
| Spectral response (μ) | 2.0 | | 7.5 |
| Operating temperature ($^{\circ}\text{K}$) | 10 | 40 | 45 |
| Array configuration (pixels) | | 32x32 | |
| Cell size (μ) | | 88 | |
| Dynamic range | | $10^4:1$ | |
| CTE ($f = 500$ kHz, F.Z. = 0) | | 0.998 | |
| CTE ($f = 500$ kHz, F.Z. = 2V) | | 0.9998 | |
| Noise (electrons, rms) | | 150 | |
| Integration time (sec) | 1.0×10^{-3} | | 10.0 |
| Charge capacity/pixel (electrons) | | $>8 \times 10^6$ | |
| Clock rate (KHz) | 250 | 500 | 1000 |
| Power dissipation (mW) | 1.0×10^{-2} | | 5.0 |
| Bias voltage | 0 | 25 | 100 |
| Responsivity (A/W at 4.5μ) | | 5.0 | |
| Nonuniformity (%) | | ± 5 | |
| Output FET (μV /electron) sensitivity | | 0.4 | |
| DC-coupling | | Yes | |
| Weight (incl. Package) | gram | 10 | |

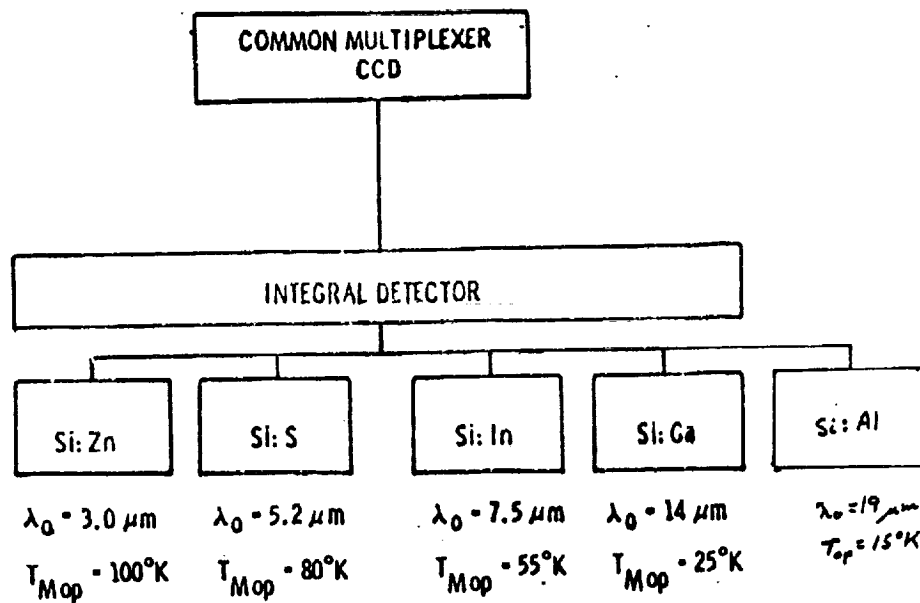


Figure 2 Hybrid Silicon Detector Options

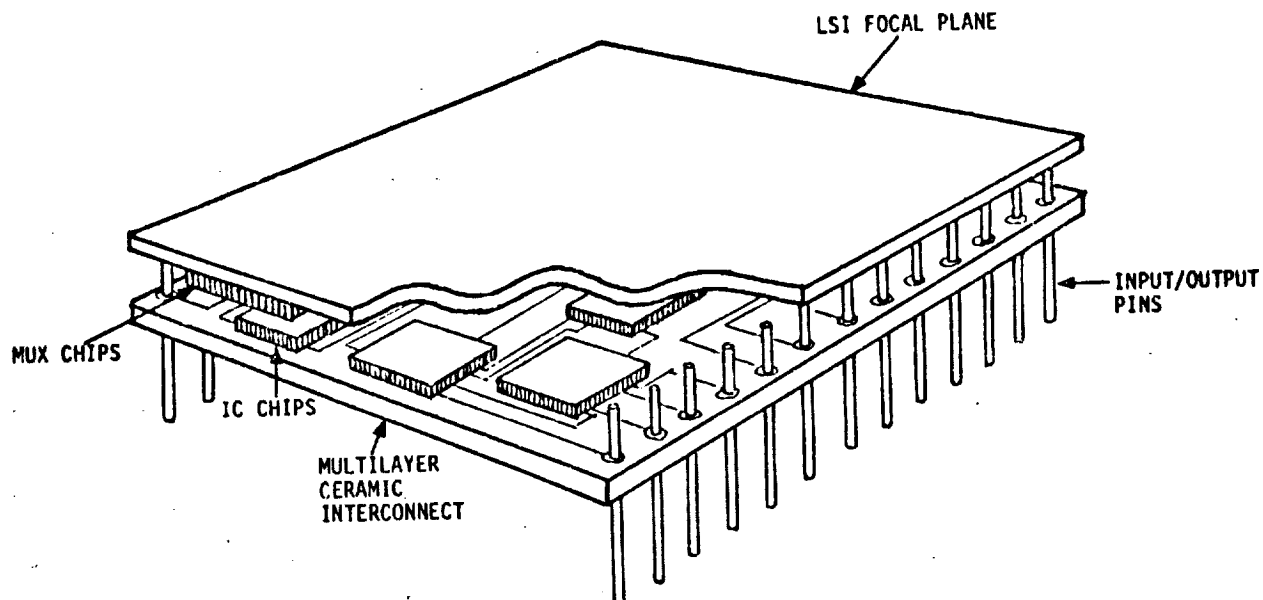


Figure 3 Rockwell Proprietary Vertically Integrated Array Module

PERFORMANCE OF HYBRID Si: In FOCAL PLANE
 CCD MUX OUTPUT VOLTAGE AS A FUNCTION OF INCIDENT RADIATION
 FOR VARIOUS INTEGRATION TIMES AT $V_B = 15$ V AND FZV = 5%

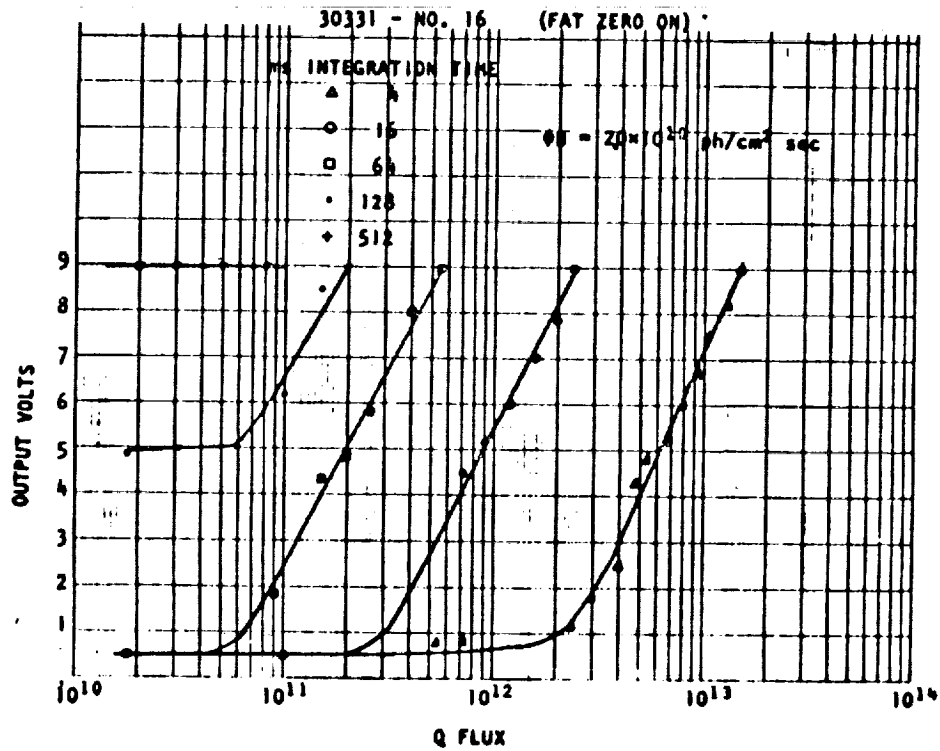


Figure 4

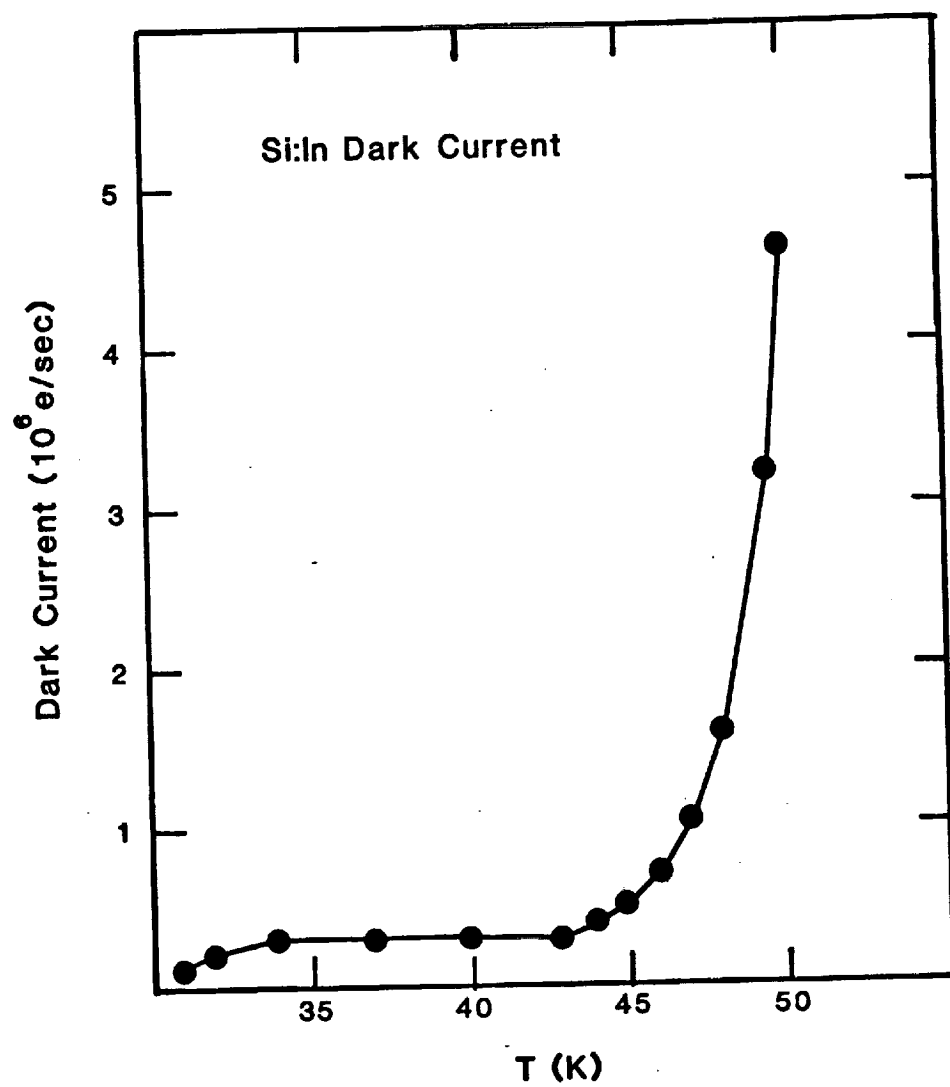


Figure 5

In order to characterize the test devices in an environment which is similar to that expected from SIRTf, The University of Hawaii has developed a set of drive and signal processing electronics and a cryogenic optical head which feeds the array in a imaging mode. This prototype IRCCD camera will be used for both laboratory tests of the device under simulated low background conditions and for system tests at the telescope. The camera's optical layout is shown in Figure 6 and a system block diagram is shown in Figure 7. The system diagram indicates that reserve capability is available in the event that a multi-output array module becomes available for testing.

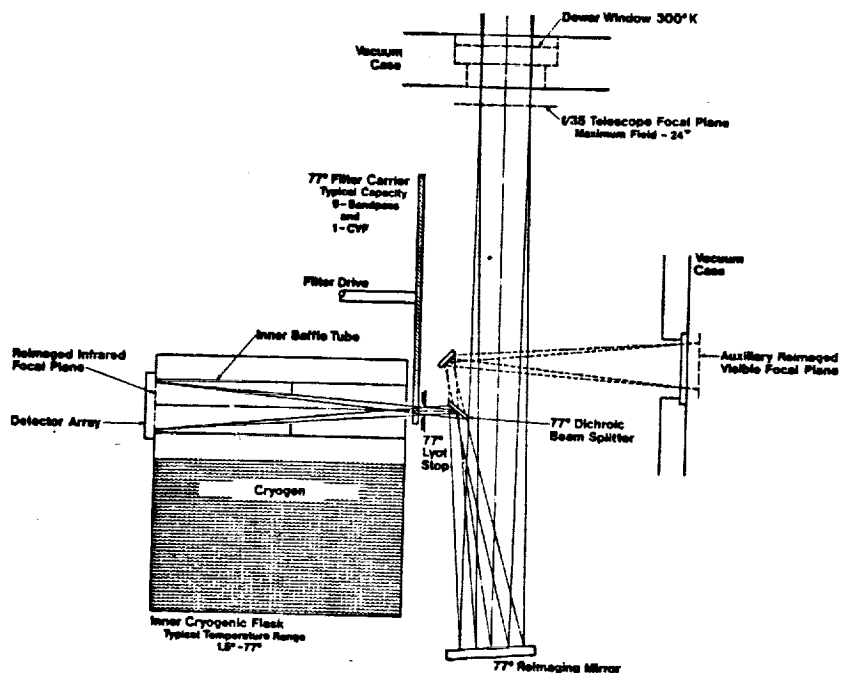
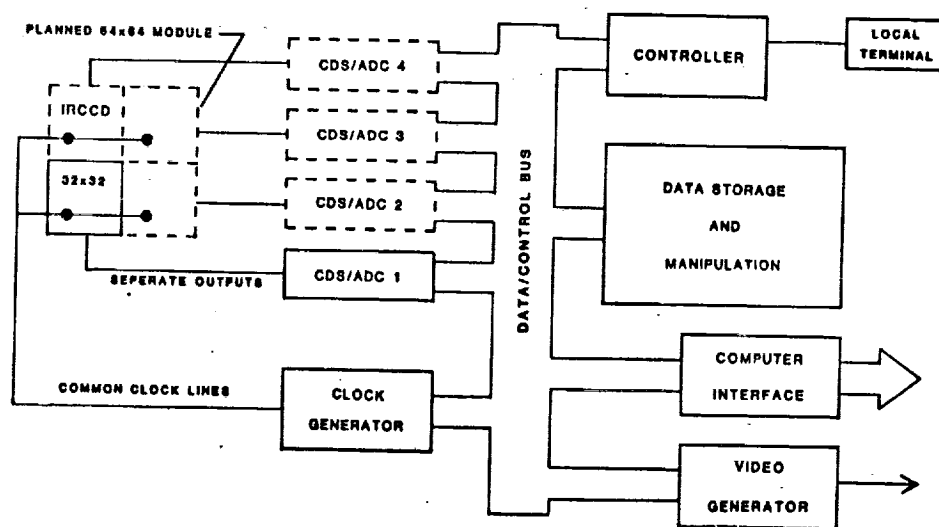


Figure 6 Arrangement of Optical/Thermal Components



UH - ROCKWELL IRCCD SYSTEM

Figure 7

An estimate of the test device's limiting sensitivity is shown in Figure 8. This figure relates integration time per read out to the limiting sensitivity due to the combination of read and dark current noise. These should be the limiting noise sources in the presence of "zilch" background. The best measured read noise is 150 electrons (rms) per pixel and the dark current should be between 50k and 1k electrons per second. Therefore, the figure indicates that the 5 micron sensitivity after a 10 second integration should be between $4.0\text{E-}18$ and $1.8\text{E-}17$ if the quantum yield ($G\eta$) is equal to 1. The quantum yield is the primary uncertainty in this estimate. The IRAS results suggest that the quantum yield (reponsivity) may have to be traded for unacceptable nonlinearities.

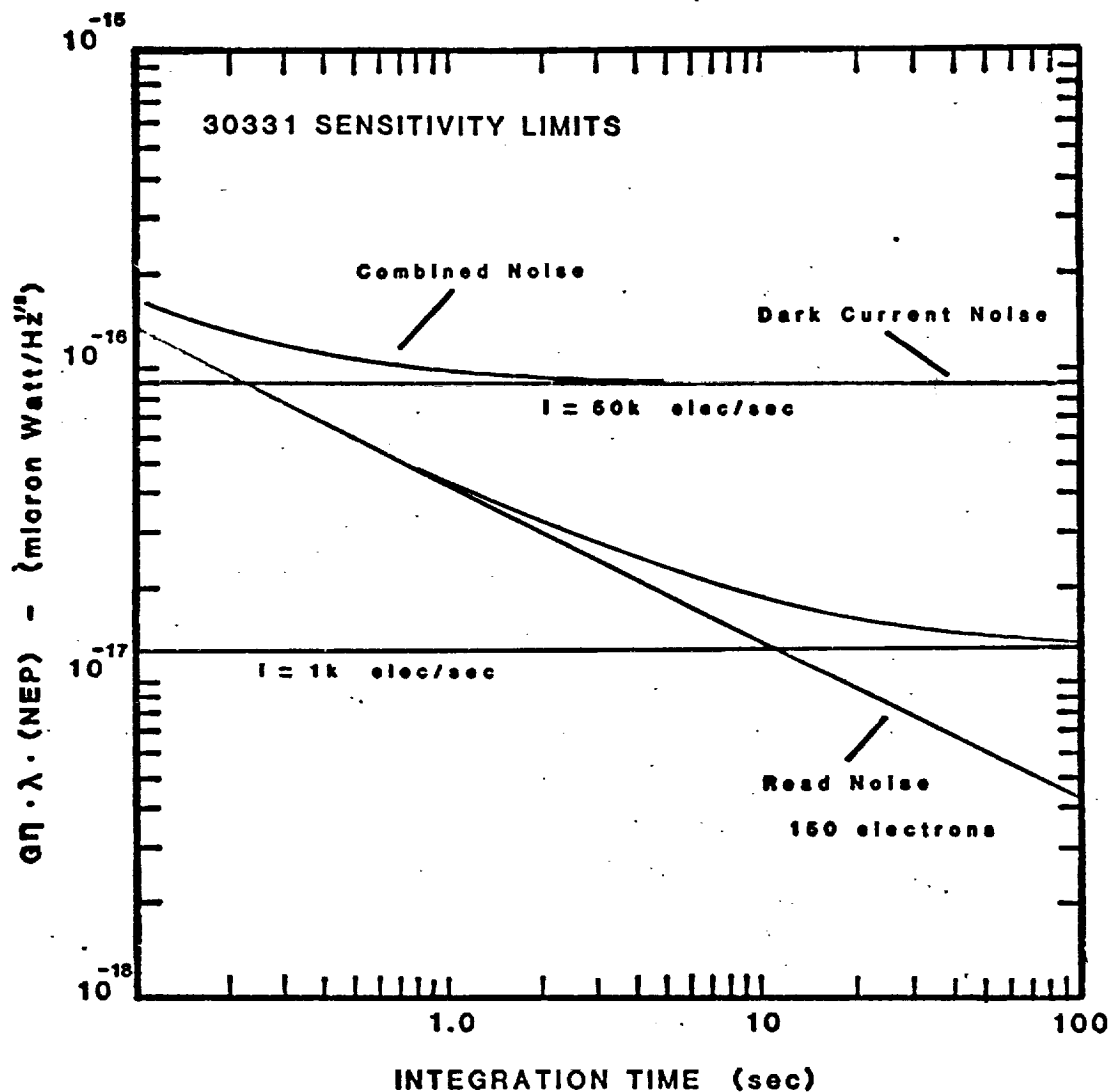


Figure 8

514-89 50
133819
N93-70650?
RW983420

"Evaluation of a 32x32 InSb CCD
for use in Astronomy"

W. J. Forrest and J. L. Pipher
University of Rochester
Department of Physics & Astronomy
C. E. K. Mees Observatory
Rochester, NY 14627 USA

I. Introduction

We have been fortunate to receive several infrared CCD array detectors on loan from Santa Barbara Research Center. The devices are evaluation samples, not commercially available at this time. Dr. Alan Hoffman of SBRC has made the arrangements for this loan and provided considerable technical support to this project. One aim of this project has been to evaluate the performance potential of this array technology, using astronomical objects. A quick summary of our findings is given in table I. In short, we have found the imaging properties to be excellent under both low and high background conditions and the sensitivity to be quite good (each pixel is competitive with current InSb single-detector systems in use for astronomy). We anticipate improved low-background performance when we run these detectors at a lower and more stable temperature.

The device characteristics are described in II, laboratory testing is summarized in III, and our first astronomical imaging is presented in IV. Various circuits we have developed (clocks, clock drivers, DC supplies, clamp-amplifier (simple correlated double sampling), and a Real Time Display System) are given in Appendix A.

II. Description of the Device

The array consists of a 32x32 InSb photo-diode array bump-bonded to a surface-channel silicon CCD. The device has been described in the literature (Parrish et al. 1978, Hoendervoogt et al. 1978) so only some brief technical comments will be made here.

A schematic of the important circuit elements is shown in Fig. 1. 1-5 μm photons incident on the array detectors generate electron-hole pairs which cause a current to flow in the photo-diodes. The holes travel into the CCD through the input diffusions (i.e. direct injection) and are stored under the V_{ST} electrodes, held negative. When sufficient charge has been accumulated, the ϕ_{T1} electrode is pulsed low, allowing the charges to spill into the ϕ_2 CCD slow mux shift registers, held at a low potential. Then the ϕ_{T1} electrode is reset high and the charge is clocked out from the slow mux shift register to the fast mux shift register and finally to the reset output amplifier. The series of 1024 signal charge packets cause a series of 1024 voltage pulses at the output with voltage proportional to charge. These voltage pulses are used to reconstruct the pattern of illumination on the detector during the previous integration time.

Some of the features of the SBRC design are:

- Individual "detector gates" at each InSb p-n junction. By properly adjusting this voltage, a uniform threshold (i.e. zero detector bias) can be achieved over the whole array as well as high detector resistance ($10^8 \Omega\text{-cm}^2$ at 60°K).
- Separation of charge integration (i.e. V_{ST}) from CCD read out (ϕ_1, ϕ_2 , etc.) by the ϕ_{T1} transfer electrode allows essentially 100% duty cycle with no smearing of images.
- Four electrodes/CCD shift register allow either 2 phase or 4 phase operation as desired.
- Provision for both slow mux ($T1$) and fast mux ($T2$) fat zero signal if desired. Low noise "Tompsetting" mode possible using control electrodes ($V2, V3, V4, V5$).
- Isolation bits between each data bit on the CCD shift registers insure essentially zero crosstalk between detectors.
- Surface channel technology allows low temperature operation (at least 40°K) and provides large bucket size (10^7 electrons for 2 phase, $\approx 2 \times 10^7$ electrons for 4 phase operation).

- Detectors provide nearly complete areal coverage (active areas FWHM 3.7×3.7 mils for detectors on 4 mil centers).
- High detector quantum efficiency ($\eta = 0.61$ measured at $3.8 \mu\text{m}$ and 60°K operation).

III. Laboratory Testing

In support of the above claims of detector performance and in preparation for astronomical observation, an extensive series of laboratory tests were performed on the three arrays we have available currently. Most of the test results will refer to the best detector, though the second backup detector would provide useable performance for some astronomical projects. The third detector is infrared inactive, and was supplied in order to test our drive electronics.

A. Equipment

An available LN_2/LHe dewar was modified to house the CCD. The optical configuration is given in figure 2. In addition to the elements shown, an extensive series of baffles painted with 3M Nextel flat black block any stray radiation. The stray light level has not been measured but must be less than 10^5 photons/sec/pixel (10^9 photons/sec/cm²) from dark current measurements. A special fan-out board was constructed with the leadless CCD chip carrier in the center. This provides dip-socket connections for the 36 wires needed to run the CCD and $1 \text{ M}\Omega$ static protective resistors on all MOS gates.

The electronics to drive the CCD were built in house. A description of the electronics is given in Appendix A. The main electronics consist of the stand-alone, hard-wired, TTL clock generator, the clocked drivers and DC supplies. In addition a post-amplifier, which clamps on the output amplifier's reset level to eliminate any drifts on $>10 \mu\text{sec}$ time scale, was built. Finally a real time display, which displays our CCD output as an image on a Textronix 2215 X-Y-Z oscilloscope, was constructed. This device is invaluable for focussing, lining up, etc.

The overall experiment is controlled by an LSI 11 computer programmed in the FORTH language. While the stand-alone clock runs the CCD shift registers continuously, charge from the V_{ST} detector storage sites (fig. 1) will only be dumped if a $\phi T1$ -enable line is held high. This line is managed by the computer, based on our parameter NF (Number of Frames per charge dump) and a TTL "FRMST" signal which interrupts the computer once per frame (typically 16-25 msec). If a Charge Dump (CD) has occurred, the computer

readies the 12bit A/D converter (Data Translation DT 2782) to convert the next 1024 pulses and DMA the data into computer memory. In addition, if desired, the computer can co-add successive CD's into a double-precision buffer in real-time. The number of CD's in one scan is controlled by our parameter NCD. Thus varying NF varies the on-chip integration time while varying NCD varies the off-chip integration time prior to writing a scan to floppy disk. A second pixel-picking mode is available which we use mostly for noise analysis. In this mode, a series of ND consecutive detectors can be specified starting at a given pixel number and 1024/ND consecutive CD's will be taken and stored in a single-precision buffer for later analysis.

B. Results of Lab Tests

1. Detector Quantum Efficiency

To measure the quantum efficiency, 3 basic steps are taken. First the gain of the output amplifier (see fig. 1) is measured. This may be done by turning off V_{SCR1} , turning on V_{SCR2} , and measuring V_{out} vs V_{reset} . Gains of $\sim 0.6 - 0.9$ are available. Next the correspondence of input voltage to input charge is calculated from the known gate capacitance of 0.41 pf. The output voltage gain is then $\sim 1.7 - 3.0V/10^7$ electrons depending on the gain selected. Finally, the CCD is allowed to look at an uniformly illuminated, black surface of known (near room) temperature. The photon flux is calculated from the known A , Ω , and filter characteristics and a quantum efficiency calculated. The result is $\eta \approx 0.6 - 0.65$ at $3.8 - 4.7\mu m$

2. Bucket (well) Capacity

By proceeding as in 1. above but flooding the array with photons, a well capacity of 10^7 electrons has been measured.

3. Charge Transfer Efficiency (CTE)

When looking at a uniformly illuminated scene as in 1. above, we note at most a 10% loss in signal of the last detector read out (after 129 charge transfers) compared to the first (1 charge transfer). Some of this degradation could be due to imperfect optics (i.e. vignetting of detectors at the peripheries). Therefore we have a lower limit on $CTE \geq (0.9)^{1/128} = 0.9992$, consistent with the manufacturers determined $CTE = 0.9994$.

4. Imaging Properties

a. High background

Excellent, sharp images of laboratory and terrestrial objects have been obtained with our 1/4" lens (see fig. 2). For example, an un-retouched image

at $3.8\mu\text{m}$ of human beings is given in fig. 3.

b. Low Background

In preparation for astronomical imaging, a series of images of a scene were taken as the scene brightness was successively reduced by factors of 10. The imaging was performed in a darkened room at $1.65\mu\text{m}$, so there is essentially no photon background. As can be seen from fig. 4, there is no noticeable degradation in the images when going from 22 msec exposure ($\text{NF}=1$) to 11 sec exposure ($\text{NF}=500$). Further, the infrared images faithfully reproduce the mask which was being imaged (the arrow star cluster).

5. Dark Current, Detector Resistance

These parameters are quite important as the ultimate detector sensitivity is limited by detector resistance and the ultimate CCD sensitivity is limited by dark current. They are also somewhat related as for a given bias setting (i.e. V_{IN}) necessary to have the working detectors in their working range (i.e. actual bias across the detector ≤ 0), the dark current will be given by $I = \Delta V/R$ where ΔV is the typical back-bias (~ 5 - 15 mv) and R is the detector resistance. We have found that dark current increases and detector resistance decreases approximately a factor of 2 for every 2 - 4°K increase in detector temperature. The minimum stable temperature we can achieve with our pumped LN_2 system is 60°K . At this temperature, looking at the cold-dark slide, a typical detector resistance of $10^{12}\Omega$ and dark current of 0.01 pA is achieved. A display of the dark current for the whole array is given in fig. 5.

6. Detector Uniformity

Using the optical setup shown in fig. 2, we can determine the pixel to pixel sensitivity uniformity by pointing the dewar at a uniform temperature, black surface. The output of our array is given in fig. 6, it can be seen that for the working detectors (~ 924), the sensitivity uniformity is quite good with pixel-pixel variation $< \pm 10\%$ from the average. In addition from fig. 5 it can be seen that aside from a blemish in the upper-left corner, the dark current uniformity is also quite good.

7. Charge-injection Efficiency

One criticism of the direct-injection scheme in infrared CCD's has been the possibility of charge injection inefficiency at low backgrounds. In practice we have found that with our device, there is always sufficient dark current to assure good charge injection efficiency at our typical operating

bias voltage. This can be seen from the following: the charge injection efficiency is given by (Steckl, 1975)

$$\eta_{inj} = \frac{g_m R_d}{g_m R_d + 1}$$

where R_d is the detector resistance while $g_m = eI_d/kT$ (Ando, 1978) is the transconductance of the input Mosfet (I_d = detector current). For good charge injection efficiency ($\eta_{inj} \geq 0.67$) we require $g_m R_d \geq 2$ and at $T = 60^\circ K$, this corresponds to $I_d R_d \geq 10^{-2} V$. Now in the worst case of photo-signal << dark current, I_d will be dark current and this implies $\Delta V \geq 10$ mV for the actual back-bias across each detector. This is the typical back-bias we use when operating and we achieve quite reasonable low-background photometry (see next section, M82 imaging).

8. Read-out Noise

We have measured the read-out noise of the CCD under a variety of background conditions and on-chip integration times. Our technique is to use our software pixel-picking program to gather sequential samples from one or more detectors. Then the data is analyzed for the average signal and the root-mean-square (RMS) noise. In addition we have performed discrete FFT analysis on some data to investigate the frequency characteristics of the noise.

a. Short Integration Time

In the laboratory, the high thermal signal with our 3.8μ and 4.7μ filters limits us to about 22 msec integration time (i.e. $NF=1$). We find that under these conditions, the RMS read-out-noise is comparable to but somewhat higher than the \sqrt{N} , shot-noise, limit (where N is the number of signal electrons). However as the background is reduced, the noise remains constant, and then at a fairly low threshold begins to diminish approximately as $\sqrt{\text{background}}$. This behavior is illustrated in fig. 7, which is a superposition of two runs made at 4.7μ . It can be seen that RMS noise $\approx 1.5\sqrt{N}$ near full buckets (4000 counts = 10^7 electrons) but is considerably higher than this at lower signals. With zero background (cold-dark slide), the noise is essentially indistinguishable from our electronic noise floor (~ 0.55 counts ~ 1400 noise electrons) and we conclude the actual electronic read-out-noise of the CCD is less than 1400 electrons RMS. However, because of the noise properties of the CCD described above, we choose an integration time (i.e. NF) that gives between 1/2 and full buckets, so that we are operating near the \sqrt{N} limit.

The reason for the noise being greater than \sqrt{N} appears to be related to the charge transfer from the detector storage sites into the CCD shift register (ϕ_{T1} transfer, see fig. 1). Looking at the oscilloscope, it can be seen that in addition to a random noise component, the output of one whole frame (1024 detectors) jumps up or down occasionally. By carefully adjusting the ϕ_{T1} , V_1 and V_{ST} voltage levels, we have managed to minimize this "clocking" noise, as shown in fig. 8. We know the "clocking" noise involves the ϕ_{T1} transfer because it entirely disappears with the same amount of slow-mux fat-zero signal. Alan Hoffman of SBRC has suggested that improved ϕ_{T1} transfer can be obtained with a different clocking scheme than we currently use. At SBRC they have found that "push" clocking, whereby when ϕ_{T1} is held low, V_{ST} is sent high to push the charge out, gives more complete and reliable charge transfer. This technique could be implemented in a next generation clock; for the present we feel the penalty of 1.5 times the \sqrt{N} noise is acceptable and prefer to concentrate on improvements in other areas of our system.

Investigations of the spectral frequency of the noise in collaboration with R. W. Boyd and M. Dimmler of the Institute of Optics have not been especially helpful as yet. There doesn't appear to be any one frequency band which dominates the noise. As an example, we analyzed several runs where 2 detectors were sampled 512 times each during an 11.3 sec period. The data was split up into 8 sets of 64 consecutive samples. In order to investigate any correlated noise, such as the "clocking" noise described above, we looked at the noise in the sum and the difference of the two signals. The difference should eliminate any correlated noise, here the frequency spectrum looked flat (white noise) for $f = 0.7$ to 23Hz. The sum should accentuate any correlated noise, here the noise appeared to increase with frequency (blue noise) for $f = 0.7 - 23$ Hz. This information may contain a clue to the source of "clocking" noise but more work is necessary.

b. Long Integration Time

Long integration times can provide the highest detector sensitivity so the noise here is quite important. Our technique is to insert the cold-dark slide and increase NF until the buckets are nearly full and then proceed as above. Typically we chose to look at one complete row from the detector and take 32 consecutive samples for noise analysis. If $NF = 1000$ giving 22 sec. integration, one run takes 12 minutes. A typical series is shown in fig. 9

for 2 detectors in row 20. This series was taken as the detector was cooling down. What is seen is a large drift in dark-current with time. Superimposed on this steady drift is a relatively small random noise component. Since our dewar has no active temperature control, the detector temperature is never completely stable. Then, because dark current approximately doubles for every 2°K temperature, a small temperature change results in a large change in signal. These large temperature induced dark current drifts can easily mask the true random component of noise. Therefore, an alternate method for determining the RMS detector noise was adopted. For white noise, the RMS noise in two samples will be $(\sqrt{2})^{-1}$ times the RMS noise in many samples. Therefore the RMS noise in successive pairs of samples was computed for all detectors in row 20 of the CCD. This was repeated for 6 pairs to assure a representative sample. The average was computed and multiplied by $\sqrt{2}$. The result for a typical run using $\Delta t = 44$ sec integration time was: the dark current gave $N \approx 5 \times 10^6$ electrons per charge dump while the RMS noise = 3900 electrons on average. Thus RMS noise $\approx 1.7 \sqrt{N}$, quite similar to the performance with $\Delta t = 22$ msec above.

In summary, the read-out noise ΔN is about $1.6 \sqrt{N}$ RMS electrons when the CCD is operated near full bucket capacity ($\Delta N \approx 3900$ electrons for $N \sim 5 - 8 \times 10^6$ electrons). With empty buckets, the read-out-noise has not been detected and we conclude $\Delta N < 1400$ electrons. Between these limits, the read-out-noise is as shown in fig. 7. We believe the excess read-out-noise is mainly caused by imperfect charge transfer from the detector storage sites to the CCD shift registers. Since it appears that this excess noise is correlated between all 1024 detectors, this will only result in a shift of the whole image up or down, an effect which can be calibrated out. Alternately, the new push-clocking scheme may eliminate this source of noise.

9. NEP

For a detector with a quantum efficiency η and an RMS noise of ΔN in an integration time t , the detector NEP will be given by

$$NEP = \frac{\sqrt{2} \Delta N h\nu}{\eta \sqrt{t}}$$

where $h\nu$ is the photon energy. Using our measured quantum efficiency at

3.8 μ m, read-out noise ΔN , and using $t = 22$ msec appropriate for high-background operation, the NEP = 4×10^{-15} W/ $\sqrt{\text{Hz}}$, which is about a factor of 2 above the blip limit. At low background, we are limited by dark current rather than background photons. For an integration time of 44 sec, which is the longest time for which we have an extensive set of noise data, the NEP = 9×10^{-17} W/ $\sqrt{\text{Hz}}$ at 3.8 μ m. It is anticipated that if the detector temperature could be reduced to 53°K or lower, an integration time of 1000 sec would be possible and NEP = 2×10^{-17} W/ $\sqrt{\text{Hz}}$ at 3.8 μ m achieved. Further, if the new clocking technique mentioned above proves successful in reducing read-out noise at small signal levels, these NEPs could be achieved with shorter time integration.

IV. Astronomical Imaging

Our techniques of astronomical imaging and image processing are described below, as well as a sample of the images produced to date.

A. Observing Technique

1. Flat-field

Using the optics shown in fig.2 in the lab, we find that the pixel to pixel sensitivity is quite uniform, varying by $\sim \pm 5\%$ over the whole array. When this dewar is mounted on the f/13.5 C. E. K. Mees 24" telescope, however, there is severe vignetting at the edges of the field of view, resulting in about a factor of 2 loss of signal at the extremes. Therefore we must correct each image frame for the unflat field. To do this we have observed the Moon, which is the only available reasonably flat source. From our investigations of the Moon described below, we recognize that much of the Moon is not flat (i.e. craters, highlands, terminator, limb). However we find that the center of a large mare near the subsolar point close to the full Moon is reasonably flat appearing. We de-focus the telescope and take images at 1.65 μ , 2.2 μ and 4.7 μ , where our detectors are not saturated. Then we take the sum of all the reasonably flat-looking frames to be used as a flat field. All the images shown here have been divided by this flat field and multiplied by a constant. Investigations involving imaging objects at various positions on the CCD have shown this technique to be accurate approximately to the $\pm 10\%$ level.

2. Standard Star Calibration

In order to calibrate the flux levels of the scenes imaged, we typically observe relatively bright standard stars through the night. We have used the stars α Boo, β Gem, α Lyr, α Leo, β Leo, α Peg and β Peg for this purpose during

March-May 1983. At each wavelength, the star will be imaged on various positions on the CCD. By subtracting two of the images, a positive and negative star image is produced with no need for a separate background frame. The fields are flattened as described above and all pixels which have signal are summed to give the total star signal. From the known star brightness a calibration quantity CFZM (counts for zero magnitude) is calculated; a table of these calibration values found in March 83 is given below (Table 2), appropriate for 1 air mass observations and 22 msec integration time. Also given is the flux density ($\text{Jy} = 10^{-26} \text{ W/m}^2 \text{ Hz}$) per count and the calculated efficiency of the telescope plus atmosphere. For the latter quantity, the quantum efficiency at $1.65\mu\text{m}$ and $2.2\mu\text{m}$ was assumed to be 0.61 as it is at $3.8\mu\text{m}$. The quite high resulting efficiencies, using a telescope with mirrors in need of recoating, at an altitude of only 2200 ft, indicate good quantum efficiencies are maintained down to at least $1.65\mu\text{m}$.

3. Astronomical Objects

a. On-chip integration

For each object observed at each wavelength, a decision must be made as to the on-chip integration time. Because of read-out noise considerations, the optimum integration time for best signal-to-noise is the longest time possible, consistent with not over-filling the charge buckets. The buckets may be filled by signal from the source, by thermal background photons (at 3.8 and $4.7\mu\text{m}$) or by dark current (at 1.65 and $2.2\mu\text{m}$). In addition with 11 sec integration, we have detected a small background signal at $1.65\mu\text{m}$ (probably OH air glow) and $2.2\mu\text{m}$ (probably thermal background, larger in the summer). The integration times we have used range from 22 msec ($\text{NF}=1$) to 22 sec ($\text{NF}=1000$).

The maximum sensitivity for low background observing ($1.65\mu\text{m}$ and $2.2\mu\text{m}$) is limited by the thermal dark current. Our procedure is to pump the LN_2 solid in the dewar and then invert the dewar and attach it to the telescope offset guider. Under these conditions, the detector temperature steadily increases with time, even though we have installed Chore Boy copper wool in the cryogen space which is heat sunk to the copper work surface. A typical example of the dark current vs time is given in fig.10. Because of this property, the maximum integration time we have been able to use when observing is 22 sec. For the most part, in fact, 11 sec integration is used in practice (i.e. M82, following section). With a dewar properly temperature stabilized to, say, 53°K , 1000 sec time integrations could be used, decreasing our NEP

by a factor of $\sqrt{1000/11} = 10$.

For the $3.8\mu\text{m}$ and $4.7\mu\text{m}$ filters, our sensitivity is limited by the high thermal background. Since our dewar has an f/8 field stop (to minimize vignetting) but the telescope is f/13.5, the thermal background is 2.8 times higher than it need be and the NEP is degraded by a factor of 1.7. Better performance at these wavelengths (as well as 1.65 and $2.2\mu\text{m}$) could be achieved if proper re-imaging optics were employed. The task is not simple as one must assure that the resulting images are not degraded over the whole CCD area from 1 to $5\mu\text{m}$ wavelength. A design for a doublet lens which accomplishes this task is given in fig.11; it was designed by Dr. Rudolph Kingslake of the Institute of Optics at the University of Rochester. We are planning on having the lens built by Infrared Industries Inc. and will use this lens in place of the dewar window. This lens design has the further advantages of being transparent in the visible for ease of alignment and non-hygroscopic. The Lyot stop will be cold and precisely aligned on the image of the telescope secondary, giving low thermal backgrounds and much flatter fields.

b. Off Chip Integration, Sensitivity

For increased signal-to-noise, successive charge-dumps may be co-added in real time in computer memory. Because of drifts in the thermal background, we have limited the total integration time to about 10 sec for $3.8\mu\text{m}$ and $4.7\mu\text{m}$, giving a sensitivity of ~ 8 mag/pixel (e.g. Jupiter, Saturn). Because of drifts in the dark current, we limit the total integration time to about 1-2 min. at 1.65 and $2.2\mu\text{m}$, adequate to reveal emission at the 13 mag/pixel level (e.g. M82).

c. Background Subtraction

The total signal we observe may be divided as follows:

$$\text{Signal} = \text{offset} + \text{background} + \text{dark current} + \text{object}$$

The offset is an electrical offset which is easily dealt with. However the signal due to the object of interest is often much less than the background + dark current signal. Therefore our procedure is to take scans in the sequence blank sky - object - object - blank sky - etc. The signals observed looking at blank sky near the object are later used to subtract the offsets from the signal of interest.

d. Nyquist Sampling

Each of our detectors image to $2.5''$ square on the sky. Since this is larger than the diffraction and typical seeing limit, we must sample each

scene with pixels moved by $1/2$ the pixel spacing on the object. Therefore a minimum of 4 scans should be acquired (i.e. $(0,0)$, $(0,1/2)$, $(1/2,0)$, $(1/2,1/2)$) to satisfy the Nyquist criterion. We currently achieve this in a somewhat haphazard manner, by taking many scans and determining the offsets after the fact. We would like to eventually automate this process, which requires us to step accurately at least to 0.05 mm or 1.25 ° .

B. Image Processing

In light of the above and other considerations, our procedure in image processing consists of:

1. Linearization

The output of the CCD is not precisely linear with input signal. We have calibrated this and find that as the signal nears full buckets, the gain decreases slightly. The maximum effect at full buckets is 14%. The first step is to linearize the raw signal counts by a factor of 1.0 to 1.14 depending on signal magnitude. The major effect of this step is to improve our calibration accuracy and linearity.

2. Background Subtraction

This is most important as often the signal of interest is much smaller than the drifting background signal (see above). We find that by taking a linear combination of the blank-sky frames just before and after an object frame, good subtraction may be obtained over the whole CCD. The most troublesome case of background interference is in the thermal infrared (3.8 and $4.7 \mu\text{m}$). There we often see drifts which give large gradients across the CCD (see Saturn image at $3.8 \mu\text{m}$ in following section); evidently the thermal background is not adequately stable over the ~ 40 sec observing period. We anticipate that higher frequency chopping, with the necessary subtraction being performed in computer memory, would give much improved thermal background subtraction.

3. Replace Bad Pixels

There are 97 pixels dead to the infrared and a handful of others with either high dark current, excess noise, or both, on our best CCD. To determine the signal at these positions on the object we are imaging, we use other images with the object shifted on the CCD. Since we must take a minimum of 4 frames to satisfy the Nyquist Sampling Theorem (see above), we choose to space these frames such that bad pixels are "covered" by other frames. In a typical sequence of 4-6 frames, 60-90 of the ~ 104 bad pixels can be replaced in this manner.

4. Fix Remaining Pixels

The bad pixels remaining after 3 above are then "fixed" by linearly extrapolating the signal from adjacent good pixels. Special care must be exercised at this stage because it is possible that important parts of the object being imaged can be hidden by bad pixels.

5. Shift and Add

Now the individual scans may be combined to form the best possible image of the object in question. First we must determine the offsets of the various scans from each other. One scan is designated the master frame, placed nicely in the CCD window. The offsets of the other scans are determined after the fact by shifting and subtracting. A computer routine has been developed which allows a scan to be shifted in increments of 0.1 pixel; the brightness at a given point is derived by linearly interpolating from the four nearest neighbor pixels. That shifted scan is subtracted from the master frame. The shift parameters (i.e. right-left and up-down) are varied to give the best appearing subtraction. On individual frames with high signal to noise (i.e. Jupiter and Saturn at $1.65\mu\text{m}$), it is relatively easy to determine the amount of shift to 0.2 pixel (0.02 mm or $0.5''$). On frames with relatively low signal to noise (i.e. Saturn at $3.8\mu\text{m}$), the method is less precise (perhaps 0.5 pixels). Eventually, if image positioning to 0.2 pixels can be achieved at the telescope, we could determine these shifts before the fact and use this knowledge to combine many frames, even if no signal is obvious on any one of them.

Next, in order to improve the image appearance and retain the most possible spatial information (i.e. Nyquist sampling) the master frame is expanded from 32×32 elements to 63×63 elements, using the same linear extrapolation routine described above. This procedure smooths out the sharp edges which can occur with square pixels. Finally, the remaining, slave, frames are expanded to 63×63 , shifted, and added to the master frame. Numerical simulations with point sources and sharp edges show that these techniques should recover most of the spatial information in a given scene, up to the resolution limit of 1 pixel or $2.5''$ square.

6. Flux Calibration

By reference to measurements of standard stars, such as those summarized in Table 2, the resulting images may be calibrated for absolute surface brightness (mag/pixel, Jy/pixel, $\text{W}/\text{cm}^2\mu\text{m}$ star, etc.). We have found significant

variations in the signal from a given star with air mass (reduced signals at large air mass) and season (reduced signal at $1.65\mu\text{m}$ and $2.2\mu\text{m}$ in May 83 compared to March 83). Therefore it is important to measure a calibration star close in time and air mass to the object of interest. Further, even if clouds are present it is possible to get quite sharp and clear images at 1.65 and $2.2\mu\text{m}$, however it is nearly impossible to calibrate those images to absolute surface brightness.

C. Astronomical Images

1. The Moon

For our first efforts at astronomical imaging we mounted our 50 lb CCD dewar on a 12" Tinsley telescope on the U. of R. campus. Extreme telescope flexure (up to $8''$) limited the effectiveness of this attempt and useful data was only obtained on bright calibration stars and the Moon. However, the Moon proved to be a quite interesting object in the near-infrared and we present some of that data here. The most extensive data on the Moon were acquired on the 27-28 January, 1983 when the Moon was just short of full phase. On this telescope the full field of view of the CCD is $2.3''$ square and each pixel subtends $4.2''$ square. After reconnoitering most of the surface of the Moon at various wavelengths using the real-time display, we selected three regions for observation: the craters Grimaldi and Riciolli near the eastern limb, the region surrounding the crater Plato and an edge of Mare Chrisium. Data was collected in 22 msec snap-shots, which effectively freezes any image motion due to seeing or telescope jitter. The data was processed as described above, a portion of that data is presented below.

a. Plato

The infrared images at $1.65\mu\text{m}$ and $4.7\mu\text{m}$ of the vicinity of the crater Plato are shown in fig. 12. For comparison, we present a visible photograph of the same region, enlarged to approximately the same scale as the CCD images. On the visible image can be seen Plato's extraordinarily dark floor and the surrounding brighter highland regions. Several bright mountains are visible in the mare to Plato's south.

At $1.65\mu\text{m}$, the light from the Moon is primarily reflected sunlight, as it is in the visible. Comparison of the $1.65\mu\text{m}$ image with the visible image reveals an overall similarity of the two, with all the visible features mentioned above present in the $1.65\mu\text{m}$ image. We conclude that, in general, for the lunar material in this region, the $1.65\mu\text{m}$ reflectivity is closely related to the visible reflectivity. Some differences in detail exist between the two images. For instance note that the bright rim surrounding the crater appears considerably broader in the $1.65\mu\text{m}$ image. This could be due to ejecta from the crater which is relatively bright at $1.65\mu\text{m}$, but not noticeable in the visible.

At $4.7\mu\text{m}$, light from the Moon is primarily thermal radiation. Thus images at this wavelength may be interpreted as a thermal map of the surface layer, with hotter regions radiating more. In contrast to the $1.65\mu\text{m}$ image, the crater floor appears bright at $4.7\mu\text{m}$; evidently the visibly dark material there is absorbing relatively more sunlight and consequently is heated to a higher temperature. Other structure is apparent in the thermal image which we don't entirely understand at present. The relatively reduced contrast apparent in the thermal image compared to, say, the $1.65\mu\text{m}$ image is understandable in that the albedo of lunar material is generally low. A change in albedo from say 0.05 to 0.10 would double the amount of reflected light but decrease the absorbed light only 5% (from 0.95 to 0.90).

Another example of lunar imagery is given in figure 13, which shows the craters Grimaldi and Riccioli near the eastern limb of the Moon. The lunar terminator was near this position during our observation so there is a strong gradient of illumination from west to east on these images. Again, the correspondence between the visual image, reproduced from a photo taken at almost the same phase, and the $1.65\mu\text{m}$ image is very good. The $4.7\mu\text{m}$

thermal image shows a strong limb darkening effect, probably due primarily to the gradient of insolation mentioned above. Only just perceptible in this reproduction is the slightly hotter floor of Grimaldi, near frame center. Enhanced emission from the dark maria to the northwest is also evident.

2. Jupiter

Jupiter was observed once on 26 March 83 UT and once on 25 May 83 UT using the C. E. K. Mees 0.6m telescope giving 2.5" pixels and a 80" field of view. Pertinent data for these observations and the calibration information for the May 83 data are given in table 3. The March 83 data are not as well calibrated but showed similar flux levels. Grey scale displays of the resulting processed images are shown in figures 14 and 15. The calibration of table 3 gives the maximum flux observed on the disk of Jupiter, for the images shown with linear scaling, the flux is linearly proportional to the image density (i.e. number of dots per pixel). These images are best viewed by de-focusing the eyes slightly, so that individual dots are seen as a blur.

The near infrared images of Jupiter are seen to be quite different than the visual appearance. This is primarily because of the strong molecular absorptions at these wavelengths. At 1.65 μ m and especially 4.7 μ m, there is relatively little molecular absorption while at 2.2 μ m and 3.8 μ m the CH₄, H₂, and NH₃ molecular vibration rotation bands are very strong. The 1.65 μ m images (figures 14 and 15) are most like the visible appearance, i.e. the whole disk is visible. Upon closer inspection, it is evident that there is strong limb-darkening at this wavelength and a somewhat asymmetric appearance (see the linear representation of figure 15). In March 83, the satellite Callisto was caught as it slowly moved by the planet (figure 14).

At 3.8 μ m and 2.2 μ m Jupiter is quite dim (maximum albedo \sim 0.01, table 3) because of molecular absorption. Referring to the 2.2 μ m image of figure 14, it is seen that much of the disk is even dimmer than this. We believe that the areas which reflect at 2.2 μ m are regions where there are high clouds in the Jupiter atmosphere, so that solar radiation doesn't have to penetrate as far before reflection. Referring again to figure 14, it is seen that high clouds were present just north of the equator and near the south pole of Jupiter. The May 83 2.2 μ m image was similar to

this. The $3.8\mu\text{m}$ radiation should also represent sunlight reflected from high clouds. Therefore it is interesting to note the difference in the appearance here (figure 15) compared to the $2.2\mu\text{m}$ image. A bright area north of the equator is present but the detailed shape is different. Also, the bright southern polar cap is not evident. These differences in appearance could be due to a differing cloud reflectivity at the two wavelengths and may provide a clue to the composition of the high clouds.

Two examples of the $4.7\mu\text{m}$ appearance of Jupiter are shown in figures 14 and 15. The most striking feature of these images are the two extremely bright bands running north and south of the equator. The band emission is more than can be explained by reflected sunlight (albedo=2.6), so it must result from thermal emission. The high brightness temperature we observe, 240°K , must come from a deep level in the Jupiter atmosphere. Similar images of Jupiter have been obtained before (Keay *et al.* 1973, Westphal *et al.* 1974). Because the $4.7\mu\text{m}$ region is a very clear window in the Jupiter atmosphere, one may see to deep hot layers through breaks in the cloud cover. Evidently such clear areas are concentrated in the bright regions seen here. Of interest in the March 83 image is the relatively cooler area on the southern edge of the southern bright band near the center of the disk. This is just the position occupied by the Great Red Spot at this time. A relatively cooler region near the GRS has been seen at times before. Interestingly, in the $2.2\mu\text{m}$ image on that date this region appears brighter, indicating a high cloud deck hovering over the Great Red Spot.

3. Saturn

Images of Saturn at 1.65 , 2.2 and $3.8\mu\text{m}$ were obtained on 25 May 83 using the C. E. K. Mees 0.6m telescope. Grey-scale displays of these images are given in figure 16 and the calibration data is given in Table 4.

The $1.65\mu\text{m}$ and $2.2\mu\text{m}$ images dramatically illustrate the effect of molecular absorption on the planetary appearance. At $1.65\mu\text{m}$, in an atmospheric window, the disk and ring of Saturn appear similar to visible images. However at $2.2\mu\text{m}$ strong H_2 and CH_4 absorption dim the disk, while the rings, which have no methane atmosphere, remain bright. One is presented with a partial ring system orbiting around the nearly invisible planet.

At $3.8\mu\text{m}$, the disk is dim (albedo=0.02) because of CH_4 absorption,

but the rings are also dim (albedo=0.05) because of the low reflectivity of water ice in this band. The net appearance is somewhere between the $1.65\mu\text{m}$ and $2.2\mu\text{m}$ images. Some structure is evident in the ring, but we have no explanation for it at present. At $3.8\mu\text{m}$, Saturn is quite dim with the maximum brightness of $+5.8\text{mag/pixel}$ on the rings and a minimum level of about $+8.2\text{mag/pixel}$ discernable. The gradient in signal across the whole CCD frame ($80''$ wide) results from incompletely subtracted background emission. We find that during the ~ 10 sec between our background frame and signal frame, the background emission, which is 6000 times as bright as Saturn, drifts in an unpredictable manner. A similar but less pronounced gradient is seen in the Jupiter $3.8\mu\text{m}$ image (figure 15). This demonstrates the necessity for faster beam switching (i.e. chopping) in the high-background thermal infrared for best sensitivity.

4. M82

The active galaxy M82 was observed on three nights in March 83 using the C. E. K. Mees 0.6m telescope. The pixel size was $2.5''$ square and the total field of view $80''$ square. The resulting $1.65\mu\text{m}$ and $2.2\mu\text{m}$ images are shown in figures 17 - 22. At each wavelength, a low and high contrast grey scale image and a contour plot is shown. M82 is not a bright source; in order to detect it an on-chip integration time of 11-22 sec was employed. The lowest contours shown represent a brightness of about 13mag/pixel . For this brightness, the dark current signal is about 400 times larger than the signal from M82. The good quality of these images demonstrate our success at subtracting the drifting dark current background using the techniques described earlier. As shown in figures 9 and 10, over short time periods the dark current drift is approximately linear and correlated from pixel to pixel. Therefore our linear interpolation technique can, with care, subtract it.

The images of M82 are quite interesting and show structure in this galaxy not heretofore revealed. First, the $2.2\mu\text{m}$ image is dominated by the very bright central core ($\sim 10'' \times 20''$), superimposed on the galactic disk stretching right across the detector. Rieke *et al.* (1980) have obtained a similar map of the core region but did not detect the disk emission, probably because of their small, $15''$ chopper throw. They showed that the brightest spot here was coincident with the dynamical center of

the galaxy and offset about 3" southwest from the brightest optical spot. Those authors argued that the near infrared emission emanated from cool giant stars remaining from a previous epoch of star burst activity. An interesting feature of this portion of our image, which wasn't apparent in the Rieke et al. data, is the extension of the lower contours to the southwest. The extension is also seen in the 1.65 μ m image. This in the region of most intense current star-formation activity, as evidenced by intense non-thermal radio signals and large 10 μ m luminosity. Perhaps

a concurrent new generation of cool giant stars is forming in this region. The 1.65 μ m image (figures 17 - 19) of M82 is similar to the 2.2 μ m image in the core region. One difference is the double peak at the very peak level, seen as a peanut or bone shape in the contour plot (figure 19). By lining up the 1.65 μ m and 2.2 μ m images at the outer contours, it is seen that the western 1.65 μ m peak corresponds to the 2.2 μ m peak position, which is the galaxy center. That puts the eastern peak right at the brightest optical position mentioned earlier. The varying appearance of M82 at these wavelengths is probably due to varying extinction and reddening, with more extinction at the 2.2 μ m peak (galaxy center).

Moving outside the core region, we see that in both the 1.65 μ m and 2.2 μ m images, there are two bright patches symmetrically placed on each side of the nucleus. We are not aware of this structure being seen before. Images of this galaxy at shorter wavelengths show a quite irregular and chaotic appearance, partly due to patchy extinction. At 2.2 μ m, the extinction is about a factor of 15 less than in the visible giving much clearer picture of the distribution of luminous matter. The emission at these wavelengths probably comes from cool giant stars. One possible explanation for the symmetric structures seen is a ring or partial disk of stars seen nearly edge on. The stars could be evidence for additional star-formation activity in a ring surrounding the nucleus. The radius of the ring would be about 25" or 400pc. It would be interesting to see if there is any evidence for star-formation in this region at present. Maps of CO millimeter wave emission or 10-100 μ m dust emission would be sensitive to this type of activity.

ACKNOWLEDGEMENTS

This research was supported by NASA Ames grant NAG 2-117.

References

Ando, K. J. (1978) NASA-CR-152, 169. "Assessment Study of Infrared Detector Arrays for Low Background Astronomical Research".

Hoendervoost, E. M. et al. (1978) "Hybrid InSb Focal Plane Array Fabrication", IEEE International Electron Devices Meeting, Washington, DC.

Keay, C. S. L. et al. (1973) Ap. J., 183, 1063.

Parrish, W. J. et al. (1978), "Characterization of a 32x32 InSb Hybrid IR Focal Plane", IEEE International Electron Devices Meeting, Washington, DC.

Rieke, G. H. et al (1980), Ap. J., 238, 24.

Steckl, A. J. (1975) Proc. 1975 CCD Appl. Int. Conference, San Diego, 85.

Westphal, J. A. et al. (1974) Ap. J., Letters, 188, L111.

UNIVERSITY OF ROCHESTER INFRARED CCD
32 X 32 InSb DETECTORS

EVALUATION SAMPLES ON LOAN FROM SBRC
(DR. ALAN HOFFMANN)

EVALUATING THEIR ASTRONOMICAL POTENTIAL FOR
SBRC AND NASA AMES RESEARCH CENTER

BUCKET SIZE: 10^7 ELECTRONS

QUANTUM EFFICIENCY: 0.65

FULL BUCKET NOISE: $1.5 \sqrt{N}$

CTE: 0.9994

AT $T = 60^\circ \text{K}$

DARK CURRENT: .01 pA

DETECTOR RESISTANCE: $10^{12} \Omega$

FOR ASTRONOMY

IMAGING PROPERTIES: EXCELLENT

REPEATABILITY: VERY GOOD

LIMITING MAGNITUDE (K, 0.6m TELESCOPE, 110 SEC): 12.4 MAG/PIXEL

TABLE 1: SUMMARY OF INFRARED ARRAY PROPERTIES

TABLE 2-STELLAR CALIBRATION DATA, MARCH 83
C. E. K. MEES 0.6m TELESCOPE

| FILTER | $\bar{\lambda}$ (μM) | $\Delta \lambda_{\text{FWHM}}$ (μM) | CFZM | JY/COUNT | EFFICIENCY TELESCOPE & ATMOSPHERE |
|--------|--------------------------------------|---|----------------|----------|---|
| H | 1.65 | 0.32 | 1500 \pm 100 | 0.68 | 0.75 |
| K | 2.23 | 0.41 | 950 \pm 50 | 0.65 | 0.75 |
| L' | 3.75 | 0.81 | 390 \pm 15 | 0.63 | 0.63 |
| M' | 4.67 | 0.18 | 39 \pm 4 | 4.2 | 0.58 |

JUPITER IMAGES

PHYSICAL DATA

| | 26 MARCH 83 | 25 MAY 83 |
|-----------------------------------|--------------|-----------|
| PHASE ANGLE (°) | 9.7 | 0.4 |
| EQUATORIAL DIAMETER (") | 40.4 | 45.4 |
| SYSTEM III CENTRAL | | |
| LONGITUDE 4.67 μ EXPOSURE (°) | 84 | 319 |
| GREAT RED SPOT | | |
| SYSTEM III LONGITUDE (°) | \approx 97 | 112 |

MAXIMUM INFRARED BRIGHTNESS 25 MAY 83

| λ | INTEGRATION TIME | MAG/PIXEL | ALBEDO | T_B |
|------------|------------------|-----------|--------|-------|
| 1.65 μ | 6.6 SEC | +2.7 | 0.26 | |
| 2.24 μ | 44 SEC | +6.3 | 0.010 | |
| 3.75 μ | 44 SEC | +5.7 | 0.015 | |
| 4.67 μ | 26 SEC | +0.1 | 2.6 | 240°K |

TABLE 3

SUMMARY OF JUPITER PHYSICAL DATA AND CALIBRATION
OF THE 25 MAY 83 INFRARED IMAGES.

SATURN IMAGES 25 MAY 83

PHYSICAL DATA

EQUATORIAL DIAMETER DISK = 18.7" RINGS = 42.0"

PHASE ANGLE = 3.5° RING TILT = $+14.9^{\circ}$

MAXIMUM INFRARED BRIGHTNESS

| λ | TOTAL TIME | MAG/PIXEL | | ALBEDO | |
|------------|---------------|-----------|------|--------|------|
| | | RINGS | DISK | RINGS | DISK |
| 1.65 μ | 10.5 SEC | +3.9 | +3.5 | 0.32 | 0.46 |
| 2.24 μ | 10.5 SEC | +4.0 | +6.0 | 0.28 | 0.04 |
| 3.75 μ | 44 SEC | +5.8 | +6.7 | 0.05 | 0.02 |

TABLE 4

SUMMARY OF SATURN PHYSICAL DATA AND
CALIBRATION OF THE INFRARED IMAGES

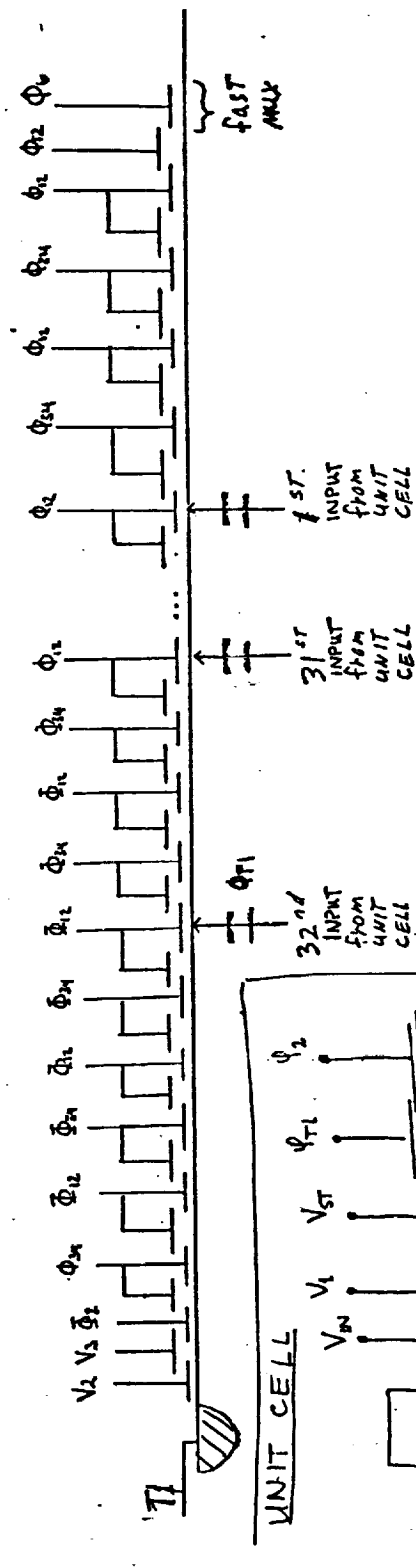
Figure Captions

1. A schematic diagram showing the layout of the silicon CCD and a typical input from one of the 32x32 InSb detectors (unit cell).
2. A schematic showing the placement of the CCD and optical elements in the LN₂ dewar. The 1/4" diameter CaF₂ lens is used for laboratory imaging and removed when mounting on a telescope.
3. Images of human beings at 3.8 μ m obtained with 22 msec exposures in the lab.
4. Images at 1.65 μ of an artificial star field set at high and low intensity. The high signal image (upper) is from one 22 msec exposure. The low signal image is the sum of 8 11 sec exposures and is about 400 times dimmer. Also included is a copy of the mask used to generate the star field. On the low signal image, one star in the upper left has been lost due to high dark current there.
5. A grey-scale rendition of the dark current across the whole CCD. The chip temperature was 62°K and the integration time 44 sec. The white cells are from saturated pixels. For most of the pixels the buckets are about 1/3 - 2/3 full.
6. Grey-scale rendition of a 4.7 μ m flat-field obtained in the laboratory. The cold-dark signal has been subtracted and the 97 black squares are dead pixels. The pixel to pixel uniformity of the working detectors is quite good.
7. The RMS noise as a function of background signal at 4.7 μ m for a 22 msec integration time. The error bar represents the expected statistical uncertainty in individual measurements. One count represents about 2300 electrons and full buckets give about 4000 counts. Solid lines representing the minimum noise of our electronics ("noise floor") and the shot noise limit ($=\sqrt{N}$) are shown.
8. An example of good (upper) and bad levels of the "clocking" noise described in the text. 32 samples of 32 detectors in row 20 have been taken, the DC level subtracted, and the remaining noise fluctuations displayed in grey-scale with time increasing downward. The horizontal bands seen across all 32 detectors are due to "clocking" noise (correlated jumping of the whole CCD output).
9. Measurements of dark current in two pixels vs time in the lab as the CCD

cooled down. The integration time was 22 sec and full buckets approximately 4000 counts.

10. Measurements of the dark current in two pixels vs time with the dewar mounted upside down on the C. E. K. Mees telescope and M82 being observed. The integration time was 11 sec.
11. A 1-5 μ m 1:1 re-imaging doublet designed by Dr. Rudolph Kingslake. All aberrations are kept to <.05 mm over the whole CCD. The placement of a cold Lyot stop is indicated.
12. Infrared images of the lunar crater Plato compared to a visible image. The contrast has been enhanced to better show the detail in the infrared images.
13. Infrared images of the lunar craters Grimaldi and Riccioli compared to a visible image.
14. Images of Jupiter at 1.65 μ m, 2.2 μ m and 4.7 μ m on 26 March 83 UT. For the 1.65 μ m the grey-scaling is logarithmic, the rest are linear.
15. Images of Jupiter at 1.65 μ m, 3.8 μ m and 4.7 μ m on 25 May 83 UT. Grey-scaling is linear.
16. Images of the Saturn system at 1.65 μ m, 2.2 μ m, and 3.8 μ m on 25 May 83 UT.
- 17-19
The 1.65 μ m image of M82 in March 83. Two different grey-scale displays and one contour interval display are shown. All displays are linear and the pixel size is 2.5 π .
- 20-22
The 2.2 μ m image of M82 in March 83. Two different grey-scale displays and one contour interval display are shown. All displays are linear and the pixel size is 2.5 π .

SLOW MIX SCHEMATIC



FAST MUX

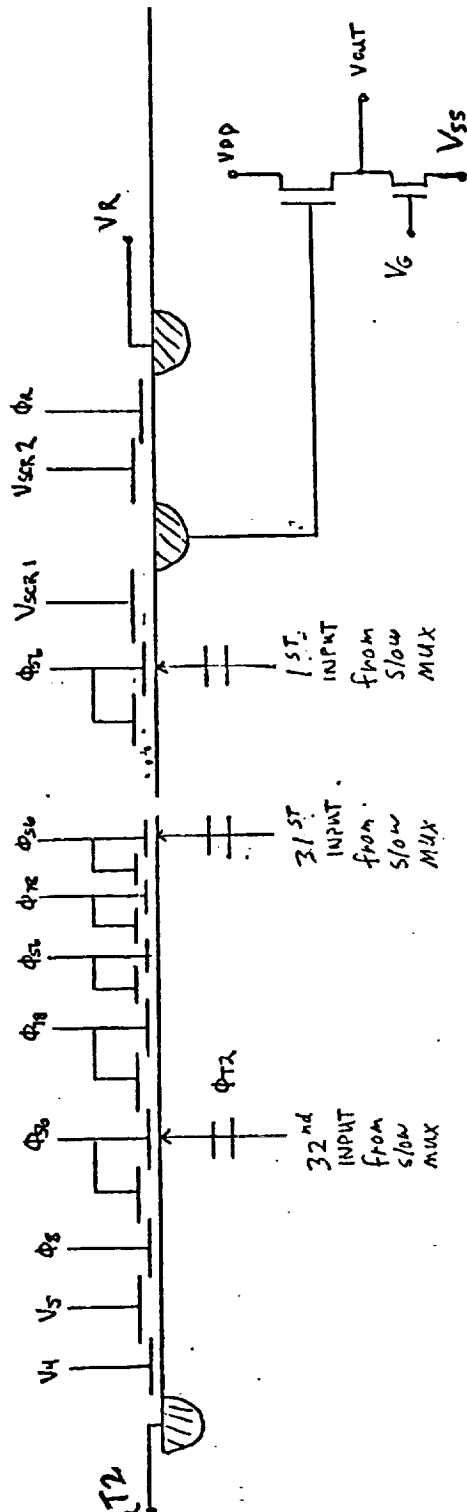


Figure 1

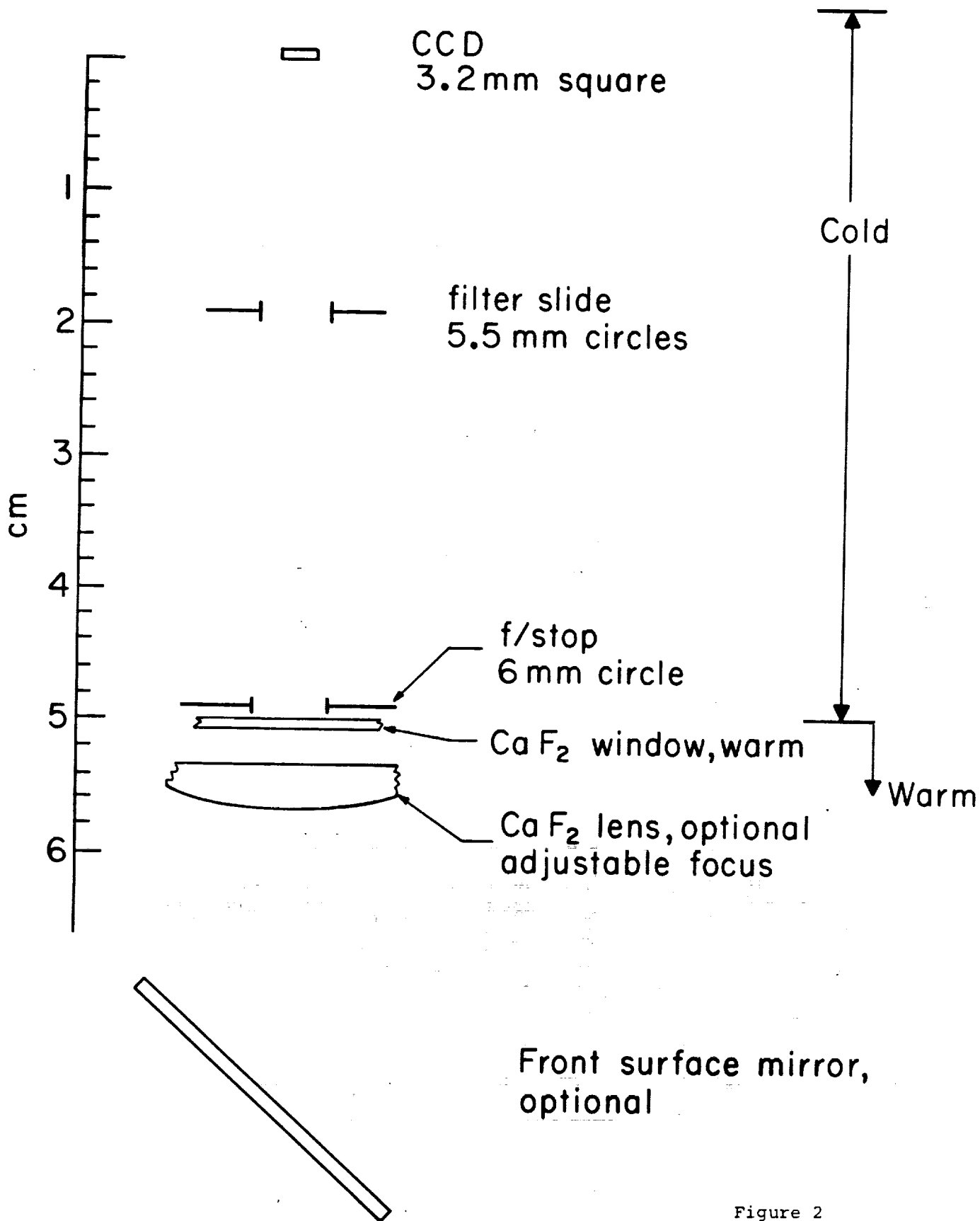


Figure 2

XXXXXXXXXXXX

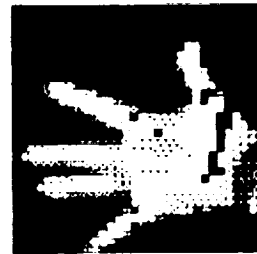
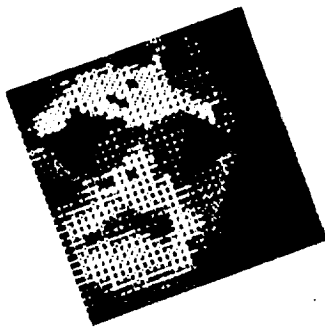
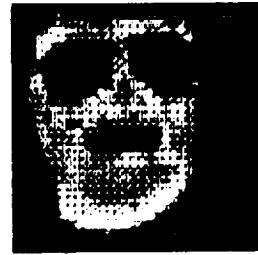
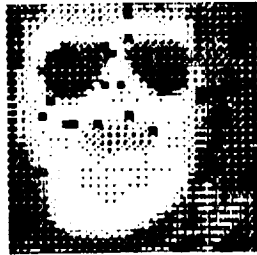
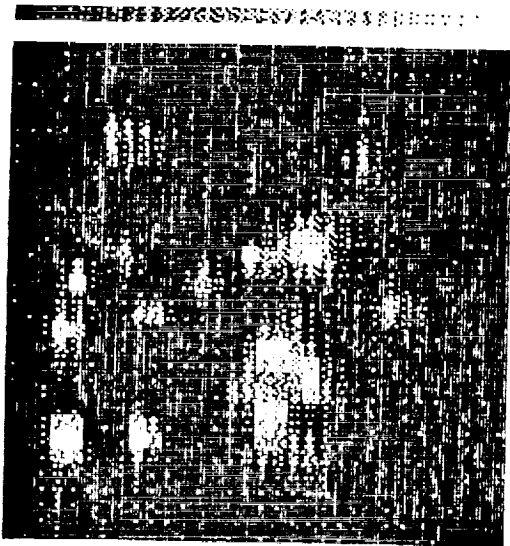
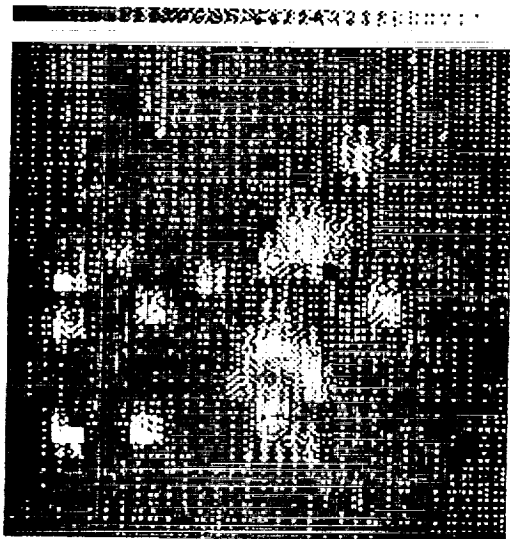


Figure 3



THE LIMITS FOR THE DATA ARE, MAX= 50 MIN= 0



THE LIMITS FOR THE DATA ARE, MAX= 550 MIN= 0



Figure 4

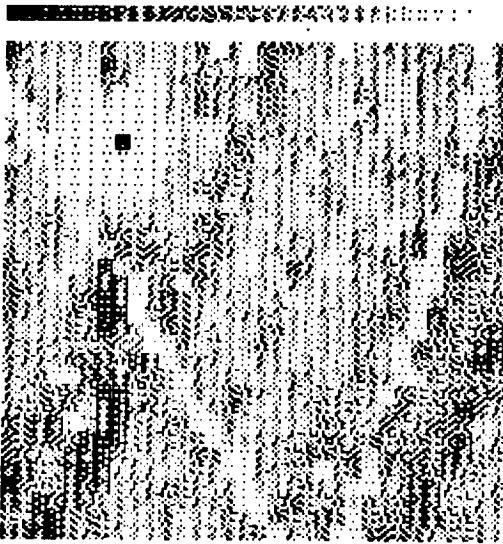


Figure 5

THE LIMITS FOR THE DATA ARE, MAX= 3600 MIN= 0

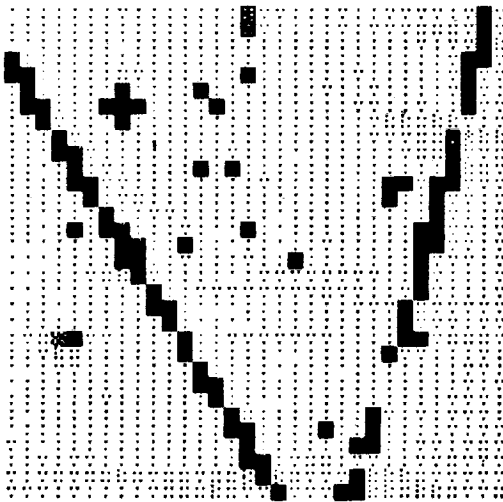


Figure 6

THE LIMITS FOR THE DATA ARE, MAX= 2700 MIN= 0

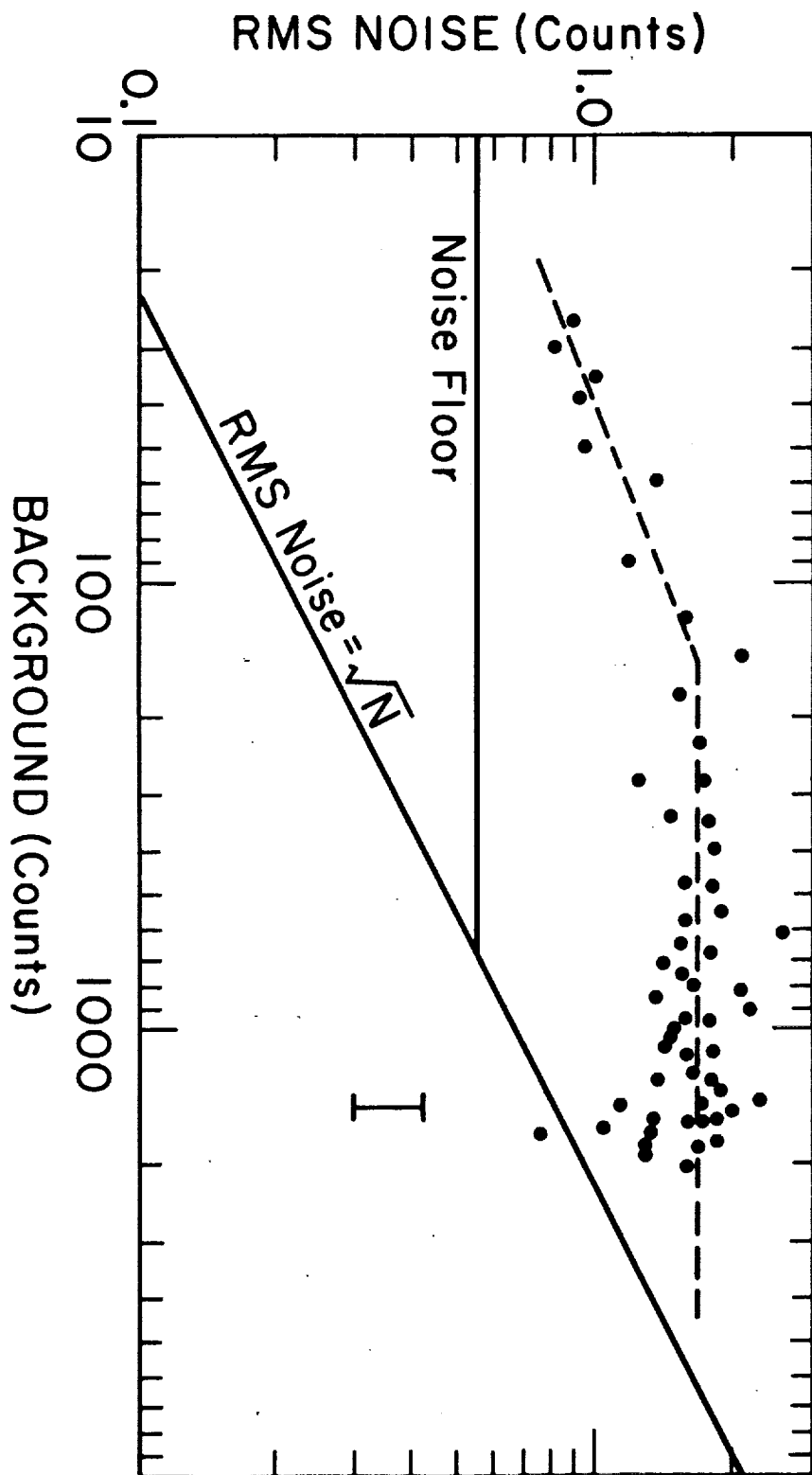
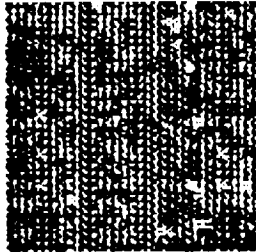


Figure 7

32 Samples of detectors 608 through 639 with 1 Frames/CD.

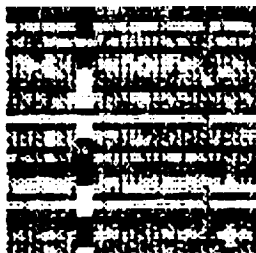
#####



THE LIMITS FOR THE DATA ARE, MAX= 8 MIN= -8

32 Samples of detectors 608 through 639 with 1 Frames/CD.

#####



THE LIMITS FOR THE DATA ARE, MAX= 8 MIN= -8

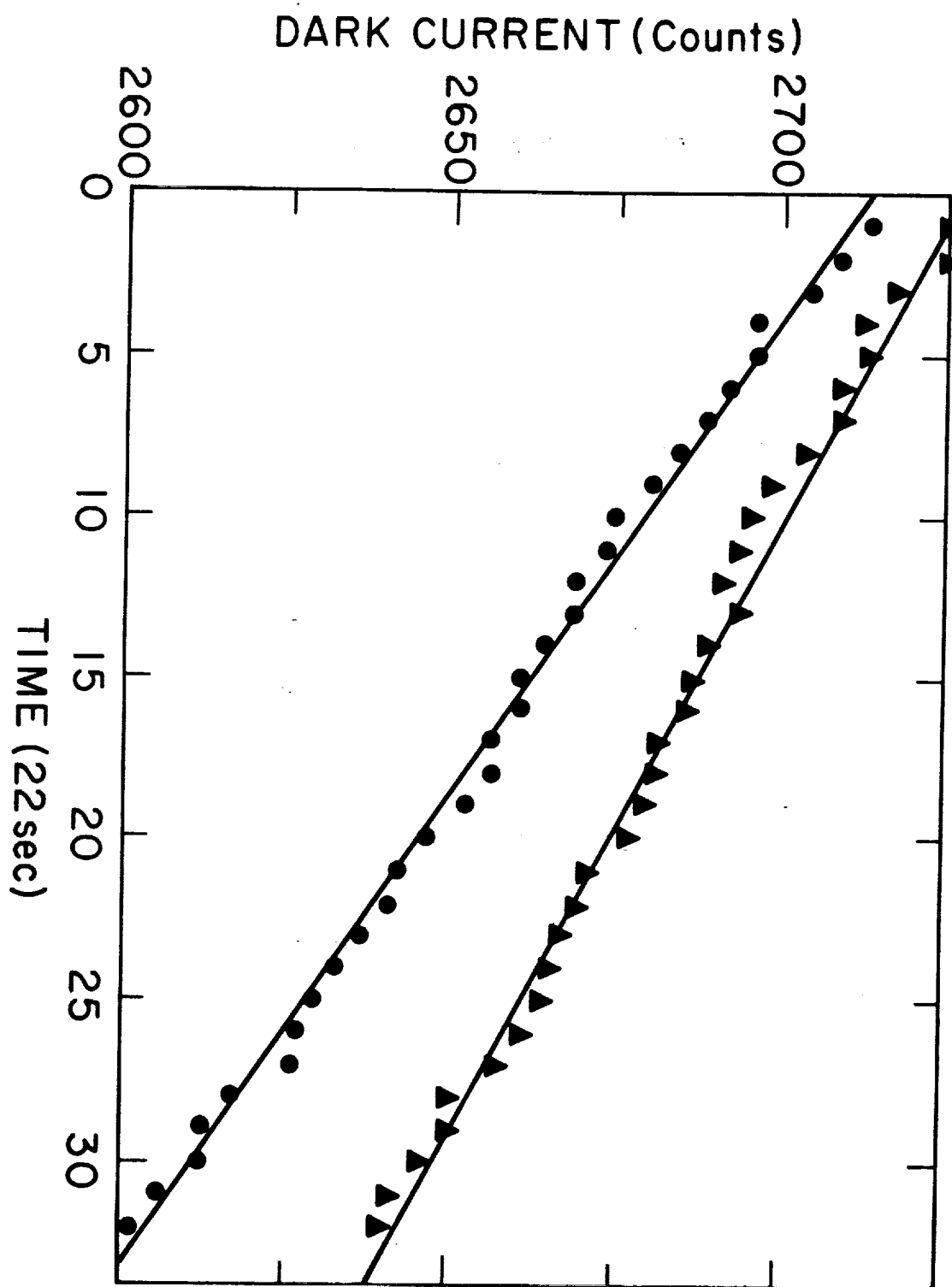


Figure 9

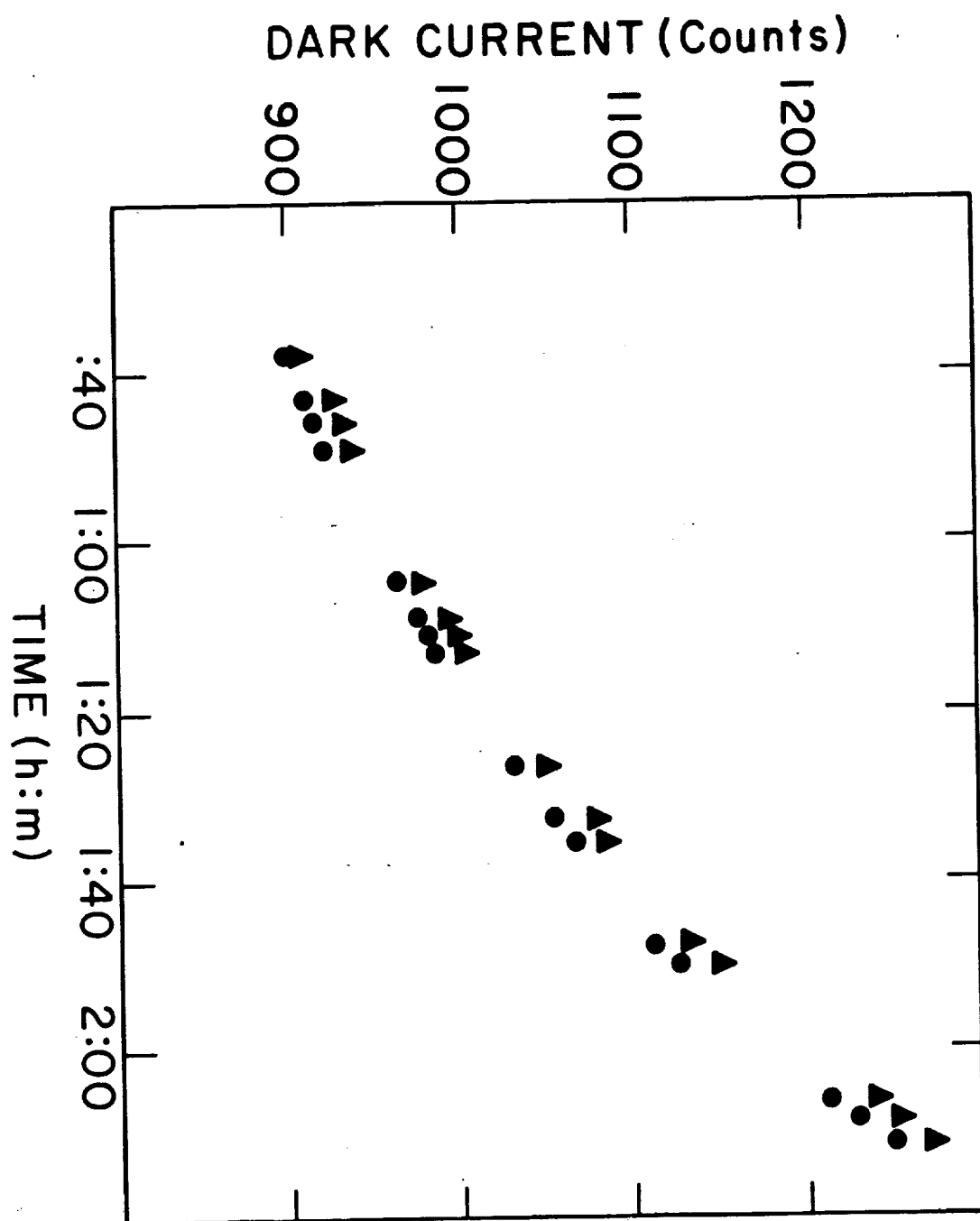
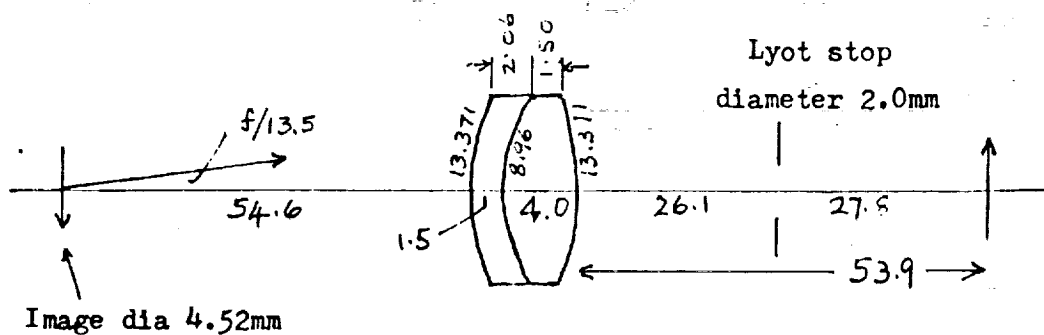


Figure 10

Infrared 1:1 relay lens

Intended for use behind the Mees Observatory telescope.



Materials

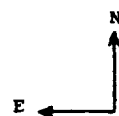
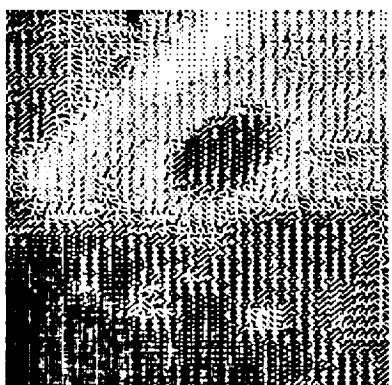
| Wavelength (in μ) | Neg lens: strontium titanate | Pos lens: calcium fluoride | Paraxial image distance |
|---------------------------|---------------------------------|-------------------------------|----------------------------|
| 1 | Index 2.31633 | 1.42888 | 55.202 mm |
| 1.4 | 2.29073 | 1.42672 | 54.194 |
| 2 | 2.26801 | 1.42385 | 53.810 |
| 3 | 2.23111 | 1.41785 | 53.871 |
| 4 | 2.18375 | 1.40963 | 54.201 |
| 5 | 2.12212 | 1.39895 | 54.596 |

Main wavelength assumed to be 3μ .

Point image everywhere smaller than 0.05mm.

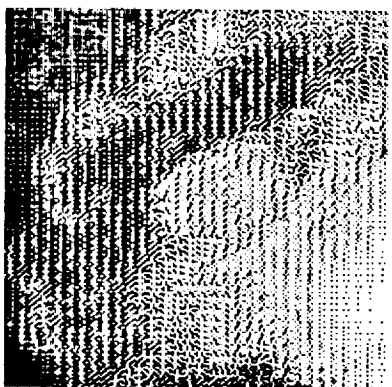
R. Kingslake
June 17, 1983

Figure 11

[illegible]

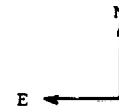
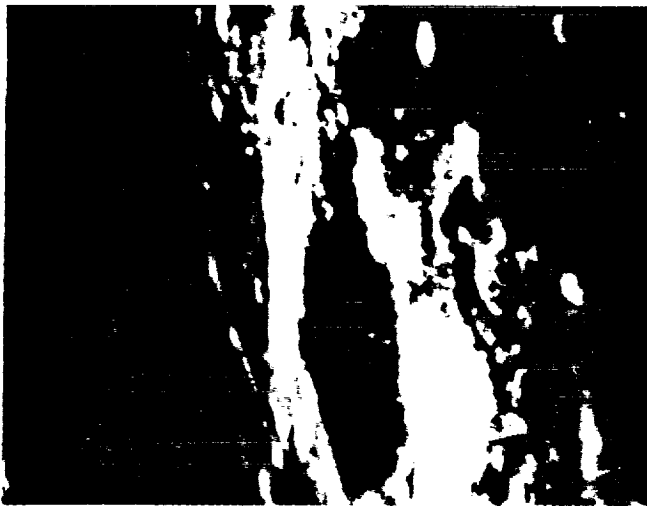
2.3 arcmin.

4.7um . Plato at

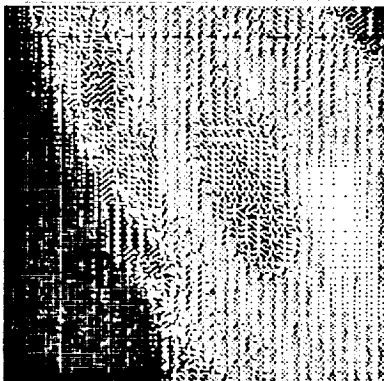


THE LIMITS FOR THE DATA ARE,
MAX= 3100 MIN= 1700

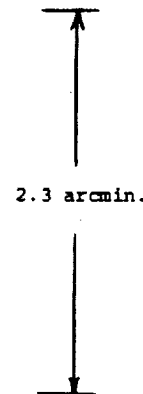
16-37



--Grimaldi and Riccioli in visible light.

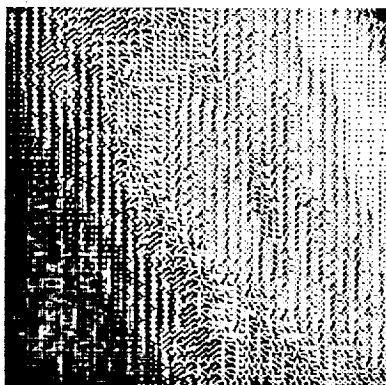


THE LIMITS FOR THE DATA ARE,
MAX= 3000 MIN= 0



-- 1.6 μ m

2.3 arcmin.



THE LIMITS FOR THE DATA ARE,
MAX= 1400 MIN= 0

-- 4.7 μ m

Figure 13

JUPITER 26 MARCH 1983 UT

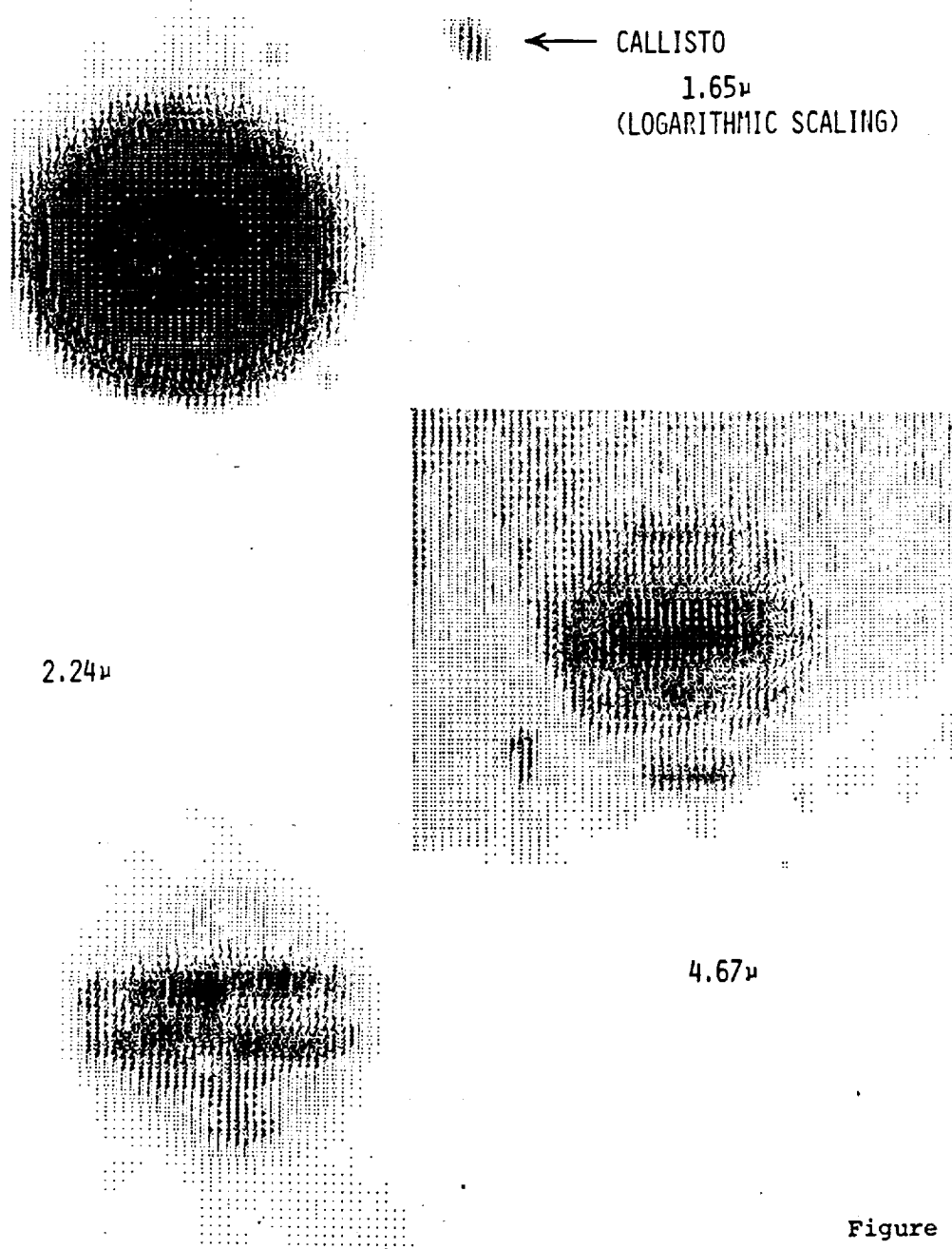


Figure 14

JUPITER 25 MAY 1983 UT

圖書在版編目(CIP)數據

1.65μ

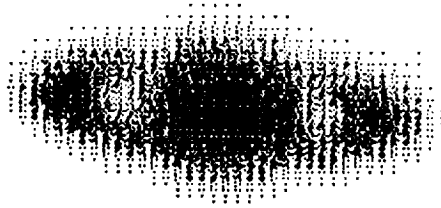
 3.75μ

4.67μ

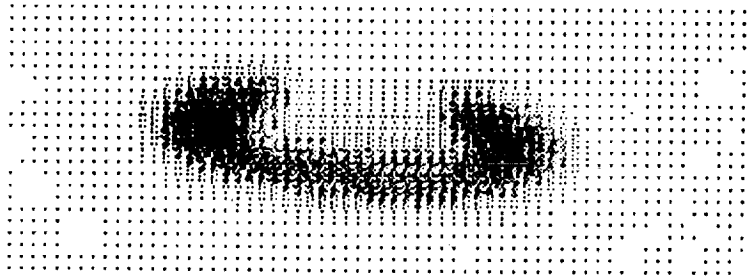
Figure 15

SATURN 25 MAY 1983 UT

1.65 μ



2.24 μ



3.75 μ

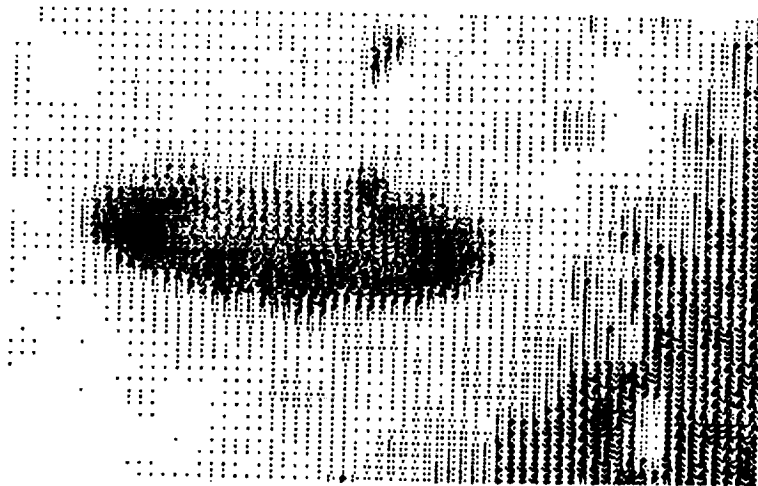


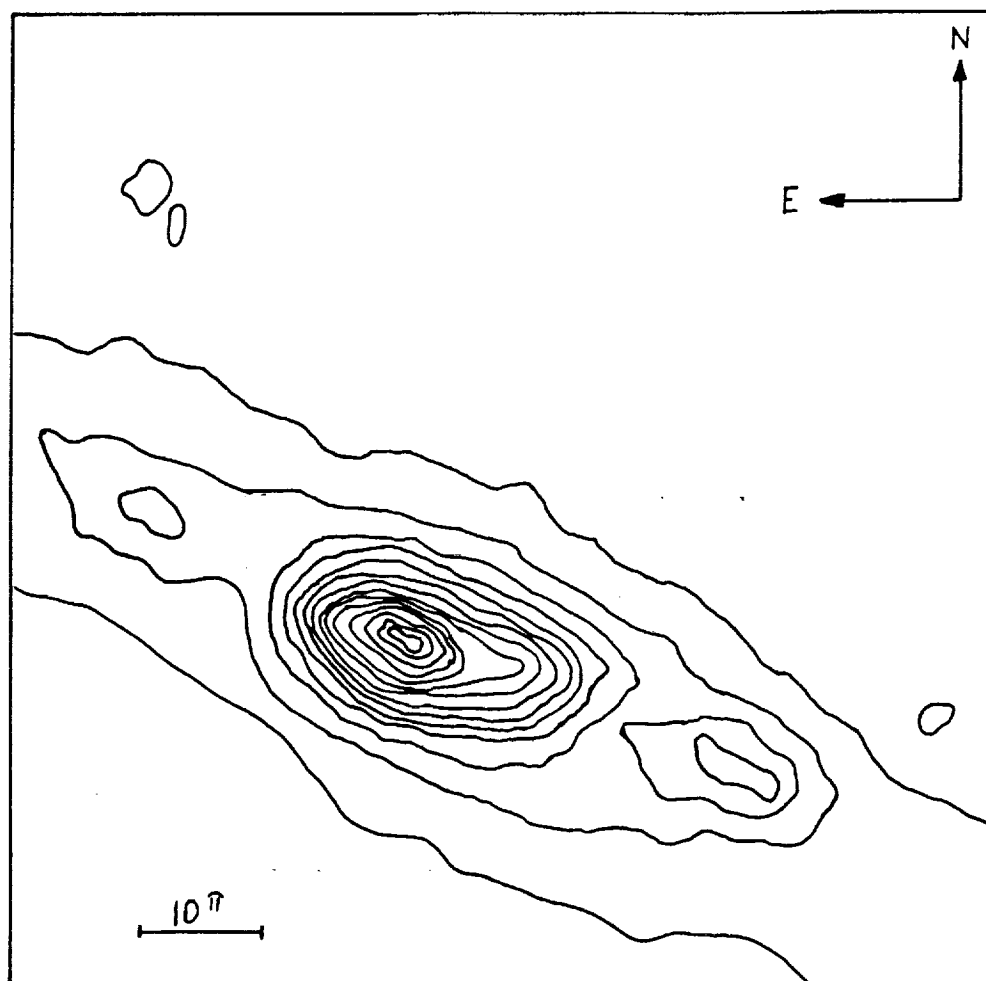
Figure 16



M 82 1.65 μ m
LOW LEVEL EMISSION

Figure 18

M 82 $1.65 \mu\text{m}$



PEAK FLUX: $B_v = 65 \text{ MJY/PIXEL}$
CONTOURS AT $N \times 4.3 \text{ MJY/PIXEL}$, $N = 1 \text{ TO } 15$
 $1 \text{ PIXEL} = 2.5'' \text{ SQUARE}$

Figure 19

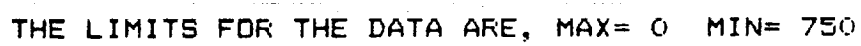
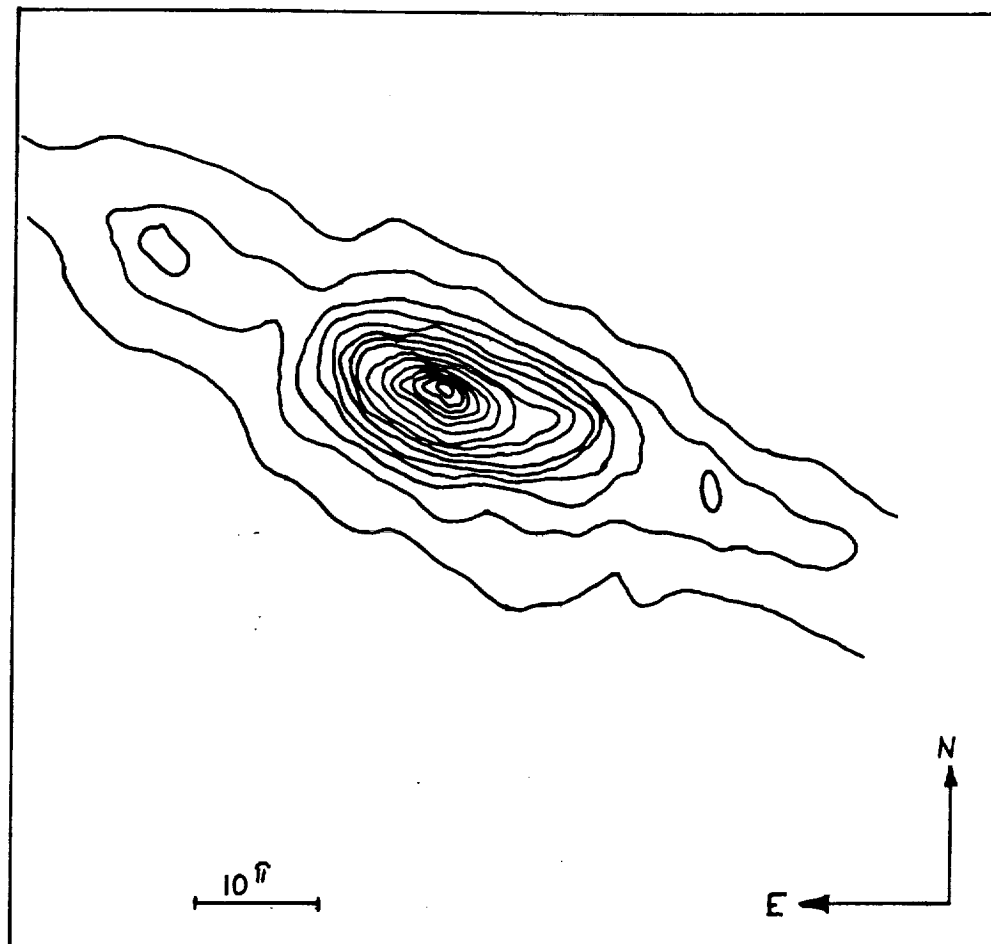


Figure 21

M 82, $2.2 \mu m$



PEAK FLUX: $B_v = 96 \text{ MJY/PIXEL}$
CONTOURS AT $N \times 6.2 \text{ MJY/PIXEL}$, $N = 1 \text{ TO } 15$
 $1 \text{ PIXEL} = 2.5'' \text{ SQUARE}$

Figure 22

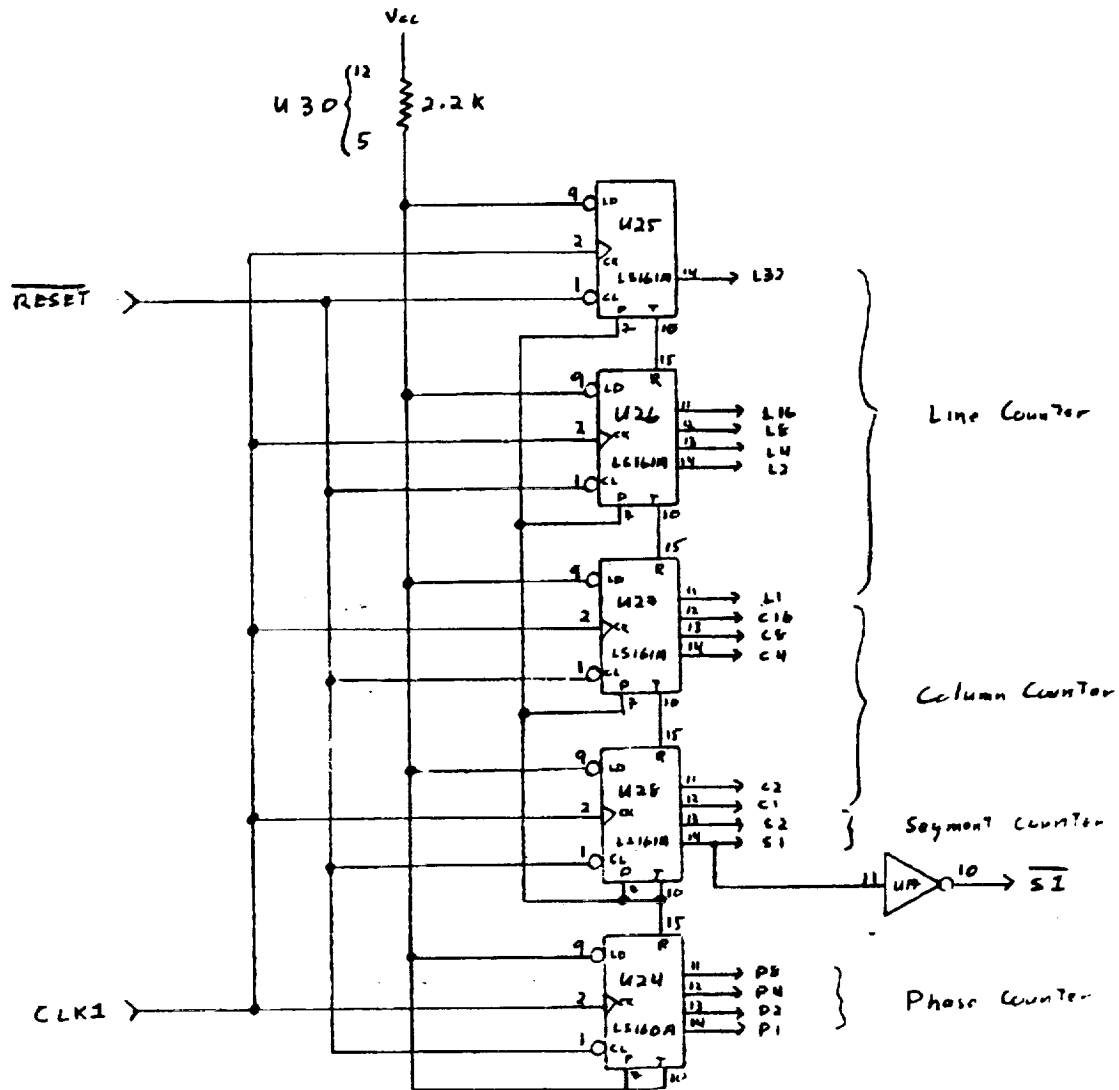
Appendix A: CCD Electronics

We include here circuit diagrams of the electronics developed at the University of Rochester to operate the SBRC 32x32 InSb array. The circuits are as follows: 1. CCD Clock 2. Clocked Drivers 3. DC Supplies 4. Clamp Amp 5. Real Time Display

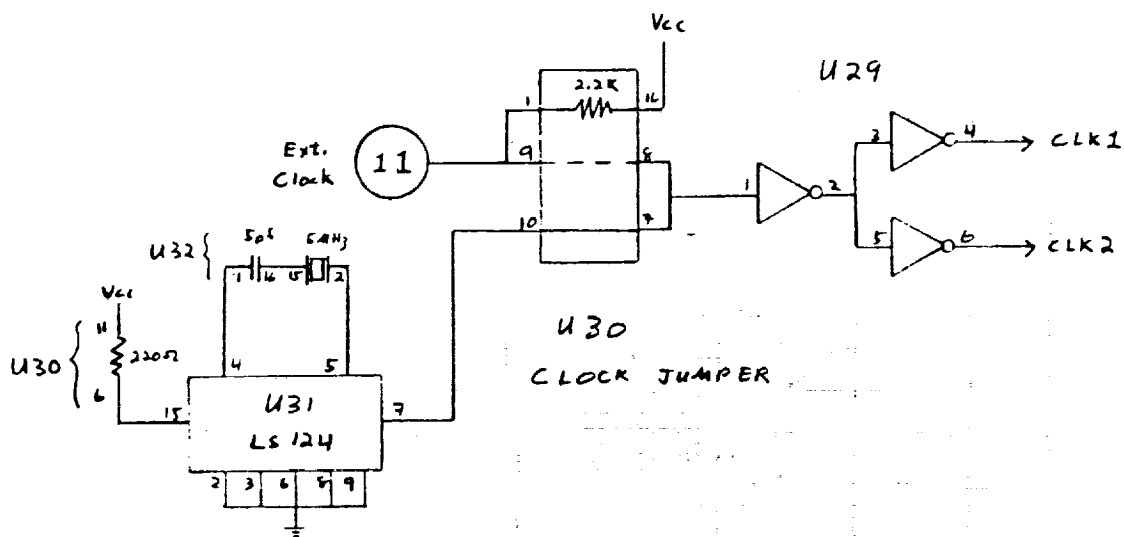
1. CCD Clock

A stand alone, hard wired, clock was designed and built by Cayuga Microcomputer Services to our specifications. The clock supplies the 9 clocked TTL levels needed to drive the CCD (see page 7) as well as two outputs (FRMST and CONV) to coordinate data taking with the computer. A new RTD pulse has been added for the Real Time Display (not shown here). All the circuitry fits on one 4x5" vector board and is wire wrapped to allow small modifications of clocking waveforms. The master clock can be internal or supplied externally to give various frame rates. A provision for external blanking, usually by computer, of the $\phi T1$ transfer pulse is provided ($\phi T1$ Inhibit, page 5).

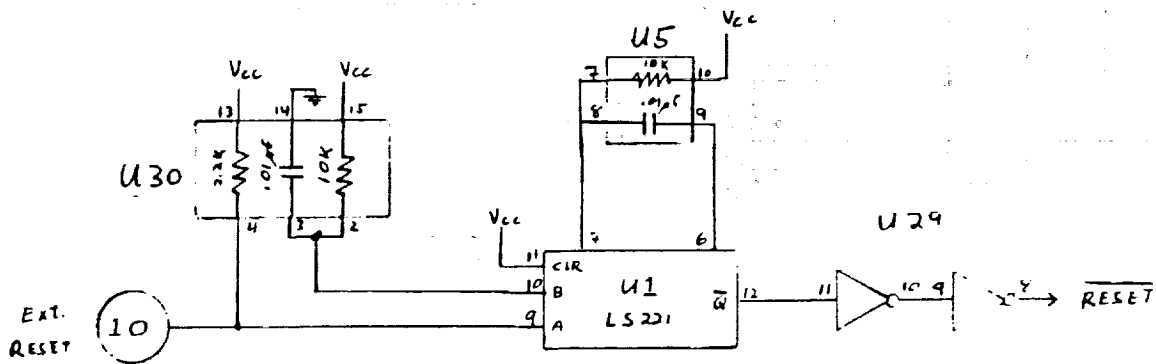
Counter Chain



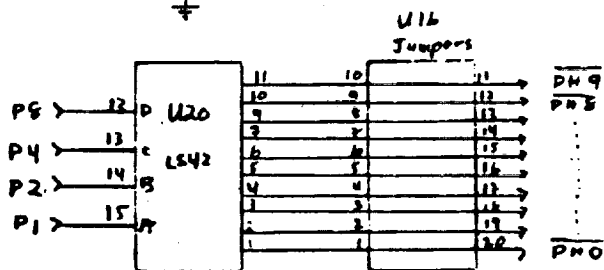
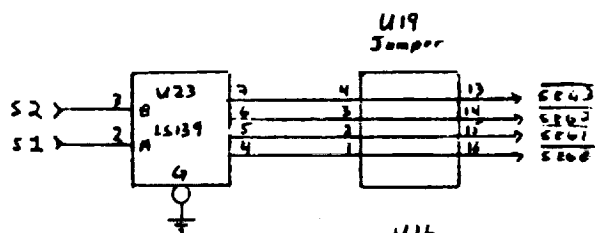
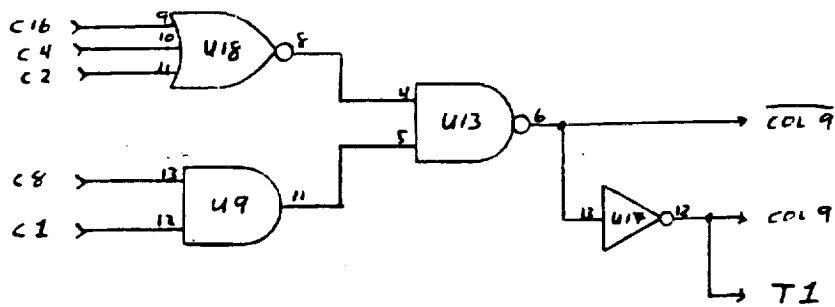
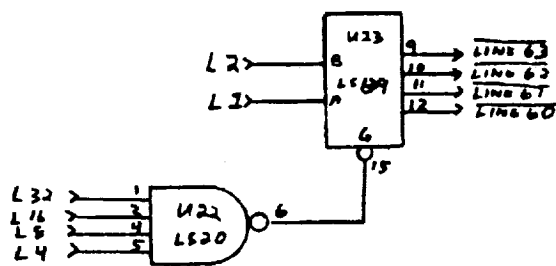
CLOCK



RESET



Counter Decoders



16-51

CCD CLOCK BOARD
Pg 3

CAYUGA MICROCOMPUTER SERVICES

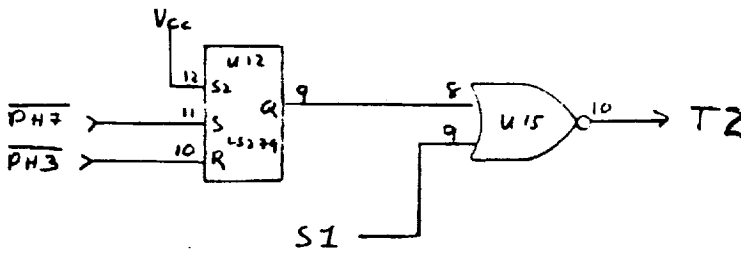
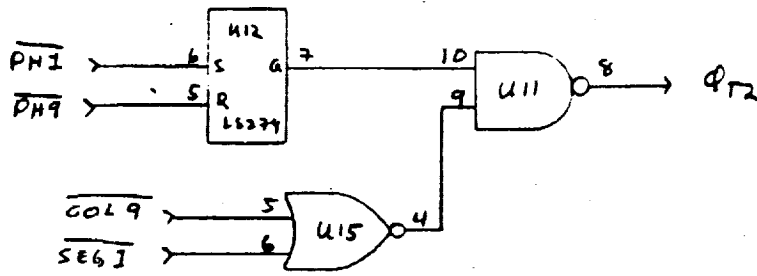
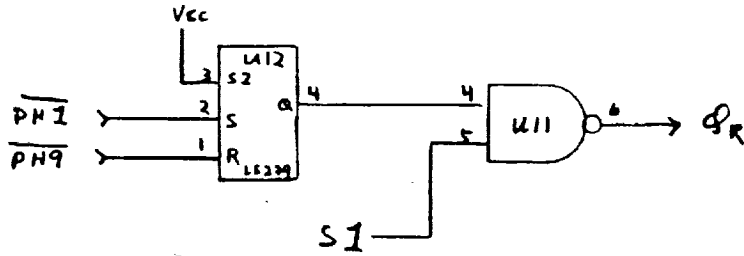
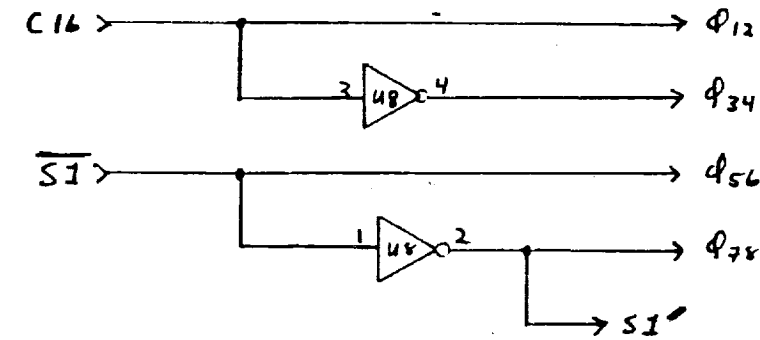
Drawn: 17-JAN-82

D.B

Revised: 17-JUL-82

D.B

Signal Generation - 1

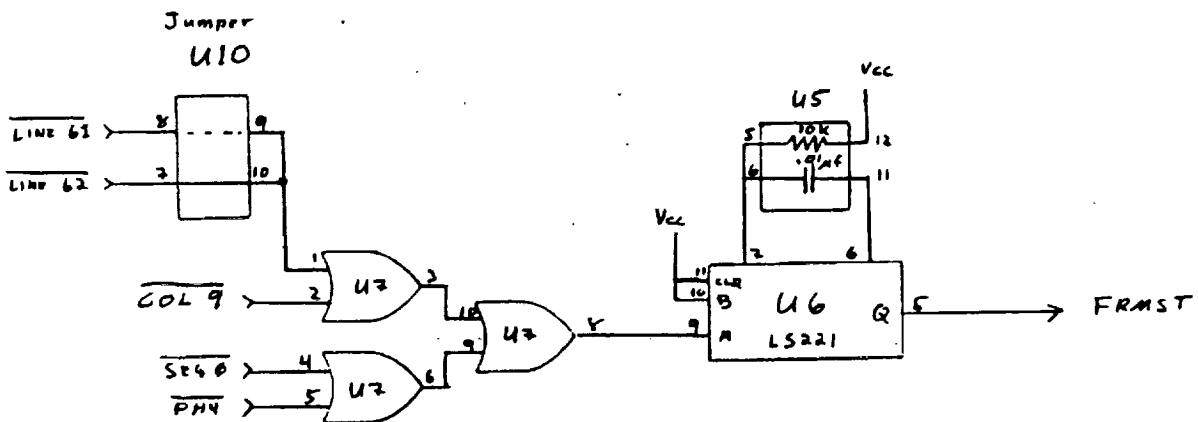
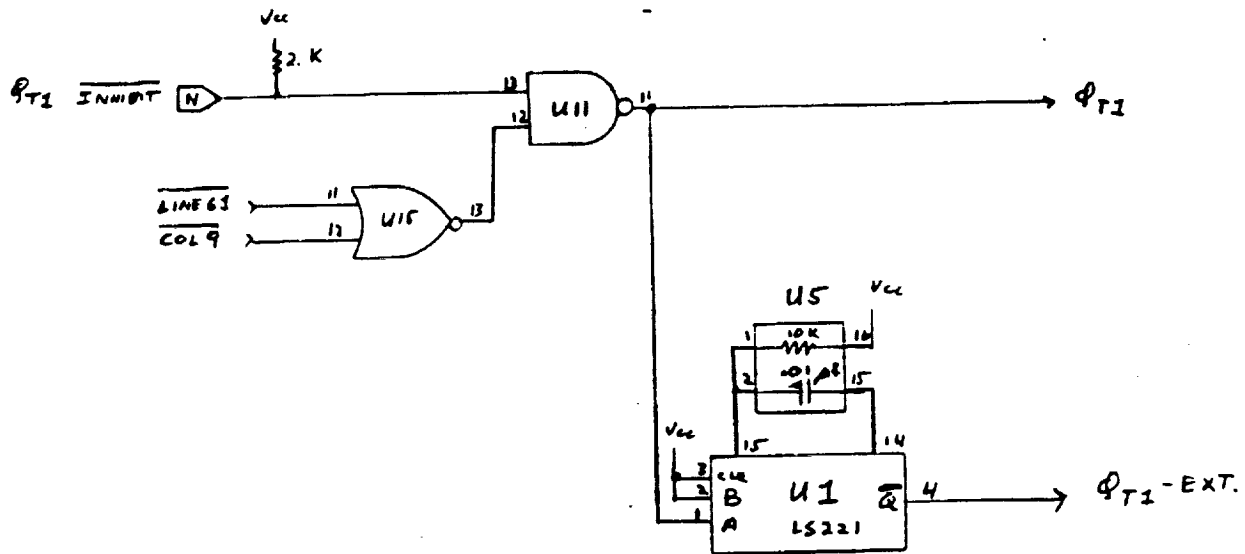


CCD CLOCK BOARD
Pg 4

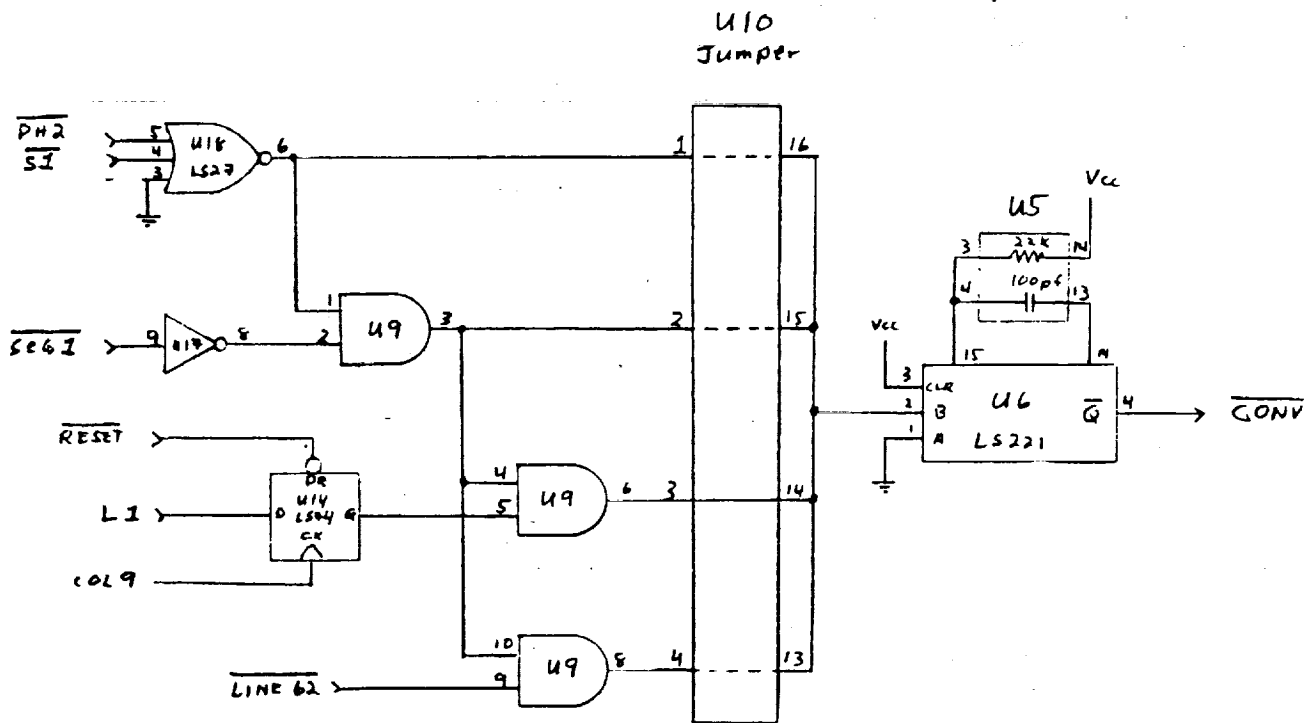
CANYON MICROCOMPUTER SERVICES

Drawn 17-JAN-82 D.B.
Revised 19-JUL-82 D.B.

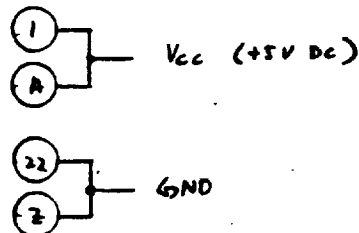
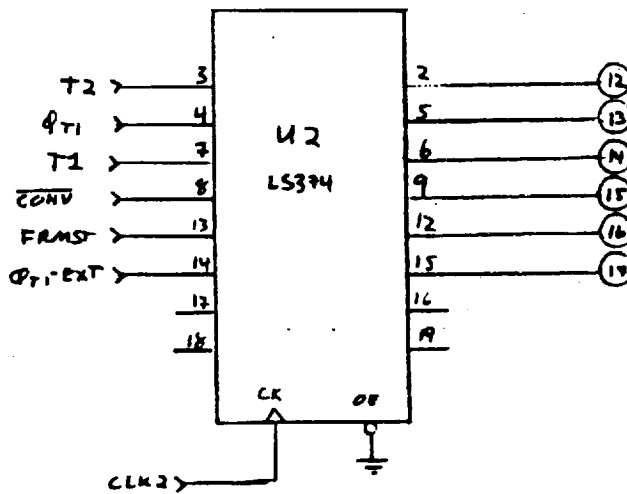
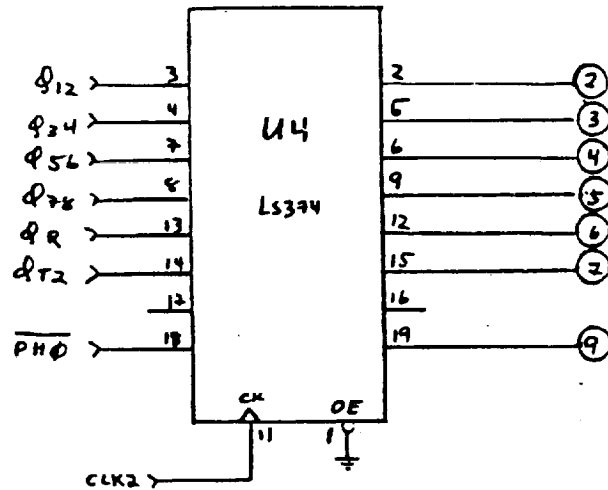
Signal Generation - 2



Signal Generation -3

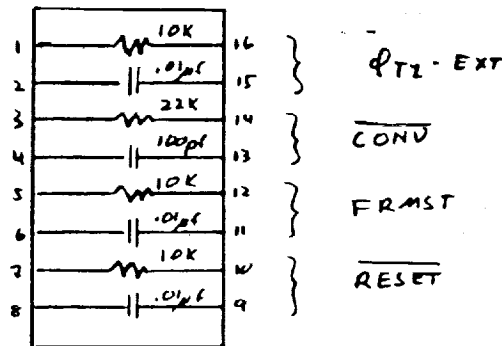


Output Buffers

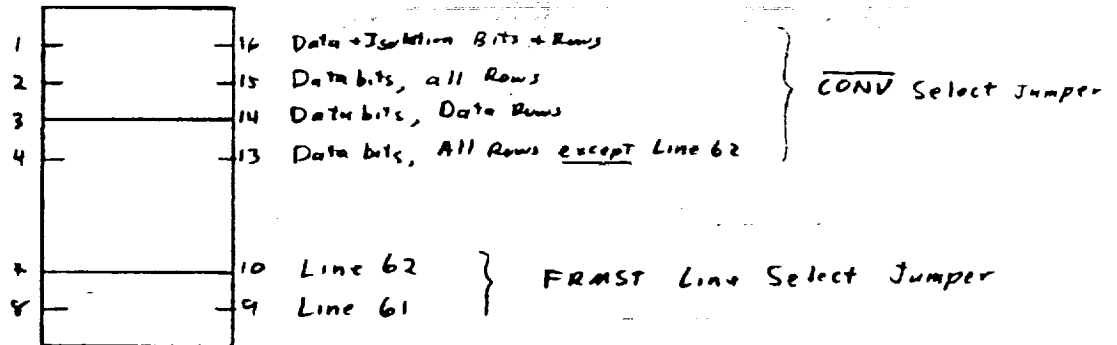


Jumper Index

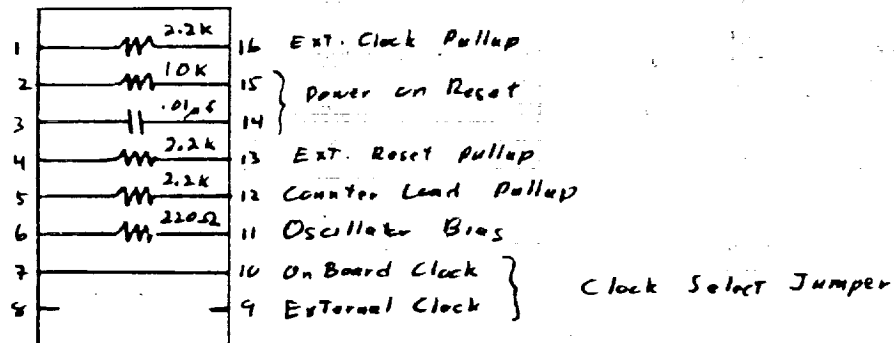
U5
One-Shot Timing



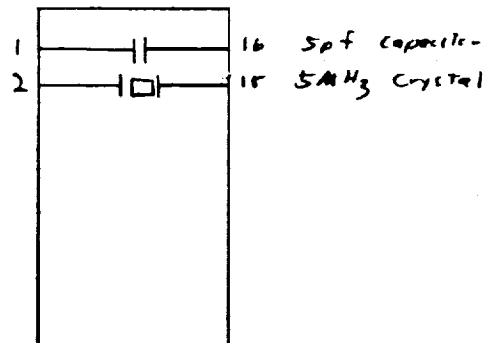
U10
CONV + FRMST
Select



U30
Pullups +
Clock Select



U32
Clock Crystal



2. Clocked Drivers

Driven by the TTL clock, each of these supply two adjustable (-13 to +13 V) voltage levels to a CCD input. Provision is made for an adjustable RC time constant.

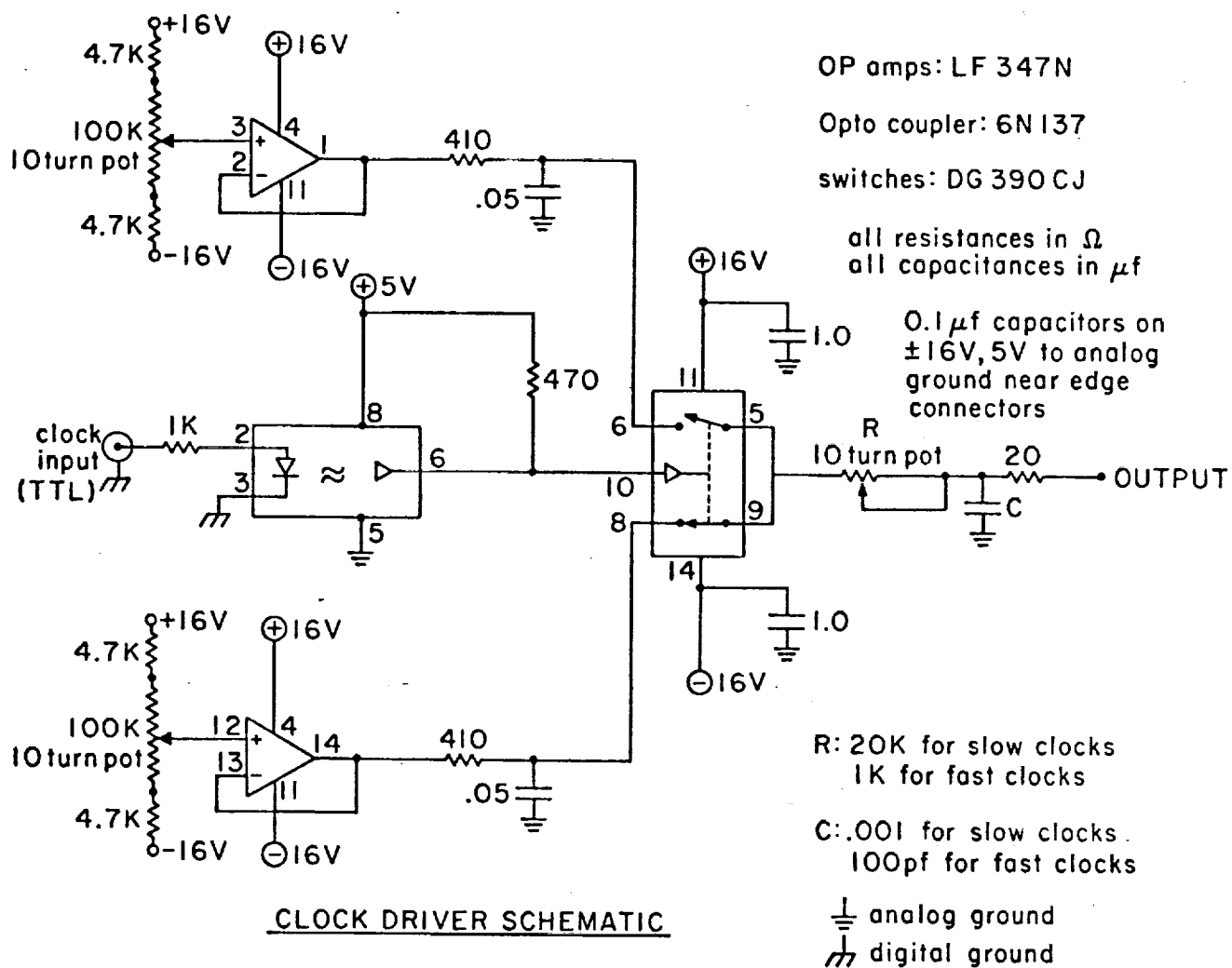
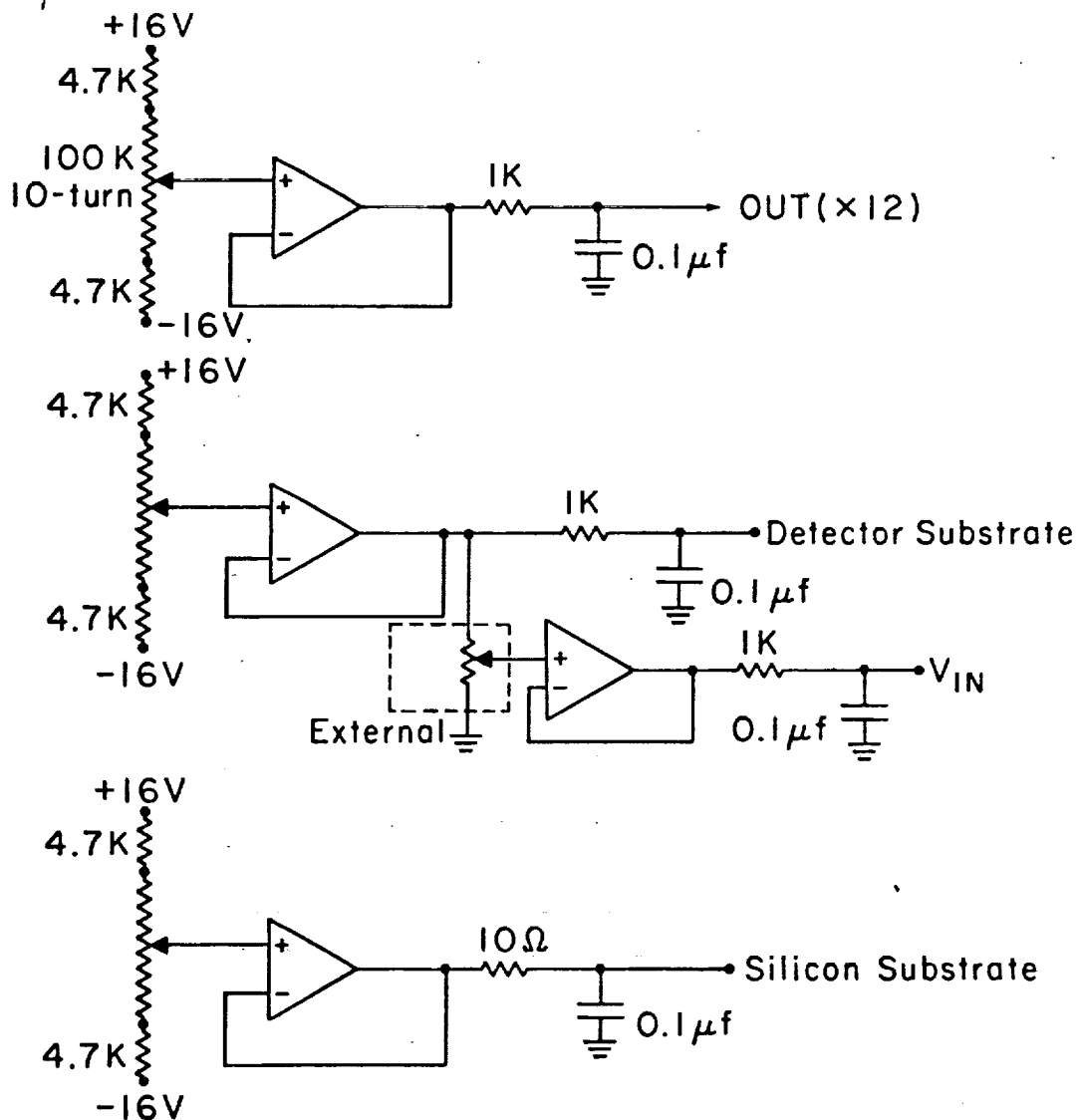


Figure 2

3. DC Supplies

The 15 DC voltages necessary for running the CCD are supplied by this circuit.

CCD DC SUPPLIES



OP Amps: LF 347 N (quad)
 all pots: 100 KΩ, 10 turn
 all resistances in ohms (Ω)

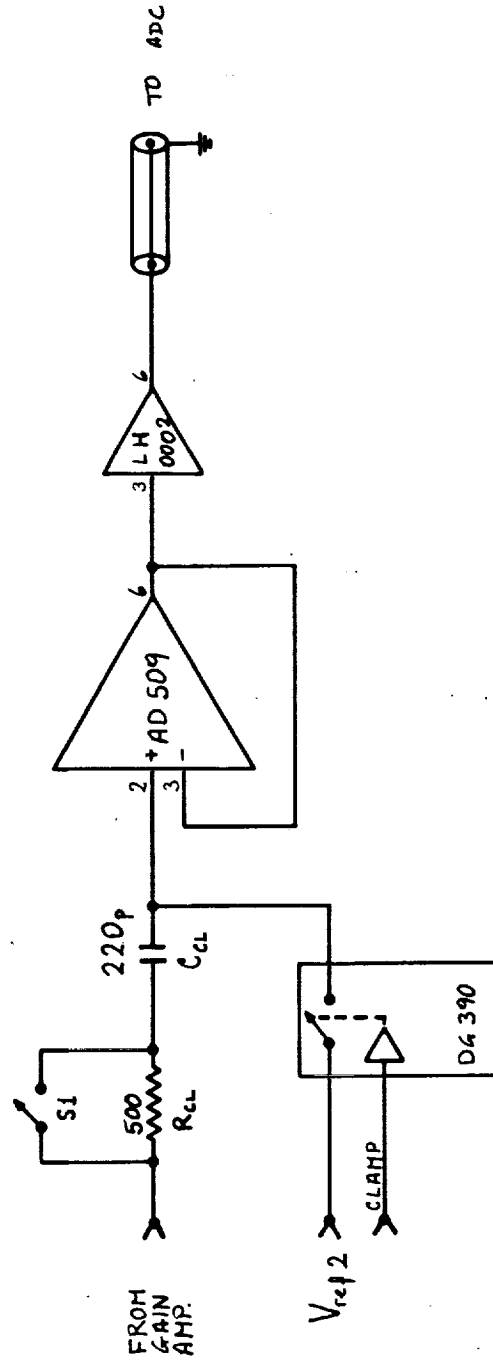
Figure 3

4. Clamp Amp

In order to eliminate any possibility of output noise due to DC drifts or the reset level, we "clamp" on the voltage of the reset plateau just before a charge packet is dumped onto the output amplifier gate. The output is then the difference between the reset level and the next output pulse, eliminating DC drift and reset noise. Gain and offset are provided to match the range of the A/D converter. The clamping scheme is shown on page 2, during the reset, the MOS switch is closed and the 220 pf capacitor charged with the difference between the reset level and the voltage reference ($V_{ref 2}$). The switch is then opened and the output is $V_{out} = V_{in} - V_{reset} + V_{ref 2}$. The 500 Ω resistor provides an RC time constant for charging the capacitor. Based on a design by Alan Hoffman.

CLAMP

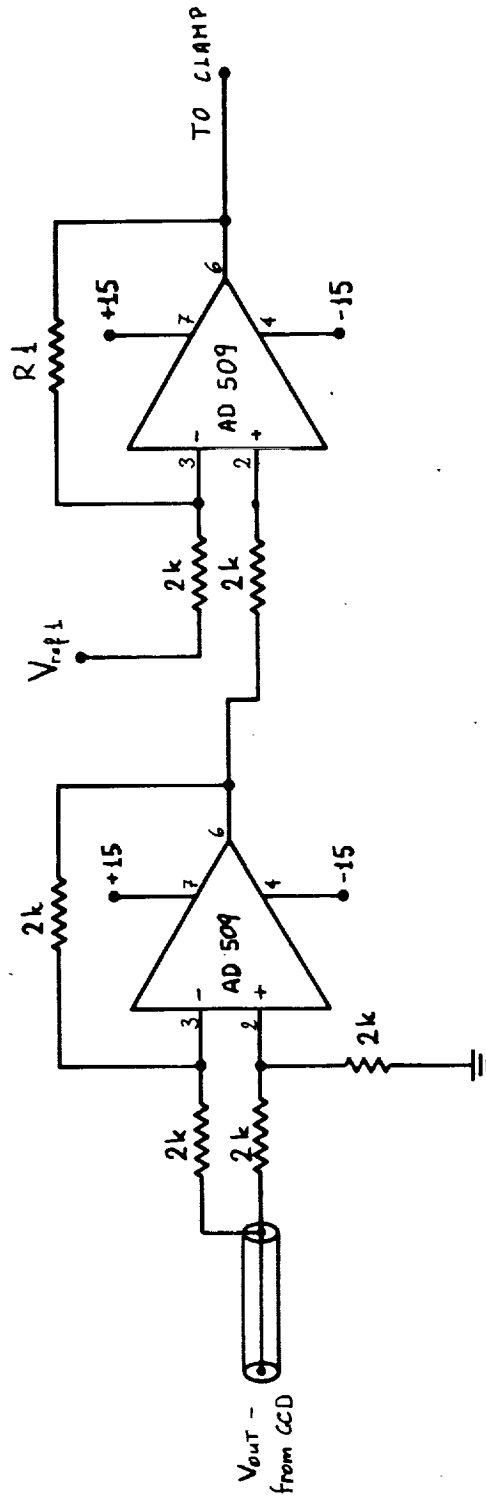
LINE DRIVER



AMP-SAMPLE/HOLD p 2 of 4
S1: 14 pin DIP switch

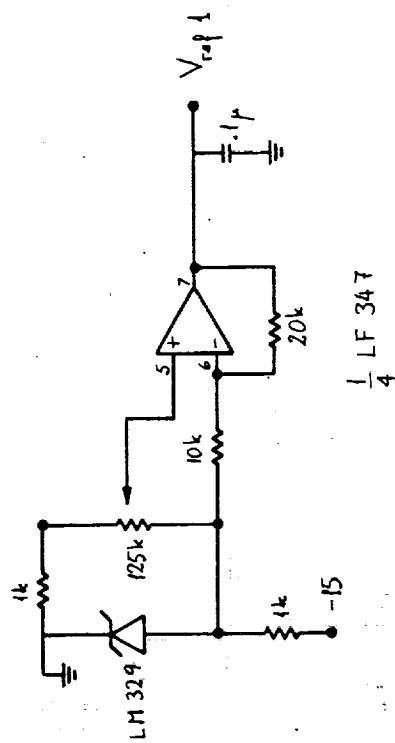
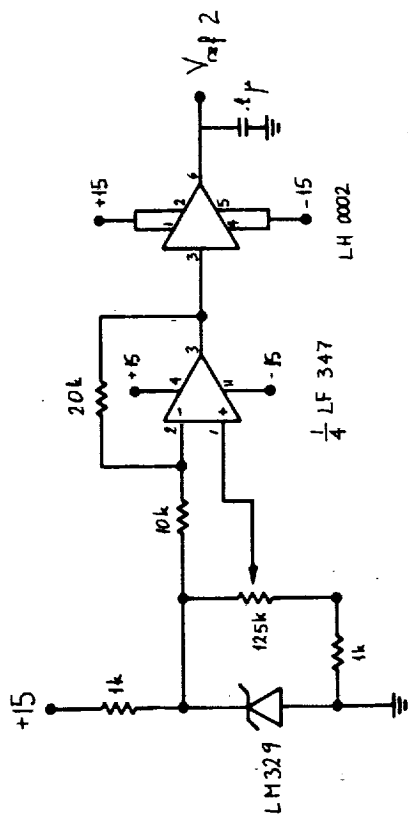
PREAMP

GAIN AMP



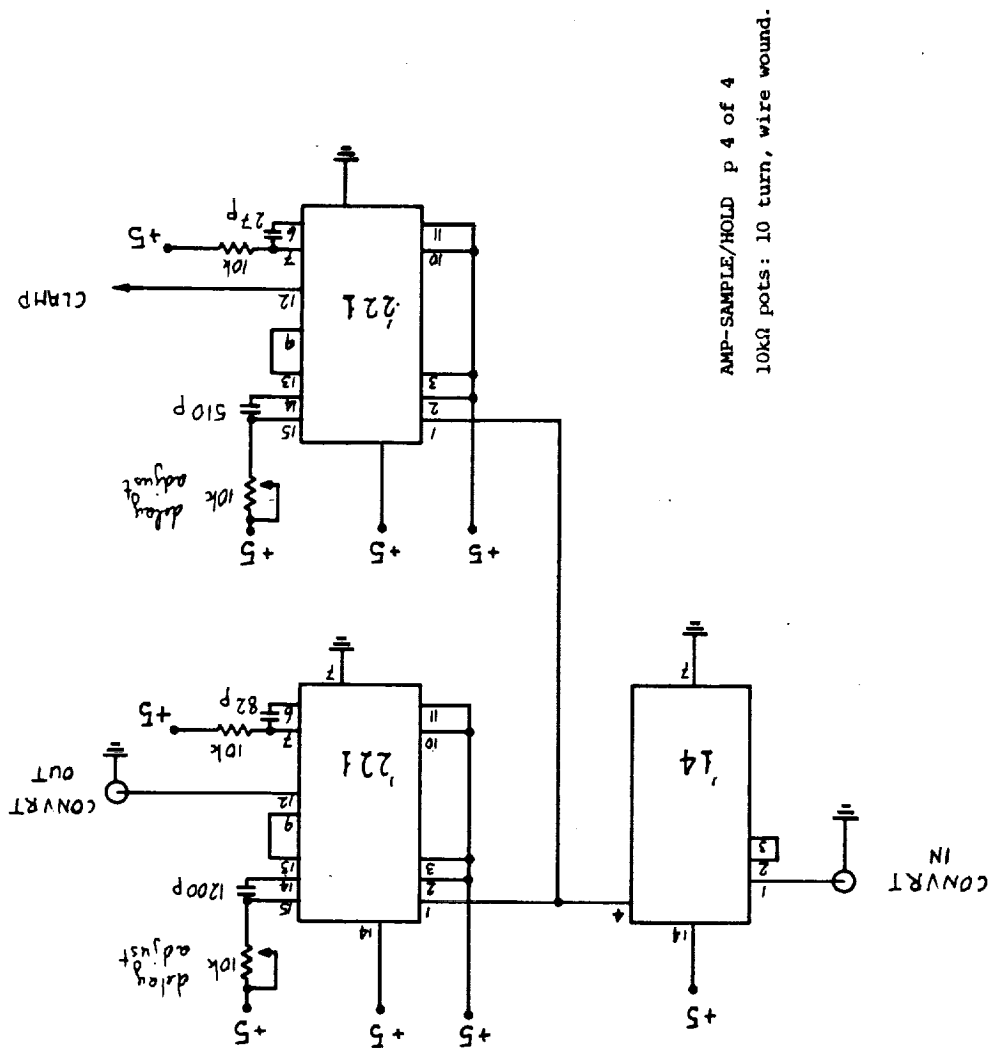
AMP-SAMPLE/HOLD p 1 of 4
 All resistances in Ω
 All resistances metal film, 1%
 R1: choose for desired gain
 Gain = $R1 / 2k\Omega$

VOLTAGE REFERENCES



AMP-SAMPLE/HOLD p 3 of 4.

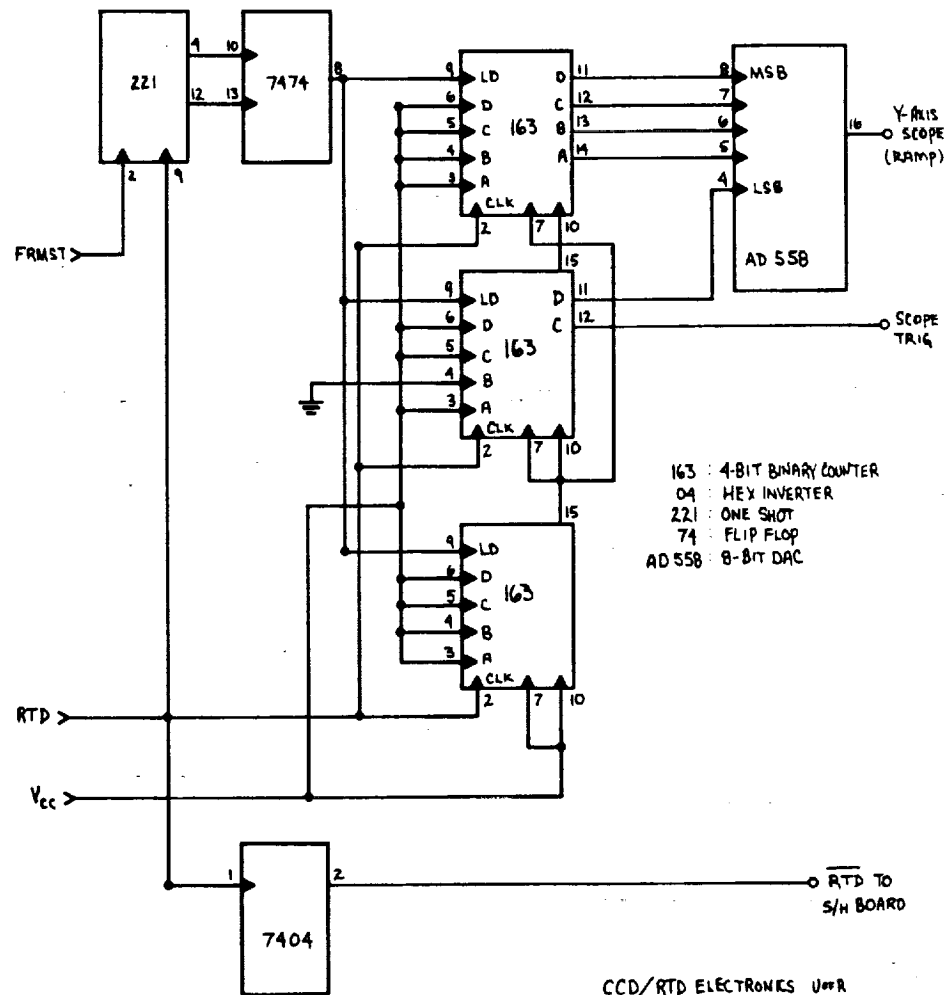
16-65



AMP-SAMPLE/HOLD p 4 of 4

5. Real Time Display

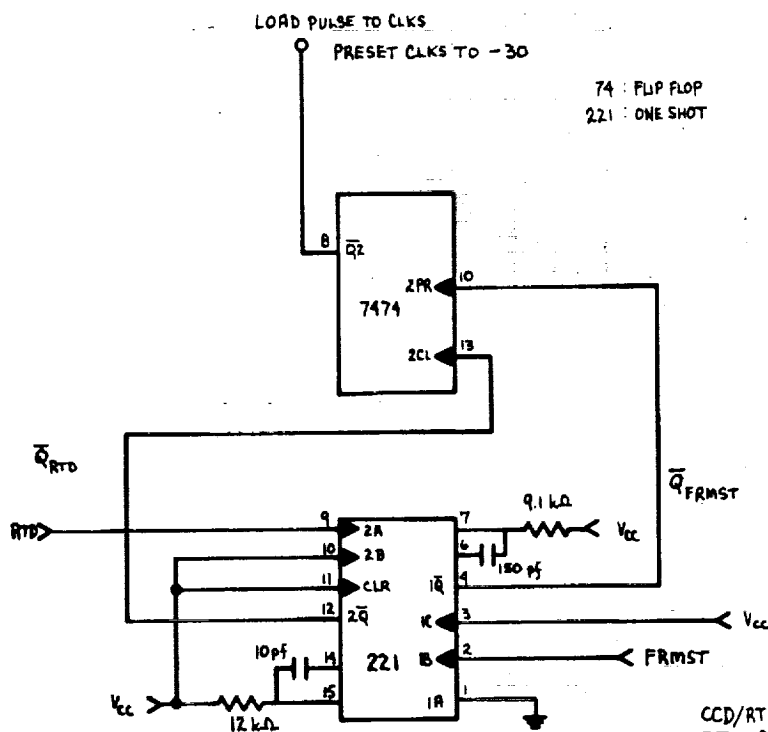
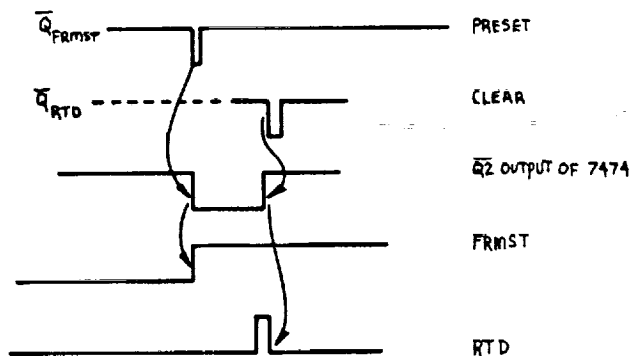
In order to have display of the image being produced by the CCD in real-time, we have designed and built this circuit. The image appears on the screen of our Tektronix 2215 oscilloscope. The z axis (intensity) is driven by the sample-and-held CCD output as shown on page 3. The y axis is driven by a ramp generator shown on page 1. The x axis is swept internally by the scope, based on the trigger pulse shown on page 1. The RTD and FRMST pulses come from the CCD clock and provide the information necessary to synchronize the display (one FRMST per frame, one RTD pulse per bit from the CCD (1024 data bits and 1024 isolation bits)). There is provision for a variable gain and offset as well as a z axis inversion.



163 : 4-BIT BINARY COUNTER
 04 : HEX INVERTER
 221 : ONE SHOT
 74 : FLIP FLOP
 AD 558 : 8-BIT DAC

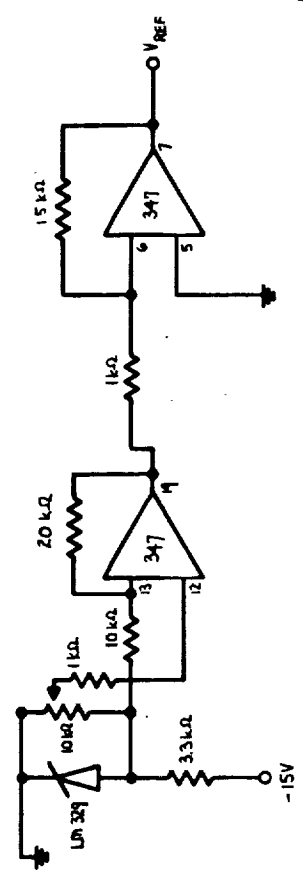
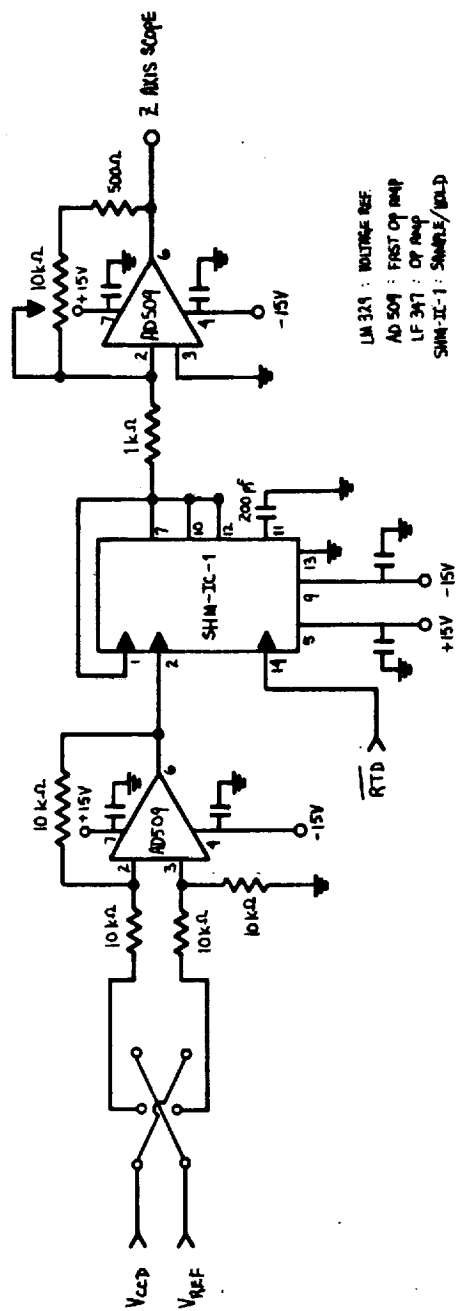
CCD/RTD ELECTRONICS U#R
 3 JUNE 83 CW PAGE 1

RTD RAMP BOARD



SYNCHRONISING PULSE GENERATION FOR CLOCK LOADING

CCD/RTD ELECTRONICS UMR
3 JUNE 83 CW PAGE 2



CCD/RTD ELECTRONICS User's
 3 June 83 CM Page 3

RTD SAMPLE/HOLD BOARD FOR Z AXIS MODULATION

515-74 51
N 93-133820 651
P-10

**InSb Array Technology in Astronomy at Kitt Peak
National Observatory**

*A.M. Fowler
J.P. Britt*

Kitt Peak National Observatory††
Tucson, Arizona 85726

KWP13918

ABSTRACT

During the past several years work has been done at Kitt Peak National Observatory(KPNO) to utilize InSb detector arrays for astronomical use. In that time we have studied charge injection devices(CID) in the greatest detail and are now looking at various photovoltaic techniques. Linear CID's suffer from a response lag which is quite serious at low flux levels, while the two dimensional CID's are limited by their reduced quantum efficiency and high read noise. Charge integrating photovoltaic arrays(CIPA) appear to offer some advantages in low background applications but may suffer from linearity and saturation problems or high read noise depending on the readout technique used. In this paper we will discuss the test results obtained on a number of InSb CID's and the concept and tests we plan to implement on the CIPA's we are in the process of testing.

July 26, 1983

††Kitt Peak National Observatory is operated by the Association of Universities for Research in Astronomy, Inc. under contract with the National Science Foundation.

InSb Array Technology in Astronomy at Kitt Peak National Observatory

*A.M. Fowler
J.P. Britt*

Kitt Peak National Observatory††
Tucson, Arizona 85726

1. Introduction

Work on InSb arrays started at Kitt Peak National Observatory(KPNO) in 1977. The reason for this work was to locate a suitable array for the 1 to 5 μm cryogenically cooled spectrometer under current development. Since that time the spectrometer, shown in Figure 1, has been completed, but there is still a need for a high performance array. We have done some work using the GE linear InSb array but it has been primarily engineering in nature. We plan to begin astronomical observations with this instrument in the 3 to 5 μm band later this year using the GE array. In addition projects for photometers have not been pursued for lack of arrays to put in them at this time. We have reason to believe that this situation will be changing in the near future.

During that time our major emphasis has been on CID's made by General Electric. We have discovered that these arrays can be made to operate successfully at LHe temperatures where dark current can be reduced to acceptable levels for long integrations. Unfortunately at these temperatures these arrays exhibit a response lag which limits their performance in low background situations. This limitation on background has been the stumbling block which has prevented their more wide spread use at KPNO. For this reason we have devoted considerable time to testing newer materials supplied by G.E. to determine the performance at low background. To date all material tested exhibits a serious response lag at low background and is not very useful for astronomy under those conditions. Recent test results suggest a method of operation which may alleviate this problem.

Recently we have been looking at some other approaches which appear to offer some advantages at low background. One is the multiplexed array concept which is being produced by Cincinnati Electronics. It uses a silicon scanner to multiplex the InSb diode array to a single output amplifier and signal processing chain. Another technique also involves integrating charge on the reverse biased photovoltaic detector, but each detector is connected to its own preamplifier. This approach, although more complicated in implementation, should be much better for low background use. In the case of the Cincinnati Electronics array we have purchased one of evaluation, and in the other case we have fabricated a test system to determine whether the approach is worth the extra complication.

††Kitt Peak National Observatory is operated by the Association of Universities for Research in Astronomy, Inc. under contract with the National Science Foundation.

2. InSb CID's at LHe Temperatures

The decision to operate the InSb CID's at $< 15^\circ\text{K}$ was based on dark current considerations. At this temperature the dark current is reduced to a level where it cannot be separated from the background in the dewar. This made it possible to integrate up to 60 seconds before the full well capacity was reached. This required that the devices be operated with a read or injection voltage below that which causes breakdown or tunneling currents to be generated. This mechanism is discussed in detail by Jost and others^{1,2} and will not be covered here.

Another problem associated with operation at $< 15^\circ\text{K}$ which will be covered here is the operation of the silicon scanner. This scanner is a two-phase, non-overlapping clock, dynamic shift register whose output controls the MOS output switches as shown in Figure 2. At very low temperatures all the even or odd numbered switches momentarily ($< 100\text{ns}$) turn on during the clock transitions period³. A successful technique has been devised to work around this problem and at the same time eliminate the charge splitting problem caused by the capacitance of the output enable line. By using a charge amplifier to read out the device we can hold the enable line at the deep depletion or integration level during the switching period when we are selecting a new detector by keeping switch SW1 closed during this time period. Once the detector is selected we float the enable line and sample on the output level 'e'. Next we inject the stored charge by pulsing the enable line to the read or inject voltage level, which results in the injected charge being represented by charge on the feedback capacitor C_F . This results in a change in the voltage 'e' which is again sampled, and the difference is the measured charge. The same problem exists in the operation of the area array, and it can be solved in a similar fashion.

The quantum efficiency for the linear and area arrays is shown in Table 1. The results of our measurements are consistent with those obtained by G.E. with the exception of the fall off at $4.7\ \mu\text{m}$, which is a consequence of our operation at $< 15^\circ\text{K}$. This reduction with temperature is expected and is consistent with other measurements made at Kitt Peak on InSb detectors⁴.

Table 1

| Linear Array | | | Area Array | | |
|----------------------|-----------------------|---------------------|----------------------|-----------------------|---------------------|
| λ Microns | Quantum Efficiency | Responsivity A/W | λ Microns | Quantum Efficiency | Responsivity A/W |
| 2.2 | 80% | 1.4 | 2.2 | 14% | 0.25 |
| 3.6 | 61% | 1.8 | 2.5 | 14% | 0.4 |
| 4.7 | 25% | 0.9 | 4.7 | 5% | 0.2 |

Noise in the linear array can be reduced to < 200 electrons, and we have measured < 300 electrons consistently in our lab set-up. In the case of the

area array the noise problem is more severe and will get much worse as the array size increases. This problem is due to the large enable line capacitance caused by connecting an entire column of detectors to it at one time and the increased bandwidth necessitated by the faster readout speed. In addition the smaller well size will make it difficult to achieve quantum noise limited performance.

The linearity of any device used for astronomy is very important. In the case of the linear array the device exhibits some peculiar problems but they appear to be repeatable, which makes it possible to correct any observational data. The large signal response as a function of integration time is shown in Figure 3. It exhibits a very definite sub-linear characteristic and the best curve fit is a power law fit.

A more important test for ground based astronomy is the effect of background signal on the small signal response. This is a test which we refer to as the differential linearity test and represents actual conditions when observing in the 3 to 5 μm band. The results of that test (shown in Figure 4) show a very definite fall-off in gain as a function of background. This effect as well as the large signal sub-linear response are probably caused by the change in the width of the deep depletion region as a function of collected charge in the well. We have been able to model this effect by taking into account the change in quantity of absorbed flux as a function of the deep depletion width³. Figure 4 is a plot of the differential linearity measured and compared with the results predicted by our model. Again this effect, like the large signal linearity, is repeatable and can be calibrated for in data reduction.

As previously mentioned, the major drawback to these arrays is their response lag under low background conditions. This is the area in which we are doing the most work. It is an effect which was not seen in the area array we tested, although it may have existed but could not be determined due to the excess noise in the system with which we were working. We still do not know whether the difference between the linear and area arrays is due to design or to material differences, but we strongly suspect design differences as the reason. Possible causes of the response lag are thought to be due either to traps around the periphery of the gate where the inversion region ends or to the collected charge not recombining when injected due to the low operating temperature. So far the only thing which influences the response lag is an increase in radiation falling on the array.

Response lag is defined as follows:

$$1 - \frac{\text{Charge Measured on First Read}}{\text{Total Charge}}$$

This definition has been used in all the following results to allow us to compare various test results. Most tests used a single detector which was exposed for a fixed integration time and then read out for 34 times before being reexposed to the input flux. A black body was used to generate a repeatable small signal for all tests while the background was generated by a lamp driven with a regulated supply. All timing was generated by the AIM65 computer which was used for data taking and reduction. Figure 5 are photographs of the test dewar and laboratory set-up.

Figure 6 shows the response lag taken on the linear array during early testing done at Kitt Peak. This was done before we developed the technique of using a single detector, and from these plots it is clear that several seconds are required to achieve a steady state result under very low

background conditions. This effect has also been observed at the 1.3 meter telescope using the Cryogenic Spectrometer and renders the instrument virtually useless short of 3 μm . Since that time we have done tests on several types of detectors to try to reduce this effect by other than increasing background flux on the detector.

Recent tests have involved a number of different types of experimental detectors and have not produced results which indicate that anything but increased background radiation will influence the response lag. On detectors which had a metal field shield, which served to define the active area, we varied the shield potential over a ± 9 volts range and did not see any significant improvement. In addition we varied the amplitude and timing of the read pulse shown in Figure 7. We first tried a two step read pulse with a larger initial amplitude to inject a larger charge before recovering to the steady state inversion level but this had no effect on performance. Varying the times t_1 and t_2 produced some improvement, but it seemed to be more a function of the total inject time rather than the relationship of the sub intervals. The problem with this approach was that the $1/f$ noise increased at a greater rate than any improvement.

As stated previously the only technique which reduced response lag was to increase the background radiation. This result is shown in Figure 8. An interesting result of further analysis of this data was the response lag computed on the 2nd and 3rd reads produced the same result as the first read. This suggests that the improvement is not a function of the collected charge but of the flux falling on the array while it is being read out. If this is true, then a significant improvement in performance can be achieved at little or no cost in system noise. The initial tests of this hypothesis will involve illuminating the array during the entire readout period and then proceed to illuminating it only during the read or inject pulse time period. Initial qualitative tests indicate the the performance is indeed improved. It remains to quantify these initial results.

3. InSb CIPA Plans at Kitt Peak

There are two charge integrating schemes being investigated at Kitt Peak. They are the multiplexed array concept which has been developed by Cincinnati Electronics and Jet Propulsion Laboratory⁵ and is now commercially available in a 32x1 configuration from Cincinnati Electronics. The second is a multiplexed array-preamplifier approach which we have used to measure dark current in CID's and has been suggested as a possible array concept by Dr. F. Low. Each of these techniques has advantages and disadvantages for astronomy, depending whether one is doing low or high background work.

The main advantage of the multiplexed array concept is its simplicity and fast readout which suits it well to high background applications. Recent tests indicate that by cooling below 77°K one can achieve integration times up to 1500 seconds, which extends this concept to lower flux level applications. The main disadvantage of this approach is the high read noise which has been reported^{5,6,7} to be from 1000 to 2000 electrons and is inherent in the design concept of the array. This noise is due to the reset or "KTC" noise and can be reduced only slightly by operation below 77°K. A simplified diagram is shown in Figure 9. The full well capacity of the array is reported to be greater than 1×10^7 which will allow for background limited performance in many cases, especially below 77°K. It is our intention to evaluate this array for an imaging application, so we expect sufficient background flux noise to overcome the system noise. We intend to determine how cold the array can be operated before the isolated J-FET preamplifier fails and what integration periods can be achieved. We will be

particularly concerned with the linearity characteristics of the array, especially the differential linearity.

The multiplexed array-preamplifier concept, shown in simplified schematic form in Figure 10 has the advantage of use in very low background applications. Its main disadvantage is its complexity which can be overcome by the use of hybrid packaging technology. This approach initializes the array by applying a reverse bias on each of the detectors and then allowing the photocurrent to discharge the charge from the reverse bias. After the array is initialized, the output of the preamplifier is repeatedly sampled while flux is being integrated on the detector node capacitance. A straight line fit is then determined for the data, and the slope of the line is the flux rate. With larger detectors where the capacitance change with reverse bias becomes significant it will be necessary to correct the data before doing the linear fit. The read noise can be reduced as a function of the number of reads used in the calculation. For this concept to work it is necessary to obtain InSb diodes which have a high tolerance for reverse bias and very low dark current as these parameters will limit the ultimate performance. Cincinnati diodes tested by us and others have these characteristics⁸.

A feature of J-FETs which we plan to utilize on using is to null the leakage currents in the preamplifier by adjusting the applied drain voltage. This will be done under closed loop control from our AIM65 processor. The array will be operated with InSb diodes seeing only the cold background of the test dewar and the drain voltage will be adjusted until the drift rate of the output is as low as possible. We plan to investigate the stability of the null output under 77°K background conditions. This technique has proven to be very good when used to measure leakage currents in CID's but we will be studying longer term effects in this application. at during the previous measurements.

Another advantage of this array is that the integration time can be varied automatically as a function of the diode output. Since we are non-destructively reading out the device, the output voltage level can be used to control when the diodes are reset. The ability to reset the the diode's individually as well as simultaneously could improve observing efficiency. This is especially useful at the 4 meter telescope where observing time is at a premium.

The serious disadvantage of the approach is the complicated circuitry required to make it work. If test results are promising the approach could be extended to a working system of 32 to 64 detectors by use of hybrid techniques but beyond that seems unlikely. For larger arrays one would have to make the preamplifier and reset FET's on a silicon monolithic chip and then use indium bump technology to bond it to the array. This would limit the array operating temperature and thus

the dark current levels. Because of the complication and cost we do not plan to investigate this approach.

The questions which we are looking to answer are how well can the read noise be reduced by successive non destructive reading of the array, stability of the null technique, and ultimate NEP with larger arrays.

4. Acknowledgement

We wish to acknowledge the helpful discussions and support received from S. Jost and D. Houston of General Electric, Syracuse N.Y., without which our extensive investigation and success in using InSb CID's in ground based astronomy would not have been possible. In addition we wish to thank J. Wimmers of Cincinnati Electronics, Cincinnati Ohio for his support in the investigation of InSb diode arrays for ground based astronomy.

References

1. G.L. Kuryshv, N.I. Khaliullin, and K.O. Postnikov, "Carrier generation process in InSb-based metal-insulator-semiconductor structures under nonequilibrium depletion conditions," *Sov. Phys. Semicond.* 15(4), pp. 374-378, American Institute of Physics (April 1981).
2. S.R. Jost, "Dark Current Phenomena in InSb Metal Insulator Semiconductor (MIS) Detectors," *SPIE Proceedings (to be published)* (April 1983).
3. A.M. Fowler and J.P. Britt, "InSb Charge Injection Device Array Performance," *SPIE Proceedings* 331 (March 1982).
4. R. Joyce, LKitt Peak National Observatory, *Private Communication*.
5. Gary C. Bailey, "Integrating 128-element linear imager for the 1 to 5 region," *SPIE Proceedings* 311.
6. Gary C. Bailey, "An Integrating 128 element InSb array: recent results," *SPIE Proceedings* 345 (1982).
7. J.T. Wimmers and D.S. Smith, "Characteristics of InSb photovoltaic detectors at 77 °K and below," *SPIE Proceedings* 364 (???)



Figure 1. Internal View of the 1 to 5 μ m Cryogenic Spectrometer

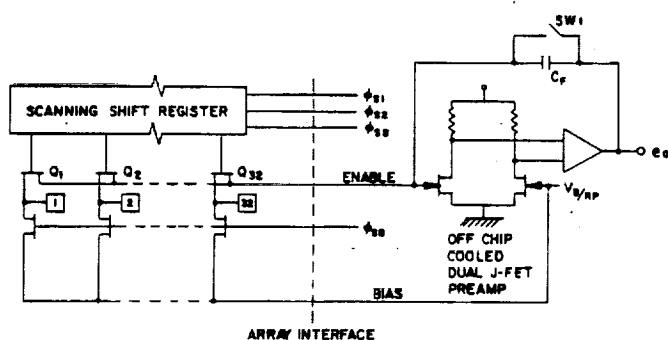


Figure 2. Simplified Schematic of the G. E. Linear CID and Pre-amplifier

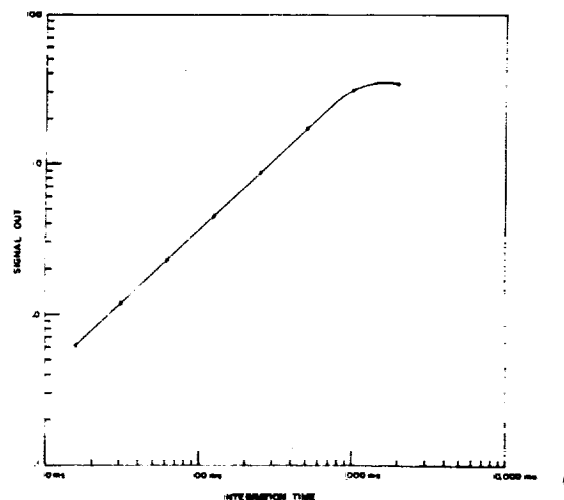


Figure 3. Large Signal Linearity:
Flux = Volts $\times 2 \times 10^5 e$

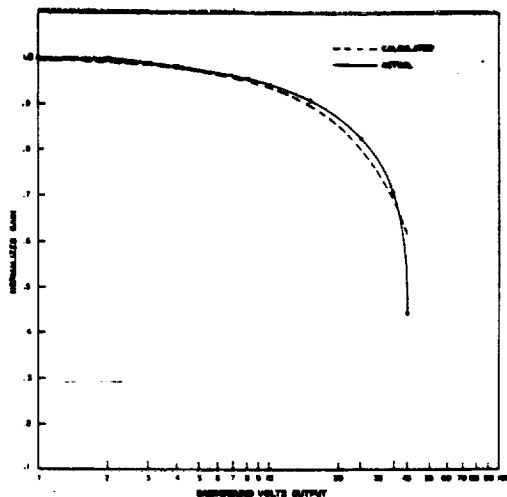


Figure 4. Small Signal Gain versus Background
Flux = Volts $\times 2 \times 10^5 e$

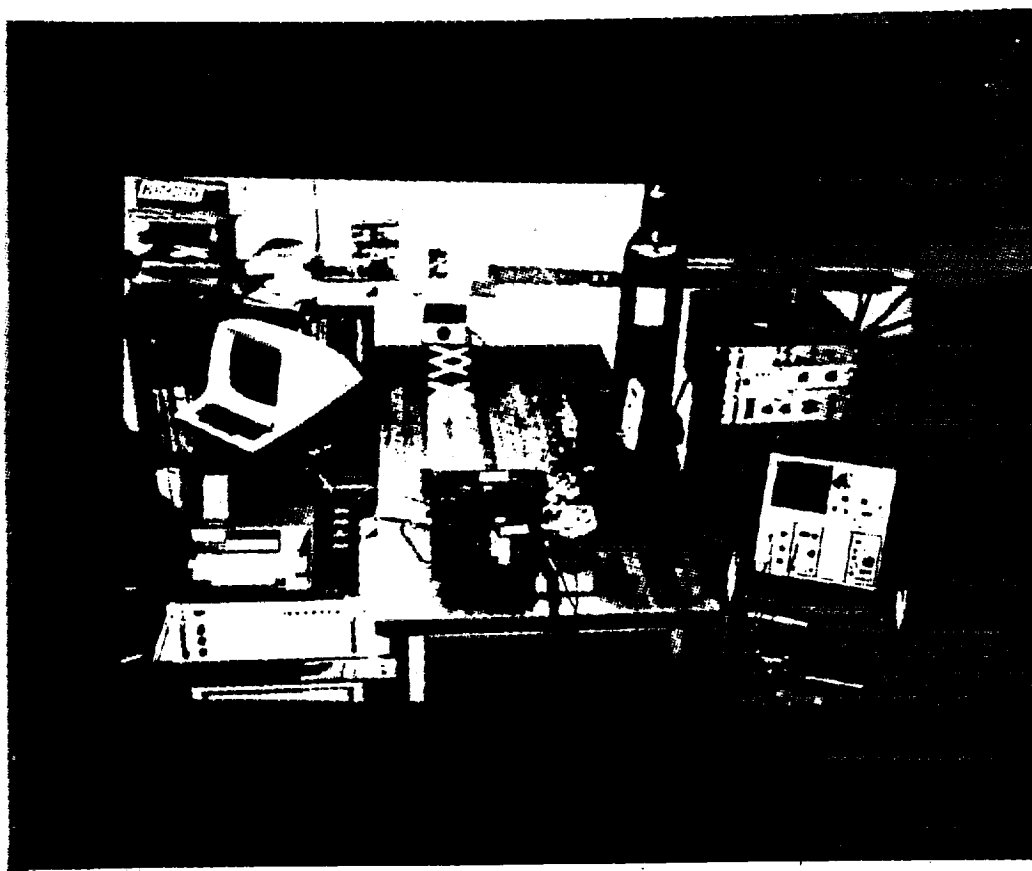


Figure 5. Laboratory Test Set-Up for CID Testing

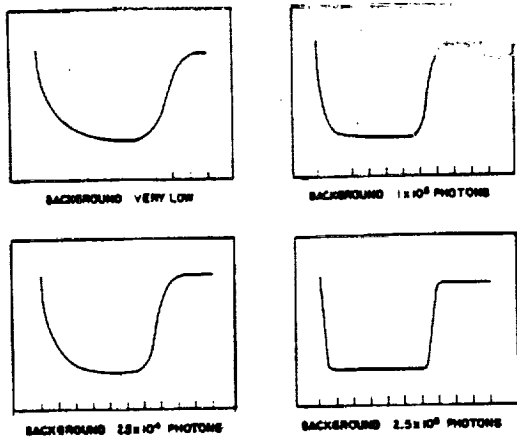


Figure 6. Signal Response Lag versus Background. Background Photons are Collected Flux in a Pixel

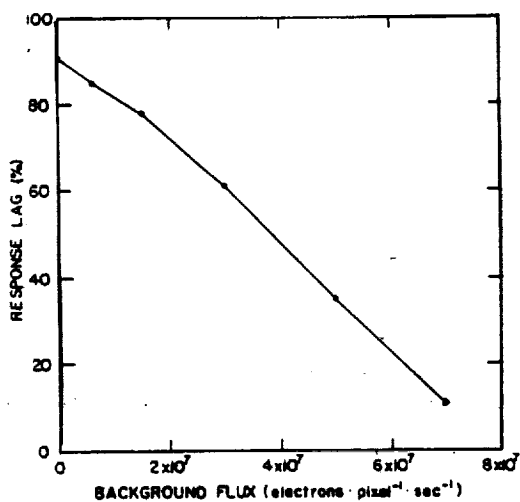


Figure 8. Response Lag versus Background Flux

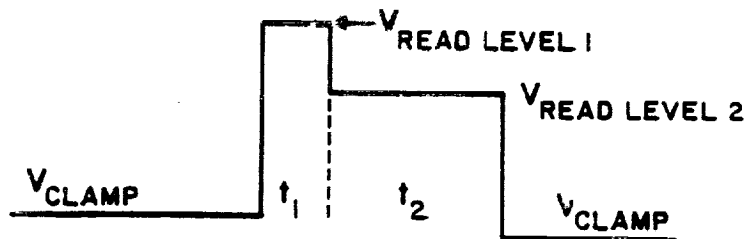


Figure 7. Two Step CID Read Pulse

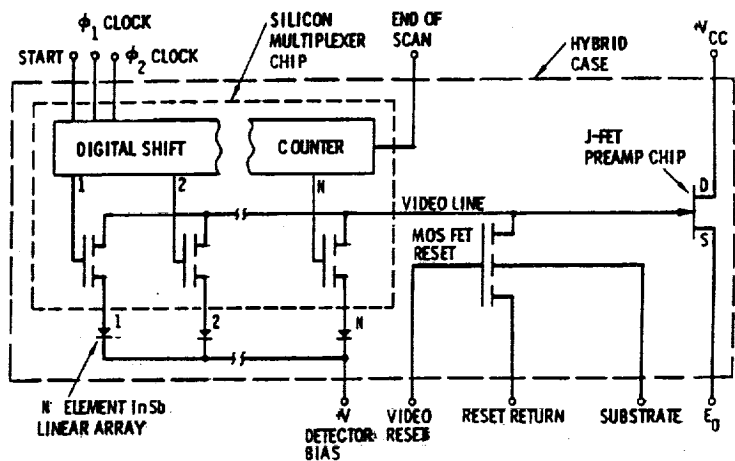


Figure 9. Simplified Diagram for Mosfet Switched Multiplexer

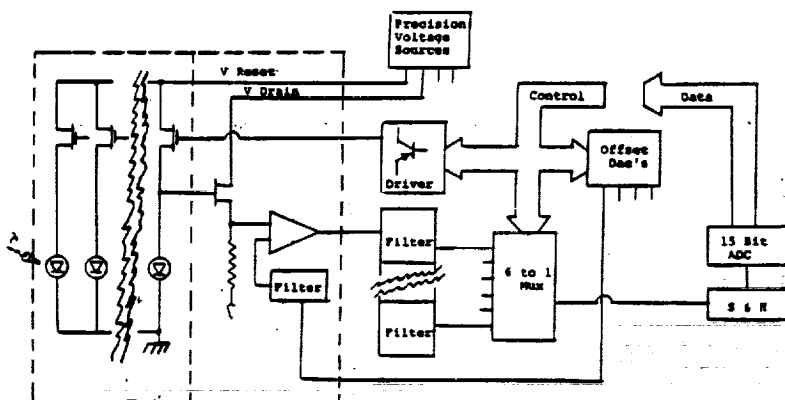


Figure 10. Schematic Diagram for the CIPA Dewar Electronics

INTEGRATING INDIUM ANTIMONIDE
LINEAR ARRAYS AT 65K AND BELOW

GARY C. BAILEY

JET PROPULSION LABORATORY
CALIFORNIA INSTITUTE OF TECHNOLOGY

516-74 52
133821
N93-70552
885744

SIMPLIFIED ELECTRONIC ARCHITECTURE OF EXPERIMENTAL 128 ELEMENT INFRARED IMAGER

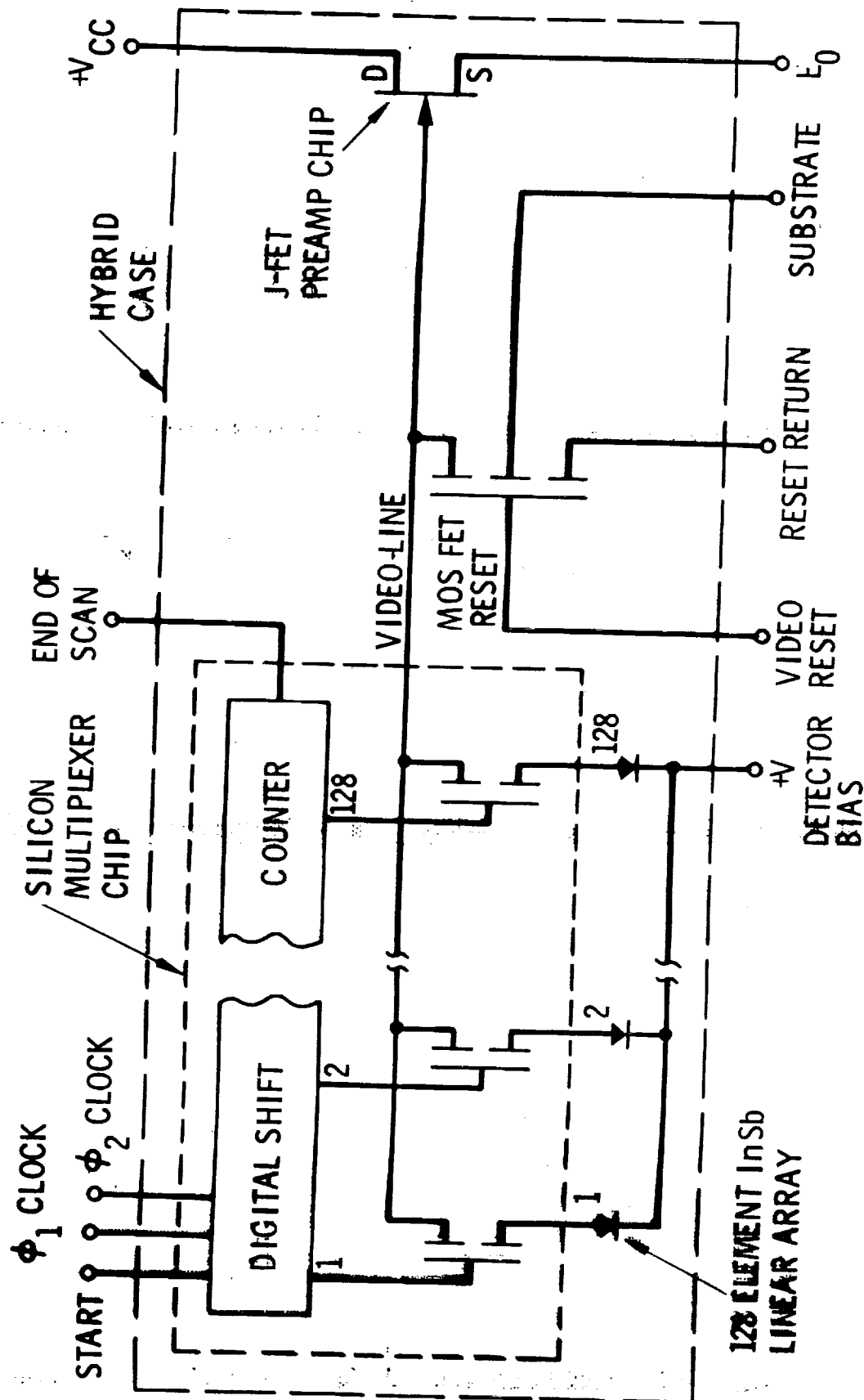


TABLE I. Sample Diode Responsivity

| Element | Responsivity (A/W) |
|---------|--------------------|
| 1 | 2.84 |
| 2 | 2.82 |
| 3 | 2.86 |
| 4 | 2.86 |
| 5 | 2.84 |
| 6 | 2.84 |
| 7 | 2.82 |
| 8 | 2.82 |
| 9 | 2.82 |
| 10 | 2.81 |
| 11 | 2.81 |
| 12 | 2.79 |
| 13 | 2.84 |

Average = 2.83 A/W or $78 \pm 1.2\%$ quantum efficiency @ $4.53\mu\text{m}$

TABLE II

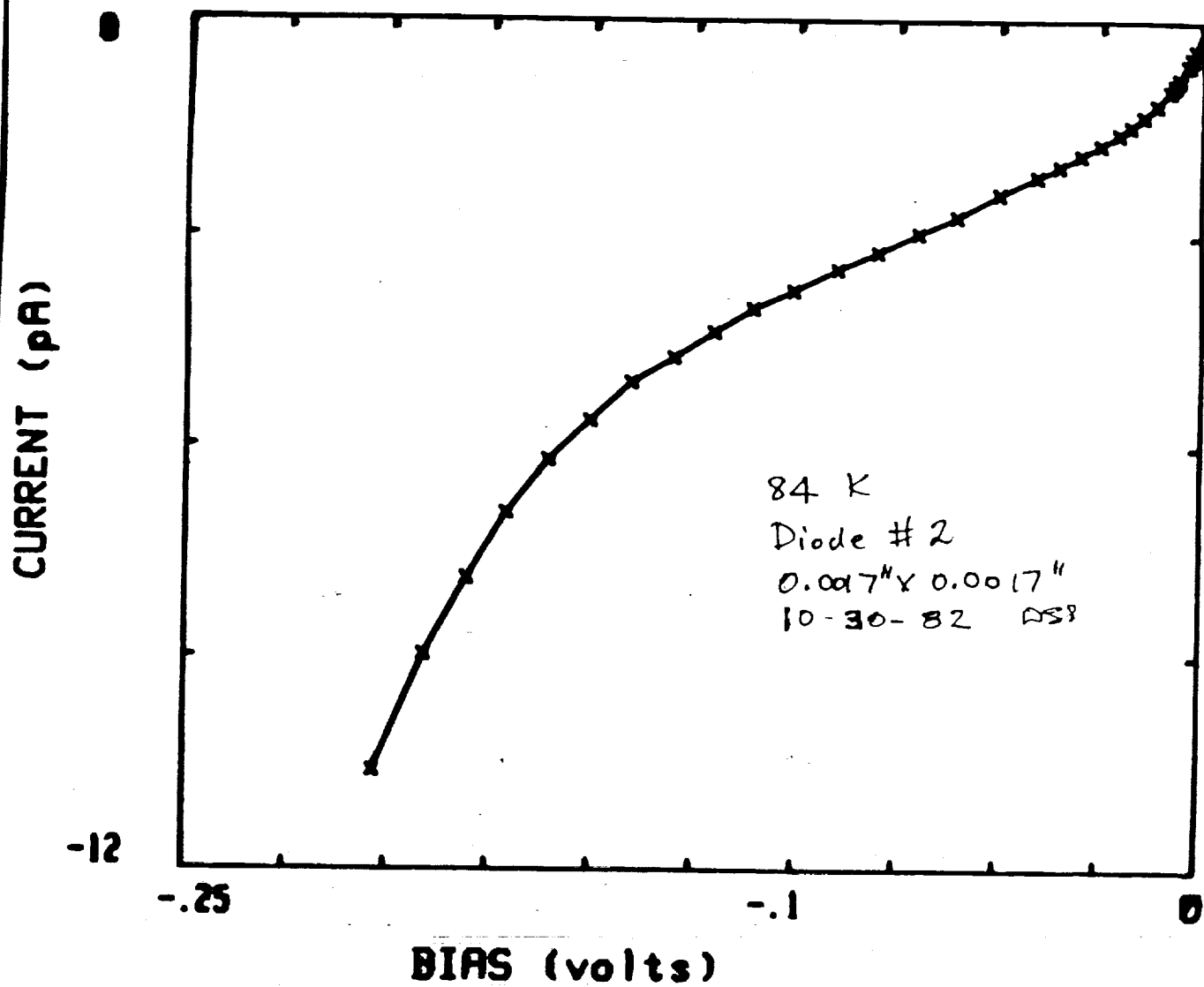
512 Element Focal Plane Performance Summary

| | |
|------------------------------|---|
| Number of Elements: | 512; 43 x 43 μm square |
| Dead Space: | 15 μm |
| Power Dissipation: | 15mW in thermally isolated JFET preamp, <2mW in silicon MUX |
| Quantum Efficiency: | 78% @4.53 μm |
| Responsivity Uniformity: | 3% peak to peak |
| Dark Current Non-Uniformity: | 3% peak to peak |
| Average Dark Current: | 2.1pa @80K integrated over a 0 to 0.33V bias change 0.07pa @65K integrated over a 0 to 0.33V bias change |
| Maximum Integration Time: | 0.35 seconds @80K @0.33V Bias 15 seconds @65K |
| Maximum Charge Storage: | $5.2 \times 10^6\text{e}^-$ @0.33V Bias |
| Noise: | 1,250e $^-$ @80K 1,185e $^-$ @65K |
| Follower Gain: | 0.898 (80K & 65K) |
| Transfer Function: | $1.875 \times 10^5\text{e}^-/\text{mV}$ at follower output |
| A.C. Signal to Noise Ratio: | 4,275:1 (peak/rms) |
| D.C. Dynamic Range: | 11:1 @2.5ms integration of dark current (80K) 29:1 @65K |
| Detector Pixel Capacitance: | 3 pf \pm 0.1 pf @0.33V bias |
| Maximum Readout Speed: | 2-1/2 MHz (80K & 65K) |

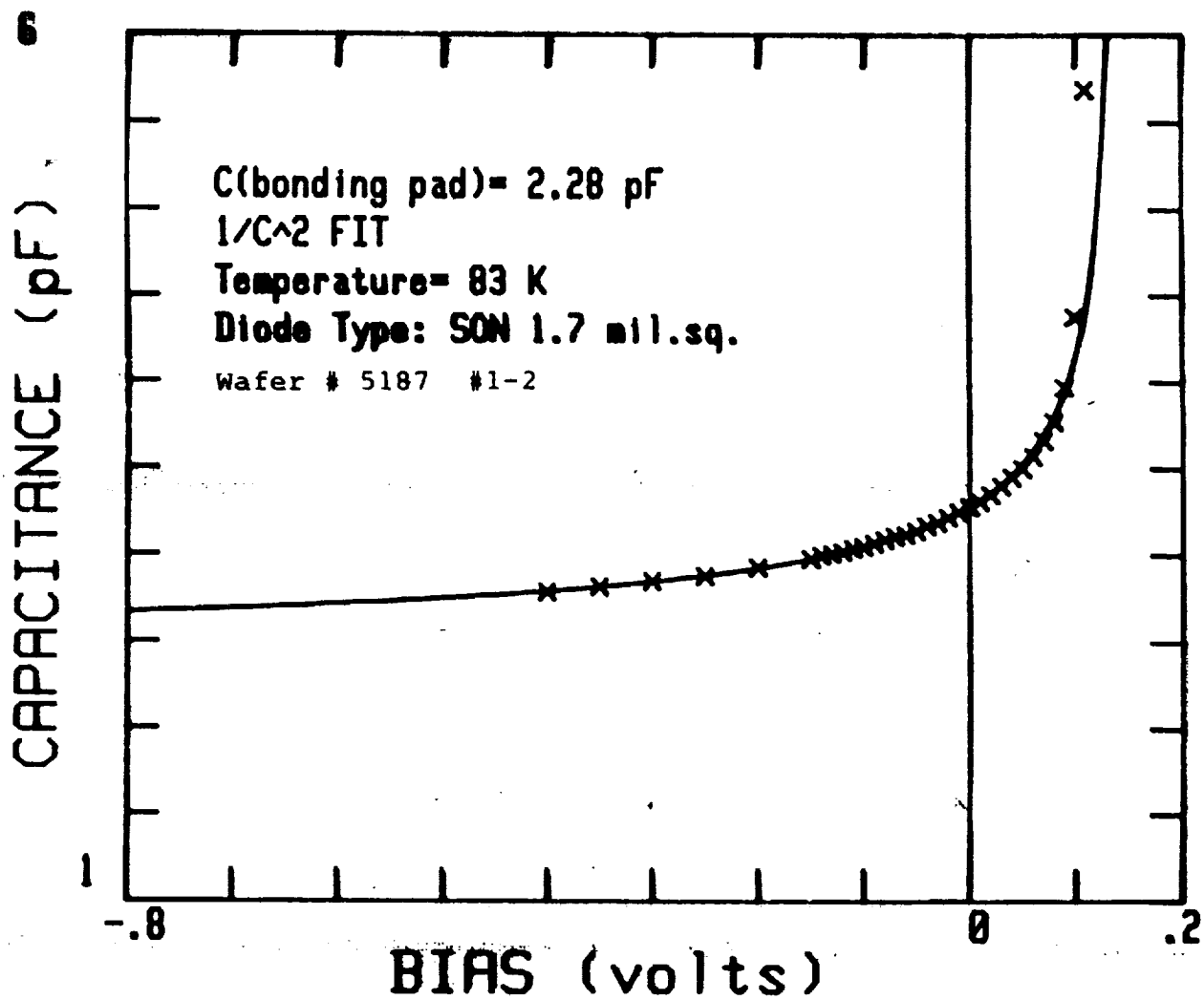
TABLE III

128-Element FPA Mechanical/Electrical Characteristics

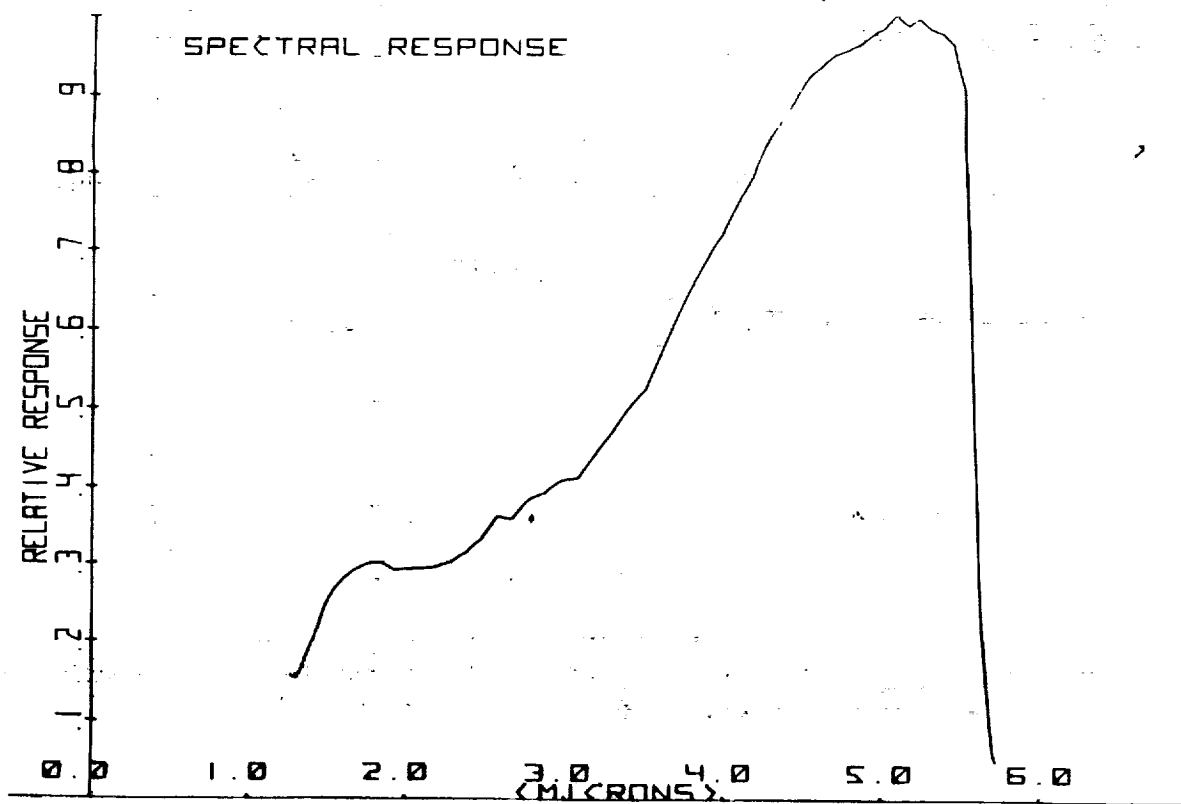
| | |
|--|---|
| Detector Material: | InSb |
| Pixel Size: | 200 μ m x 200 μ m |
| Number of Pixels: | 128 |
| Dead Space: | 30 μ m between pixels |
| Array Package Size: | 1-3/4" x 1" x 1/8" |
| Power Dissipation: | <2mW MUX; 15mW in thermally isolated JFET preamp |
| Number of Package Leads: | 15 |
| Average Dark Current: | 4pa @80K integrated over a 0 to 0.25V bias change ~0.7fa @46K integrated over a 0 to 0.25V bias change |
| Quantum Efficiency: | 0.8 (1 to 5 μ m) |
| Responsivity Uniformity: | 3% peak to peak |
| Dark Non-Uniformity: | 3% peak to peak @0.25V |
| Maximum Integration Time: | 80K = 0.4 seconds, 62K = 28 seconds, 46K >3600 sec |
| Dark Current Temperature Coefficient: | Drops in half every 3.5K |
| Maximum Charge Storage: | 2 x 10 ⁷ electrons @0.25V reverse bias |
| AC Signal-to-noise Ratio: | 8000:1 @80K (peak/rms) |
| Readout Noise: | ~1200 electrons @80K ~900 electrons @46K |
| Spectral Noise Density: | white, 100Hz to 100khz |
| Maximum Readout Speed: | 1MHz (80K & 46K) |
| Detector Pixel Capacitance: | 12.3pf \pm 0.1pf @0.25V bias |
| JFET Preamp Freezout: | ~20K |



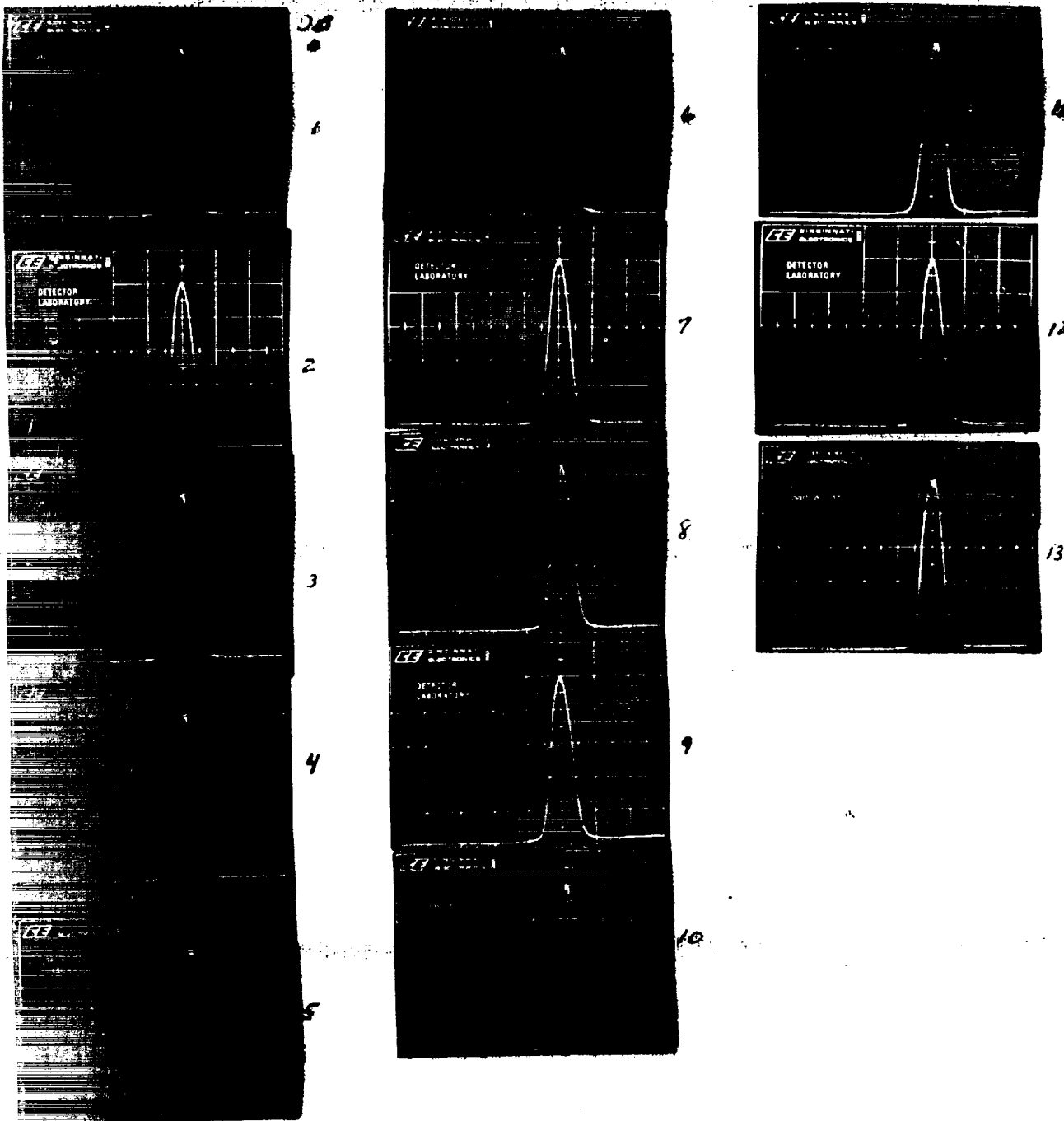
Typical 43 x 43 μ m detector IV characteristic @84K.



Typical 43 x 43 μ m InSb CV characteristic @83K.

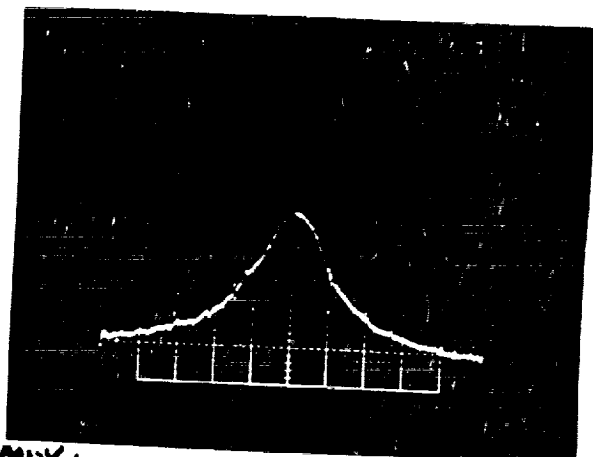


Relative spectral response for a typical $43 \times 43 \mu\text{m}$ InSb diode.



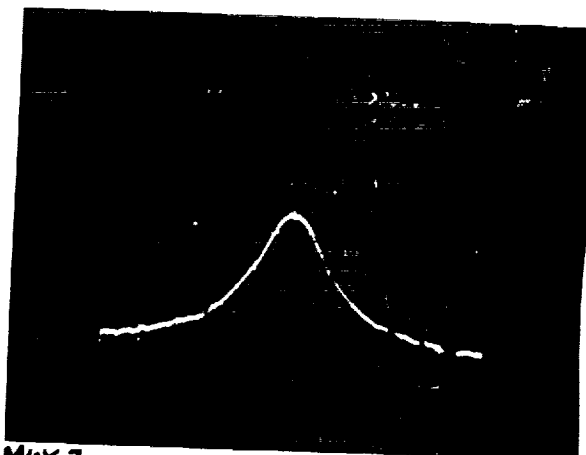
Spot scan profile of the $43 \times 43\mu\text{m}$ InSb detector active area.
Spot size is $25\mu\text{m}$, horizontal axis $25\mu\text{m}$ per division.

ORIGINAL PAGE IS
OF POOR QUALITY



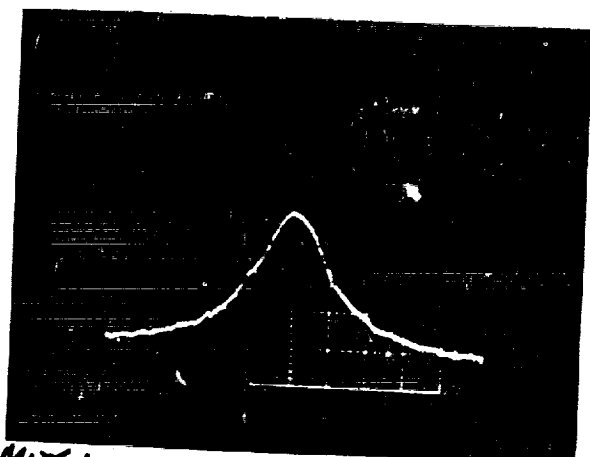
MUX 1

80K



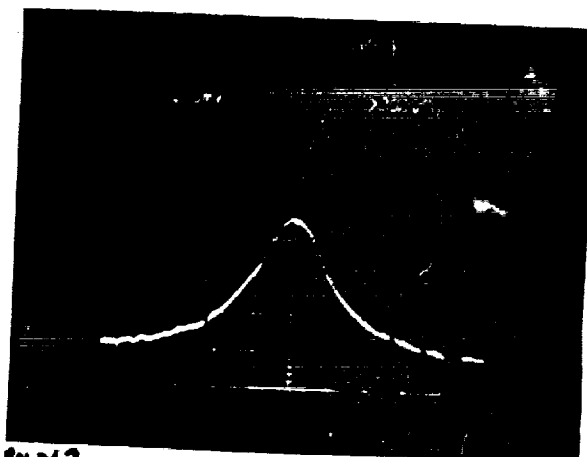
MUX 2

80K



MUX 1

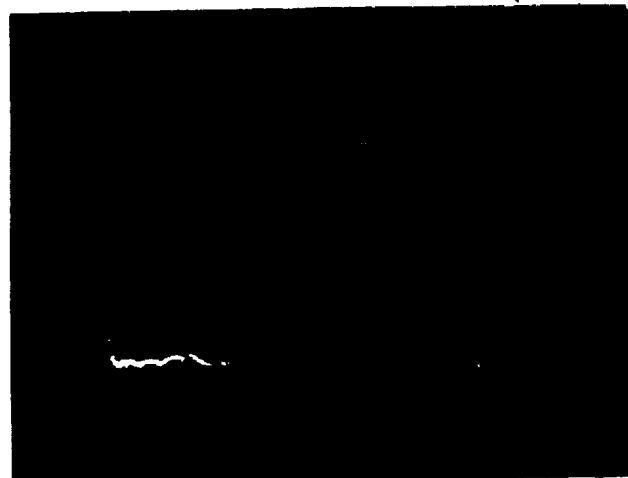
65K



MUX 2

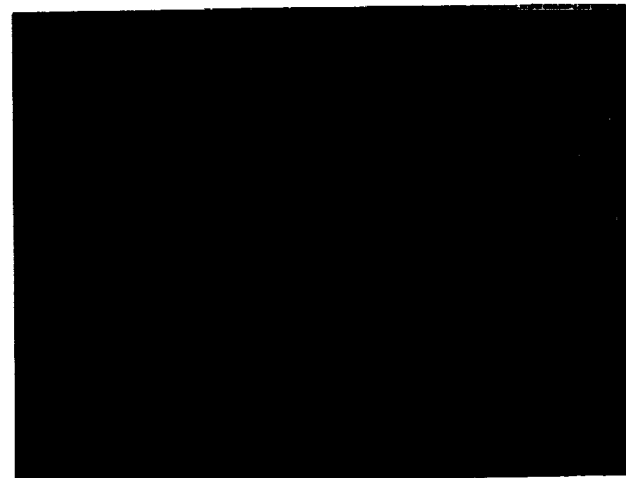
65K

Signal response due to a 5.6ms integration of a 300K flat field thru a cooled $4.8\mu\text{m}$ ($0.05\mu\text{m}$ B.W.) bandpass filter and 4mm aperture. Total integrated charge $\sim 3 \times 10^6$ electrons. Note the smoothness of the curves and same peak amplitudes as temperature drops to 65K.



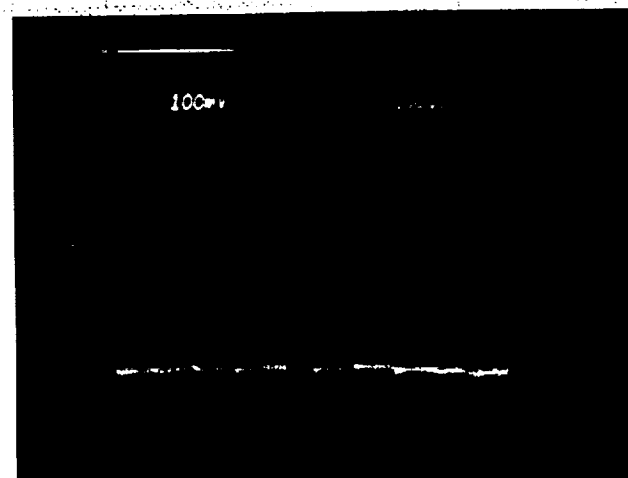
MUX 1

80K



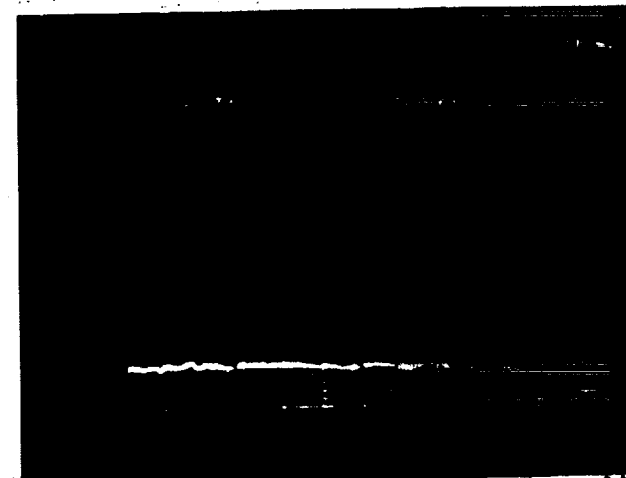
MUX 2

80K



MUX 1

65K



MUX 2

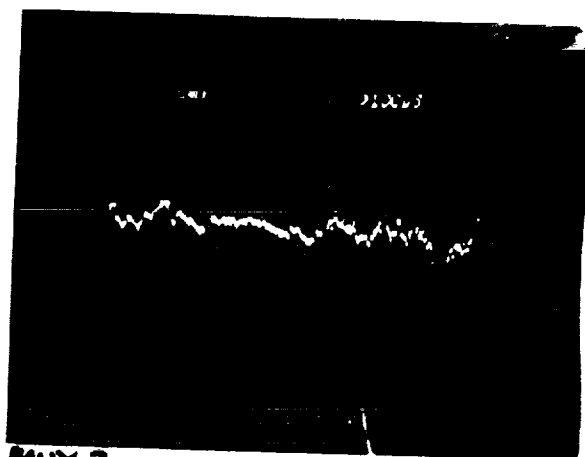
65K

Dark current non-uniformity for MUX 1 and 2; all 256 elements displayed. Saturation at sample and hold output equals 570mV (0mV reference is first graticule line).



MUX 1

80K



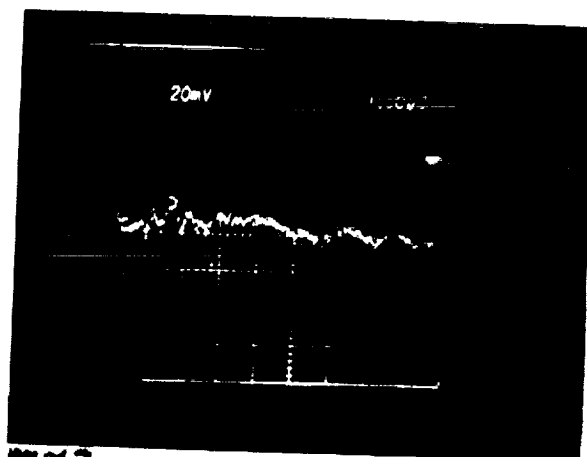
MUX 2

80K



MUX 1

65K



MUX 2

65K

Dark current non-uniformity at 3% peak to peak per cm.